UC Berkeley
UC Berkeley Electronic Theses and Dissertations

Title
Electron Trajectory Reconstruction for Advanced Compton Imaging of Gamma Rays

Permalink
https://escholarship.org/uc/item/8mq6304m

Author
Plimley, Brian Christopher

Publication Date
2014

Peer reviewed|Thesis/dissertation

eScholarship.org Powered by the California Digital Library
University of California

Electron Trajectory Reconstruction for Advanced Compton Imaging of Gamma Rays

by

Brian Christopher Plimley

A dissertation submitted in partial satisfaction of the
requirements for the degree of
Doctor of Philosophy

in

Engineering – Nuclear Engineering

in the
Graduate Division
of the
University of California, Berkeley

Committee in charge:

Professor Kai Vetter, Chair
Professor Stanley Prussin
Professor Steven Boggs

Spring 2014

Electron Trajectory Reconstruction for Advanced Compton Imaging of Gamma Rays

Copyright 2014 by Brian Christopher Plimley.
All rights reserved.

Abstract

Electron Trajectory Reconstruction
for Advanced Compton Imaging of Gamma Rays

by

Brian Christopher Plimley

Doctor of Philosophy in Nuclear Engineering

University of California, Berkeley

Professor Kai Vetter, Chair

Gamma-ray imaging is useful for detecting, characterizing, and localizing sources in a variety of fields, including nuclear physics, security, nuclear accident response, nuclear medicine, and astronomy. Compton imaging in particular provides sensitivity to weak sources and good angular resolution in a large field of view. However, the photon origin in a single event sequence is normally only limited to the surface of a cone. If the initial direction of the Compton-scattered electron can be measured, the cone can be reduced to a cone segment with width depending on the uncertainty in the direction measurement, providing a corresponding increase in imaging sensitivity.

Measurement of the electron's initial direction in an efficient detection material requires very fine position resolution due to the electron's short range and tortuous path. A thick (650 µm), fully-depleted charge-coupled device (CCD) developed for infrared astronomy has 10.5-µm position resolution in two dimensions, enabling the initial trajectory measurement of electrons of energy as low as 100 keV. This is the first time the initial trajectories of electrons of such low energies have been measured in a solid material. In this work, the CCD's efficacy as a gamma-ray detector is demonstrated experimentally, using a reconstruction algorithm to measure the initial electron direction from the CCD track image. In addition, models of fast electron interaction physics, charge transport and readout were used to generate modeled tracks with known initial direction.

These modeled tracks allowed the development and refinement of the reconstruction algorithm. The angular sensitivity of the reconstruction algorithm is evaluated extensively with models for tracks below 480 keV, showing a FWHM as low as 20° in the pixel plane, and 30° RMS sensitivity to the magnitude of the out-of-plane angle.

The measurement of the trajectories of electrons with energies as low as 100 keV have the potential to make electron track Compton imaging an effective means of reducing image background for photons of energy as low as 500 keV, or even less.

The angular sensitivity of the reconstruction algorithm was also evaluated experimentally, by measuring electron tracks in the CCD in coincidence with the scattered photon in a germanium double-sided strip detector. By this method, electron tracks could be measured with the true initial direction known to within 3° FWHM, and the angular response of the algorithm compared to the known direction. The challenge of this experiment lay in the low geometric efficiency for photons scattering into the germanium, the poor time resolution in the current CCD implementation, and the resulting signal-to-background ratio of about 10^{-4} for photons scattered from the CCD into the germanium detector. Nonetheless, 87 events were measured in the FWHM of the total energy deposited and the angular resolution measure, with electron tracks between 160 keV and 360 keV in energy. The electron tracks from true coincident event sequences showed a FWHM in the pixel plane of 23°, and excellent agreement with the distribution calculated with models, with likelihood p-values of 0.44 and 0.73. Thus, the models used for the more thorough evaluation of angular sensitivities are shown to be consistent with the measured tracks from true coincident event sequences.

to the One who designed the electron

Acknowledgments

Many people have provided tremendous support to help me accomplish this doctorate degree. Even the recurring question, "How's the thesis?" from many friends, family, and colleagues has spurred me on to finish, though it may be unwelcome in the moment[1]. I want to name a few people in particular to whom I am especially grateful.

Without Kai, I would not be in the field of nuclear engineering or radiation detection, and I would perhaps not even be a scientist. It goes without saying that my accomplishments in the electron track work are largely due to the opportunities and guidance he has provided. He has been patient with me through many distractions from research, some of which I hope were productive and worthwhile.

Dan was the driving force behind much of the early experimental work, and I would have quickly been in over my head without his experience and direction. Dan and Kai together imparted the vision of electron track Compton imaging to me.

Stan has taught me many things about scientific thinking, language and writing, through our conversations over the past several years and especially through his feedback on this dissertation. I am also very grateful to Steve for joining my committee on short notice.

Amy has shared with me the ups and downs of the electron track project for the last n years. I would not have gotten far without the modeled electrons that she has continually persevered in producing and debugging.

Ryan has been very gracious even as I dumped all of my lab responsibilities on him so that I could write. In addition, I've enjoyed many engaging conversations with him on CCDs, electron tracks, fear-mongering anti-nuclear activists, and other diverse topics.

Yigong has been a committed friend and student, and a sounding board for my speculations and excogitations. Lazar has provided much encouragement and camaraderie in our late nights in 50C. And Quinn, Tim A., and Mark are continually uplifting me with their fellowship, prayers, and entertaining scientific speculations.

[1] `http://www.phdcomics.com/comics/archive.php?comicid=47`

Living Hope Evangelical Church, and the In Christ Alone college ministry, have been my Berkeley family as long as I have been here. My doctorate degree has been as much a battle of faith as of science, and I could not have come this far without this community and the continual reminders of the grace and peace that are ours to claim. Danny and Vieng have always encouraged me and reminded me of the higher things.

Brandon, Phoebe, and Mike have been the most supportive and loving friends, neighbors, and/or roommates over the last several years.

Joshua, my godson, helps remind me of the more important things of life, through smiles, frowns, moans, and giggles (but mostly frowns).

I can hardly begin to express the encouragement and faithful friendship I have found in Tim L., throughout my various struggles in graduate school.

And finally, my family has continually shown me patience and support, and my parents are always glad to welcome me home for a weekend of respite from the chaos.

Contents

Abstract 1
Acknowledgments ii
Contents iv
List of Figures vi
List of Tables x
List of Acronyms xi

1 Introduction **1**
1.1 Gamma-ray spectroscopy: source identification 1
1.2 Gamma-ray imaging: source mapping 4
1.3 Approaches to gamma-ray imaging 6
1.4 Previous work in electron track Compton imaging 10
1.5 Current work and outline 11

2 Basic Concepts **12**
2.1 Gamma-ray physics 12
2.2 Fast electron interactions in matter 17
2.3 Gamma-ray detection 28
2.4 Gamma-ray imaging 40
2.5 Summary 48

3 Experiment **49**
3.1 Setup and operation 49
3.2 Irregularities 60
3.3 Coincidence experiment 63
3.4 Summary 76

4 Models of Electron Track Images in the CCD **78**
4.1 Interactions of gamma rays and fast electrons 79
4.2 Device response 81

4.3 Tracks from the coincidence experiment 89
4.4 Summary 91

5 Data Analysis **93**
5.1 Energy measurement in the charge-coupled device 93
5.2 Trajectory reconstruction algorithm 104
5.3 Data analysis in the coincidence experiment 120
5.4 Summary 129

6 Results **130**
6.1 Metrics for angular sensitivity 131
6.2 Modeled algorithm performance 137
6.3 Results of the coincidence experiment 146
6.4 Comparison between modeled and measured error distributions 153
6.5 Summary 158

7 Conclusions **160**
7.1 Summary and highlights 160
7.2 Potential impact 162
7.3 Future work 162

Bibliography **166**

List of Figures

1.1 Illustration of the mechanics of Compton imaging, with and without the electron track. . . . 8
1.2 Electrons deviating from their initial direction . . . 9

2.1 Photon interaction cross-sections in silicon . . . 14
2.2 Compton scattering of a photon on an electron. . . . 15
2.3 Klein-Nishina differential cross section for several energies. . . . 16
2.4 The Landau probability distribution of energy loss . . . 22
2.5 Average specific energy loss of fast electrons in silicon . . . 25
2.6 Differential cross sections for various interaction mechanisms for a 300 keV electron in silicon . . . 26
2.7 The definition of extrapolated range . . . 27
2.8 Cross-sectional CCD pixel diagrams . . . 35
2.9 CCD charge shifting process . . . 36
2.10 The coordinate system defined for the CCD . . . 37
2.11 Photo of an LBL SNAP CCD wafer . . . 38
2.12 A CCD image of an electron track . . . 39
2.13 Illustration of the mechanics of Compton imaging, with and without the electron track. . . . 45
2.14 Modeled electron trajectories showing deviation from initial direction 47

3.1 Photos of the CCD readout and control electronics . . . 51
3.2 Photos of the CCD cryostat interior . . . 52
3.3 Design diagrams of the thermal mounting of the CCD . . . 54
3.4 Photos of the thermal mounting of the CCD . . . 55
3.5 Photo and thermal offset results from the thermal test device in cryostat 57
3.6 Screenshot of the main window of the Voodoo CCD control software. 58
3.7 Photo of the CCD cryostat with aluminum foil for noise reduction . . 59
3.8 An electron track showing charge transfer problems . . . 61

3.9 Black level fluctuations over time 62
3.10 An electron track traversing an undepleted region of the CCD 64
3.11 Conceptual diagrams of the coincidence experiment 67
3.12 Photos of the coincidence experiment in its final configuration 68
3.13 Photos of the Ge2 strip detector cryostat interior and exterior 70
3.14 Photos of the collimator shutter assembly 72
3.15 Conceptual diagrams of fan beam collimation 75

4.1 Benchmark of Geant4 extrapolated range to Tabata et al.'s formulae 82
4.2 A muon track 84
4.3 Distribution of measured muon widths 85
4.4 Comparison of the shapes of charge distribution from diffusion, repulsion, and their combination 87
4.5 An example Geant4 modeled track with modeled device response . . 90

5.1 Comparison of pixel offset calibration methods 95
5.2 Single-pixel energy spectrum of a ^{55}Fe source 96
5.3 An example ^{241}Am track image, illustrating the pixel segmentation threshold 98
5.4 Energy spectra from ^{241}Am showing the effect of including neighbor pixels in the segmentation 99
5.5 Measured ^{133}Ba energy spectrum of segmented tracks 100
5.6 Modeled responses from CCDs of five different pixel pitches to the same simulated track 102
5.7 The effect of read noise on modeled track images from Figure 5.6 . . 103
5.8 Diagram of angles used to define the 3D electron direction 104
5.9 Example tracks showing threshold effects 106
5.10 Example tracks showing the result of the thinning method 108
5.11 Example track showing the pixels used for measuring end energies . . 109
5.12 Example track showing the first step of the ridge-following method . 112
5.13 Example modeled track showing the selection of measurement points 113
5.14 Diagram illustrating the measurement of β 114
5.15 Example track showing the measurement of α and β 116
5.16 Example of a track which induces an "infinite loop" error 119
5.17 Example tracks in which the algorithm identifies the wrong end . . . 121
5.18 Example tracks in which the algorithm measures the correct end but performs poorly 122
5.19 Conceptual illustration of a double-sided strip detector 124

5.20 An example showing the measurement of the z position of interaction using the dt_{50} method. 125
5.21 Energy spectrum of Ge2 over the course of the coincidence experiment. 125
5.22 Conceptual illustration of the plot used to identify the true coincident event sequences. 128

6.1 An example distribution of Δ_α 132
6.2 Two examples of Δ_α distributions, with the components fitted 134
6.3 The distribution of $|\beta_{\text{true}}|$ and $|\beta|_{\text{alg}}$ for all the modeled tracks. 135
6.4 Example distributions of $|\beta_{\text{true}}|$ and Δ_β for tracks selected by $|\beta|_{\text{alg}}$. 136
6.5 An example distribution of Δ_β, with the RMS shown 137
6.6 The FWHM and f of the Δ_α distribution, as a function of electron energy and geometry 139
6.7 The RMS of the Δ_β distribution, as a function of electron energy and geometry 140
6.8 The FWHM of the Δ_α distribution, as a function of electron energy and pixel pitch 141
6.9 The peak fraction, f, of the Δ_α distribution, as a function of electron energy and pixel pitch 142
6.10 The RMS of the Δ_β distribution, as a function of electron energy and pixel pitch 144
6.11 The FWHM and f of the Δ_α distribution, as a function of electron energy and readout noise 145
6.12 The RMS of the Δ_β distribution, as a function of electron energy and readout noise 146
6.13 The energy spectrum of the CCD over the course of the coincidence experiment. 148
6.14 Summed image of all the electron tracks measured in the CCD over the course of the coincidence experiment 149
6.15 The energy spectrum of interactions in Ge2, over the course of the coincidence experiment 150
6.16 The distribution of positions of interactions in Ge2, over the course of the coincidence experiment 150
6.17 The distribution of coincidence candidate event sequences, in angular resolution measure (ARM) and total energy deposited (E_{tot}) 152
6.18 Distribution of scatter energy and β 153
6.19 The calculated and measured distributions of α and $|\beta|$ for events in the true coincidence FWHM 154

6.20 The distributions of Δ_α and Δ_β for the events in the true coincidence FWHM 155
6.21 Comparison of the measured and modeled distributions of Δ_α and Δ_β 157
6.22 The distributions of log-likelihood values produced by Monte Carlo, and the values from experiment 158

List of Tables

1.1 Isotopes relevant to nuclear security applications. 3
1.2 Isotopes relevant to nuclear accident mitigation. 4
1.3 Isotopes and other sources relevant to astronomy applications 6

2.1 Extrapolated ranges of electrons in materials. 46

5.1 Energy resolutions measured on photopeaks of ^{133}Ba and ^{137}Cs . . . 101

List of Acronyms

ACT	Advanced Compton Telescope
ADC	Analog-to-digital conversion
ARM	Angular resolution measure
BeARING	Berkeley Applied Research on the Imaging of Neutrons and Gamma rays
CCD	Charge-coupled device
CTE	Charge transfer efficiency
FWHM	Full width at half maximum
RMS	Root mean square
SBR	Signal-to-background ratio
SNAP	SuperNova Acceleration Probe
SNR	Signal-to-noise ratio

Chapter 1

Introduction

Vision has always been the primary sense by which mankind has learned about the world around us. For millenia our natural eyes observed the world around us, and then in recent centuries telescopes have revealed the universe beyond our planet, and microscopes the universe of microorganisms. Then we crafted eyes to see other kinds of light, both natural and manmade: radio revolutionized communications, and x-rays transformed medical diagnosis.

As the highest energy range of electromagnetic waves, gamma radiation is unique in that it reveals the radioactive world around us. This radioactive world was first revealed through basic types of detectors which measured the presence, and later the energy, of gamma rays from any sources nearby. Later, systems were designed to map the incident direction of the radiation, as a gamma-ray camera.

1.1 Gamma-ray spectroscopy: source identification

The precise energy of gamma radiation released in a radioactive decay is a unique fingerprint of the radioactive isotope that produced it. This property allows a radioactive isotope to be identified if the energy of its gamma-ray emissions can be measured. This field of gamma-ray spectroscopy began with detectors such as those measuring scintillation light in the 1940s and 1950s [12], and developed further with semiconductor-based detectors which could measure the energy more precisely [51]. Gamma-ray spectroscopy is useful in a number of fields.

1.1.1 Nuclear physics

Measuring the energy of gamma rays has allowed fundamental questions about the nature of the atomic nucleus to be answered. Gamma rays are released upon the transition of the nucleus from one state to a lower-energy state, so by measuring the energy, the structure of the nucleus and the forces holding it together can be studied.

Finer details of nuclear states such as spin and parity can be elucidated by measuring gamma rays in coincidence with other decay particles (alpha, beta, or other gamma rays) [56]. Some modern gamma-ray measurement systems such as Gammasphere [82] and GRETA [38] allow the characterization of complex decays through the near-simultaneous emission of several gamma rays. Nuclear physics has led to technologies such as medical imaging (MRI and PET), radiometric dating in archaeology and geology, neutron activation analysis for nondestructive assay of materials, and of course nuclear energy and many advances in reactor design.

1.1.2 Nuclear security

In 1945, the destructive potential of nuclear fission was demonstrated to the world through the atomic bombs dropped on Hiroshima and Nagasaki. In addition, the advent of nuclear fission-based reactors shortly thereafter enabled the production of many radioactive fission products. In this nuclear age, the measurement of gamma rays is an important capability for national and global security.

Terrorist organizations are known to be seeking material for nuclear or radiological attacks [89]. Nuclear attacks involve the detonation of either a nuclear warhead obtained from a state, or an improvised nuclear device using obtained weapons-grade material. A radiological attack, on the other hand, uses conventional explosives to distribute radioactive material for social and economical disruption. Both nuclear and radiological attacks are highlighted by the United States Department of Homeland Security in their mission to prevent terrorism and enhance security [39].

Many of the materials required for these types of weapons emit characteristic energies of gamma radiation. Some examples are shown in Table 1.1. Detection of the gamma radiation from the material, for example during transport, may be useful for interdicting the material. The international Nuclear Security Summit in March 2014 named "enhanced detection capability" as a useful tool to help combat the trafficking of nuclear and radiological materials [92]. In some cases the material may be shielded such that most gamma rays are absorbed and cannot be detected, and other methods of detection are necessary. However, the grave consequences of these types of attacks imply that every available tool should be utilized.

Isotope	Origin; significance	Half-life (yr)	Energies of significant gamma rays (keV)
^{235}U	naturally occurring; enriched in nuclear fuel and nuclear weapons material	7.04×10^8	186
^{239}Pu	produced in reactors; primary isotope for nuclear weapons	2.411×10^4	none of significant intensity
^{137}Cs	prevalent fission product; common industrial source	30.08	662
^{60}Co	neutron capture on ^{59}Co; common medical and industrial source	5.27	1173 1332

Table 1.1: Some radioactive isotopes relevant to nuclear security applications. ^{235}U and ^{239}Pu are the two most common fissile isotopes in nuclear weapons, while ^{137}Cs and ^{60}Co could be used in radiological weapons. Isotopic data taken from [46]; origin and significance from [42].

1.1.3 Nuclear accident mitigation and safety

Radioactive material may be released into the environment not only by malicious intent, but also through accidents and natural catastrophes where radioactive material is produced or stored, in particular at nuclear reactors. The Chernobyl disaster of 1986 spread large amounts of radiological contamination through an explosion and fire, as a result of operator error as well as poor reactor safety design and management [66]. More recently, the tsunami following the magnitude 9.0 Tōhoku earthquake in Japan in 2011 caused a loss of power at the Fukushima Daiichi nuclear power plant, ultimately resulting in meltdown and large releases of radioactivity into the environment [37]. The health risks of concentrated radioactivity near the accident sites necessitate the evacuation of local residents until or unless the area can be decontaminated to a safe level.

In these situations, detection of gamma radiation is critical to evaluating the level of contamination. The radioactivity released at Fukushima and Chernobyl was in the form of many isotopes [8, 104]. Several of the most significant isotopes are listed in Table 1.2. Almost all of the isotopes emit gamma rays with characteristic energies, including the primary releases from Fukushima of iodine and cesium [117].

Isotope	Half-life (yr)	Energies of significant gamma rays (keV)
^{132}Te	3.204 days	228
^{131}I	8.02 days	364
^{103}Ru	39.26 days	497
^{95}Zr	64.02 days	724 757
^{134}Cs	2.065	569 605 796
^{90}Sr	28.79	none
^{137}Cs	30.08	662

Table 1.2: Some of the most common radioactive isotopes released from nuclear accidents such as at Chernobyl and Fukushima [8, 104, 117]. Isotopic data taken from [46].

With gamma-ray spectroscopy, leaks of radioactive material can be identified, and the quantity of radiation present in an area can be evaluated for health risks.

1.2 Gamma-ray imaging: source mapping

Gamma-ray imaging requires a system capable of measuring the incident direction of detected gamma rays. Imaging can be useful for localizing an unknown source, for example in mapping the radioactive contamination over an area in a single measurement, instead of performing a large number of measurements using a non-imaging detector. Most often, imaging is combined with spectroscopy in one instrument.

However, on a more fundamental level, imaging can allow the distinction between gamma rays from the source of interest and gamma rays from natural background or other sources. Thus, even if the source location is known, imaging may enable a more precise measurement of the source activity, energy, or other characteristics by allowing most of the background radiation from the surrounding environment to be ignored. For example, in detecting illicit nuclear material at a transportation checkpoint, the rate of naturally-occurring radiation from the environment may vary significantly with weather, but a high rate of radiation from a compact object might be cause for alarm. This background reduction will be discussed mathematically in the next chapter.

Gamma-ray imaging can improve spectroscopy by reducing background for the applications above, but in other applications, the imaging capability is absolutely necessary.

1.2.1 Nuclear medicine

Gamma-ray imaging was first developed for use in medicine [4]. Nuclear radiation can be used to treat cancer by damaging and killing the cancer cells. However, gamma rays can also be used to trace the path of various biological substances in the body, if the substances are marked with a radioactive isotope. This is useful for locating cancerous tumors, because they require more energy than most other cells, and therefore preferentially absorb glucose. Alternatively, the transport of many substances can be tracked in order to understand normal transport or diagnose problems. Medical imaging with gamma-rays is used on animals such as mice, rats, or pigs for testing and understanding the basic biology, as well as on humans for diagnosis and treatments.

Two types of gamma-ray imaging are particularly useful in nuclear medicine. Single photon emission computed tomography, or SPECT [131], measures gamma rays emitted from the body in multiple directions in order to generate a three-dimensional map of the source location. Positron emission tomography, or PET [90], utilizes the annihilation of positrons, the antimatter equivalent of the electron. The annihilation occurs near the radioactive source, and releases two photons at gamma-ray energies in roughly opposite directions. The measurement of these two photons defines a line on which the source is located.

1.2.2 Gamma-ray astronomy

Gamma-ray imaging in astronomy is essential for correlating measured radiation with features observed in other wavelengths of light. In addition to radioactive isotopes produced in heavy stars and supernovae, photons in the energy range of keV, MeV and above are produced directly by various energetic electromagnetic interactions, due to the astronomical energy scale of cosmic events.

Table 1.3 shows a number of photon sources important in gamma-ray astronomy. Isotopes such as ^{26}Al and ^{56}Ni measure nucleosynthesis and the dynamics of massive stars and supernovae. Precise measurements of the concentration of these isotopes in various astronomical objects can provide a reference for models of stellar evolution and supernovae. On the other hand, ^{22}Na is predicted by current theories of novae on the surface of oxygen-neon type white dwarfs, but has not yet been detected directly [22]. Improved gamma-ray telescopes can clarify our scientific understanding, not

Isotope or Source	Origin; significance	Half-life (yr)	Energies of significant gamma rays (keV)
^{26}Al	fusion in heavy stars; indicates star forming regions and supernovae [93]	7.17×10^5	1809
^{22}Na	novae in oxygen-neon white dwarfs; constrains novae models	2.6	1275
^{56}Ni	fusion in Type 1A supernovae; differentiates Type 1A supernovae progenitors	6 days	158 812 847† 1238†
annihilation of positrons with electrons	the relative importance of sources of positrons in our galaxy are not well understood	n/a	511 keV
energetic electrons	active galactic nuclei, black holes, neutron stars, pulsars, cosmic ray interactions	n/a	MeV–TeV

Table 1.3: Sources of gamma rays relevant to astronomy. Isotopic data taken from [46], origin and significance from [22] unless already cited.
†Actually emitted after the decay of a daughter isotope in the decay chain.

only of many astrophysical processes, but also of the history of the universe and the synthesis of all heavy elements.

1.3 Approaches to gamma-ray imaging

Gamma rays are more difficult to image than visible light, because photons at gamma-ray energies do not refract to the extent that optical photons do. In other words, gamma rays cannot be focused with a simple lens. Therefore, more subtle methods of measuring the incident direction of gamma rays must be utilized.

It is evident from Tables 1.1, 1.2, and 1.3 that the energies of relevant photons are almost entirely in the range of 100 keV to 2 MeV, with the energies of photons

emitted by most sources in the range of 500 keV. This energy range defines which imaging methods will be effective.

In general, the imaging instrument must be capable of measuring the incident direction of gamma rays that it detects, and it must have enough mass of sensitive material for many gamma rays to interact within it. The weight of the detection material might not be reduced without decreasing the efficiency for measuring gamma rays, but the volume can at least be minimized by using a dense detection material. For all of the above applications, a more compact-sized instrument is desirable from an operational perspective, and for several applications, a compact size is essential. In security and accident applications, a portable instrument is advantageous or necessary for efficient searching for, or mapping of, source material. In medicine, a more compact instrument can measure gamma rays closer to the patient, providing more precise information on the source location inside the body. In astronomy, the instrument must be placed in orbit, and cargo space is very limited.

A few basic approaches of gamma-ray imaging are presented here, and then the advanced method which is the focus of this work.

1.3.1 Collimator-based imaging

The simplest types of imaging use dense materials such as lead to absorb gamma radiation in a certain mask pattern or geometry in front of the detector. Such a mask is called a collimator. A collimator with a single pinhole in it can be used for imaging, because the pattern of interactions in the detector behind the mask is an inverted map of the incident angles of radiation on the pinhole. The Anger camera as well as many modern medical gamma-ray cameras uses a parallel-hole collimator, with many narrow holes through the mask in order to only admit photons which have trajectories parallel to the holes. When placed close to a target, the map of interactions in the detector directly indicates the map of the emitted gamma rays.

A more advanced method uses a unique pattern of collimator elements, called a coded mask. Measuring the position of the shadow of these elements on the detector allows the location of a source to be determined.

Collimator-based imaging can be very effective for photon energies below about 200 keV, which are easily absorbed in about a centimeter of lead. However, as the photon energy increases, a thicker collimator is required in order to be effective. For higher photon energies, Compton imaging can be effective instead.

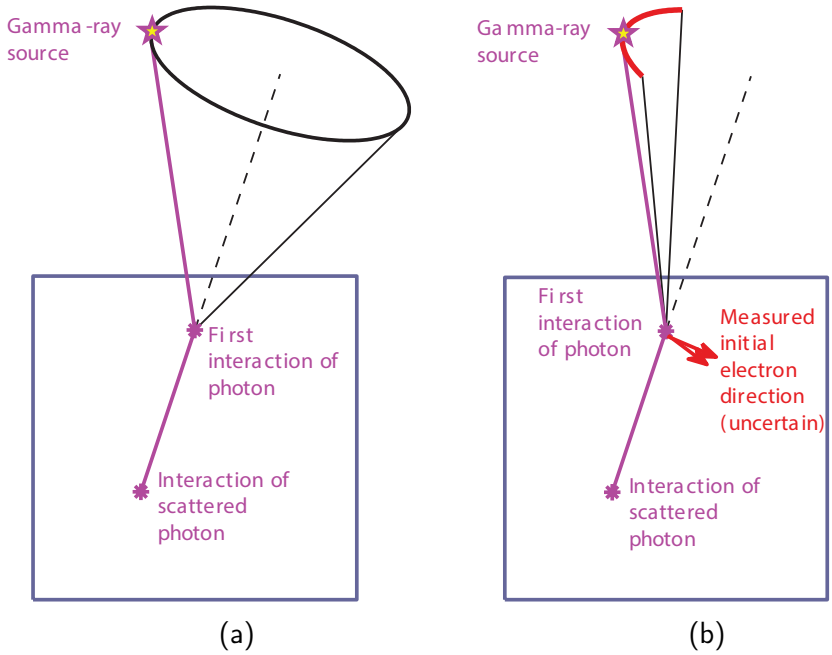

Figure 1.1:
(a) An interaction sequence of conventional Compton imaging, producing a full cone of possible locations of the source of the photon.
(b) An interaction sequence of electron track Compton imaging, producing a cone segment of possible locations of the source of the photon. In both cases, the axis and the opening angle of the cone have an uncertainty, but this can be small (a few degrees) for semiconductor detector systems.

1.3.2 Compton imaging

Compton imaging uses the positions and energies of gamma-ray interactions to calculate a cone of possible source locations for each measured gamma ray, as illustrated in Figure 1.1a. This method was first developed in the 1970s [109, 123], and since then improved in resolution through design and detector developments [5, 20, 127]. Compton imaging provides a cone of possible source locations for each measured source photon, while maintaining a large field of view, although at a cost of requiring a detector that can provide precise measurement of photon interaction energies and positions. This imaging modality can be effective for photons between roughly 300 keV and 3 MeV, depending on the detector material and design.

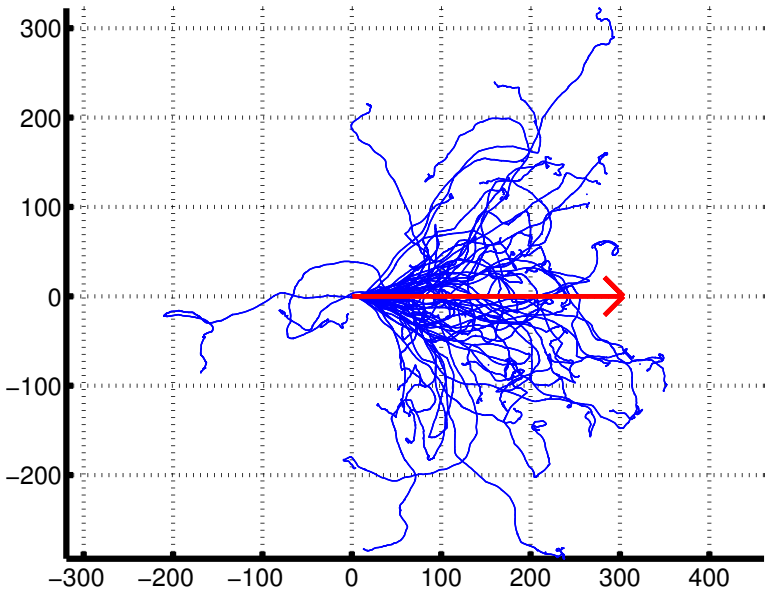

Figure 1.2: Electrons quickly lose their initial direction through interactions in material. Here, each electron begins at (0,0) and moves to the right (red arrow) with 300 keV of energy in silicon (2.33 g/cm^3). Both axes are in units of micrometers.

1.3.3 Electron track Compton imaging

The cone of possible source locations can be reduced to a single ray in space, if the instrument measures the initial path of the electron on which the gamma ray scatters (Figure 1.1b). Uncertainties in the measurement of the initial electron direction result in a cone segment rather than a ray. Compton imaging with measurement of the initial electron direction is known as *electron track Compton imaging*. The reduction of the full cone to a cone segment allows a greater separation between background radiation and source radiation as described in section 1.2.

However, tracking the electron's initial direction is challenging to measure precisely, because the electron deviates from its initial direction within a short distance, as shown in Figure 1.2. Each blue track is a two-dimensional projection of a modeled electron track (Chapter 4), each of which starts at the same location with the same initial direction. The average distance over which the initial direction is lost depends on the material and the electron energy. As will be discussed in Chapter 2, the distance is longer for higher electron energies and less dense materials. However, less dense materials require more volume in order to have enough material to detect enough gamma rays to form an image. The challenge arises because the electron energy is always lower than the incident photon energy, and dense materials are needed

to design an instrument with a compact size.

1.4 Previous work in electron track Compton imaging

Electron tracking has been performed as an aspect of particle physics for many decades, to understand the interactions and decays of various nuclear particles. This particle tracking has been done, for example, in cloud chambers [53], bubble chambers [29], spark chambers [48], and silicon strip detectors [9]. For advanced Compton imaging, however, the development has been more recent, and electron tracking for Compton imaging has been secondary to the tracking of electron-positron pairs for imaging much higher energy photons.

The first electron tracking imager was the Tracking and Imaging Gamma-Ray Experiment (TIGRE) developed in the 1990s for astronomy [124]. TIGRE used 16 layers of silicon in a double-sided strip configuration (see section 2.3.5) to track the electron's path from one layer to the next. Each layer was 300 µm thick, limiting tracking to electrons with energy greater than about 300 keV on average[1].

Two other projects utilizing electron track Compton imaging have followed TIGRE. First, the MEGA project (Medium-Energy Gamma-ray Astronomy) used a very similar implementation as TIGRE, although only electrons above about 500 keV could be tracked [47, 133].

Second, a micro-TPC (time projection chamber) has been utilized with various fill gases for electron track Compton imaging [99, 119, 125]. The imager can track electrons from gamma rays as low as 364 keV [68], but only with an argon/ethane gas mixture at atmospheric pressure, which is very low density. Denser gas mixtures result in a shorter electron track, so that electron track Compton imaging can only be performed for higher photon energies.

In order for electron track measurements to improve Compton imaging for photon sources in the range of 500 keV while maintaining high detector density, a detector is needed that can measure a very short distance of electron path. None of the detector implementations described so far have this capability.

[1] The value of 300 keV is estimated from modeled results indicating that TIGRE could track electrons from 9 %, 57 %, and 82 % of gamma rays at 511 keV, 1 MeV, and 2 MeV, respectively [16]. A threshold of 300 keV on the Compton continuum for each energy gives roughly the correct percentages.

1.5 Current work and outline

Scientific charge-coupled devices (CCDs) can have the combination of features needed to measure electron paths at high resolution [60, 112]. These CCDs have the necessary position sensitivity (10.5 μm in two spatial dimensions) in solid-state silicon, which is dense enough for a compact instrument but has low enough electron density to allow measureable electron track lengths.

The remainder of this dissertation will describe electron track measurements with silicon CCDs, including an algorithm to measure the initial electron direction, an experiment to demonstrate the electron track Compton imaging, and models to explore the potential direction sensitivities.

In Chapter 2, the essential scientific and technical concepts and formulae will be presented briefly. The topics include gamma-ray interactions, fast electron interactions, gamma-ray detection principles, and gamma-ray imaging.

The experimental methods are described in Chapter 3, beginning with a more thorough description of the particular device used in this work, and the methods of operation. In addition, a coincidence experiment using an additional detector is described, which provides measured electron tracks with a known initial direction, and allows electron track Compton imaging to be performed.

Chapter 4 presents the models which are essential to developing the electron tracking algorithm, and understanding the algorithm's effectiveness. The models include the physics of electron interactions, as well as the CCD response.

The angular sensitivity, and thus image background reduction, depends on the precision with which the initial direction of each electron can be measured. This is accomplished through the tracking algorithm described in Chapter 5. The more fundamental methods of calibrating the CCD image and segmenting out individual tracks are also explained, along with their basic performance.

The tracking algorithm's angular sensitivity is discussed thoroughly in Chapter 6. Most of the results are calculated using modeled tracks, since they intrinsically carry the knowledge of the true track direction for comparison. However, the coincidence experiment provides experimental data for the algorithm performance. The models and experiment are also compared for consistency.

These methods and results will demonstrate that scientific charge-coupled devices can effectively measure the initial direction of electrons of energy as low as 100 keV. These CCDs have the potential to be used for electron track Compton imaging of a wide variety of relevant gamma-ray sources in a compact package.

Chapter 2

Basic Concepts

Some background information is necessary to understand the research presented in the remaining chapters. This background includes the physics of gamma-ray interactions, energetic electron interactions and radiation detectors (silicon charge-coupled devices in particular), and basic concepts in gamma-ray imaging (electron track Compton imaging in particular). In all of these categories, the essential and relevant concepts are presented, while most of the details are left in the references.

2.1 Gamma-ray physics

Sources and interactions of gamma rays are essential for any discussion of a gamma-ray detector. In particular, the process of incoherent (Compton) scattering is fundamental to Compton imaging.

2.1.1 Sources of photons at gamma-ray energies

Strictly speaking, gamma rays are photons emitted through de-excitations of atomic nuclei. However, other electromagnetic processes also release photons in the same range of energy as gamma rays. A gamma-ray detector does not inherently distinguish among methods of photon production, so all of these methods are relevant to detection and imaging.

Nuclear de-excitations commonly occur in the daughter nucleus after an atom of a radioactive isotope undergoes α or β decay. This process produces the gamma rays from the isotopes in Tables 1.1, 1.2, and 1.3. In addition, energetic collisions between nuclei can excite a nucleus to an excited state from which it decays with the emission of a gamma ray. This occurs in particle accelerator targets, for example.

Another process generating a discrete energy of photon is the annihilation of a positron and electron, which produces two photons of about 511 keV each. In addition, several processes involving energetic electrons (at least keV or MeV in energy) can generate high-energy photons over a continuum of possible photon energies. These processes include the acceleration of electrons in the electric field of a nucleus (producing bremsstrahlung), acceleration of electrons in a strong magnetic field (producing synchrotron radiation), and energy transfer from an energetic electron to a low-energy (e.g. optical) photon. All of these processes are observed in astronomy as mentioned in Table 1.3, as well as in ground-based environments such as particle accelerators and medical x-ray machines.

2.1.2 Gamma-ray interactions[1]

Gamma rays can interact with matter through several processes. The dominant interaction depends on the photon energy, E, and material atomic number, Z. Figure 2.1 shows the energy dependence of interactions in silicon, each of which will be described in the next sections.

The mean free path for gamma rays, λ, is defined as the depth of material after which exactly $1/e$ of the initial photons will not have interacted yet. This quantity is useful because gamma rays tend to travel some centimeters before interacting. The mean free path can be calculated from the microscopic cross sections:

$$\lambda(E, Z) = \left(n \sum_i \sigma_i \right)^{-1} \tag{2.1}$$

In this equation, n is the number density of atoms, and σ_i is the microscopic cross section for an interaction of type i.

2.1.3 Photoelectric absorption

At low energies, the predominant interaction is the complete absorption of a photon, with the majority of the energy going to an atomic electron, and a small recoil of the remaining atom.

The scaling of the cross section for photoelectric absorption can be described approximately by

$$\sigma_{\mathsf{PE}} \propto \frac{Z^{4.5}}{E^{3.5}}. \tag{2.2}$$

[1] See section 14.2 of Prussin [106].

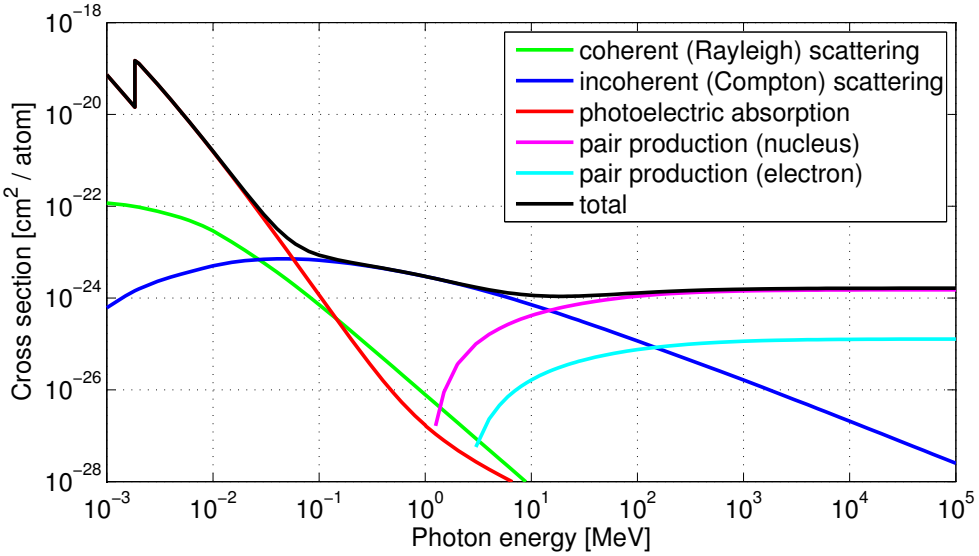

Figure 2.1: The cross sections for interactions of high-energy photons in silicon, as a function of energy. Data from [13].

The cross section scales strongly with Z, because more tightly bound atomic electrons are favored; the stronger coupling between electron and atom allows the gamma ray to transfer momentum to the atom more effectively [106]. In addition, at photon energies below the binding energies of electron shells in the atom, the cross section is reduced because those electrons are not energetically available for absorption.

In silicon, photoelectric absorption is the dominant interaction below about 60 keV.

2.1.4 Incoherent scattering

At medium energies, the dominant interaction is an inelastic scattering of the photon on an atomic electron, transferring some fraction of the photon energy to the electron. Incoherent scattering is often simplified to the case in which the recoil electron is initially unbound and at rest; this approximation is known as Compton scattering and is illustrated in Figure 2.2. ("Compton scattering" is also used as a general term for incoherent scattering, even when the initial electron momentum and binding energy are not negligible.) The incoherent scattering process is the basis for Compton imaging.

In the Compton approximation, the energy of the scattered gamma ray, E', is

$$E' = \frac{E}{1 + E/m_0c^2(1 - \cos\theta)}, \tag{2.3}$$

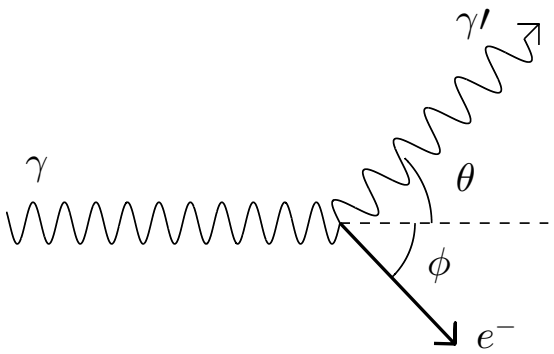

Figure 2.2: Compton scattering of a photon on an electron.

in which m_0c^2 is the rest energy of an electron and θ is the scattering angle [34]. From equation 2.3 it is evident that forward scatters transfer a small amount of energy, approaching $E - E' = 0$ as θ approaches 0; while backscatters transfer a maximum energy, $E - E' = E/(1 + 2E/m_0c^2)$ at $\theta = 180°$. This relationship between photon energies and scattering angle will allow the Compton "cone" to be calculated on an event-by-event basis, as explained in section 2.4.3.

The nonzero binding energy and initial momentum of the atomic electron on which the photon scatters, which cannot be measured, produce an uncertainty in the relationship between energy and scattering angle. An ideal measurement of the photon energies, then, restricts the possible scattering angle to a range of angles. This range of possible scattering angles is small, if the photon energy is much greater than the electron binding energy.

The electron scatters at an angle ϕ from the initial direction of the gamma ray, ranging from 0° to 90°, which can be found through conservation of momentum and energy for the Compton approximation:

$$\cos\phi = \frac{1 + \frac{m_0c^2}{E}}{\sqrt{1 + \frac{2m_0c^2}{E-E'}}}, \tag{2.4}$$

where E and E' still correspond to the gamma-ray energies, and the electron is in the same plane as the initial and scattered gamma ray. Again, the binding energy and initial electron momentum contribute to an uncertainty in the angle and non-coplanar scattering.

The differential cross section for scattering into a differential solid angle depends on the photon energy, and is given by the Klein-Nishina formula [73] for the Compton

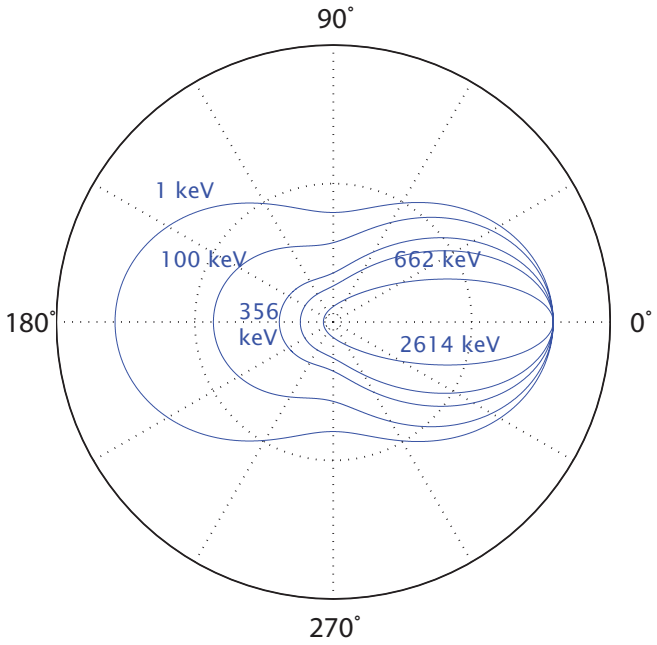

Figure 2.3: Klein-Nishina differential cross section. Energies of 1, 100, 356, 662, and 2614 keV from outside to inside. The angular axis represents scattering angles; the radial axis represents differential cross section per atomic electron, with a maximum value of 7.9×10^{-26} cm^2/sr at 0°.

approximation:

$$\frac{d\sigma_{\mathrm{CS}}}{d\omega} = Zr_0^2 \frac{1+\cos^2\theta}{2\left[1+\alpha(1-\cos\theta)\right]^2}\left(1+\frac{\alpha^2(1-\cos\theta)^2}{(1+\cos^2\theta)\left[1+\alpha(1-\cos\theta)\right]}\right) \tag{2.5}$$

Here, $r_0 \equiv e^2/m_0c^2$ is the classical electron radius, θ is the scattering angle, and $\alpha \equiv E/m_0c^2$. Because the gamma ray does not need to transfer momentum to the atom as in photoelectric absorption, the cross section depends only on the total number of electrons in the atom (Z). The differential cross section is plotted for several energies in Figure 2.3. This cross section is strongly peaked in the forward direction for higher energies of photons. The distribution of scattering angles defined by equation 2.5 is particularly significant for Compton imaging, because multiple interactions must be measured in the detection system for each photon.

Incoherent scattering is the dominant interaction mode in silicon from about 60 keV to 15 MeV.

2.1.5 Pair production in the field of the nucleus

At energies above $2m_0c^2 = 1022\,\text{keV}$, it is energetically possible for a photon to be converted into an electron-positron pair, in the electric field of an atomic nucleus which recoils to conserve momentum. The energy of the photon is shared by the electron and positron, and the atomic nucleus undergoes a small recoil. Conservation of momentum sends the two particles forward at an acute angle from the photon direction. After losing most of its kinetic energy, the positron will annihilate with an atomic electron.

The cross section for pair production increases sharply with energy, and scales with Z^2. In silicon, pair production is the dominant interaction above about 15 MeV.

2.1.6 Other interactions

Pair production can also occur in the Coulomb field of an electron at photon energies above $4m_0c^2 = 2044\,\text{keV}$ [43]. The cross section is smaller than that of nuclear pair production at all energies.

Two types of elastic scattering are significant, although not dominant, at low energies (below about 100 keV in silicon). In Thompson scattering, the photon scatters elastically on a single atomic electron [106]. In Rayleigh scattering, also known as coherent scattering, the photon interacts coherently with all electrons of an atom, and scatters elastically [106]. In both cases, the photon does not lose energy, but changes direction.

All three primary interaction mechanisms (photoelectric absorption, incoherent scattering, and pair production) result in energetic electrons in the interaction medium. The next section describes the interactions of these fast electrons.

2.2 Fast electron interactions in matter[2]

The primary interactions of gamma rays in matter all produce energetic electrons, which then transfer energy into various forms in the material. That energy transfer occurs through a variety of interactions as the electron travels and scatters through the material. Electron interactions are fundamental to the measurement of the electron trajectory for electron track Compton imaging, and each mode of interaction described here has specific consequences for electron direction measurements.

All of the relevant modes of interaction arise from Coulomb interactions between the fast electron, known as the primary electron, and either atomic electrons or nuclei.

[2] See chapters 18 through 20 of Evans [43].

The modes relevant to electrons in the range of 10 keV to 1 MeV can be described as inelastic scattering on atomic electrons ("soft" and "hard" collisions), elastic scattering on nuclei, and inelastic scattering on nuclei (usually producing bremsstrahlung). An exact and comprehensive calculation of cross sections for these processes depends on the subtleties of atomic shell effects and is beyond the scope of this work, although approximate calculations of energy loss and differential cross sections are shown later in Figures 2.5a and 2.6.

Throughout this section the following variables are defined:

- T, the kinetic energy of the primary electron
- Q, the energy transferred to a single secondary particle such as an atomic electron
- N, the number density of atoms
- Z, the atomic number of the material
- I, the geometric mean of all ionization and excitation energies in an atom of the material
- β, the primary electron velocity in units of the speed of light in vacuum
- m_0c^2, the rest mass energy of the electron
- e, the elementary charge
- σ, a cross section for interaction
- ds, a differential path length of the primary electron
- θ, the angle through which the primary electron scatters
- $d\omega$, a differential solid angle into which the primary electron scatters

The quantities of interest will be *specific energy loss* (dT/ds), *differential cross section* in angle ($d\sigma/d\omega$), and differential cross section in energy ($d\sigma/dQ$). Not all of these quantities will be relevant for each type of interaction.

2.2.1 Electron collisions

Atomic electrons in the vicinity of the primary electron path will experience a Coulomb repulsion which may be sufficient to excite or ionize the atom (or in a semiconductor, to promote an electron to the conduction band, as described in section 2.3.4). In the limit of an unbound electron, the energy imparted to an atomic electron depends on the distance between the atomic electron and the path of the primary electron; an atomic electron directly in the path will receive all of the primary electron's kinetic energy, like the head-on collision of two billiard balls.

The cross section for Coulomb interactions between a charged particle and stationary electrons was derived classically by Bohr [23], and adjusted for the effects of relativity and exchange of identical particles by Møller [88]. The general form of this differential cross section is

$$\frac{d\sigma_{\mathsf{EC}}}{dQ} = \frac{2\pi e^4}{\beta^2 m_0 c^2}\left(\frac{1}{Q^2}\right)\left(\frac{T}{T-Q}\right)^2 \tag{2.6}$$

with additional second-order factors for relativity and quantum mechanics [43]. Since the colliding particles are indistinguishable, T is defined as the greater energy after scattering, and Q the lesser. Because of the identical particles, the cross section is defined for $0 \leq Q \leq T/2$, and it is symmetric between Q and $T-Q$.

The $1/Q^2$ scaling of the cross section strongly favors interactions at lower energies. Therefore, the vast majority of electron collisions are "soft" collisions and impart an energy near the ionization energy or less, while a few collisions are "hard" collisions which transfer a significant fraction of the primary electron's energy. A boundary between these two collision regimes can be defined at several times the atomic binding energy, so that "hard" collisions can be approximated as scattering between free electrons [43].

2.2.2 Soft electron collisions

Most secondary electrons will only receive a small amount of energy, and cause a very small deflection in the primary electron trajectory. Because soft collisions occur at intervals similar to atomic separations, in many measurements it appears as a continuous energy loss along the path of the electron, so it is considered *pseudo-continuous*. It is also the dominant form of energy loss along the electron path, due to the $1/Q^2$ in equation 2.6.

The average energy loss due to soft electron collisions can be calculated by taking

a differential cross section of the form in equation 2.6 and integrating.

$$-\left.\frac{dT}{ds}\right|_{\mathsf{SEC}} = NZ\int_{Q_{\mathsf{min}}}^{H} Q\frac{d\sigma_{\mathsf{EC}}}{dQ}\,dQ \tag{2.7}$$

The maximum energy transfer is H, the boundary between soft and hard collisions. A minimum energy transfer, Q_{min}, must be included to keep the result finite. This corresponds to a minimum excitation energy for the average atomic electron. It can be approximated as an average excitation energy, I. Then the average specific energy loss for soft collisions, calculated by Bethe including relativistic effects [15], is

$$-\left.\frac{dT}{ds}\right|_{\mathsf{SEC}} = \frac{2\pi e^4}{m_0c^2\beta^2}NZ\left[\ln\frac{2m_0c^2\beta^2H}{I^2(1-\beta^2)} - \beta^2\right]. \tag{2.8}$$

The β^2 in the denominator indicates that the specific energy loss decreases with energy.

Soft electron collisions are the primary means of energy loss for any electrons with energy greater than about the minimum excitation energy. Soft collisions also contribute to a gradual deviation of the electron from its initial direction.

2.2.3 Hard electron collisions

If an atomic electron is close enough to the path of the primary electron, a significant fraction of the primary energy can be transferred to the atomic electron. This secondary electron can then travel a significant distance and collide with many more electrons. This higher-energy secondary electron is known as a *recoil electron* (or elsewhere sometimes as a knock-on electron or δ-ray).

The differential cross section of hard electron scattering at angle θ, as calculated by Rutherford per atomic electron, is

$$\frac{d\sigma_{\mathsf{HEC}}}{d\omega} = \left(\frac{e^2}{m_0c^2}\right)^2\left(\frac{1}{\beta^4}\right)\left(\frac{1}{\sin^4\theta} + \frac{1}{\cos^4\theta}\right)4\cos\theta, \tag{2.9}$$

for $0 < \theta < \pi/4$ such that θ is defined as the scattering angle of the more energetic scattering product. The cross section increases as the scattering angle approaches zero, corresponding to Q approaching zero in equation 2.6.

The average energy transfer to recoil electrons in hard collisions can be calculated similarly to that of soft collisions,

$$-\left.\frac{dT}{ds}\right|_{\mathsf{HEC}} = NZ\int_{H}^{T/2} Q\frac{d\sigma_{\mathsf{EC}}}{dQ}\,dQ. \tag{2.10}$$

However, since the cross section decreases as the energy transfer increases, hard collisions are infrequent events, although they may represent significant energy transfers when they do occur.

Recoil electrons appear as a branch from the path of the primary electron. However, from equation 2.6 lower energy recoils are more common, with short electron ranges. For example, a 10 keV electron has an extrapolated range of only 1.1 µm in silicon. Because of this, in a detector of finite position resolution, hard collisions often appear as point-like (discrete) depositions of significant energy.

In terms of angular deviation of the primary electron, the larger the energy transfer in the electron collision (the "harder" the collision), the greater the angular deviation. The upper limit of the scattering angle in the non-relativistic case is 45°, corresponding to a transfer of half of the primary kinetic energy to the atomic electron. (As mentioned above, a transfer of more than half of the energy can be represented by exchanging the identical particles.) The $1/Q^2$ in equation 2.6 indicates that larger energy transfers have a much smaller cross section than smaller energy transfers. Correspondingly, the $1/\sin^4\theta$ in equation 2.9 indicates that larger scattering angles (from the larger energy transfers) have a much smaller cross section than small scattering angles. (An example of this cross section dependence is presented later, in Figure 2.6.)

2.2.4 Total collisional energy loss

Soft electron collisions produce a pseudo-continuous energy loss along the path of the electron, while the occasional hard collisions deposit greater energy in a localized area, and may appear as a branch from the main track if the recoil electron's range is long enough (compared to the detector's position resolution, defined in section 2.3.2). The average total specific energy loss to electron collisions is simply

$$\left.\frac{dT}{ds}\right|_{\mathsf{EC}} = \left.\frac{dT}{ds}\right|_{\mathsf{SEC}} + \left.\frac{dT}{ds}\right|_{\mathsf{HEC}}. \tag{2.11}$$

The specific energy loss for hard collisions may be evaluated using assumptions more accurate than those used in equation 2.8. However, in practice the exact assumptions have little effect, because the differences are small and the average energy loss is dominated by soft collisions. Thus, the total energy loss can be approximated as

$$\left.\frac{dT}{ds}\right|_{\mathsf{EC}} \approx \left.\frac{dT}{ds}\right|_{\mathsf{SEC}} \left(H = \frac{T}{2}\right) \tag{2.12}$$

as described in Evans [43].

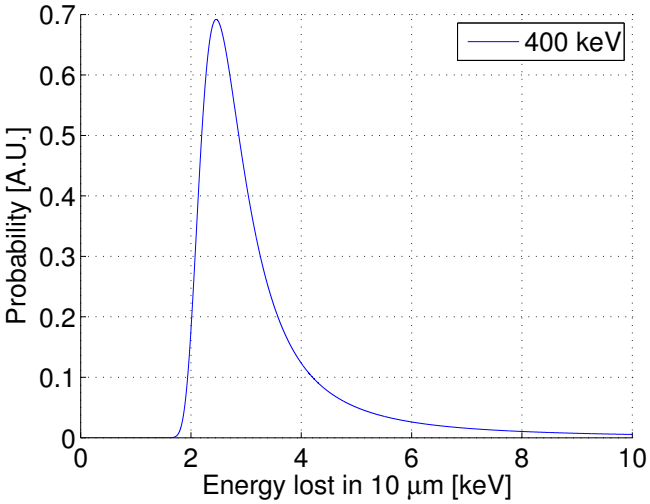

Figure 2.4: Distribution of energy lost in 10 µm of silicon for 400 keV electrons due to electron collisions. The curve was calculated using [130].

The probability distribution of energy loss due to electron collisions for primary electrons of a given energy consists of a sharp peak corresponding to soft collisions and a high-energy tail corresponding to hard collisions. The shape was first calculated by Landau [80, 121, 130]. Figure 2.4 shows this Landau distribution for 400 keV electrons in silicon traveling 10 µm.

2.2.5 Elastic nuclear scattering

Elastic nuclear scattering is a Coulomb interaction between the primary electron and a nucleus. Because the nucleus is more than three orders of magnitude more massive, the electron can scatter at any angle and deposit a negligible amount of energy. As with electron collisions, the cross section for elastic nuclear scattering increases sharply for lower-angle scatters.

The classical differential scattering cross-section was derived by Rutherford.

$$\frac{d\sigma_{\mathsf{ENS}}}{d\omega} = \frac{Z^2}{4}\left(\frac{e^2}{m_0 c^2}\right)^2 \left(\frac{1-\beta^2}{\beta^4}\right) \frac{1}{\sin^4(\theta/2)} \tag{2.13}$$

Additional second-order corrections for quantum mechanics and relativity reduce the cross section at larger scatter angles [85]. As with electronic scattering, the cross section increases sharply as the scattering angle approaches zero, so nuclear scattering most frequently occurs at small angles.

Equation 2.13 is similar to equation 2.9, with differences arising from the greater mass and charge of the nucleus and the non-identical particles. However, nuclear scattering scales with Z^2 per atom, while electron scattering scales with the number of electrons per atom, Z, so elastic nuclear scattering is increasingly important at higher Z.

Elastic nuclear scattering allows the primary electron to deviate significantly from its initial direction in a single collision. Along with soft electron scattering, elastic nuclear scattering is an important means by which the fast electron loses its initial direction. Unlike hard electron collisions, the scattering on a nucleus is not marked by an increased energy loss or additional particle track.

2.2.6 Bremsstrahlung production

In a nuclear scattering interaction, the electron may also transfer energy inelastically through either nuclear excitation or emission of a photon. Nuclear excitation is much less common, and is ignored here. The radiation emitted in inelastic nuclear scattering is known as bremsstrahlung. In bremsstrahlung production, like elastic nuclear scattering, the electron can scatter through a large angle. The differential cross section in energy is

$$\frac{d\sigma_{\text{brems}}}{dQ} = \frac{1}{137}\left(\frac{e^2}{m_0c^2}\right)^2 BZ^2\frac{T+m_0c^2}{TQ}, \tag{2.14}$$

where B is a slowly varying function of Q, T, and Z, with values of order 10 [43]. Again, the scattering is most likely for a small Q.

The average specific energy loss due to bremsstrahlung emission is

$$-\left.\frac{dT}{ds}\right|_{\text{brems}} = N\int_0^T Q\frac{d\sigma_{\text{brems}}}{dQ}\,dQ \tag{2.15}$$

$$= \frac{NZ^2}{137}\left(\frac{T+m_0c^2}{T}\right)\left(\frac{e^2}{m_0c^2}\right)^2\int_0^T B\,dQ \tag{2.16}$$

which can be approximated [76] as

$$-\left.\frac{dT}{ds}\right|_{\text{brems}} = \frac{NZ^2(T+m_0c^2)}{137}\left(\frac{e^2}{m_0c^2}\right)^2\left(4\ln\frac{2(T+m_0c^2)}{m_0c^2}-\frac{4}{3}\right). \tag{2.17}$$

However, like hard electron scattering, the energy loss occurs infrequently in discrete events, rather than pseudo-continuously.

Radiative emission is uncommon at energies below 10 MeV in silicon, compared to the other modes of interactions. However, when it does occur, the photon may

travel far enough in the silicon to be detected as a separate gamma-ray event. In this case, the primary electron will be measured with a lower energy than its actual initial energy.

2.2.7 Other interactions

Coherent scattering of the primary electron on an atom's electron shells is significant only at very low energies (below 100 eV), and so it is ignored here.

2.2.8 Total energy loss

The total specific energy loss is a combination of the losses due to electron collisions (equation 2.12) and the loss due to radiative emission (equation 2.17):

$$\frac{dT}{ds} = \left.\frac{dT}{ds}\right|_{\text{EC}} + \left.\frac{dT}{ds}\right|_{\text{brems}} \tag{2.18}$$

Figure 2.5a shows the approximate contributions of soft electron collisions, hard electron collisions, and bremsstrahlung production to the average total specific energy loss in silicon for $10\,\text{keV} < T < 2\,\text{MeV}$. As described above, the energy loss due to soft electron collisions predominates in this energy range, and bremsstrahlung is negligible. At higher energies, hard electron scattering is more significant than it is at low energies, because soft collisional losses are reduced.

The negative slope of the total energy loss curve in Figure 2.5a over most of this energy range means that the electron will lose energy more rapidly as it slows down. In particular, the end of the electron path will be marked by a concentrated energy deposition. This behavior was first described by Bragg [25], and the energy loss as a function of distance along the path is known as the *Bragg curve*. An ideal average Bragg curve is shown in Figure 2.5b, for a 500 keV electron in silicon. The curve is generated by calculating the average specific energy loss at each point, and then adjusting the electron energy and position for the next point, and repeating. The Bragg curve for an actual electron will show significant fluctuations due to the statistical nature of hard electron collisions and bremsstrahlung production. However, the concentrated energy deposition at the end of the track is universal, and is useful for the reconstruction algorithm in Chapter 5 to identify the initial end of an electron track.

In addition to components of the total energy loss, the differential cross sections for different types of scattering can be plotted as a function of recoil energy or scattering angle. Figure 2.6 shows the differential cross sections for electron collisions and bremsstrahlung as a function of Q, and the differential cross section for elastic nuclear

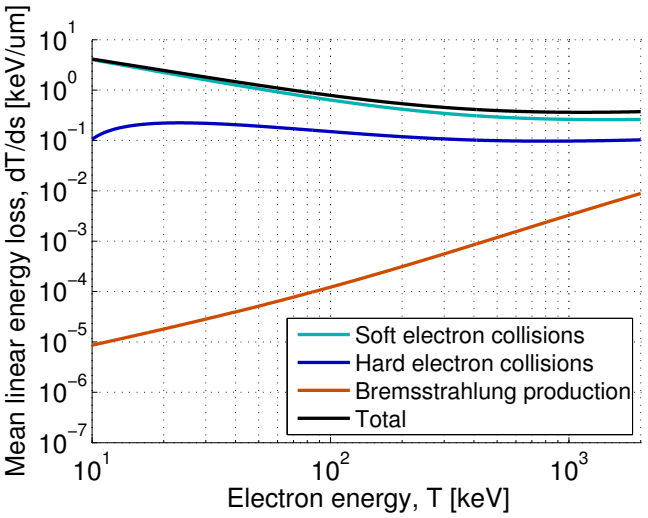

(a)

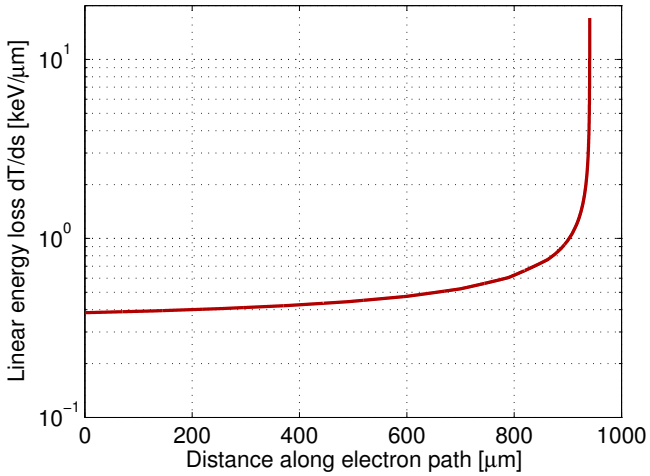

(b)

Figure 2.5:
(a) Approximate contributions of different mechanisms to the average specific energy loss of fast electrons in silicon. Soft and hard electron collisions have been distinguished using a threshold of $H = 4\,\mathrm{keV}$.
(b) An ideal, average Bragg curve for a 500 keV electron in silicon. The curve was generated using data from [91].

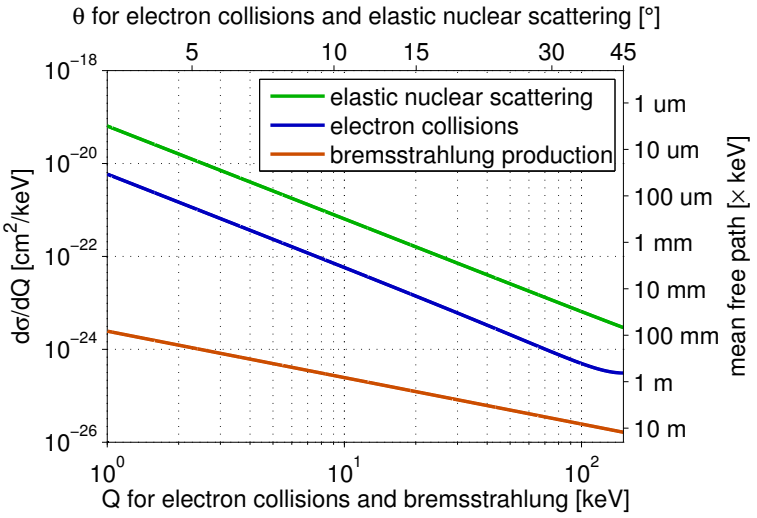

Figure 2.6: Calculated differential cross sections for electron collisions, elastic nuclear scattering, and bremsstrahlung production, for a 300 keV electron in silicon. See text for details.

scattering as a function of θ, for a 300 keV electron in silicon. The dependencies of Q and θ are overlaid according to their correspondence for electron collisions: the θ of elastic nuclear scattering is converted into the Q of an electron collision in which the primary electron scatters through an angle θ. The correspondence between θ and Q is calculated using non-relativistic kinematics, and so the elastic nuclear scattering curve can be compared with the hard electron collisions only in an approximate way. Nonetheless, it is clear that elastic nuclear scattering through any given angle is more likely than electron scattering, and electron scattering for any given Q is more likely than bremsstrahlung production. All three processes are more likely at low energy transfer or low scattering angle. The differential cross section is also expressed as the mean free path corresponding to the differential cross section integrated over 1 keV ($= (Nd\sigma/dQ)^{-1}$), on the right-hand axis.

The probability distribution of total specific energy loss for a given electron energy is very similar to the distribution from electron collisions alone (Figure 2.4). Bremsstrahlung production will increase the high-energy tail slightly.

The well-defined peak in the distribution of energy loss is important for part of the trajectory calculation, described in section 5.2.8.

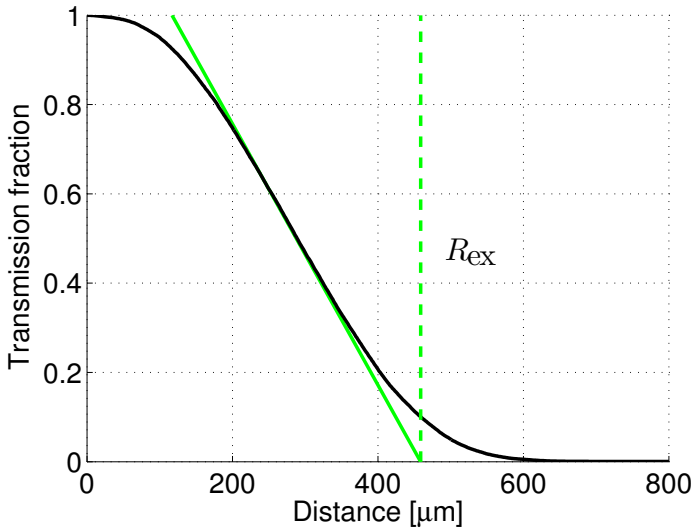

Figure 2.7: An illustration of the definition of extrapolated range. The green line is tangent to the curve at the point of steepest slope; the dashed green line indicates the calculated range.

2.2.9 Extrapolated range

Although several different processes contribute to the energy losses and angular deviations of energetic electrons, the overall behavior can be described by the parameter of *extrapolated range*. Extrapolated range describes a thickness of material through which most electrons of a certain energy will not penetrate. Extrapolated range should not be confused with the path length of the electron as shown for example in Figure 2.5b, which is the *continual slowing-down approximation (CSDA) range*.

Extrapolated range is calculated using an electron transmission graph, as shown in Figure 2.7. In this case, electrons are modeled in a block of silicon with similar energies (400 ± 10 keV) and identical initial positions and directions (also see Figure 1.2 for an example). The transmission fraction is calculated as the fraction of tracks that cross a plane perpendicular to the common initial direction and at various distances from the initial position. The extrapolated range is defined as the x-intercept of a line tangent to the transmission curve at the point of its steepest slope.

Extrapolated range can serve as a reference length for the electron's angular deviations, because a track with fewer angular deviations will generally travel farther along the initial trajectory. The electron interaction physics models will also be

benchmarked to extrapolated range.

To summarize, four significant types of interactions of energetic electrons have been discussed. Soft electron collisions are the primary process by which a fast electron loses energy, and the energy loss is pseudo-continuous. These soft collisions also cause a gradual deviation from the electron's initial direction. Elastic nuclear collisions are a means by which the fast electron can deviate suddenly from its initial direction, although the energy loss is negligible. Both hard electron collisions and bremsstrahlung production make less frequent contributions to energy losses and angular deviations, the former process potentially creating a branch from the main electron track and the latter potentially creating a separate track in the material. The general behavior of the track through all these processes can be characterized by the Bragg curve and the extrapolated range.

2.3 Gamma-ray detection

The gamma-ray and fast electron interactions described in the previous two sections describe the particles' behavior on a fundamental level. For making measurements with an engineered device, however, a number of other concepts are important.

In order to learn something about the gamma-rays in one's surroundings, the gamma rays must be detected in some detection system. In the following sections, the basic concepts of detection will be described, including properties of the gamma-ray environment, detector, and a specific measurement. Then, the properties of silicon as a detector material will be discussed, along with charge-coupled devices and the specific device used in this work.

2.3.1 Properties of the gamma-ray environment

The field of gamma rays in a location can be described as the gamma-ray environment. The environment may include photons from all kinds of sources, and can be described as a *flux*: the number of gamma rays of a given energy and a given direction at a given position passing through a unit area perpendicular to their direction, per unit time. The flux from a point source will be proportional to the rate of emission and inversely proportional to the square of the distance.

If some radioactive material or volume is defined as the source of interest, the flux due to this material or volume can be described as *source* flux, and all other flux as *background* flux. The probability that a photon emitted from the source enters a volume where the gamma-ray detector will be is the *geometric efficiency*.

2.3.2 Properties of a detector

The detector used for a measurement will have certain intrinsic characteristics which depend on the material composition, size, shape, housing, and information processing design.

First, the detector has an *intrinsic efficiency* for photons to interact in it, defined as the probability for a gamma ray entering the detector's volume to be detected. The intrinsic efficiency depends on the gamma ray energy and direction, according to the detector size, shape, housing, and the photon interactions described in section 2.1. Intrinsic efficiency is also related to *effective area*, equal to the product of intrinsic efficiency and the detector's cross-sectional area.

Gamma rays interacting in the detector may not deposit their full energy, if one of the interaction products escapes from the sensitive volume. The probability for a gamma ray to deposit its entire energy, given that it interacts, is the *peak-to-total ratio*. The peak-to-total ratio is greater for a larger size detector, due to greater absorption of scattered gamma rays, and also greater for a higher-Z detector, due to the higher cross section for photoelectric absorption. The peak-to-total ratio can also be combined with the intrinsic efficiency, and the product is an *intrinsic full-energy efficiency*.

Several parameters of an individual gamma-ray interaction can be useful to know, especially for imaging as will be discussed in section 2.4. These parameters include interaction energy, interaction position, and interaction time. The precision with which a detector can measure one of these parameters for a single photon is the *resolution*. Resolution in general is usually quantified as a full width at half maximum (FWHM) of a histogram of measurement error, or a root mean square (RMS) error, called σ for a normal (Gaussian) distribution of error. A normal distribution has a FWHM equal to 2.355 times σ.

Time resolution can be described by the *pulse-pair resolution*, which is the minimum time between interactions that can be measured and differentiated by the detector and system of operating electronics. A large pulse-pair resolution can mean that the detection system is insensitive (*dead*) for a length of time after measuring one interaction, or that all interactions within a time window cannot be differentiated from each other in time (as is the case for the charge-coupled device discussed later).

Position resolution indicates how accurately the detector can measure a point interaction. In reality, gamma-ray interactions deposit energy through charged particles (electrons and sometimes positrons) which have a path length in the material as discussed above. If the position resolution is larger than the electron range, the interaction will appear as a point, and the most likely position measured in the device usually corresponds to the centroid of energy deposition. Since electrons deposit most

of their energy near the end of their path according to the Bragg curve, the position resolution of the initial interaction position, which is relevant to the gamma-ray kinematics, is limited by the electron range. On the other hand, if the position resolution is similar to or smaller than the electron range, the interaction will not appear pointlike and some information about the electron path is available. If the electron path is resolved well, not only can the actual position of gamma-ray interaction be measured, but electron track Compton imaging is possible.

Energy resolution represents the ability of the detector to accurately measure the energy deposited in an interaction. Both *statistical* and *electronic* factors contribute to the energy resolution. The statistical broadening of the energy measurement arises from the physics of producing some quantized particles which can be measured or counted to provide an estimate of the interaction energy. Because the detection system is not able to measure every mode of energy absorption, and the amount of energy needed to generate one information carrier is not constant, the number of information carriers will not be exactly proportional to the energy deposited. The variance in the number of information carriers is the variance of Poisson statistics, but with a coefficient [44, 74].

The electronic contribution to the energy resolution arises from the imperfect conversion and/or amplification of the initial information carriers. This *electronic noise* in the signal can be measured either as the energy in the signal to which the electronic variations are equivalent, or as the amount of electric charge in the variations. Low-noise systems achieve electronic noise of only a few electrons of charge.

If statistical and electronic noise sources are both normally distributed, the total energy resolution can be determined by adding each component in quadrature:

$$\mathrm{FWHM}^2_{\mathrm{total}} = \mathrm{FWHM}^2_{\mathrm{stat}} + \mathrm{FWHM}^2_{\mathrm{elec}} \tag{2.19}$$

2.3.3 Properties of a measurement

The properties of the gamma-ray environment and the properties of the detector both influence the data that can be gathered. In addition, certain properties are relevant to a certain detector collecting data in a certain environment over a certain length of time, which is referred to in this section as a *measurement*.

The *absolute efficiency* is the product of the geometric efficiency of a source and the detector's intrinsic efficiency.

The detector will measure some number of *counts* of radiation, based on the flux and intrinsic efficiency. The *source counts* are equal to the number of photons emitted from the source times the absolute efficiency. If the detector measures energy

or position, the counts in a specific *energy window* or position volume can also be defined. Counts are subject to Poisson statistics. In addition, the *countrate* can be defined by dividing counts by measurement time.

Two quantities compare the source counts to background counts. First, the *signal-to-background ratio* (SBR) is equal to the source countrate divided by the background countrate, and is independent of measurement time (other than Poisson variations). If an energy window is defined, then the SBR is the number of source counts in the energy window divided by the number of background counts in the energy window; this is not the same as the ratio of source and background fluxes in the energy window, unless the peak-to-total ratio were 1. A low SBR means that only a small fraction of the counts are from the source.

Second, the *signal-to-noise ratio* (SNR) is equal to the number of source counts divided by the uncertainty in the number of background counts. The SNR depends on measurement time, because the uncertainty in background counts increases with the square root of time, while the source counts increase directly with time (assuming static source and detector positions). The SNR represents how *significant* the measurement of the source is. A low SNR means that the measurement does not clearly show the presence or strength of the source, because those counts could be explained by fluctuations in the Poisson statistics. The SNR is a measure of data statistics, while the SBR is a measure of the system and environment.

2.3.4 Semiconductor detectors[3]

Various materials are suitable for the detection of gamma rays, including gases, liquids, and solids which can act as scintillators, semiconductors, or superconductors [74]. Semiconductor detectors can achieve a finer energy resolution than gas or scintillator detectors [78], and are much more flexible in implementation than, for example, the very precise superconducting transition-edge sensors [41]. In particular, germanium and silicon are excellent materials for Compton imaging.

2.3.5 Germanium detectors

Germanium has been used for radiation detection for several decades, first in lithium-drifted germanium detectors and later in high-purity germanium (HPGe) detectors [74]. It offers a reasonable density ($5.3\,\mathrm{g/cm^3}$) and Z (32) for full-energy absorption. Both electrons and holes have long lifetimes and large mobilities in germanium, so the signal charge can be collected efficiently. The band gap in germanium is small

[3]For an introduction to semiconductors see Sze [114]; for semiconductors as radiation detectors see chapter 11 of Knoll [74], chapters 1 and 2 of Spieler [113], or Lutz [84].

(0.7 eV), meaning that less energy is needed to produce an electron-hole pair, leading to more charge carriers per event and a finer energy resolution. However, the small band gap also means that the thermal energy at room temperature will generate an unacceptably high leakage current when a reverse bias voltage is applied. Therefore, germanium detectors must be cooled significantly, often using liquid nitrogen which boils at 77 K.

For applications requiring position resolution, including gamma-ray imaging, the electrical contacts on a germanium detector can be segmented. In particular, a planar detector can be segmented in strips on either side, with the strips on one side orthogonal to those on the other. This allows an interaction position to be deduced by the strip on each side which collects the signal charge.

High-purity germanium detectors are commonly used when energy resolution is important, including Compton imaging (e.g. [20, 86, 87]). In this work, a HPGe double-sided strip detector was used as part of the experiment (described in section 3.3).

2.3.6 Silicon detectors

Silicon is an attractive detector material to use for electron track Compton imaging, for both its semiconductor properties and its particle interaction properties.

As a semiconductor, silicon is useful for a few reasons. The charge transport properties of silicon are excellent, allowing efficient and consistent signal charge collection. The band gap in silicon is 1.1 eV, which is large enough to minimize thermal leakage current at or near room temperature [74], yet small enough to provide many charge carriers per unit energy deposition, improving the energy resolution [36]. As an elemental semiconductor, silicon crystals can be grown with a higher purity and fewer defects than compound semiconductors, although not as pure as germanium [74]. However, silicon has long been used in the computer and microchip industry, so smaller and more complex structures can be fabricated on the surface than can be for germanium [84]. This last point is necessary for fabricating a charge-coupled device with very fine position resolution.

Silicon is also a good choice for electron track Compton imaging, due to its low density (2.33 g/cm^3) and atomic number ($Z = 14$) compared to other semiconductor materials. As discussed below in section 2.4.3, Compton imaging requires at least two separate interactions of a gamma ray. Since photoelectric absorption and pair production both scale strongly with atomic number Z, a material with lower Z improves the relative probability of Compton scattering and thus the fraction of useful events [35, 98]. The scattered gamma ray can also penetrate farther before the next interaction, allowing better imaging resolution using the same position resolution.

Also, the intrinsic limit to angular resolution (Doppler broadening) is better in silicon than in higher-Z materials [22, 98]. Even more importantly, the relatively low density of silicon means that electron trajectories are longer and therefore easier to measure. Silicon represents a good compromise between denser solids, in which the electron track would be harder to measure, and gas detectors, which suffer from a very low interaction efficiency [120]. (See Table 2.1 later in this chapter for electron extrapolated ranges in different materials.)

2.3.7 Lateral diffusion and repulsion of charge carriers in silicon

Because the position resolution of an electron tracking semiconductor detector must be very fine, the details of charge transport can impact the measurement significantly.

After the radiation excites electrons from the valence band to the conduction band, the electrons and holes drift toward opposite electrodes in the electric field induced by the reverse bias voltage. The initial distribution of charge carriers expands in three dimensions through two processes: Coulomb repulsion, and diffusion along the concentration gradient [28].

The expansion due to repulsion depends on the density of charge carriers. For an infinite cylinder of uniform charge, starting with a radius of 0, the radius as a function of time due to repulsion alone is approximately

$$r(t) = \sqrt{\frac{\mu_0 \lambda}{\pi \epsilon} t}, \tag{2.20}$$

where μ_0 is the low-field mobility for the charge carrier species of interest, λ is the linear charge density along the cylinder, ϵ is the permittivity of the material, and t the time over which the carriers are free to expand. The relevant time is the duration of the charge drift from the interaction position to the electrode (or potential well, described below), which depends on the position of interaction.

Diffusion is an overall movement of the charge carriers down a concentration gradient due to random thermal motion. In an electron track, the carriers diffuse from the track outwards, spreading the charge cloud more than Coulomb repulsion alone. In the limit of pure diffusive transport in a uniform material, charge carriers at a point will diffuse in three dimensions with a Gaussian profile in each dimension, with a width parameter given by

$$\sigma(t) = \sqrt{2Dt}. \tag{2.21}$$

Here, t is the time over which the charge diffuses, and D is a diffusion coefficient equal to $\mu_0 kT/e$, in which k is Boltzmann's constant, T the absolute temperature, and e the elementary charge.

To understand the relative importance of repulsion and diffusion, the Gaussian σ of diffusion can be compared to the radius due to repulsion. However, since σ represents a radius which contains 68% of the charge, the comparison will be slightly more reasonable if 68% of the repulsion radius is used. Since both parameters scale with $\sqrt{t}$, the relative importance in silicon depends only on the charge density (λ):

$$R = \frac{0.68 \cdot r(t)}{\sigma(t)} = 0.68\sqrt{\frac{\lambda e}{2\pi\epsilon kT}} \tag{2.22}$$

The critical linear charge density, for which repulsion and diffusion are of approximately equal importance ($R = 1$), is

$$\lambda_c = \frac{2\pi\epsilon kT}{(0.68)^2 e} \tag{2.23}$$

$$= 105\,\mathrm{e/\mu m}. \tag{2.24}$$

This linear charge density is equal to the average density of charge carriers generated by a specific energy loss of 378 eV μm^{-1} in silicon, which is about the most probable linear stopping power of 175 keV electrons. Electrons above this energy have a lower specific energy loss on average, and so diffusion is relatively more important, but as the electron slows down repulsion will generally be more important for the charge transport. This quantitative comparison of repulsion is approximate, because as the charge diffuses the force of repulsion also decreases. However, it is clear that both diffusion and repulsion are significant for the transport of charge from electrons in the range of hundreds of keV. This is relevant to the models of charge transport described in Chapter 4.

2.3.8 Charge-coupled device[4]

The charge-coupled device, or CCD, relies on a unique method of collecting charge carriers in a series of potential wells at one surface, and then shifting the charge from one well to the next in a controllable manner [24]. A single amplifier can sequentially measure the amount of charge in each well as the charges are shifted toward the amplifier. The structure of a pixel is shown in Figure 2.8; the precise nature of each component is in the references [11, 61, 95]. Figure 2.9 illustrates the movement of charge using three voltage potentials.

[4] See section 6.6 of Lutz [84], and Janesick [67].

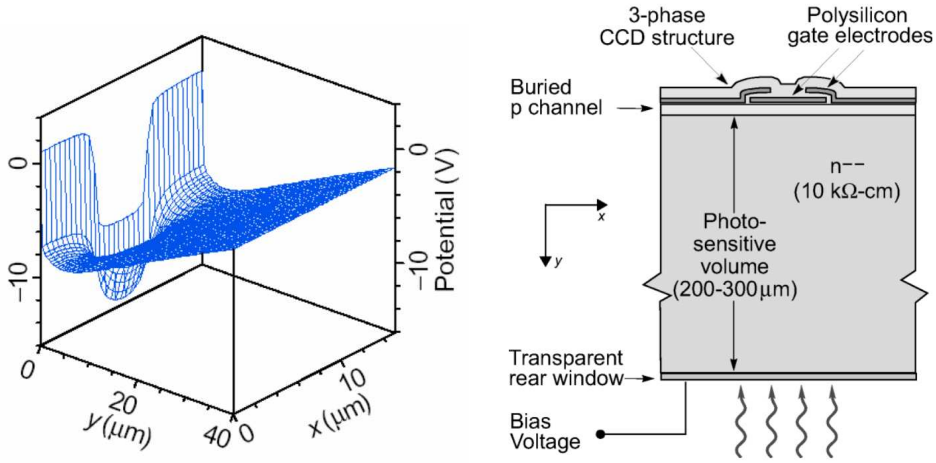

(a) (b)

Figure 2.8: (a) The electric potential of one pixel. x is the axis along a row of pixels, and y extends from the pixel plane ($y = 0$) into the bulk of the device. Figure from Oluseyi [95]. (b) A section through the thickness of a device, showing one pixel and illumination by visible or infrared photons at the bottom. The x and y dimensions are identical to (a). Figure from Holland [62].

The potential wells are formed by a series of narrow conductive channels on the surface of a silicon device. By structuring the potential wells in two dimensions, the positions of deposited charge can be measured on a scale of micrometers while using one, or very few, readout channels. By exposing the CCD to ionizing radiation before the charge transfer and measurement, an image of the radiation flux can be measured [19]. The potential wells are then known as *pixels*. If the distance between pixels (the *pixel pitch*) is smaller than the size of the distribution of charge carriers from the electron track, diffusion, and repulsion, then multiple pixels contribute to the measurement of a single interaction.

Throughout this paper, the phrase *pixel plane* is used to describe the side of the device on which the potential wells lie. The opposite side is the *back side* of the device, and the borders are the *edges*.

A number of parameters describe the performance of a charge-coupled device. *Dark current* is a measure of the leakage current through the bulk of the device when it is not exposed to any photons ("dark"). The dark current increases exponentially with temperature, because thermal energy excites charge carriers into the conduction band of the semiconductor.

The readout of the CCD involves shifting the charge in each pixel to an amplifier

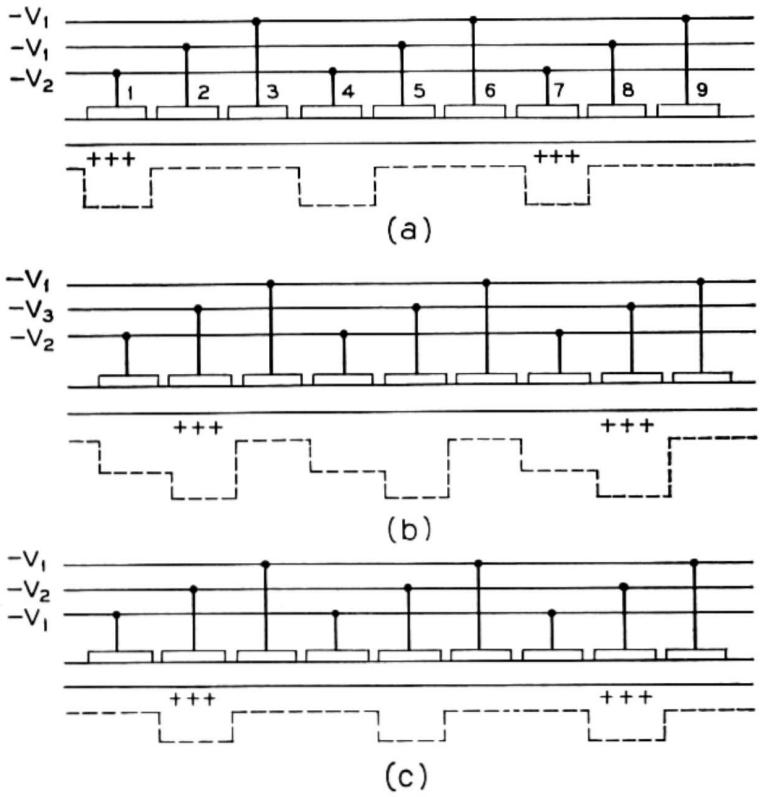

Figure 2.9: A conceptual illustration of the charge-shifting process in a 3-phase CCD. After two steps, the original charges are shifted from positions 1 and 7 to positions 2 and 8. Figure from Boyle's original CCD publication [24].

at the corner of the device, for an entire row, then shifting a new row into the readout row. Each shift operation is accomplished by sequentially raising and lowering voltage lines on the surface of the CCD, known as clock voltages, as shown in Figure 2.9. The charge from each entire row is simultaneously shifted into the next row, and the direction of this shift is called the *parallel* direction. Then, in a row at an edge of the device, the charge from each pixel is shifted along the row and toward the CCD amplifier, and the charge from each pixel is measured individually in the CCD amplifier. This shift direction is the *serial* direction. *Charge transfer efficiency* (CTE) is the fraction of charge shifted from one pixel to the next during CCD clocking, both in the serial and parallel directions. Ideally the CTE should be 1. The time required to shift and measure the charge in every pixel is the *readout time*. The pulse-pair resolution of a CCD cannot be better than the readout time, because multiple interactions during readout can appear in the same image and not be differentiated in time.

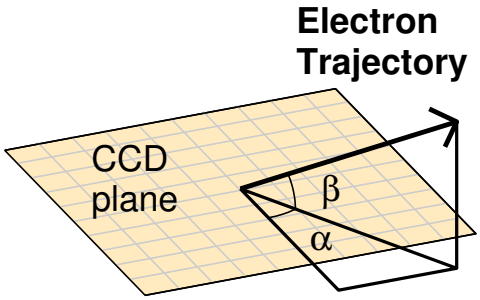

Figure 2.10: The two angles of the coordinate system defined for a CCD, defining the initial direction an electron might travel.

It will be convenient for the discussion of electron directions to define angular coordinates based on the plane of the CCD. The azimuthal angle in the pixel plane (i.e. the arctangent of y pixels divided by x pixels) will be known as α. The angle of elevation above or below the pixel plane (i.e. the angle through which a vector can be projected onto the pixel plane) will be known as β. Angles α and β are illustrated in Figure 2.10.

With the above concepts and terms, the specific device used in this work can be described.

2.3.9 The SNAP CCD

In this work, a silicon charge-coupled device was used which was developed at Lawrence Berkeley National Laboratory (LBNL) for the SuperNova Acceleration Probe (SNAP). SNAP used CCDs to measure distant supernovae and galaxies in near-infrared wavelengths [10]. A CCD wafer fabricated at LBNL is shown in Figure 2.11. The thick, fully-depleted nature of the SNAP CCD is suitable not only for collecting infrared light as in the SNAP mission, but also for measuring tracks of high-energy electrons induced by gamma-ray interactions in the bulk of the CCD [112]. An example electron track image from a SNAP CCD in the Berkeley Applied Research on the Imaging of Neutrons and Gamma rays (BeARING) laboratory is shown in Figure 2.12. (Chapter 5 will discuss in detail how the electron track is processed.)

The CCDs developed for the SNAP project have a variety of size formats and pixel pitches. The device used for electron tracking is $0.75\,\text{cm} \times 1.5\,\text{cm}$ of active area, filled with square pixels of $10.5\,\mu\text{m}$ pitch, although similar devices as large as $(3.5\,\text{cm})^2$ have been developed. The three-phase CCD is fabricated onto a $650\,\mu\text{m}$-thick wafer

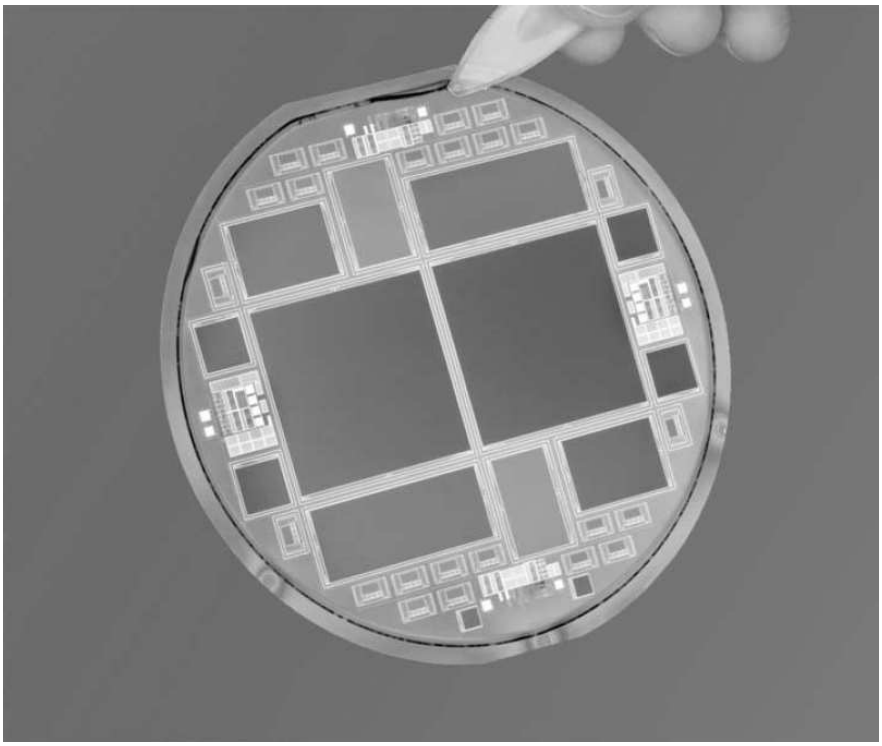

Figure 2.11: Photo of a full 100 mm wafer with several CCDs fabricated at LBL. (Taken from [59])

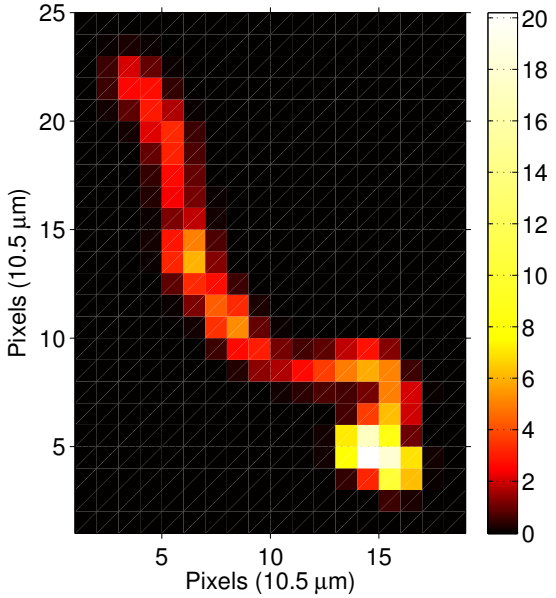

Figure 2.12: A CCD image of an electron track. The electron apparently started at the upper left. The units of the color axis are keV per pixel, and the total track energy was measured to be 254 keV.

of high-resistivity (∼10 kΩ cm) n-type silicon. The wafer process was designed and tested at LBNL but transferred to DALSA Semiconductor for production [60]. For the SNAP project the devices are normally thinned to 200 µm to 300 µm, but the device used for electron tracking was from a test batch of unthinned 650 µm devices. The CCD is reverse-biased by a positive voltage applied to the back side, and holes are collected in the potential wells.

At the operating temperature of 130 K to 140 K, the dark current has been measured to be less than 10 electrons per pixel per hour [59]. The pixel plane is divided into four equally-sized quadrants, each with its own amplifier at a corner of the full device. The parallel direction is along the 1.5 cm axis of the device, and the serial direction along the 0.75 cm axis of the CCD. The charge transfer efficiency in SNAP CCDs is typically above 0.999 995 in both the parallel and serial directions [62]. However, the CTE is reduced if the temperature is too low, precluding effective operation of the CCD at temperatures below about 130 K. The amplifier noise on the measurement of the charge in each pixel depends on the clock speed; slower clocking allows a more accurate measurement. At 10 µs sampling time, the readout (electronic) noise has been measured by the CCD team to be as low as 2 electrons RMS [62]. However,

in the cryostat in the BeARING laboratory, with 10 µs sampling time and about 95 kHz clocking frequency, a noise of about 5 electrons RMS is measured. The relatively long sampling time, which is required for achieving low electronic noise, leads to a slow readout time of 2.8 s.

The result of repulsion and diffusion in the CCD is a spreading of the cloud of charge carriers over multiple pixels at the pixel plane, in general. The width of spreading depends on the depth from which the charge carriers drift, as well as the ionization density. The average distribution of charge from an idealized point of energy deposition at a certain depth and charge density is called the *point spread function*. The point spread function in the CCD is a few pixels across for most tracks in the middle of the CCD, as shown in Figure 2.12.

The suitability of these characteristics to the requirements of electron track Compton imaging will be discussed in section 2.4.7.

2.4 Gamma-ray imaging

So far, the measurements described have included the energy, time, and position of a gamma ray's interaction. Another very useful attribute is the gamma ray's incident direction, which enables the generation of an image of the directions from which gamma rays are originating. The following section discusses the measurement of this attribute, including what terms are useful in discussing imaging and what methods can be used with a detection system to image gamma rays, culminating in the method of electron track Compton imaging, which is the focus of this research.

2.4.1 Imaging concepts

The detection concepts of efficiency as well as energy, position, and time resolutions are important for describing the imaging capabilities of a detection system. In addition, the following properties of a detector or detection system are relevant.

Imaging efficiency is the fraction of events incident on the imaging detector system that are actually useful for generating an image.

Angular resolution is the apparent angular size of an imaged point source. A smaller angular resolution corresponds to a more precise measurement. An angular resolution measure (ARM) for Compton imaging can be found in the reference [134].

Field of view refers to the solid angle over which an image is formed. The field of view can be as large as 4π steradians, depending on the detector and the type of imaging.

A variety of methods may be employed for gamma-ray imaging. The methods may be broadly divided into those that use a mask to cast a shadow on the detector (*collimation*), and those that do not.

2.4.2 Collimator-based imaging

Imaging methods using collimators range from the simple pinhole camera to complex coded masks. Pinhole, multiple-pinhole, and parallel-hole collimation are commonly used in biomedical imaging [55, 128, 131]. These can be effective in near-field imaging, but for more distant sources, pinholes do not provide enough efficiency and parallel holes do not provide enough angular resolution.

By placing a unique pattern of shielding (*coded mask* or *coded aperture*) in front of a position-sensitive detection plane, a gamma-ray shadow is cast on the detection elements. Conversely, the detection of a gamma-ray at a certain position indicates that the source was located somewhere with an open line of sight through the mask. After detecting a number of counts, the position of a localized source can be computed [27, 45]. Coded aperture imaging can provide excellent (sub-degree) angular resolution for point sources of radiation, but the field of view is usually limited by the size of the mask and its orientation relative to the detector [27, 49, 50]. Imaging of extended sources is more challenging [107]. A coded mask with half open and half shielded elements produces the best SNR for point sources that are weak compared to background, but this reduces the imaging efficiency by a factor of two [27, 111]. Also, each event detected provides only a 50% constraint on the possible source location in the field of view.

Another collimation strategy is to use the time domain, instead of the spatial domain, to observe a detector response. This can be achieved through two sub-collimators masking a position-insensitive detector from the same direction, but at widely separated distances. The sub-collimators rotate relative to each other, and sources in the field of view can be imaged using the time signature of counts. Angular resolution of arcseconds can be achieved [65], but the field of view is limited.

All collimator-based imaging methods are limited in measuring higher-energy photons, because these can pass through the mask elements, rendering the counts meaningless for imaging.

2.4.3 Compton imaging

Collimator-less modalities of imaging have the advantage of increased interaction efficiency and potentially increased imaging efficiency, since no gamma rays are blocked by collimators. However, for Compton imaging and pair production, described below,

more advanced measurements are needed in order to extract directional information from interactions [87].

As shown previously in Figure 2.1, the dominant interaction over a wide range of gamma-ray energies is incoherent scattering, also called Compton scattering. Equation 2.3 relates the scattered gamma-ray energy to the total energy and scattering angle. If the energy deposited by an initial Compton scattering is measured, and the initial energy of the photon is known, then a scattering angle may be calculated [109]:

$$\theta = \arccos\left[1 - m_0c^2\left(\frac{1}{E'} - \frac{1}{E}\right)\right]. \tag{2.25}$$

If the positions of the initial Compton scattering and the next interaction are measured, the path of the photon between the two interactions defines an axis. By combining the calculated scatter angle with the measured axis, a cone of possible source locations can be constructed [123]. The ideal cone is broadened by uncertainties in the measured positions and energies, as well as the fundamental physical uncertainty in the scattering angle due to the unknown initial state of the scattered atomic electron. The effect of the unknown electron binding energy and initial momentum is known as Doppler broadening, and broadens the angular resolution by 1° FWHM or less above 400 keV photon energy in silicon [134]. The cone broadening from position and energy resolutions can be comparable with Doppler broadening for semiconductor systems [21, 98]. After constructing several cones from different photon interaction sequences, a point source, for example, may be located by combining the knowledge from multiple cones [123, 127]. Figure 2.13a illustrates the mechanics of conventional Compton imaging.

An effective Compton imaging system has several requirements. At least two interactions of the gamma ray must be measured individually. A photoelectric absorption in the first interaction, or consecutive interactions too close to be resolved by the detector, are not useful. Position resolution is important for locating the two initial interactions in order to accurately construct the photon scattering axis, and achieve good angular resolution in the image [7]. Energy resolution is also important for calculating the scatter angle accurately, which also directly affects angular resolution [22]. Normally the total photon energy must be calculated, either by absorbing the full energy in the system, or by measuring at least three interactions so that the initial energy can be calculated [40, 78]. The system must be able to group all the interactions from one gamma ray together, while separating the interactions from a different gamma ray. This time-segmenting requires pulse-pair resolution, and the total countrate the system can image can be limited by this time resolution [110]. The countrate of a detector in response to a weak source with background depends on the efficiency of the detector. For 50 cm^3 of germanium, a typical countrate due

to natural background might be 100 counts per second. For accurate grouping of interactions in a variety of situations, then, the time resolution should be in the range of 100 µs or better.

If the time resolution is worse than the interaction separation distance divided by the speed of light, then the sequencing of the interactions will not be directly measured. This is often the case for compact Compton imaging systems utilizing semiconductor detectors [22, 108, 126]. Then the interaction sequence must be deduced by other means, for example by comparing the measured energies and scatter angles with the Compton equation (equation 2.3) [108].

A specific example of required characteristics for a Compton imager is the Advanced Compton Telescope (ACT), a mission concept for the next generation of gamma-ray space telescopes in the energy range of 0.2 MeV to 10 MeV. The concept study report [22] describes basic quantitative performance requirements. The ACT requires an effective area of about 1000 cm^2, energy resolution between 0.2% and 1% of deposited energy, and an angular resolution of about 1°. This angular resolution implies a position resolution better than $d \sin 1^\circ = 0.017d$, in which d is the average distance between the first two gamma-ray interactions. For interactions 10 cm apart, the position resolution must be on the order of 1 mm.

2.4.4 Pair telescopes

The electron and positron pair generated by the interaction of a high-energy photon have trajectories directed forward, at an angle determined by the photon momentum [94]. The initial photon energy and direction can be reconstructed by measuring the energies and trajectories of the electron and positron [58, 71].

The requirements for an effective pair telescope are similar to the requirements for an electron track Compton imager, described below. However, the cross section for pair production limits pair telescopes to photon energies above around 10 MeV [64, 70], at which the electron and positron have kinetic energies of several MeV or higher.

2.4.5 Other collimator-less methods

One final method of imaging without a collimator relies on the principle of diffraction of gamma rays in a crystal through small angles (Bragg diffraction). Although the angular resolution of such an imager can be excellent (arcseconds) [6], the field of view is very small (arcminutes) [83], so this method is limited in applications.

For the photon energy range of around 500 keV, then, Compton imaging is generally the most effective method of gamma-ray imaging with a wide field of view. In

addition, Compton imaging can be enhanced through electron tracking.

2.4.6 Electron track Compton imaging

Conventional Compton imaging, as described above, is limited in sensitivity by the azimuthal symmetry around the scattered photon axis, which is the backprojected cone axis. For a single event, the position of the source is known only to the surface of a cone, which is the result of measuring one vector (the photon scattering direction) and one angle. The azimuthal symmetry of the cone can be broken if an additional measurement is made. In particular, the symmetry can be broken by the vector of the initial direction of the Compton-scattered electron [96, 97]. This is known as electron track Compton imaging. For otherwise equal imaging measurements, the electron tracking image will be more sensitive because each event provides more specific information, reducing the background of possible source locations [22, 96]. Figure 2.13b shows how the meausurement of electron direction breaks the cone symmetry.

In an ideal Compton scattering event this measurement could reduce the cone to a ray pointing precisely to the origin of the gamma ray. However, the uncertainties of conventional Compton imaging apply, including detector resolutions and Doppler broadening. In addition to these photon uncertainties, the initial electron direction will be uncertain, based on the position resolution of the detector compared to the angular deviations in the electron path described in section 2.2 [17, 31]. The backprojection result for a single event is a cone segment [18, 105, 118].

A cone has only one angular degree of freedom. Thus, electron track Compton imaging only requires one component of the electron direction vector: the component perpendicular to the scattered photon vector. If both components of the electron direction are measured, the parallel component may be used to confirm the predicted gamma-ray interaction sequence [22, 122].

The sensitivity gains of electron tracking are not easy to realize in practice. Gamma ray detectors need mass to be efficient, and dense materials are necessary to achieve efficiency while maintaining a compact size of instrument. Unfortunately the range of electrons scales inversely with electron density, making the initial direction harder to resolve in more efficient materials, as shown in Table 2.1 [17, 77]. Also, the initial direction of the electron is quickly lost near the beginning of the track, as illustrated in Figure 2.14. It is evident to the eye that the electron direction changes significantly within half of the extrapolated range, and several of the 33 electrons are even traveling backwards within 100 µm path length. These factors imply that an electron-tracking detector must have an effective position resolution much smaller than an electron range [31, 132].

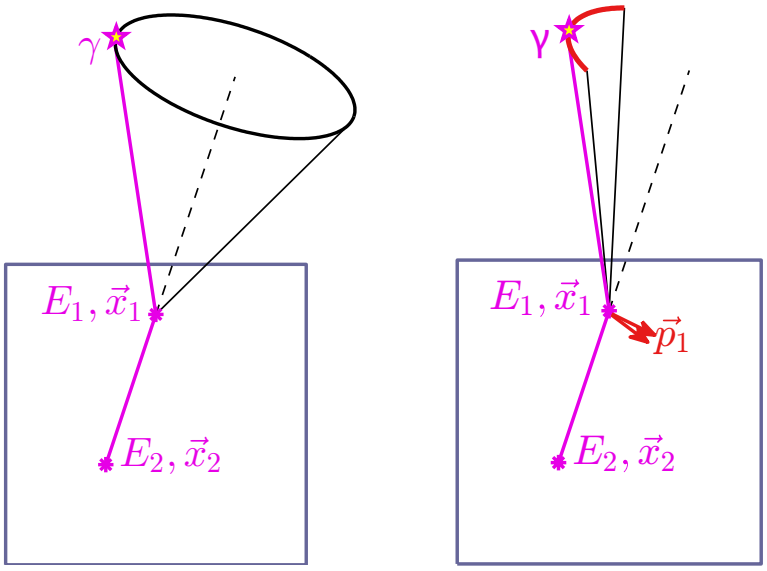

Figure 2.13:
(a) An interaction sequence of conventional Compton imaging. γ is the source which emits gamma rays; $E_1, \vec{x}_1$ and $E_2, \vec{x}_2$ are the deposited energies and interaction positions of the first and second photon interactions in the event sequence, respectively.
(b) An interaction sequence of electron track Compton imaging. $\vec{p}_1$ is the initial momentum of the Compton-scattered electron, which is uncertain.

For 662-keV photons from ^{137}Cs, the Compton electron varies in energy from 0 keV to 480 keV, and a silicon electron tracking detector must have a position resolution of about 100 µm, or preferably much less in order to maximize the fraction of electrons tracked as well as to increase the accuracy of tracking. To achieve similar electron tracking performance in germanium or cadmium zinc telluride, a finer resolution of 20 to 50 µm would be necessary. In air at atmospheric pressure, a position resolution of centimeters would be sufficient, but the efficiency for gamma-ray interactions would be very small. Thus, there is inherently a compromise between interaction efficiency and the required position resolution for tracking.

2.4.7 Suitability of the SNAP CCD for electron tracking

The approximate minimum requirements described above for conventional Compton imaging and electron track Compton imaging can be summarized as follows. The

Electron energy (keV)	Extrapolated range (µm) in			
	air (dry)	Si	Ge	CdZnTe
50	35 000	17	6.6	5.3
100	115 000	53	20	16
250	506 000	231	85	65
500	1 409 000	640	237	180
1000	3 540 000	1617	611	472

Table 2.1: Extrapolated ranges of electrons in materials. Data are calculated using Tabata's range formulae [115, 116] with values of mean excitation energy from NIST ESTAR [91].

detector should have an energy resolution of about 1%, a position resolution of about millimeters for all photon interactions and about 100 µm (in silicon) for the Compton electron from the first interaction, and a pulse-pair resolution of about 100 µs. In addition, the detector must have enough mass to provide a significant intrinsic efficiency or effective area. The quantitative requirement depends entirely upon the application. The ACT mentioned above requires about 1000 cm^2 of effective area for a large space telescope [22], while a portable instrument for security or accident applications might still be useful with much less effective area (perhaps 1 to 10 cm^2). The mass and effective area of a number of individual detectors can be combined in a larger instrument system.

In the following, the performance of the SNAP CCD from section 2.3.9 will be compared to these requirements.

The fine energy resolution of about 1% is needed in order to achieve a good angular resolution in the image. An energy resolution of 0.9% has been measured on 59.5 keV photopeak events (Section 5.1.5).

Good position resolution is needed to establish the axis of the Compton-scattered photon, as well as the initial electron trajectory. The CCD pixel pitch is 10.5 µm, although for events near the backside of the CCD the diffusion of charge carriers results in a point-spread function of 35 µm FWHM at worst, according to the model described in Chapter 4. However, if the electron trajectory is relatively straight, the electron trajectory can be determined with a precision of even less than one pixel by calculating centroids of the charge distribution. The position resolution in the third dimension is not as fine, and at worst could be considered to be equal to the thickness of the CCD (650 µm). However, another method will help to estimate the third dimension component of the electron direction (section 5.2.8). Overall, the lateral position resolution is excellent for establishing the scattering axis, and suitable

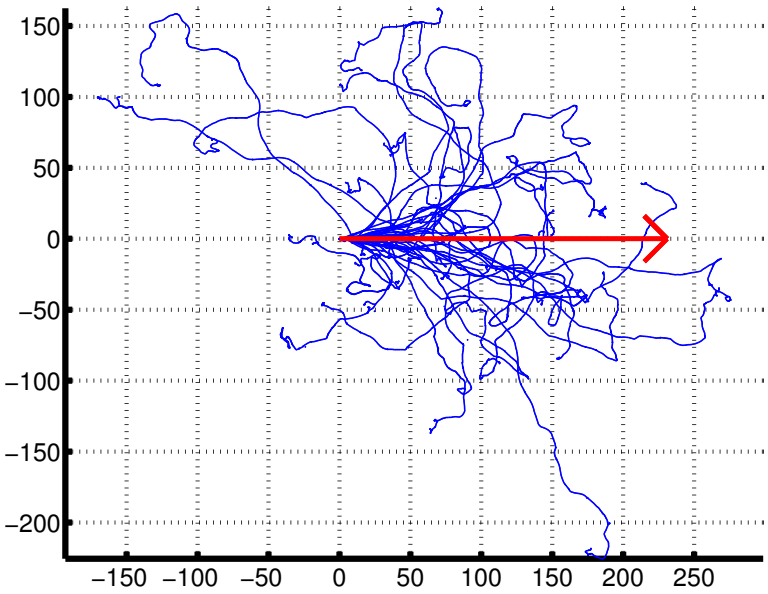

Figure 2.14: Thirty-three modeled trajectories of 250 keV electrons in silicon. Axes are in μm. The arrow indicates the initial direction of all tracks, and its length is equal to the extrapolated range.

for measuring initial electron trajectories for electrons as low as about 100 keV in energy (Table 2.1).

Good time resolution is needed to correlate interactions in the CCD with interactions in the detector absorbing the scattered photon. The pulse-pair resolution should be small compared to the average time between interactions, so that unrelated interactions can be rejected from the time correlation. In this aspect the SNAP CCD falls severely short; the pulse-pair resolution is at least 2.8 s for the readout of a full frame. Therefore, the CCD is not suitable for Compton imaging in its current configuration. However, work is in progress to develop a CCD with good time resolution, as described in section 7.3.1. In the present work, the poor pulse-pair resolution is a challenge to work around for the demonstration of the concept (section 3.3).

Detector mass and effective area are needed to provide imaging efficiency. The CCD used in the BeARING laboratory consists of only 0.17 g of silicon, although devices with the same resolution have been built as large as 1.8 g. These masses correspond to effective areas of 0.013 cm^2 and 0.14 cm^2, respectively. A single CCD is not enough effective area for many applications, but an array of tens of CCDs could have a more useful efficiency. Because the device is made of silicon, an array of devices could be much more compact than a gas-based detector with a similar effective area.

In summary, the position and energy resolutions of the CCD compare favorably with the requirements, while the time resolution is very poor and the effective area is quite small. However, an important practical advantage of the CCD is that it has already been designed and developed, and was essentially ready for immediate use in the laboratory. The time resolution is being addressed by new device designs, while the small effective area can be compensated for by using more devices in a combined system. The SNAP CCD is not ideal in all respects, but the excellent position resolution allows electron trajectory measurements for low electron energies while maintaining the material density needed for a compact instrument.

2.5 Summary

In this chapter, sources of gamma rays, interactions of gamma rays and electrons, and the detection and imaging of gamma rays have been described. The sources of gamma rays, including radioisotopes as well as high-energy astrophysical processes, define the relevance and utility of gamma-ray imaging. An understanding of gamma-ray imaging, and electron track Compton imaging in particular, requires a foundation in the types of interactions that both gamma rays and electrons undergo. Gamma-ray detectors provide the basic information needed for imaging, with the charge-coupled device being the focus of this work. Finally, different methods of imaging in gamma-ray wavelengths provide the context for electron track Compton imaging. The requirements of Compton imaging and electron tracking were described and the SNAP CCD compared to the requirements. Although the device is not ideal in its current implementation, the essential upgrade in capability is a work in progress.

In the next chapter, the setup and operation of the SNAP CCD will be described, along with one key experiment that has demonstrated electron track Compton imaging.

Chapter 3

Experiment

The primary goal of this work is the experimental evaluation of electron track measurement for electron track Compton imaging. Although much of the work does rely on modeling, the models are not meaningful without a benchmark to experiment. Our measurements rely on the SNAP charge-coupled device (CCD) described in section 2.3.9, which has been shown to have strong potential for electron track Compton imaging for photon energies in the range of 500 keV in a compact instrument (section 2.4.7).

The first section of this chapter describes the setup and operation of the CCD, including an overview of the cryostat mounting and wiring, cryostat thermal design, and software control of the device. Next, some observed irregularities of the device in the BeARING laboratory will be described, along with possible explanations and the effect of the irregularities on the measurements.

The final section describes the main body of the experimental work, a coincidence experiment. In this experiment the tracks of electrons with known initial trajectories were measured in the laboratory, allowing an analysis of the performance of the trajectory reconstruction algorithm. Two possible methods to accomplish this goal are described, and then the components of this experiment are examined, including the HPGe detector, collimated beam with shutter, position calibrations, and data acquisition.

3.1 Setup and operation

The CCD used in this work was the first CCD to be operated in the laboratory of the Berkeley Applied Research on the Imaging of Neutrons and Gammas (BeARING) research group. The CCD engineering team provided much-needed guidance,

but nonetheless the setup and operation of the CCD was challenging. This section provides an overview of the technical aspects of the CCD control and readout.

3.1.1 Wiring and electronics

The CCD requires external components to control the charge shifting, provide high voltage, and process the output signals. The SNAP device is designed to be operated using control electronics from Astronomical Research Cameras, Inc. (ARC) [81] in combination with custom boards designed by the CCD group for their devices. Most of the electronics are located in a housing module which supplies power and allows communication between boards through a built-in backplane. The housing and boards are shown in Figure 3.1a, although several cables are not shown. Signal routing, filtering, and voltage amplification are performed on boards at the side of the cryostat (at room temperature) (Figure 3.1b), and further routing is required in the cryostat around the CCD itself. The boards in the cryostat consist of the "Cryo Connector Board", designed to help route wires in the cryostat (Figure 3.2a) [30], and the "picture frame board" supplied by the LBNL CCD group, upon which the CCD had been mounted (Figure 3.2b). In this section, the paths of input and output signals are described.

The clocking signals control the movement of charge in the serial and parallel directions, as well as triggering the amplifier's charge measurements and the reset between measurements. The ARC-22 timing board controls the signal timing, while the ARC-32 clock driver board generates the analog voltages. These signals are routed to the interface board at the side of the cryostat (Figure 3.1b), where the signals are filtered with RC circuits in order to lengthen the rise and fall times. The interface board passes the filtered signals through electrical feedthroughs to the inside of the cryostat. Inside the cryostat, the clocking signals are carried (by non-magnetic "phosphor bronze" cryostat wire) to the Cryo Connector Board. This board routes the signals to either side of the CCD, and plugs into connectors on the picture frame board. The picture frame board then routes the signals to finely-spaced pads next to the CCD, which are wire-bonded to pads on the CCD device itself.

The bias voltage is generated by a high-voltage bias board designed by the CCD group at LBNL. The board sets the bias level, uses filters to reduce any voltage noise, can ramp the voltage up and down, and is controlled digitally. The bias voltage, along with some additional voltages, is routed to the interface board and passed through to the CCD in the same manner as the clocking signals.

The wiring of the output signals from the CCD is critical for minimizing noise in the charge measurements and thus the resulting image. The charge stored in the electric potential wells of the CCD pixels is measured sequentially by amplifiers at

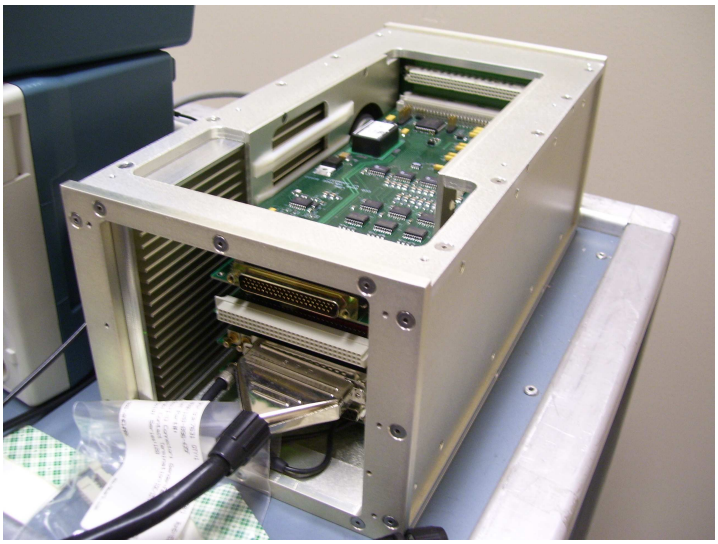

(a)

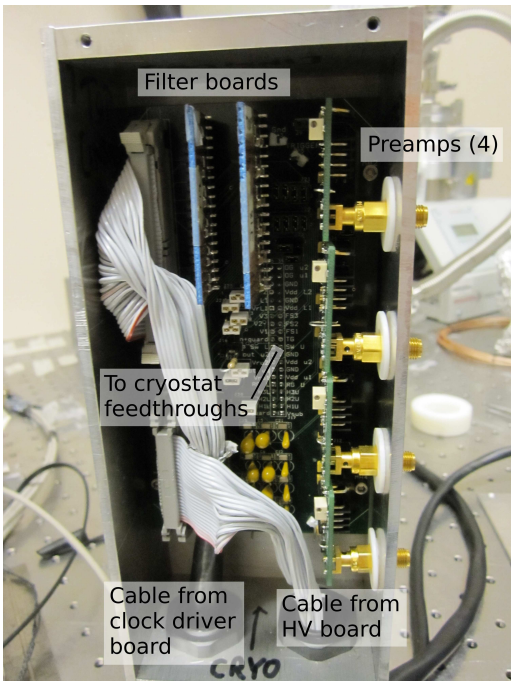

(b)

Figure 3.1:
(a) The electronics boards for the CCD operation, mounted in the housing.
(b) The interface board at the side of the CCD cryostat.

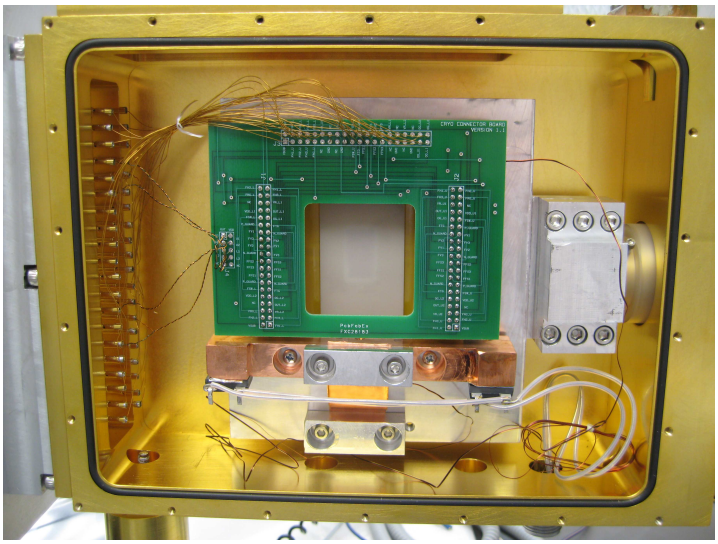

(a)

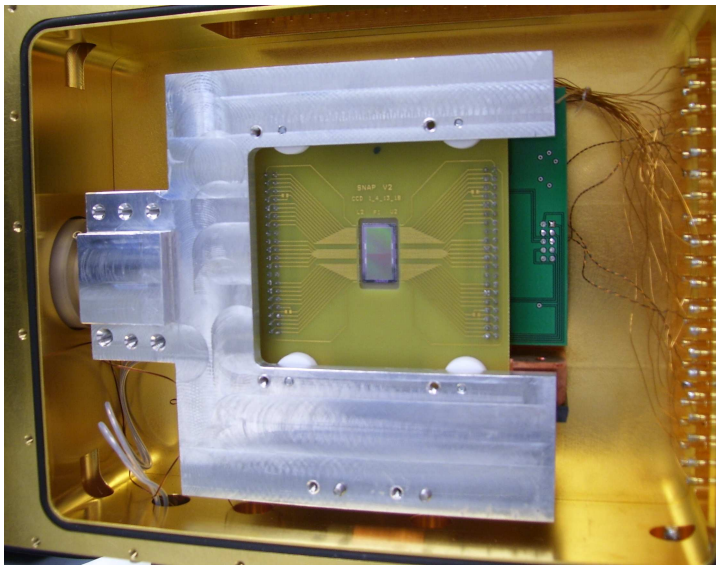

(b)

Figure 3.2:
(a) The final version of wiring, using the green "Cryo Connector Board". The picture frame board is behind in yellow, with the CCD visible through the translucent white aluminum nitride layer (see also Figure 3.4a).
(b) The view from the opposite side as (a). (Note that the picture frame board is mounted in the wrong orientation in this photo; compare Figure 3.5a)

each of the CCD's four corners[1]. The amplifier output signals are connected to the cryostat feedthrough in twisted pair with a drain voltage in order to reduce the impact of electromagnetic interference. Each CCD amplifier output signal drives the inputs of another preamplifier, which are located on the interface board at room temperature. These preamplifiers invert the signals and provide buffered signal outputs. The output signals of the preamplifiers are connected to the ARC-48 video board, where the analog voltages are converted to digital values and sent to the computer.

Communication from the ARC electronics to each other and the computer are controlled by the ARC-22 timing board, which also has a dual fiber optic cable for digital communication with a PCI board in the computer.

3.1.2 Thermal design

The CCD performs best at a temperature of about 130 K to 140 K. This requires significant cooling from room temperature, which can easily be performed with liquid nitrogen, but nitrogen boils at 77 K which is too cold. In order to achieve the proper temperature, as well as allow the temperature to be adjusted, the CCD was mounted on a separate thermal stage which is partly isolated from the *cold finger*, the thermal interface of the cryostat to the liquid nitrogen. The thermal stage is coupled to the cold finger by a thin copper foil. The cooling power of the cold finger at liquid nitrogen temperature is balanced by heating resistors on the thermal stage. The design is shown in design drawings in Figure 3.3 and in photographs in Figure 3.4. The temperature can be adjusted over a wide range (as high as about 350 K), in order to study the performance of the CCD at warmer temperatures which would be more practical for a portable device in the future. However, the temperature-dependent behavior is not part of this work.

The thermal stage, maintained at a temperature of about 130 K, consists of the following components:

- a copper bar, which provides thermal mass to stabilize the temperature
- the picture frame board and CCD. The CCD is centered in a cutout in the center of the board, supported by an aluminum nitride layer which also conducts heat to and from the device
- two power resistors mounted on the copper bar for heating

[1] In technical terminology, these amplifiers are floating gate p-channel JFETs configured as source follower amplifiers with 20 kΩ load. Explanations are in the references [63, 67].

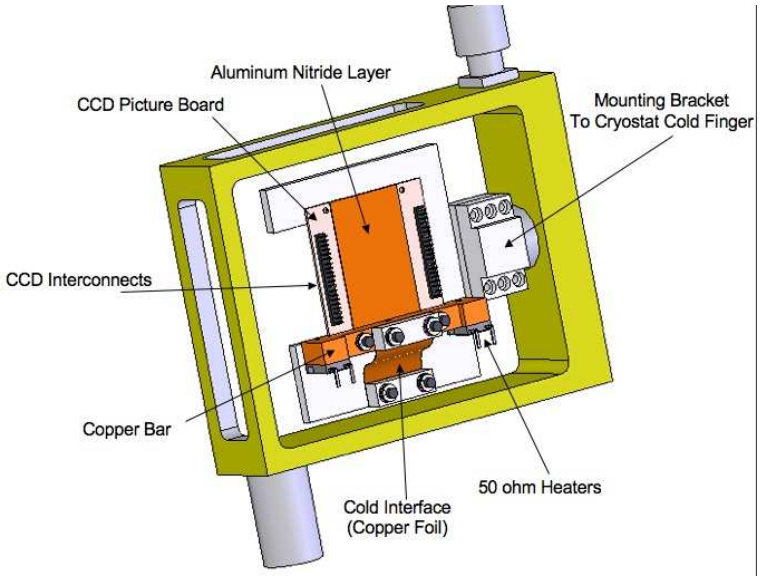

(a)

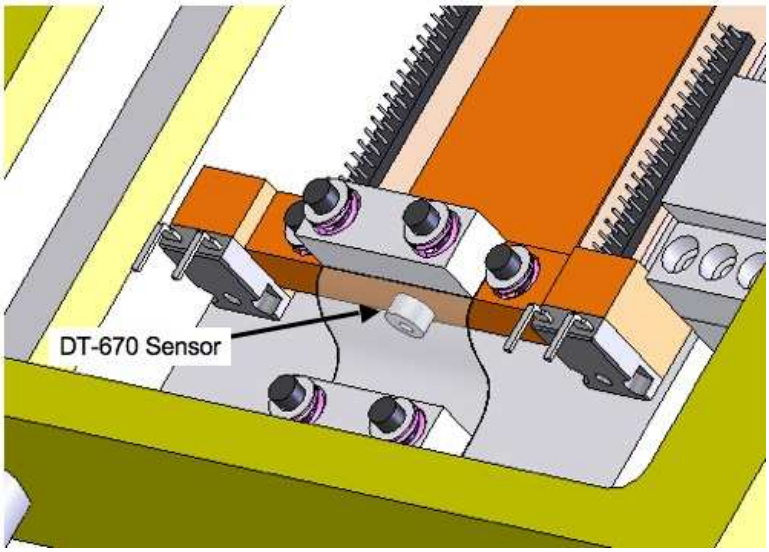

(b)

Figure 3.3: Design diagrams of the thermal stage design.
(a) Full view of the cryostat.
(b) Close view of the interface between the warmer thermal stage and the cold plate. The copper foil is made transparent to reveal the thermal sensor.

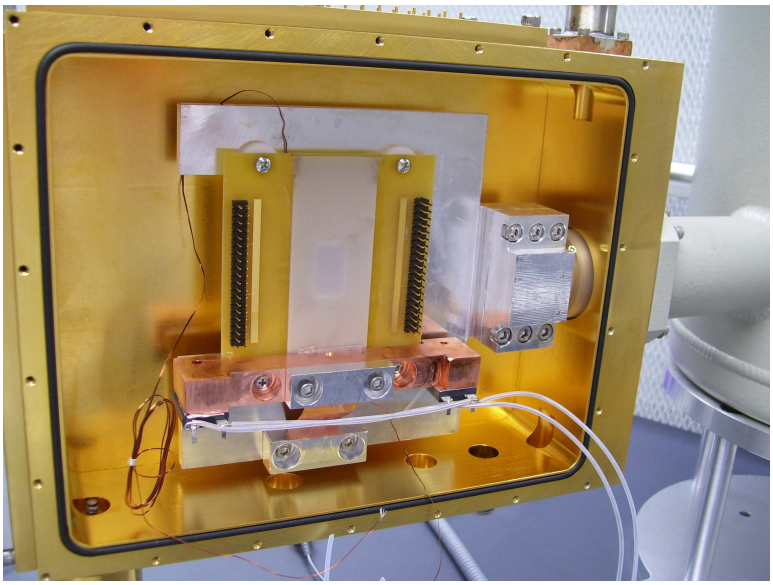

(a)

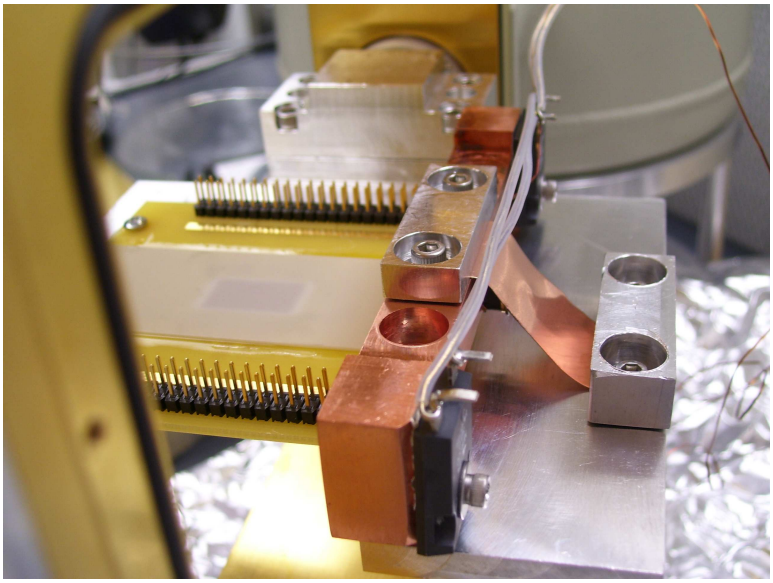

(b)

Figure 3.4: Photos of the thermal stage in cryostat.
(a) Full view of the cryostat, like that in Figure 3.3a. The wires are not yet attached to feedthroughs on the cryostat.
(b) Close view of the interface between the thermal stage and the cold plate. In this photo, the entire cold plate has been rotated with respect to the cryostat, for assembly.

- a temperature sensor (Lakeshore DT-670 calibrated silicon diode [79]), which is mounted on the copper bar

The resistors and sensor are connected to a Lakeshore 325 temperature controller [79].

Without any infrared shield between the CCD and the cryostat wall, the CCD will be warmed by the black-body radiation of the room-temperature wall of the cryostat. This radiative heat flow will offset the conductive heat flow between the CCD and the copper bar, and so the CCD itself will have a temperature offset from the sensor on the copper bar. To measure the offset as a function of CCD temperature, the first CCD mounted in the cryostat had a thermal sensor attached to the CCD by thermally conductive epoxy (Figure 3.5a). This device was known as "CCD0". By setting the temperature controller to a series of temperatures, letting the system come to equilibrium at each one, and measuring the temperature on the CCD itself, the temperature-dependent thermal offset was measured (Figure 3.5b). This may vary slightly based on laboratory temperature and other qualities of the thermal environment, but the variations in laboratory temperature are very small compared to the temperature difference between the laboratory and the CCD thermal stage. Some initial testing was performed using CCD0 at temperatures of 130 K to 140 K, but the bond to the thermal sensor induced artifacts in the image and increased the noise in the pixel image.

After finishing the measurement of the thermal offset, a new CCD was mounted without the hindrance of a thermal sensor on it. This CCD is known as "CCD1", and was used for the remainder of the experiments described in this document. During all operation of CCD1 in the BeARING laboratory, the temperature of the copper was maintained at 130 K and the calculated temperature on the CCD itself is 137.5 K.

3.1.3 Control software

The user controls the array of CCD electronics through a computer program named "Voodoo". Voodoo is a Java-based software package which communicates with the ARC timing board via the fiber-optic data link. It was developed by San Diego State University and ARC with customization by LBNL, and the clocking signal code was configured for the SNAP CCD by LBNL with minor additional modifications in this work.

A screenshot of the main window of Voodoo is shown in Figure 3.6. Configuration includes setting the CCD image dimensions in pixels, loading a timing code file which defines the sequence of raising and lowering clock voltages, and setting voltage values for the clock signals, reverse bias, and gate and drain voltages. After applying high

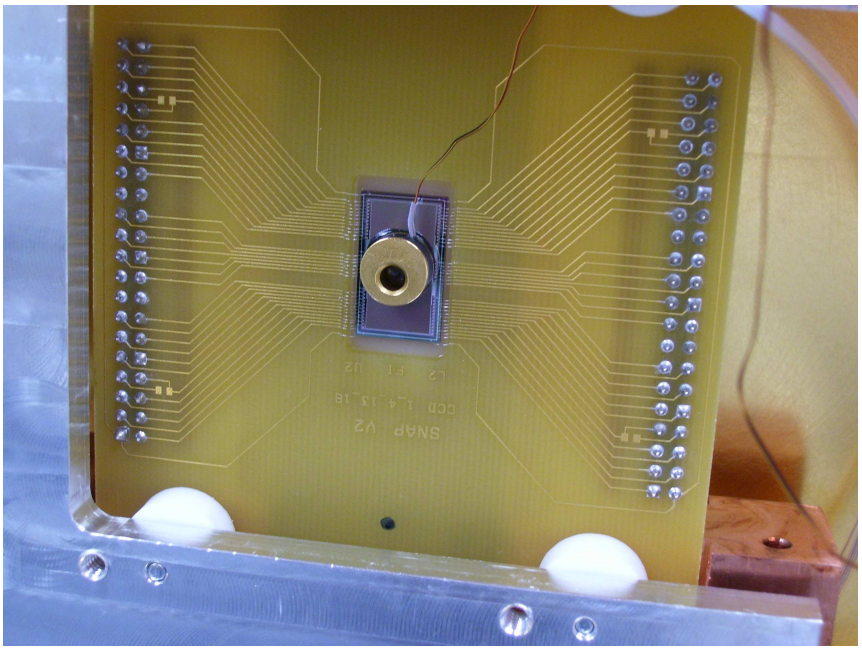

(a)

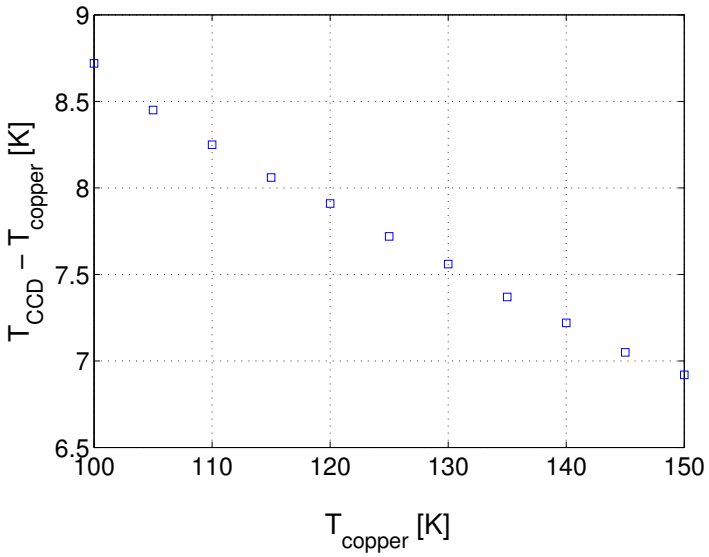

(b)

Figure 3.5:
(a) The thermal test CCD (CCD0) and picture frame board, mounted on the thermal stage.
(b) Thermal offset between the device and the copper bar, as a function of temperature. The uncertainties are smaller than the data points.

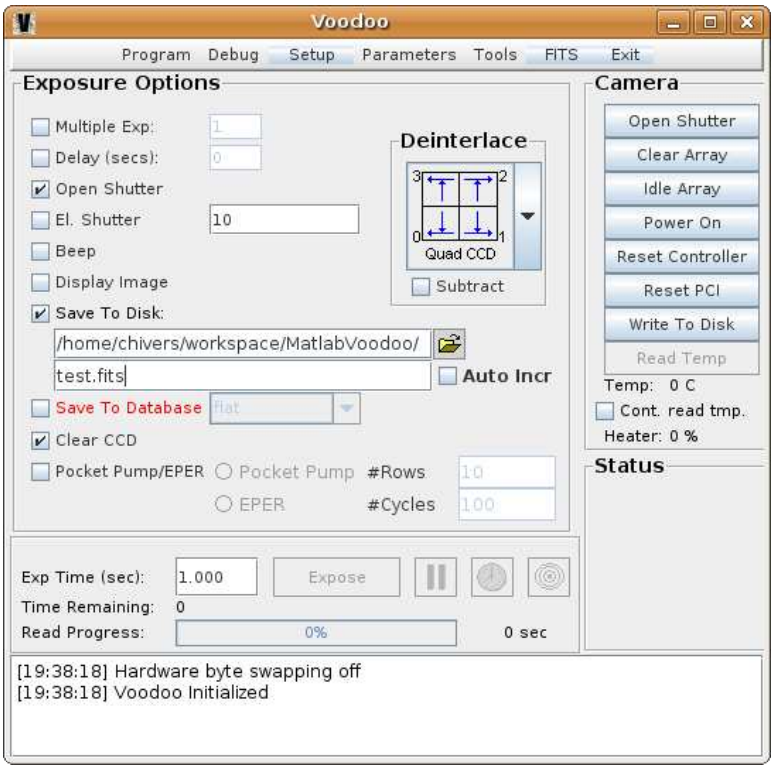

Figure 3.6: Screenshot of the main window of the Voodoo CCD control software.

voltage to the device, basic operation of the CCD involves setting an exposure time, providing a filename, and clicking "Expose". After waiting for the exposure time, the charges are shifted through the CCD while being measured by the amplifier, preamplifier, and digitizer, and the resulting image is saved to a FITS-format file on the computer [129]. Additional options include multiple consecutive exposures, auto-incrementing filenames, and an electronic open-shutter logic signal which was utilized in the coincidence experiment (Section 3.3).

The FITS file contains a digital value for each pixel, which represents the amount of charge measured in that pixel. However, the video board adds an offset to the digital value, so that the value is always positive even if the noise contributes a negative charge. The average value of pixels in a quadrant without radiation-induced charge is called the *black level*. The black level includes any dark current measured in the device over the exposure time, but in these measurements, the exposure times are short (no more than a few seconds) and dark current is negligible. The black level is useful for measuring the readout noise (Chapter 5), and was found to fluctuate in this device (section 3.2.2).

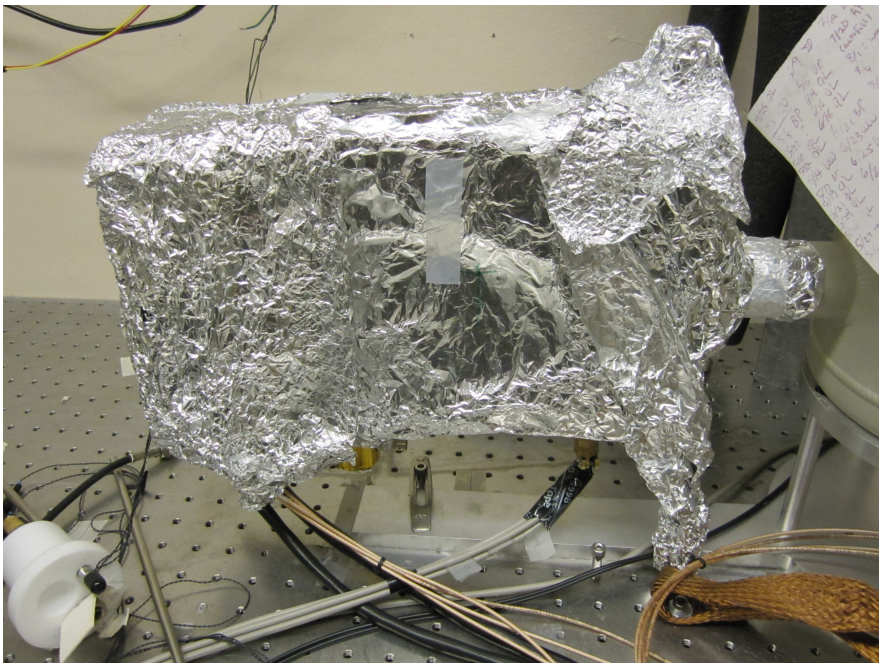

Figure 3.7: The CCD cryostat in the final configuration of aluminum foil for noise reduction. The foil is grounded to the experiment table on the lower right.

3.1.4 Noise reduction

The electronic readout noise in the CCD was initially measured to be the equivalent of over 200 eV (FWHM), which is quite high compared to the less than 20 eV achieved by the LBNL CCD group. In an attempt to reduce possible electromagnetic interference, the interface board box was covered with aluminum foil, which was found to reduce the noise significantly. Aluminum foil around the main part of the cryostat also helped to reduce the measurement noise (Figure 3.7). Initially it was unclear why the foil made a difference when the device and electronics are contained in a grounded metal box. However, more recently it was found that light can leak through the seals of the cryostat [101], even though the cryostat holds vacuum effectively. Thus, some or all of the foil's noise reduction effect may be due to it being optically opaque.

In the final configuration, the electronic readout noise is measured to vary between 30 eV and 50 eV per pixel (FWHM; or 13 eV to 20 eV σ).

3.2 Irregularities

The CCD does not always behave as expected. This is not surprising, given that the thick CCD was not tested extensively by the LBNL engineering group, and the CCD electronics and cryostat were assembled in the BeARING laboratory for the first time.

The observed irregularities include the depletion thickness in the device, qualitative differences between readout quadrants, and fluctuations in the black level and readout noise. A full understanding of the CCD operating in the BeARING laboratory requires some discussion of these observed features.

3.2.1 Readout quadrants

As described in sections 2.3.9 and 3.1.1, the charge in the pixels is normally read out from each corner, through an on-chip amplifier and a preamplifier, and then converted to a digital value in the video card.

One quadrant (top left in the coincidence experiment, quadrant "1") was never operated successfully. Only faint blurry streaks are occasionally visible in this quadrant. The CCD was not tested in any other system before this work, so the problem may be leftover from the fabrication process.

Two quadrants (top right and bottom right, quadrants "2" and "3") worked properly throughout the experimental measurements, exhibiting similar gain coefficients and noise characteristics.

The last quadrant (bottom left, quadrant "4") was reading out properly during early testing stages, but soon began exhibiting a streaking behavior which precluded the use of this quadrant. Tracks were visible, but streaks or trails were also visible in pixels to the right of any pixels containing charge (Figure 3.8). The streaking behavior is consistent with a very low charge transfer efficiency (CTE) of at least one serial clock in the quadrant. The data are approximately consistent with a single pixel in the readout row having a CTE of roughly 35 %. Charge which is not transferred in the clocking operation adds to the signal measured in the pixel after it, resulting in the appearance of a streak away from the readout amplifier. In addition, some rows appeared dark even though they clearly were positioned in the middle of a track. This could be caused by an occasional failure to transfer charge in the parallel direction. Two dark rows are visible in Figure 3.8.

The full operation of every quadrant is not necessary for acquiring meaningful electron tracks. Besides the thermal test CCD, only one CCD was operated with the readout system. Due to the complexity of the readout, and the lack of readily available CCD expertise, the only attempts to resolve the readout problems consisted of checking and re-fastening wiring connections, and adjusting settings in Voodoo.

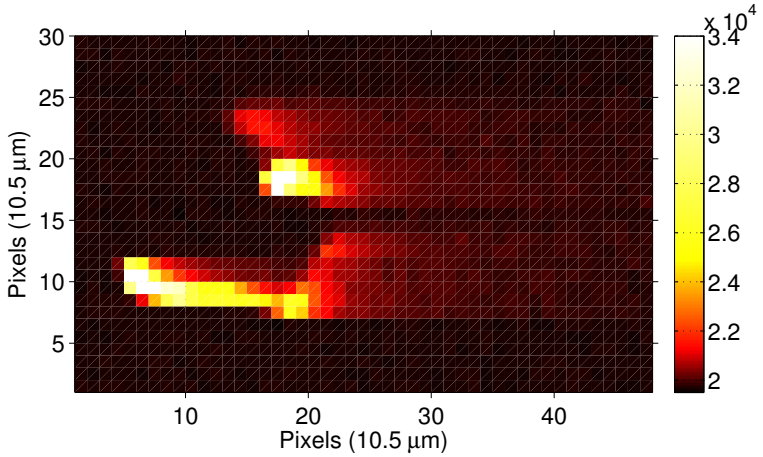

Figure 3.8: An electron track from quadrant 4, showings problems related to serial and parallel charge transfer. The tentative interpretation is an electron starting at the top and moving clockwise to the lower left corner, despite the two dark rows in the middle. The color scale is in the raw digital units of the data file, because energy calibration is not feasible.

More extensive testing would require precise electrical tests on the CCD surface, using an oscilloscope to probe voltages at different points in the system, testing of the readout system with a different CCD, or testing with different channels of the interface board, preamplifiers, cables, and video card. These steps were not attempted for the sake of time, because the operation of two quadrants was sufficient for the experiments.

The result of these quadrant issues is that only half of the CCD is useful for measurements. Specifically, the coincidence experiment was less efficient because the beam spot covered quadrants 3 and 4, but only quadrant 3 gave useful data.

3.2.2 Black level and noise fluctuations

The black level occasionally shifts beyond statistical fluctuations. Some of the shifting is correlated with the first several minutes after beginning operation. The reasons for shifts at other times in the middle of operation is unknown, and could be related to either the CCD itself or anything in the signal chain. These variations are not a problem as long as the black level is not too close to the upper limit of the 16-bit digitizer range ($2^{16} = 65\,536$), and as long as they are compensated for in each image calibration (see section 5.1.1).

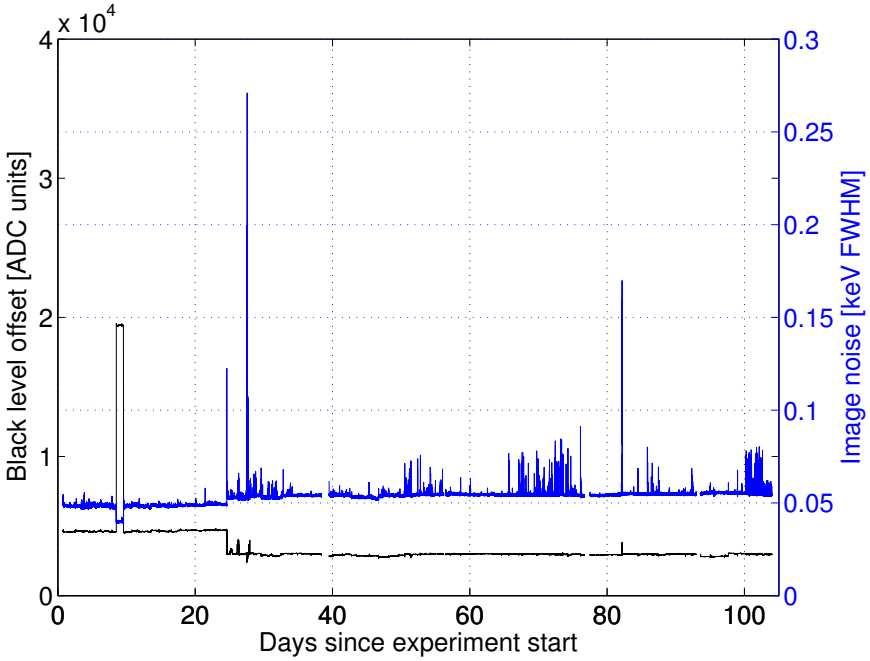

Figure 3.9: Fluctuations in the black level offset and black level noise for quadrant 3, over the course of the coincidence experiment (described in Section 3.3). The upper data are described by the right axis, and the lower data by the left axis. ADC units are the digital units provided by the analog-to-digital converter (digitizer).

The magnitude of the black level noise, or *image noise*, also fluctuates significantly. Image noise is defined as the width of the distribution of measured pixel values from one whole quadrant. Since the vast majority of pixels do not contain deposited energy, the distribution is dominated by normally-distributed noise centered on the black level (see also Figure 5.1).

Figure 3.9 shows both of these properties fluctuating over the course of the coincidence experiment (described in section 3.3 below). The major discontinuities in the offset data are correlated with fluctuations in the noise as well. The noise graph frequently shows additional fluctuations. Most of the peaks in the image noise graph are rapid fluctuations occurring continuously over a period of a few hours. The fluctuations occur both during the day and at night, so they do not seem to be directly associated with human disturbances in the laboratory environment.

It is not clear what factors contribute to these variations, but temperature, electronic components, and external vibrations may play a role. However, only a handful of images are badly affected by an increase in noise (22 images above 0.1 keV FWHM, out of 1.73×10^6 images total).

The data analysis algorithms described in Chapter 5 are specifically designed to compensate for fluctuations in the black level. Noisy images will degrade energy resolution and electron track measurement, but the noisy images are few enough that the overall impact is minimal.

3.2.3 Depletion thickness

The LBNL CCD group has found that 200 V reverse bias is sufficient to deplete the full thickness of 650 µm-thick devices, although the thick devices are only for testing. However, in the BeARING laboratory, tracks have been observed showing a charge cloud width too wide to be explained by the drift time through a fully-depleted bulk, and also with parts of the track showing very little charge collection (Figure 3.10). These wide tracks include roughly 3 % of tracks from ^{137}Cs, or less than 1 % of tracks from ^{241}Am due to the shorter track length. In particular, the one corner of the device (bottom right in the coincidence experiment) shows a higher rate of these wide tracks, suggesting a greater thickness of undepleted bulk there.

The existence of undepleted volume indicates that either the bias voltage applied is not applied properly across part or all of the CCD back plane, or the impurity concentration in part or all of the CCD bulk is higher than in devices which the LBL group has measured. It is not clear which of these factors is present.

Energy deposited by electrons in the undepleted volume will be only partly collected in the track pixels, and largely lost due to diffusion in other directions. This is comparable to the loss of energy when an electron escapes the CCD entirely. In essence, the undepletion reduces the active volume of the CCD.

Although the irregularities in readout and depletion have an effect on the measurements, electron tracks can still be measured accurately. The inactive quadrants and undepletion reduce the sensitive volume of the CCD, but do not affect tracks measured in the remaining sensitive volume. The fluctuations in black level have little effect on the measurements, since the image calibration removes any offset, and the variations in noise are insignificant for the vast majority of images. Therefore, the electron tracks which are measured are not hindered by these irregularities.

3.3 Coincidence experiment

Gamma-ray interactions were successfully measured in two different devices (CCD0 and CCD1) in the BeARING laboratory. Analysis of modeled electron track images in the CCD indicated that the trajectory reconstruction algorithm was capable of measuring the initial electron direction with some precision (Chapters 4, 5, and 6).

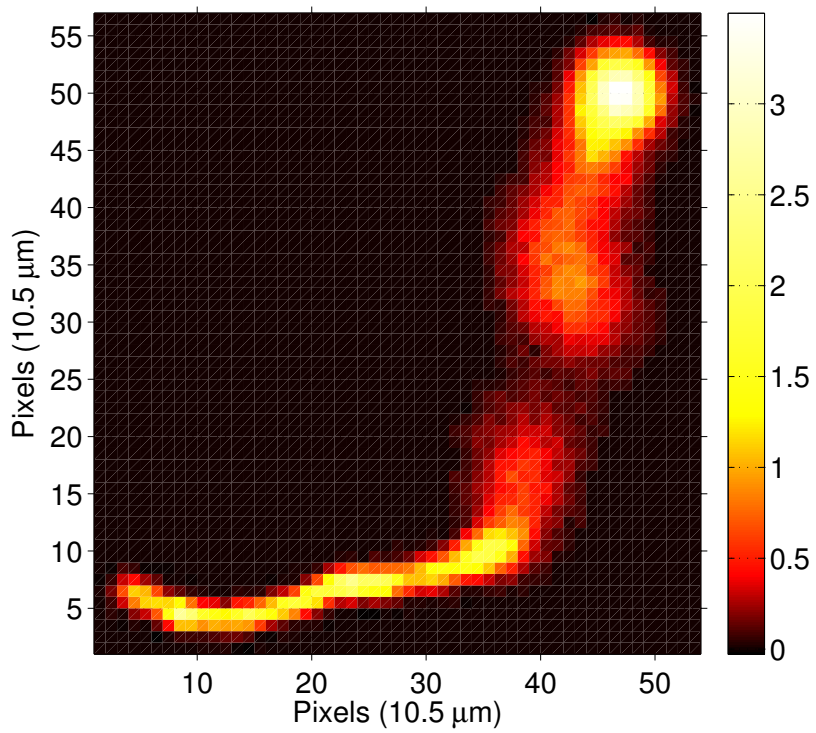

Figure 3.10: An example of the effect of undepletion in the CCD. The electron track begins at lower left and ends at upper right, but in between traverses a region near the back of the CCD which is not depleted, and from which most charge carriers are not collected. The color scale is in units of keV.

However, in order to experimentally evaluate and confirm the sensitivity of the electron trajectory reconstruction algorithm, individual electron tracks with known initial directions had to be measured. This was the general goal of the coincidence experiment.

The electron tracks measured will have several different parameters that influence the resulting angular sensitivity of the reconstruction algorithm. The most relevant parameters are the energy of the track and the angle to the pixel plane, β. Another relevant parameter is the depth of interaction in the CCD, because the track width depends on this depth. Depending on the design of the experiment, the measured tracks will cover some range in each of these parameters. A larger range of energy, β, and depth allow the models to be tested more fully. However, if the measured tracks are limited in number, a smaller range provides a more sensitive comparison to the

model in that range.

In principle, the full range of parameters should be evaluated in the experiment. However, in practice, this is not feasible, as discussed below. Nonetheless, the experiment covers a significant range of electron energies from 160 keV to 360 keV and $-27^\circ < \beta < -2^\circ$.

3.3.1 Possible methods

There are two main ways one might envision measuring electrons with known trajectories on an event-by-event basis.

The most direct method would be to employ an electron accelerator source to propel electrons directly into the CCD, with a known energy and direction. However, this method has some disadvantages. First, this method would require the CCD to be in the same cryostat as an electron source, which would require difficult design and engineering work. Second, all electron trajectories would begin at one of the surfaces of the CCD, rather than inside the bulk where gamma rays interact. This would inhibit the comparison between the electron-source tracks and the gamma-ray-induced tracks used for electron-tracking-based Compton imaging. Third, a precise understanding of layers of inactive material on the entrance surface of the CCD would be needed to deconvolve physical electron deviations from uncertainties in the algorithm measurement. In addition, the directional uncertainties inherent in an electron source are fundamentally different than the uncertainties inherent in Compton scattering. Both may be well understood, but the use of an electron source would require additional analysis to account for the difference in uncertainties. Finally, using an electron source would allow only a single electron direction to be probed at a time. A number of separate measurements would have to be taken to probe different energies and angular ranges of electron direction.

Instead, the method selected for measuring electrons with known initial trajectories is to measure Compton-scattered electrons in the CCD, in coincidence with a detector that measures the scattered photon. One advantage of this method is that the electrons are generated in the exact same manner as those in Compton imaging. Also, electron track Compton imaging can be directly demonstrated by calculating Compton cone segments for the events from the experiment. Each coincident event results in an electron track with its trajectory known to the limits of Doppler broadening and the position and energy resolutions of the CCD and absorber detector.

There are two significant disadvantages to the coincidence method, however. In order to correlate events between the two detectors, the combined time resolution should be better than the time separation of interactions in either detector. This is difficult because the CCD only resolves events to the exposure time of the image,

and takes 2.8 s to read out the image. If the exposure time is made shorter to better time-resolve events, the proportion of time that the CCD is active is greatly reduced. Secondly, the geometric efficiency for the photon to scatter from the CCD toward the absorber detector is limited by the size of the absorber and the proximity to the CCD. If the absorber is in a cryostat of its own, the dimensions of both cryostats prevent the detectors from being placed very close together, and limit the geometric scatter efficiency. The combination of limited live time fraction, necessitated by the time resolution issue, and small geometric efficiency suggests that a lengthy measurement time would be needed to achieve significant results.

3.3.2 Experiment overview

The coincidence experiment includes a collimated, shuttered gamma-ray source; the CCD placed in the collimated beam as a scatter detector; and a high-purity germanium double-sided strip detector (HPGe DSSD) located away from the collimated beam. The conceptual layout is illustrated in Figure 3.11, and the final configuration with shielding is shown in Figure 3.12. Data are acquired digitally for both the CCD and DSSD, with the acquisition controlled by MATLAB code. The experiment operated for 104 days.

The initial direction of the electron is known to about 3° FWHM, depending on the exact scattering angle from the CCD to the HPGe. This uncertainty is primarily due to the unknown initial electron momentum, with a contribution from the position resolution of the germanium strip detector. The experiment measured electrons between 160 keV and 360 keV, $-27° < \beta < -2°$, and throughout the depth of the CCD. The energy and angular range are limited by the size and distance of Ge2. A smaller distance would allow a greater energy and angular range to be covered, but at the expense of greater uncertainty in the calculated initial electron direction.

In the rest of this section, these components are described in greater detail. The chain of analysis codes is described in Chapter 5, and the results are described in Chapter 6.

3.3.3 Germanium double-sided strip detector

An absorber detector is required to detect the Compton-scattered photon, in order to determine the scattering angle and energy. It should be large enough to absorb the scattered gamma ray with a significant efficiency, and also have good position and energy resolutions. Position resolution is necessary to define the direction of the scattered photon and allow a precise calculation of the initial electron direction. Energy resolution is important for rejecting background events, which dominate due to the

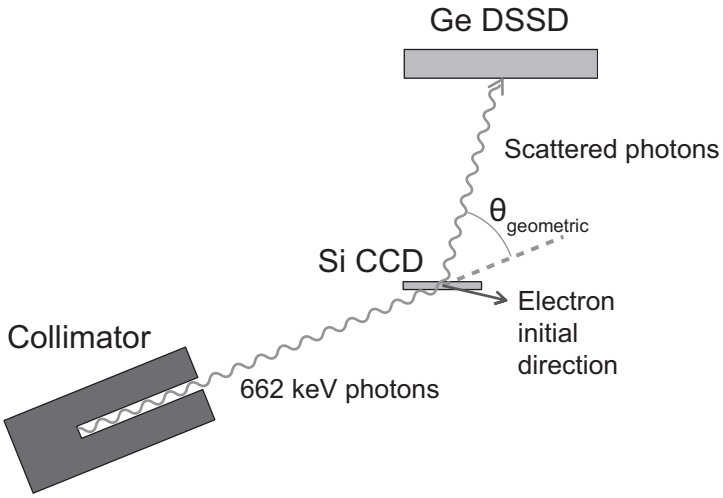

(a)

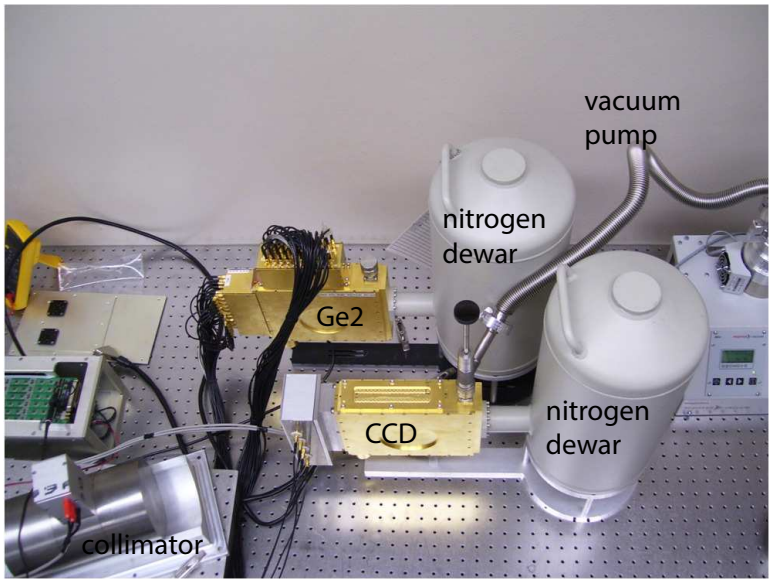

(b)

Figure 3.11:
(a) Schematic diagram of the coincidence experiment, from a top view. Sizes and distances are not to scale, although the angle of the photon beam and scattering are approximately accurate.
(b) Illustrative representation of the coincidence experiment setup, using the actual equipment, from a top view. In the actual experiment, Ge2 was rotated 180° and much closer to the CCD (Figure 3.12). The coordinate system is shown at the back left.

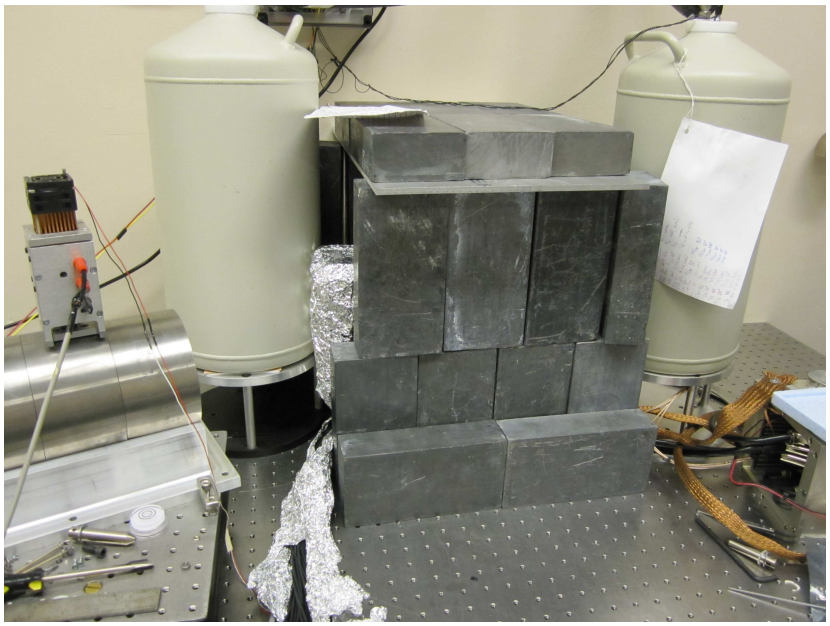

(a)

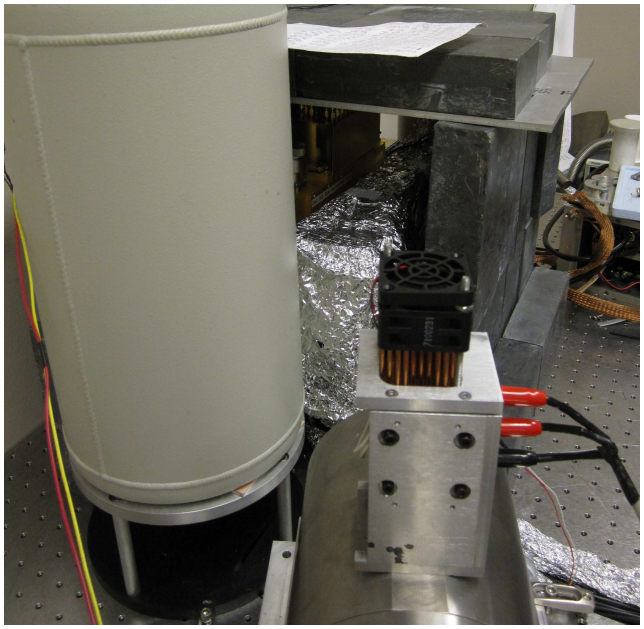

(b)

Figure 3.12:
(a) A front view of the experiment, with a lead cave around both cryostats.
(b) The view along the beam line. The beam emerges from the far side of the tungsten-alloy collimator at bottom center.

very low geometric efficiency of about 3×10^{-3} (see also section 6.3.2). Background can be rejected by requiring a full-energy deposition between the CCD and absorber.

This experiment used a high-purity germanium double-sided strip detector, designated "Ge2". The detector and cryostat system were designed and fabricated at Lawrence Livermore National Laboratory. The detector crystal is a disk 90 mm in diameter and 11 mm thick. One face of the crystal is held at high voltage (+1000 V), while the other is grounded. Each face is patterned with 38 strip electrodes at 2 mm pitch and with a 0.25 mm gap between strips. The strips on one side are orthogonal to those on the other side, such that the strips which trigger on each side define two position coordinates of the interaction location. A guard ring electrode around the outside edge protects the strip electrodes from surface leakage current along the sides of the cylinder. Figure 3.13a shows the detector crystal.

Each strip electrode is connected to a room-temperature preamplifier stage. The preamplifier produces a voltage signal that is digitized at a rate of 100 MHz, with a voltage resolution of 16 bits, in a Struck Innovative Systeme 3302 module [57]. The cables from the preamplifiers, along with the cryostat and dewar configuration, are shown in Figure 3.13b. If strips on both sides of the detector trigger within a short time window, then the digital voltage traces of all triggering channels and their neighbors are saved to a buffer and transferred to a computer via a universal serial bus (USB) cable. If multiple channels on each side trigger, then MATLAB code reconstructs the likely interaction positions and energies to produce those triggers.

The position resolution in the strip dimensions is limited by the strip pitch to 2 mm. The position in the depth dimension can be reconstructed with an accuracy of about 1.9 mm FWHM (see Section 5.3.1). The energy resolution of Ge2 over all operational strips and the duration of the experiment is measured to be 11 keV FWHM at 1461 keV. This energy resolution is rather poor for a HPGe detector, and is due to high leakage current and microphonic vibrations in the preamplifiers.

The history of Ge2 includes some operational errors including accidental warming to room temperature with high voltage applied, which resulted in increased leakage current. In addition, seven strips on the DC-coupled (grounded) side are inoperable due to high leakage current.

Data from interactions in Ge2 are collected in the digitizer buffers during the open-shutter time (see Section 3.3.5), and then while the shutter is closed, a global veto signal is applied to the digitizers and the data are transferred to the computer.

3.3.4 Collimation

The low intrinsic efficiency of the CCD, low geometric scatter efficiency, and limited time resolution in the CCD all dictate that sources of background events must be

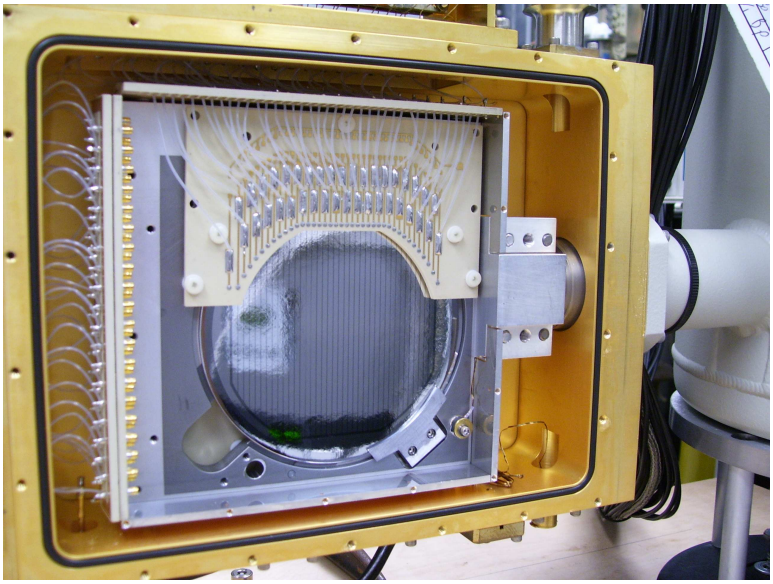

(a)

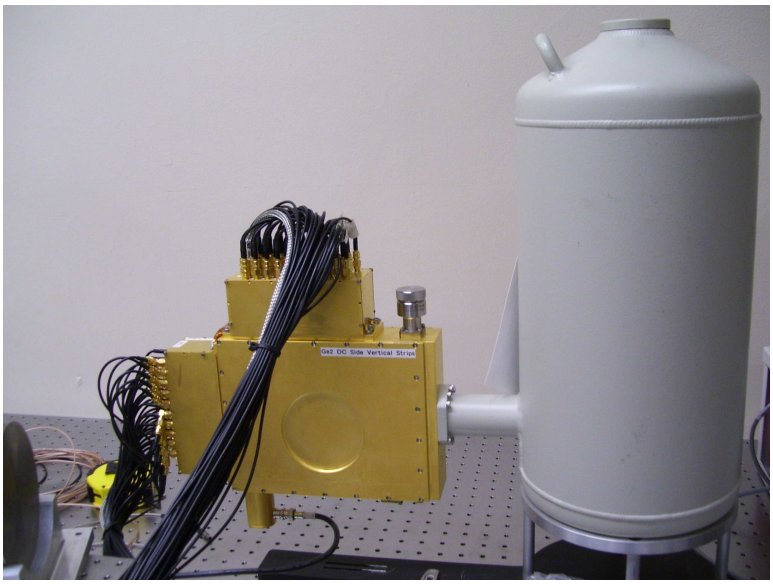

(b)

Figure 3.13:
(a) The HPGe double-sided strip detector, Ge2, mounted inside its cryostat.
(b) Ge2 cryostat, dewar, and cables which carry signals to the digitizers, on the experiment table.

reduced as much as possible for the true coincident event sequences to be distinguishable. Therefore, the gamma-ray source is collimated into a narrow cylindrical "pencil" beam to minimize scattering from the cryostats and surrounding materials into either detector. If the CCD were replaced by a larger detector, the collimator would also be needed to restrict the possible kinematics of photon scattering to the desired range, but for the small size of the CCD this is not necessary.

The collimator is comprised of four cylindrical sections machined from tungsten alloy. The backmost section holds the source and shields it on all sides except the direction of the beam. One of the two center sections encloses a separate block of tungsten alloy, which is the shutter for the beam. The block stops the beamline until lifted by a solenoid. The frontmost section is closed except for a 1 mm-diameter cylindrical opening. The total distance from the source to the outside of the 1 mm opening is 24 cm, and the angular spread at the CCD is less than 0.5°.

3.3.5 Shuttering

The beam is controlled by lifting the shutter block using a solenoid on top, mounted in an aluminum housing. The solenoid pulls a rod up when electric current is applied. Several challenges were encountered, including critical overheating (burnout) of the solenoid and inconsistent lifting of the shutter. The final design is described below and shown in Figure 3.14.

A small compressive spring was inserted around the rod where it emerges from the top of the collimator to help lift the shutter block out of the lower position. The beamline is still blocked by the shutter when the rod is resting on the spring, but the force needed to lift the block is reduced. Also, a copper heatsink was affixed to the top surface of the solenoid housing with an electric fan blowing air through it. Thermally conductive epoxy helped transfer heat from the solenoid housing to the heatsink. The heatsink coupled with a lower current in the solenoid prevented burnout of the solenoid.

In order to maximize the effective open-shutter time, the delay of the shutter's mechanical lifting and falling was calibrated. The cylindrical collimator insert which provides the 1 mm opening was removed to leave a 10 mm opening, and a sodium iodide scintillator detector was placed in front of the opening. The start time of rapid pulses in the scintillator was compared to the start of the electronic shutter signal on an oscilloscope. Repeated measurements gave a delay of $45\,\text{ms} \pm 2\,\text{ms}$ between the electronic shutter signal and the actual lifting of the shutter, and a delay of $67\,\text{ms} \pm 2\,\text{ms}$ between the cessation of the signal and the actual falling of the shutter.

The effect of this physical delay is to decrease the SBR. Without a delay, the source is not exposed at the beginning of the exposure when the shutter has not

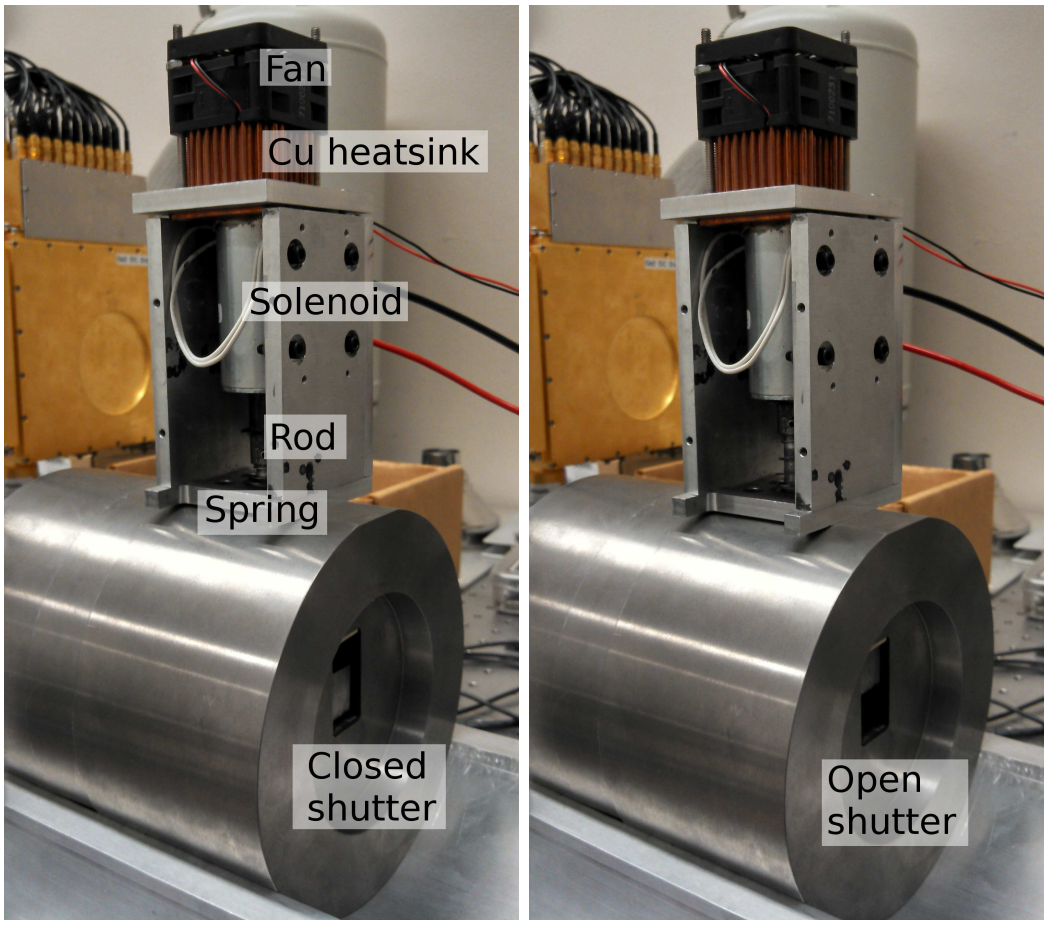

(a) (b)

Figure 3.14: View of part of the collimator and shutter assembly, with the shutter (a) closed, and (b) open. The collimator is not in position for the coincidence experiment in these photos.

yet lifted. In addition, interactions immediately after the exposure time are lost even though the source is still exposed. The magnitude of these effects are 18 % and 27 %, respectively, relative to the exposure time of 0.25 s. With the delay implemented, the effective shutter time is 0.27 s.

An electronic gate and delay generator was used to convert the shutter lifting signal into a "physically-open shutter" signal, which is logically inverted to produce the veto signal on the Ge2 event acquisition. The CCD exposure time cannot be modified, because the shutter signal is controlled by the CCD software. However, the background rate in the CCD before the shutter lifts is negligible, and the interactions

occurring as the shutter begins to fall occur during the first 5% of the image readout. The tracks will appear in the wrong vertical position in the image, because they are generated after some row shifting of the readout, but the position offset is sub-mm and insignificant compared to other position uncertainties.

3.3.6 Background countrates

Both detectors were heavily shielded with lead bricks in order to reduce counts induced by background radiation in the laboratory (Figure 3.12).

In the CCD, the SBR comparing interactions of beam gamma rays to interactions of background radiation was on the order of 100, so background interactions were not significant[2]. The total interaction rate in the CCD, averaged over the course of the experiment, was $1.0776 \pm 0.0015\,\mathrm{s}^{-1}$.

Background radiation was much more significant for Ge2, because of the much larger detector mass. The total background rate in Ge2, averaged over the course of the experiment, was $1.5915 \pm 0.0019\,\mathrm{s}^{-1}$. The signal in Ge2 was not caused by direct beam interactions, but by photons scattered from the CCD into Ge2, which was a very small signal due to the geometric efficiency of about 3×10^{-3}. The SBR, calculated from the true coincident event sequences described in sections 5.3.3 and 6.3.3, was about 10^{-4}. However, the SBR was increased by applying windows to the total deposited energy and the angular resolution measure, as described in section 5.3.3.

With appropriate energy windows corresponding to the range of possible scatter geometries (see Section 5.3.2), and the shutter time of 0.27 s, the false coincidence rate due to random pairings of events in the same shutter was acceptably low (about 6×10^{-3} per shutter).

3.3.7 Position calibrations

In order to calculate the true initial direction of the Compton electrons as accurately as possible, the relative positions of the source, CCD, and Ge2 must be well-known. The coordinate system is defined as follows:

- x is horizontally toward the right, while facing the experiment table;

[2]The background in the CCD was not measured accurately in the final shielding configuration. The estimated SBR of 100 comes from the ratio of counts in the Compton edge to the counts in the Compton valley. This estimate is correct if the energy spectrum of background interactions is similar to the energy spectrum of the source, and none of the counts in the Compton valley are induced by the source. Neither of these conditions is quite accurate, so this is only a rough estimate.

- y is vertically up, perpendicular to the surface of the table;
- z is horizontally toward the back of the table.

This forms a right-handed coordinate system in which x and y correspond closely with the dimensions of the CCD pixel plane (Figure 3.11b).

The solid angle of possible gamma-ray trajectories within the collimated beam is small. It follows that the gamma rays can be treated as traveling parallel to each other, and the distance from the gamma-ray source to the CCD is not important. Then it is convenient to describe the beam not by the 3D location of the source, but by the direction in which the source photons are traveling. The direction can be represented by a vector which points from the source location down the center of the beam.

This beam vector can be determined by measuring the 3D position of two different locations along the beam. The beam position measurements were greatly simplified by using optical light instead of gamma radiation. A small HeNe laser replaced the gamma-ray source, with a small diverging lens placed over the laser to produce even illumination of the inside of the collimator. The beam position was measured with an optical CCD sensor mounted on a small three-dimensional positioner on the experiment table. Then the three-dimensional positioner was adjusted by 1 cm in the x direction, and y and z were adjusted until the collimated laser beam spot illuminated the CCD sensor in the same location as in the first measurement. The difference in 3D coordinates of the two measurements defines the direction of the collimated beam.

The measured beam vector was

$$\vec{v}_{\text{beam}} = (10.000, 0.045, -4.045)\ \text{mm} \pm 0.005\ \text{mm}, \tag{3.1}$$

Or, normalizing to produce a unit vector,

$$\hat{v}_{\text{beam}} = (0.9270, 0.004\,17, -0.375) \pm 0.0005. \tag{3.2}$$

The relative positions of the two detectors were measured using a *fan beam* of collimated gamma rays: the gamma-ray source was placed in the face of one tungsten-alloy brick, and centered behind a narrow (sub-mm) gap between two tungsten-alloy bricks. The gamma-ray field emerging from between the bricks forms a thin plane in space, and interactions measured in the detectors are located within this plane (Figure 3.15). The source and collimator were located on a heavy-duty two-dimensional positioner, controlled by computer through a serial interface. By arranging the fan beam horizontally and vertically, and also shifting the fan beam to another side of the detector setup, the relative positions can be determined in three dimensions.

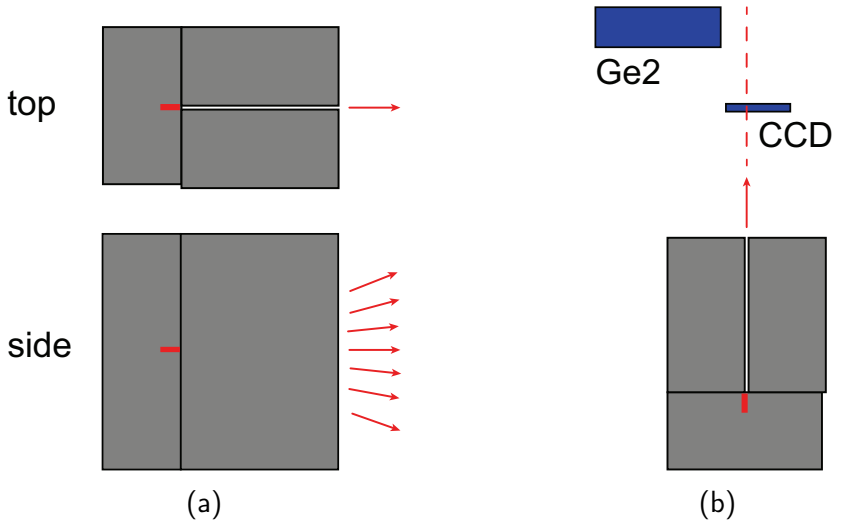

Figure 3.15:
(a) Illustration of a vertical fan beam using tungsten-alloy bricks. The source location is highlighted in red in each view.
(b) Schematic top view of the vertical fan beam with the two detectors. Detector positions and sizes are not to scale.

The detector positions were determined in an early iteration of the experiment layout, in which Ge2 was positioned with the dewar adjacent to the CCD dewar as pictured in Figure 3.11b. When it was decided that Ge2 needed to be closer to the CCD for efficiency, the position of the Ge2 cryostat base was carefully marked on the experiment table with masking tape and pen marks across the interface between Ge2's base and the table. After Ge2 was reconfigured into the position pictured in Figure 3.12, the position differential and rotation were measured and used to calculate the new position of Ge2 in the laboratory coordinate system. A new calibration with the fan beam was not performed due to the significant time needed for such a calibration.

However, several weeks into the experiment, the initial results showed that the scattering angle calculated from the position calibration did not match the scattering angle calculated from the energy deposition (see Section 5.3.3). With the beam vector and CCD position well known, it was evident that the position of Ge2 was not correct. The simplest position adjustment to bring the data into agreement was to shift the position of Ge2 7 mm in the $-x$ direction.

It is not clear when this error was introduced. However, a position error is the only reasonable explanation that is consistent with the results.

3.3.8 Data acquisition

The data acquisition for both detectors was controlled by a MATLAB framework, which accesses drivers for Ge2's SIS interface as well as the Voodoo software controlling the CCD readout. The acquisition program also controls the shutter logic signal, which removes the electronic veto for the Ge2 acquisition as well as controlling the physical shutter on the collimator. Because the shutter and both detectors are controlled by the same top-level code, the data from each detector in one shutter period can be saved with the same index number in the filename, simplifying the data analysis in post-processing.

This concludes the discussion of the components of the coincidence experiment. Chapters 5 and 6 describe other aspects of the experiment analysis and results.

3.4 Summary

The CCD developed at LBNL for the SNAP project was discovered to be suitable for measuring electron tracks. The CCD group provided sample CCDs which were installed in a cryostat in the BeARING laboratory, with a thermal design for keeping the device at about 140 K. The CCD was operated using a combination of electronics boards designed at LBNL and boards from Astronomical Research Cameras, Inc. Aluminum foil wrapped around the cryostat and preamplifiers was found to reduce the electronic readout noise, likely by blocking light leaking into the cryostat. Several interesting irregularities have been observed in the CCD operation, but none prevent the use of the device for investigating electron trajectory measurements.

An experimental understanding of the accuracy of electron trajectories measured in the CCD requires the acquisition of electron tracks with known kinematics. To this end, a coincidence experiment was designed and performed, involving finely collimated gamma-rays incident on the CCD, with a germanium double-sided strip detector (Ge2) measuring scattered photons. The collimator was fitted with a tungsten-alloy shutter, which was opened during the exposure time of the CCD and closed during readout to prevent additional interactions. Because the CCD only resolves interaction timing to the exposure length, the exposure time was reduced to minimize the false coincidence rate. This short exposure time, coupled with 2.8 s readout time and the very low coincidence efficiency of the system, demanded that the experiment run for a long period of time in order to accumulate events. Finally, the entire data acquisition was controlled by a master MATLAB process which controls communication with both the CCD and Ge2.

The experimental equipment and methods described here form the basis for the

models and analysis tools described in the next two chapters. Furthermore, the coincidence experiment allows the angular sensitivity of the reconstruction algorithm to be evaluated by measurements, in order to confirm the sensitivity predicted by the models.

Chapter 4

Models of Electron Track Images in the CCD

Physical models reflect a scientific understanding. In addition, accurate models are critical for simulating experiments that are difficult or impossible to perform, designing and optimizing an experiment, evaluating the capability of a potentially deployable system, or facilitating a deeper understanding of any type of experiment. However, it is essential that the model reflect the physical truth to a reasonable degree of precision, or else the results are not meaningful.

In this work, the experiment to measure electron tracks with known initial directions is quite challenging, and a limited number of tracks were measured (Chapter 6). Therefore, the models are essential for developing a broader understanding of the potential angular sensitivity to the initial direction of electrons in the CCD. In the future, the same models may be used for guiding the design of a useful and deployable instrument for electron track Compton imaging.

The model may be divided into the Monte Carlo portion which handles the physical interactions of gamma rays and fast electrons, and the device response portion which handles charge carrier drift, lateral spreading, and the pixel values of the CCD. The physical interactions are handled by Geant4 modeling code, customized for the requirements of electron tracking. The device response is modeled using MATLAB code developed as part of this work. Although calculations show that repulsion and diffusion are both significant for the lateral spreading of charge, the model used for this work only includes diffusion. The validity of this diffusion-only approach requires careful consideration.

Modeled electron tracks can include accurate information about the initial direction of the electron, therefore they are ideal for extensively evaluating the direction

reconstruction algorithm of Chapter 5. The modeled tracks will be used for a detailed evaluation of the algorithm's angular sensitivity with respect to track energy, β angle, device pixel pitch, and device readout noise, presented in Chapter 6. In addition, a set of modeled tracks will be compared to the measured tracks from the coincidence experiment, in order to compare the angular sensitivity directly between measurements and models. The method of appropriately selecting modeled tracks is described in the last section of this chapter.

4.1 Interactions of gamma rays and fast electrons

The first need is to model the interactions of gamma rays and electrons (sections 2.1 and 2.2). Fortunately, several codes have already been extensively developed and benchmarked for radiation transport [1, 103]. This work is based on Geant4 models, which are described briefly here. The physics configuration, model geometries, and data extraction have been performed separately from this work [33].

Geant4 uses a Monte Carlo method of modeling, in which the histories of individual particles are simulated by randomly sampling the possible physical interactions in sequence [26].

This work is based on version 4.9.2 [1, 2]. Our models used the Geant Low Energy Compton Scattering (GLECS) package for gamma-ray interactions [72] and the Penelope package for electron interactions [3, 69].

4.1.1 Photon interactions

The Geant4 model includes the geometry of a volume of silicon with dimensions equal to those of the CCD. Rather than modeling specific energies of electrons with specific initial directions in the CCD, the electrons are generated through Geant4's model of photon interactions. Photons with an energy of 662 keV are generated from a variety of directions over the full 4π steradians of solid angle, with each photon incident on the center of the surface of the CCD. The direction of each photon is sampled from a user-defined angular distribution, using pseudorandom numbers.

If the modeled incident photon directions are isotropic, the photons incident from the side of the CCD have a larger path length through silicon and thus a higher probability of interaction than if the photon is incident in a direction perpendicular to the pixel plane. Specifically, in the limit that the CCD is infinitely wide, the length of silicon is equal to $d/|\sin\beta|$, where d is the CCD thickness and β is the angle of elevation from the pixel plane as defined in Chapter 2. Then the distributions

of electron energy and angle are biased. In particular, electrons from backscattered photons at 478 keV are strongly biased toward small $|\beta|$ angles, because the photons incident at small $|\beta|$ angles are much more likely to interact.

For point sources in the laboratory, this bias is balanced by the reduced solid angle of the CCD for photons incident from the side. Because the modeled photons are always incident on the center of the CCD, the solid angle is irrelevant, and the interactions of a modeled isotropic photon source are heavily biased.

In order to avoid this bias and collect a roughly even distribution of modeled electrons in both energy and angle, the sampling of the incident photon direction is weighted by $\sin\beta$. Thus, photons incident on the CCD from the edge are unlikely to be generated, but when they are generated they are very likely to interact due to the long path length in silicon, while photons perpendicular to the face of the CCD are much more likely to be generated, although they tend to pass through the 650 µm thickness of the CCD without interacting.

4.1.2 Electron interactions

When a modeled photon is found to interact in silicon in the Monte Carlo simulation, the scattered particles are produced and tracked through their interactions in the silicon. Most importantly, the Compton electron (or more rarely, photoelectron) is tracked.

Although the Geant4 toolkit as a whole implements standard theoretical and empirical models for cross sections, the user must find a compromise between speed and accuracy, setting parameters such as range cuts and step limits [1]. For electron track Compton imaging, the trajectory of the electron must be realistic in order to provide a realistic evaluation of angular sensitivity. To accurately model electrons, as benchmarked in the next section, a step limit of 0.1 µm was found necessary [32].

The electrons are simulated in 0.1 µm steps, with the position, energy deposition, and the production of any secondary particles written to file every 10 steps or 1 µm. The result of this is a table of energy depositions in three spatial dimensions, representing the interactions of one Compton-scattered (or photo-) electron.

4.1.3 Electron interaction physics benchmark

The interactions of fast electrons are rather complex, as discussed in section 2.2. It is not feasible to separate each type of interaction in Geant4 to verify the energy losses and scattering. However, the aggregate effect of interactions can easily be checked using the extrapolated range described in section 2.2.9.

The extrapolated ranges calculated from the Geant4 model used for this work are benchmarked to ranges calculated from analytical expressions developed by Tabata et al. Their first expression calculates the particle path length in the continuous slowing-down approximation (CSDA) [115]. The second expression calculates the extrapolated range from the CSDA range [116]. The root mean squared error of Tabata's final result for aluminum is 1.5% for electrons between 100 keV and 50 MeV compared to accepted Monte Carlo models, and 14% between 10 keV and 100 keV compared to experimental results (due to discrepancies in the experimental data) [116].

Figure 4.1 shows the benchmark of the customized Geant4 model to the analytical result, evaluated over 20 keV energy bins. The agreement is within 3% for all energies above 60 keV. The poorer performance at low energies is permissible, because it will be shown that the initial electron direction measurement is not sensitive at these energies. The agreement between Geant4 and the Tabata calculation suggests that the interactions of fast electrons are modeled reasonably accurately.

4.2 Device response

The table of energy deposition in three dimensions represents the physical path and interactions of the electron, but the CCD measurement of the electron path consists of a two-dimensional projection of the path, and is limited by lateral charge spreading during the charge carrier drift time, and by pixelization. These factors must also be modeled carefully to generate a modeled electron track image that is equivalent to a measured track image.

The CCD response represents the drift of charge carriers from the interaction location through the bulk of the device to the pixel plane, and the subsequent measurement of charge in each pixel. The drift time is important to define the width of diffusion and repulsion described in section 2.3.7. Charge measurement must include the variance in the number of charge carriers and the electronic noise inherent in the measurement.

4.2.1 Drift and diffusion

The energy deposited in the silicon is mainly in the forms of lattice vibrations (phonons) and excitation of electrons into the conduction energy band, with the accompanying generation of a "hole" in the valence band. Since the variance in the number of charge carriers is proportional to the expected number [74], it makes no difference whether the statistics are evaluated here, at the actual point of ionization, or in the

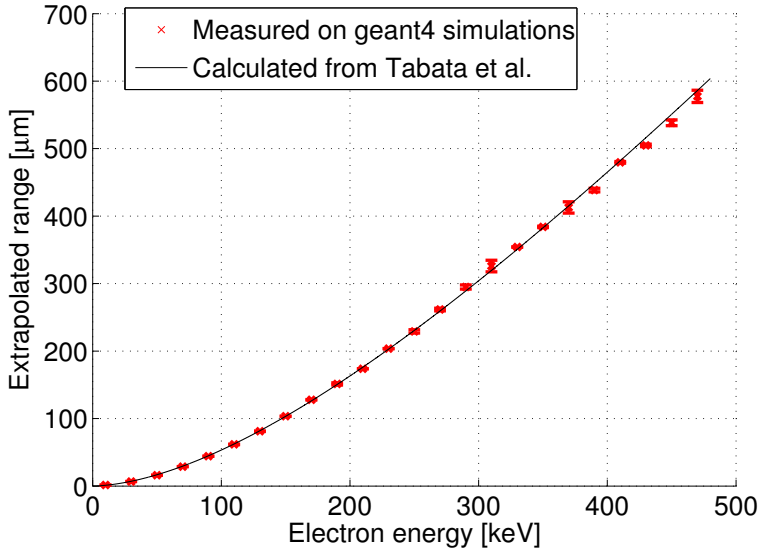

(a)

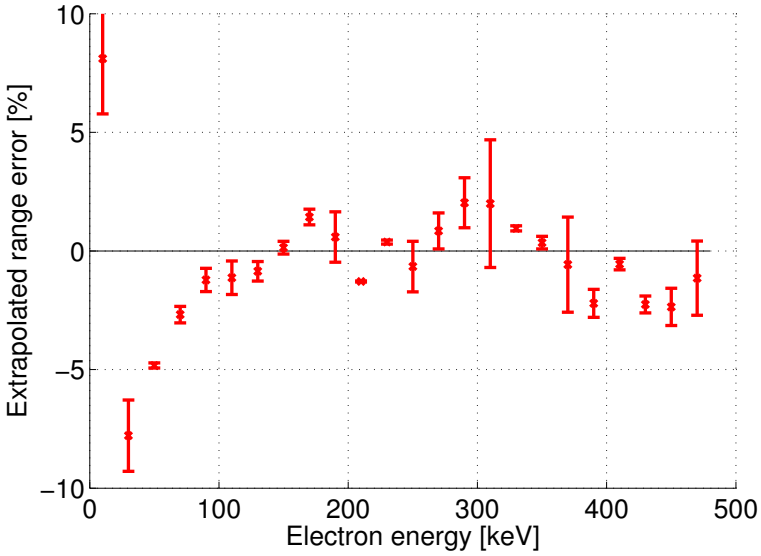

(b)

Figure 4.1:
(a) Extrapolated range of Geant4 models, benchmarked to the range calculated with Tabata et al.'s formulae [116].
(b) Error in extrapolated range relative to the Tabata formulae, as a function of energy.

pixels, at the point of measurement. It simplifies the model to evaluate statistics at the point of measurement, and so up to that point the model uses energy units, which represent the expectation value of the number of charge carriers times the average energy per charge carrier in silicon.

As described in section 2.3.8, the initial charge cloud expands through both repulsion and diffusion. However, at the time the device response model was created, repulsion was assumed to be negligible. Later calculations, showed that this assumption is not accurate. This fundamental inaccuracy will be discussed below in section 4.2.3, after this description of the transport model and its benchmark to experiment.

The exact impurity concentrations in the CCD are not well known, but according to engineers in the LBNL CCD group, the 650 µm device was fully depleted at a reverse bias voltage near 200 V [75]. The charge transport model assumes a depletion voltage of 199.5 V, and a MATLAB code uses this value to estimate the electric field [113], the field-dependent drift velocity for holes [100], and therefore the drift times for holes generated at each depth in the device (at a depth resolution of 0.5 µm). For interactions at the back plane of the CCD, the drift time in this model is calculated to be 3.4×10^{-8} s. From the drift time, the width of diffusion can be calculated by equation 2.21. This width of diffusion is used to calculate the distribution of charge at the pixel plane, as described below in section 4.2.4.

4.2.2 Charge transport benchmark

The lateral spreading of charge carriers from diffusion and repulsion can be experimentally measured. In general the depth of the particle track is not known, but if a track passes out of the back side of the CCD, then the end of the track must be at the full depth of 650 µm. Electrons which travel out of the back side of the device could be used, but it is not always evident whether the track has escaped through the backplane, or simply ended at some depth in the detector.

A useful alternative are muons produced in the cascade of cosmic rays in the atmosphere, which are ubiquitous in the above-ground environment [14]. Muons follow linear trajectories and penetrate large thicknesses of materials. A muon incident on the CCD is very likely to enter from one face of it (the pixel plane or the back plane) and exit the other face, because the device is thin compared to its other dimensions. It follows that the measured track from a muon will have the minimum lateral spreading on one end (where it passes through the pixel plane) and the maximum lateral spreading on the other (at the back plane). Figure 4.2 shows an example of a muon track. The maximum diffusion width can be compared with what is calculated from the model.

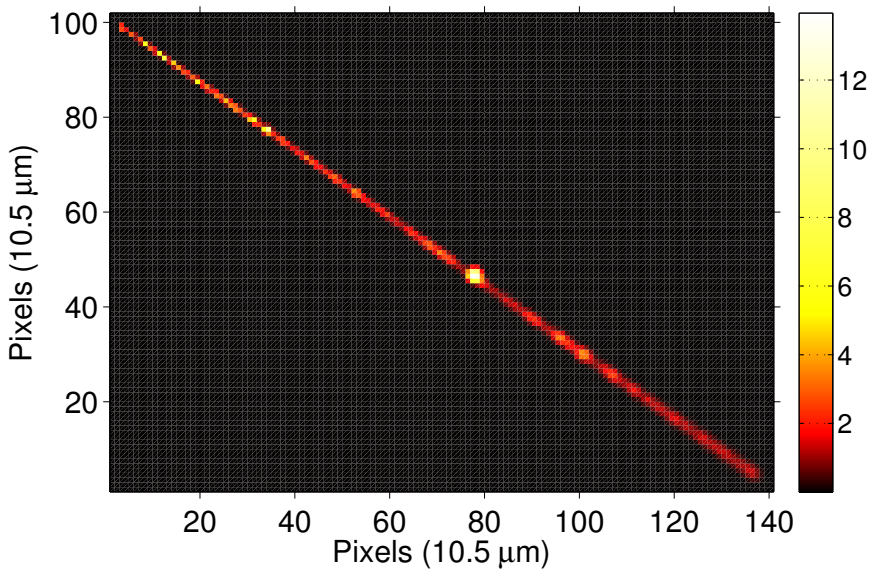

Figure 4.2: An experimentally measured CCD image of a muon track, passing through the pixel plane at top left and the back plane at bottom right.

The challenges of this method include recoil electrons generated along the muon track, as well as noise and pixelization which make width measurements imprecise. However, over 78 muon tracks, a narrow distribution of track widths was measured.

Figure 4.3 shows the distribution of measured muon widths at the back plane, with a vertical dashed line indicating the value calculated with the non-repulsive model described above in section 4.2.1. The mean width is 12.9 µm, with a standard deviation of 1.0 µm. The width calculated by the model at the back plane is 14.76 µm, which is about 13%, or two standard deviations, above the mean.

Although the model does not include repulsion, a true drift time can be estimated from the muon tracks, taking into account both the diffusion and repulsion. The repulsion is calculated using equation 2.20, which assumes that the track consists of an infinitely long cylinder of infinitesimal diameter. The linear charge density is taken to be the average from the muon tracks, corresponding to about 0.37 keV µm^{-1} of energy deposition. If both diffusion and repulsion produced Gaussian distributions of charge, and the two forms of spreading were independent, the parameter σ for the total width would be equal to the quadrature sum of the parameters $\sigma_{\text{diffusion}}$ and $\sigma_{\text{repulsion}}$. In truth, repulsion is not independent from diffusion, because the diffusion

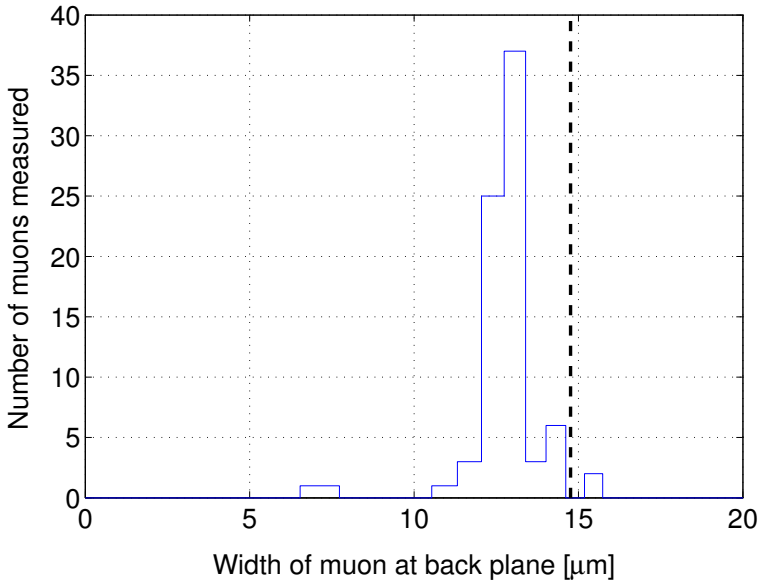

Figure 4.3: Distribution of measured muon widths. The bin widths vary, being larger toward the left.

reduces the charge density and thus reduces the force of repulsion. However, for calculations in this chapter the effect of diffusion on repulsion will be ignored, causing some overestimation of repulsion. In addition, repulsion does not produce a Gaussian distribution of charge, but a uniform distribution within the volume of a cylinder[1]. In order to more easily combine the repulsive distribution with the Gaussian diffusive distribution, a σ-like parameter is defined, $\tilde{\sigma}_R = 0.68 r_R$, where r_R is the radius of the cylinder of charge from repulsion alone. If the total width at the back plane, σ_{tot}, is then approximated as the quadrature sum of $\sigma_{\text{diffusion}}$ and $\tilde{\sigma}_R$, the drift time can be estimated from the average measured muon width:

$$t = \frac{\sigma_{\text{tot}}^2}{2D + 0.68\frac{\mu_0 \lambda}{\pi\epsilon}} \tag{4.1}$$

$$= 1.1 \times 10^{-8}\,\text{s}. \tag{4.2}$$

[1]The uniformity of charge within a cylindrical volume is based on the assumption that the mobility is constant, such that the velocity is directly proportional to the electric field. Within a cylinder of uniform charge, the electric field is proportional to radius, so under the constant-mobility assumption the charge will remain uniform within an expanding cylindrical volume.

The mobility actually saturates at high electric fields, but this saturation corresponds to very small radii and can be neglected for the drift times in the CCD and the approximate nature of this calculation.

Since this calculation includes repulsion, this estimated drift time is less than the drift time in the non-repulsive model which produces lateral spreading through diffusion alone. This drift time will be used for further estimates of the importance of repulsion, in the next section.

The non-repulsive model of charge drift and diffusion overestimates the lateral spreading from muons at the back plane, despite neglecting the contribution of repulsion. This overestimation implies that the assumed depletion voltage used to calculate electric field and drift times is too high, and thus the electric field is stronger and the drift times shorter than was assumed. The difference in lateral spreading between muons and the model is small, compared to the variation of lateral spreading from the pixel plane to the back plane.

4.2.3 Justifying the use of the non-repulsive model

The benchmark of charge transport indicates that the overall spreading of charge from muons at the back plane is modeled reasonably well by the non-repulsive model. The specific energy loss by muons is in the same range as the specific energy loss of 100 keV to 500 keV electrons, so the repulsion in muon tracks is similar to the repulsion in the electron tracks in this range. Both diffusion and repulsion are proportional to the square root of the drift time, so the overall dependence on the position in the detector is identical. However, unlike diffusion, repulsion varies with the charge density, and generates a distribution of charge with a different shape.

The shapes of the charge distributions for repulsion and diffusion are shown in Figure 4.4. The charge distributions represent the drift of an infinite line of charge from the CCD back plane onto the pixel plane, with the charge density of the line corresponding to the most probable specific energy loss of a 300 keV electron in silicon. Equation 4.2 is used as the estimated drift time for repulsion and diffusion. The horizontal axis represents the distance perpendicular to the projection of the line onto the pixel plane. Repulsion alone produces a cylinder of uniform charge density, while diffusion alone produces a Gaussian distribution. The teal line is the convolution of the diffusion and repulsion distributions, which is a close approximation of the actual charge distribution from the combination of diffusion and repulsion (again, neglecting the dependence of repulsion on diffusion). The black line is a Gaussian distribution with width σ equal to the quadrature sum of $\sigma_{\text{diffusion}}$ and $\tilde{\sigma}_R$.

The distribution given by the convolution is similar to the Gaussian approximation. The reconstruction algorithm discussed in Chapter 5 measures the initial electron direction by attempting to track the projected path of the electron, corresponding to a lateral distance of 0 µm in Figure 4.4, and the charge spread to either side of the track (lateral distance > 0 µm) is only used to help follow the center of the track.

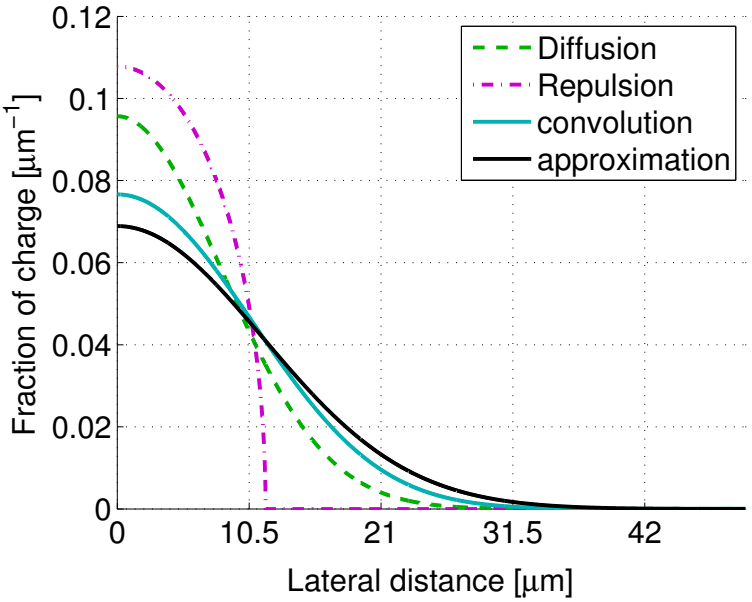

Figure 4.4: Comparison of the shapes of charge distribution from diffusion, repulsion, and their combination. "Convolution" shows the convolution of the diffusion and repulsion shapes, representing a more accurate evaluation of the combined shape. "Approximation" shows a Gaussian distribution with width equal to the quadrature sum of the diffusion width and 68% of the repulsion radius, as described in the text.

Therefore, the minor difference in shape can be expected to have little effect on the performance of the algorithm.

The second potential danger in ignoring repulsion is that repulsion depends on the charge density while diffusion does not. Therefore, although the model reconstructed the muon widths relatively well, tracks with charge density greater or less than that of muons may not be modeled as accurately.

Total widths of lateral charge spreading can be calculated easily using equations 2.20, 2.21, and the quadrature-sum approximation described above. For charge densities corresponding to the most probable energy deposition from 100 keV, 150 keV, and 450 keV electrons, and drift from the back plane to the pixel plane, the total widths are

$$\sigma_{\text{tot}}(100\,\text{keV}) \approx 15.7\,\mu\text{m}$$
$$\sigma_{\text{tot}}(150\,\text{keV}) \approx 14.3\,\mu\text{m}$$
$$\sigma_{\text{tot}}(450\,\text{keV}) \approx 12.4\,\mu\text{m}.$$

The width increases further at electron energies below 100 keV. However, the initial

segment of an electron track, when the electron has its full kinetic energy, is the relevant portion for defining the angular sensitivity of the algorithm. It will be apparent in Chapter 6 that the algorithm has very little angular sensitivity for tracks below 100 keV, so the increased width from repulsion in that energy range is unimportant to the angular sensitivity results. The width will decrease slightly at track energies above 450 keV, although the specific energy loss only decreases gradually between 450 keV and 1 MeV (Figure 2.5), and the maximum track energy considered in this work is about 480 keV. The track energy at which the non-repulsive model exactly matches the estimate is between 100 keV and 150 keV.

As mentioned above, the total width of diffusion from the back plane in the non-repulsive model is 14.76 µm. The difference between the more accurate estimation of diffusion and repulsion, and the non-repulsive model, is slight. The greatest discrepancy is for 450 keV electrons, for which the FWHM of spreading from diffusion and repulsion is about 29 µm, while the FWHM in the non-repulsive model is 35 µm. However, even for this case, the difference is only about half a pixel.

Although the non-repulsive model lacks some details that arise from repulsion, the differences are small. The overall accuracy of the models are further validated by the good agreement between modeled and measured angular sensitivity in section 6.4.

Because the modeled width is larger than the width calculated using repulsion for tracks above 150 keV, the effective position resolution in the non-repulsive model is coarser than the repulsive estimate, and any adjustments for repulsion would improve the angular sensitivity of the reconstruction algorithm. At 10.5 µm pixel pitch this effect should be very small, since the difference in widths is significantly less than one pixel pitch. However, for models of CCDs with smaller pixel pitch, the difference may be significant. Therefore, while the overall trends in the results in section 6.2.2 for small pixel pitch will not change, the values of the FWHM for small pixel pitch should represent an upper limit for tracks of energy greater than 150 keV.

4.2.4 Pixel energy measurement

The non-repulsive model of charge transport produces track widths close to those measured in muons, and the differences from a repulsive model are slight. With the lateral spreading of the drift model validated, the remaining steps in the overall model of the device response will be described next.

Previously, the two-dimensional Gaussian distributions corresponding to the lateral spreading of charge from various depths of energy deposition in the CCD were described. The two-dimensional distributions are evaluated at a resolution of 0.5 µm $\times$0.5 µm, much finer than the actual device pixels of 10.5 µm, and stored in a table for quick look-up operations in the modeling code.

In order to generate the total energy (charge) distribution for a Geant4 electron track, the three-dimensional position of every recorded point of energy deposition is rounded to the nearest 0.5 µm. The model code initializes an empty matrix, representing an image large enough to contain the electron track with a two-dimensional resolution of 0.5 µm. This image at 0.5 µm resolution is called the *fine grid*. For each point of energy deposition, the two-dimensional distribution for the corresponding depth is found from a table, the values are multiplied by the energy deposited at that point, and then the scaled distribution is added into the initialized image.

After adding in the contribution of every point of energy deposition in the track, the fine grid contains an image of the energy (charge) distribution at the pixel plane, but at a finer resolution than the pixels. The actual pixelized image, at the resolution of the modeled pixel pitch, is generated by summing together the fine grid over the area of each modeled pixel. This *coarse grid* image contains values of energy, which, again, represent the expectation value of the number of charge carriers times the average energy per charge carrier in silicon.

The actual number of charge carriers in each pixel will differ from the average based on the statistics of charge carrier generation. The variance in the number of charge carriers differs from pure Poisson statistics by the Fano factor [44, 74]. In addition to statistical fluctuations, the charge measured in each pixel varies by the electronic noise in the readout electronics, which is Gaussian (see Chapter 5). The modeling code adds a noise component to the value in the coarse grid to get the final modeled image, with the noise component sampled from a Gaussian, with width corresponding to the electronic noise and statistical noise added in quadrature:

$$\sigma^2_{\text{total}} = \sigma^2_{\text{electronic}} + \sigma^2_{\text{statistical}} \tag{4.3}$$

An example Geant4 track is shown in Figure 4.5. The first two views show the 3D path of the electron, as computed by Geant4. The last view shows the device response, including electronic noise.

This final image undergoes the same segmentation process as experimental tracks, described in Chapter 5.

4.3 Tracks from the coincidence experiment

The coincidence experiment described in Chapter 3 measured electron tracks with a known initial trajectory. This provided a measurement of the angular sensitivity of the track reconstruction algorithm to the initial electron direction. The angular sensitivity from the measured tracks can be compared to the angular sensitivity calculated from models, to confirm that the modeled sensitivity is consistent with the measured

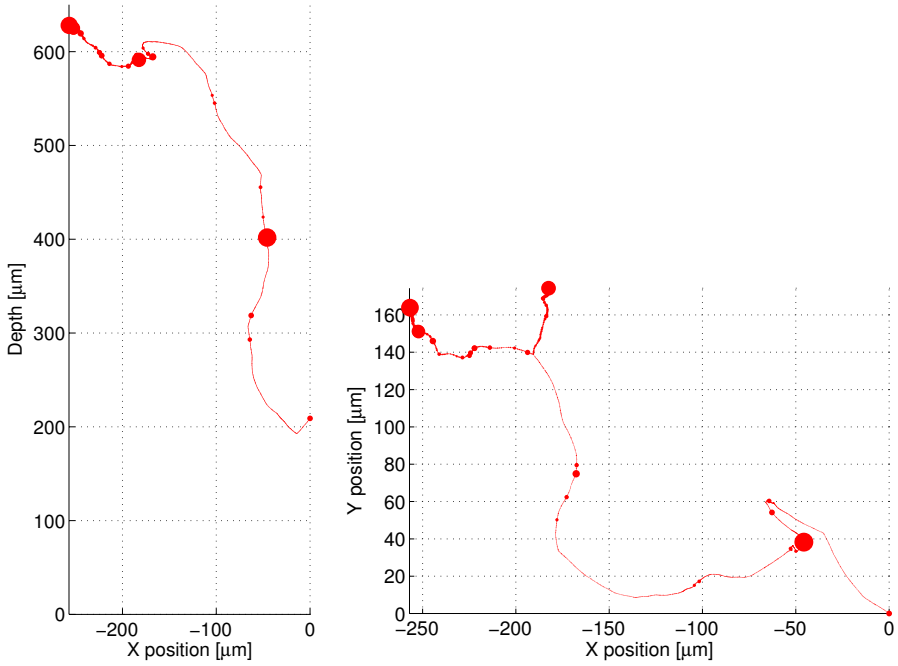

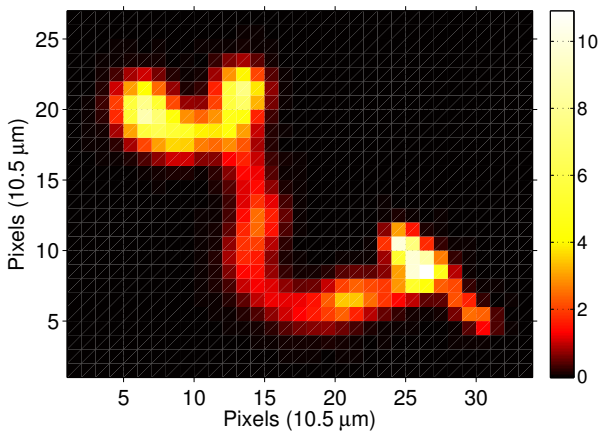

Figure 4.5:
(a) Side view of a 420 keV modeled track with pixel plane at the bottom. Larger points indicate higher energy deposition; the electron starts at the right side.
(b) Projection of the modeled track onto the pixel plane.
(c) Device response to the modeled track.

sensitivity. However, the measured tracks should be compared to model tracks that are similar in characteristics, since the angular sensitivity depends strongly on track energy and angle from the pixel plane ($|\beta|$), as shown in Chapter 6.

Tracks with appropriate characteristics could be generated by modeling the detector positions and photon kinematics of the experiment in Geant4. However, such an extensive model is beyond the scope of this work. Instead, knowing that track energy and $|\beta|$ are the most important characteristics affecting the angular sensitivity, modeled tracks can be chosen with values of energy and $|\beta|$ very close to the values for the measured tracks.

As will be discussed in Chapter 6, a limited number of tracks from true coincident event sequences were measured. Many more tracks were available from the model described above in sections 4.1 and 4.2. A more accurate average modeled response was produced by using more than one modeled track for each measured track.

Specifically, each measured track was represented in the model by 69 modeled tracks with energy within 2.5 keV and $|\beta|$ within 2° of the measured track. The factor of 69 is limited by the number of modeled tracks available with energy and $|\beta|$ in the correct range. For N measured true coincident event sequences, a total of $69 \times N$ modeled events were chosen. The measured and modeled distributions of the reconstruction algorithm's angular response can be compared by reducing the counts in the modeled distribution by the factor of 69.

The comparison of the angular sensitivity measured and modeled tracks provides a direct benchmark of the modeled angular sensitivities, which are the result of the combination of Geant4 and MATLAB models.

4.4 Summary

Geant4 is used to model the photon and fast electron interactions, with the electron interactions benchmarked by extrapolated range. MATLAB code is used to model charge transport in the CCD and the pixel image response. The lateral spreading of charge is modeled as diffusion without repulsion, but it is apparent that the difference in the shape of the distribution is small, and the difference in width of the distribution is also small. The lateral width of spreading of charge carriers drifting from the backplane calculated from the diffusion-only model is only 13% different than the average spreading measured from the tracks of muons, which pass through the detector. The energy in each pixel is modeled by summing the charge from lateral spreading over the pixel area, and then sampling a Gaussian distribution of readout noise and charge carrier statistics.

The coincidence experiment from Chapter 3 measured a limited number of tracks

with known initial directions. The angular sensitivity of the reconstruction algorithm to these tracks is compared to the angular sensitivity of model tracks, which are chosen to have the same distribution of track energy and $|\beta|$, but with 69 times as many tracks. In this way, the combined characteristics of the modeled tracks that affect the angular sensitivity are benchmarked to experiment.

In the next chapter, the methods of data analysis will be described, including the reconstruction algorithm which calculates the initial electron direction from an electron track image from either measurements or models.

Chapter 5

Data Analysis

The goal of this work is to measure the initial direction of electrons in the CCD. A critical part of this goal are the algorithms for CCD image calibration, segmentation, and track reconstruction. For measured electron tracks, the initial direction as well as accurate energy measurement require careful calibration of the CCD images, since the black level (image offset) varies in each quadrant and even within the quadrant. For both measured and modeled tracks, the reconstruction of the initial electron direction from the track image requires a complex algorithm. This reconstruction algorithm measures the angle in the pixel plane (α) and the magnitude of the angle out of the pixel plane (β). The angular sensitivity of these measurements will be presented in Chapter 6.

In addition, the coincidence experiment includes a germanium double-sided strip detector, which requires its own event reconstruction methods to provide interaction positions, deposited energies, and interaction times. The combination of CCD data and germanium data from the coincidence experiment must be carefully analyzed to extract the signal of true coincident event sequences from the large background of false coincident event sequences. The last section of this chapter will discuss this analysis of the coincidence experiment data.

5.1 Energy measurement in the charge-coupled device

The initial output of the CCD is a two-dimensional array of integer values corresponding to the charge found in the pixels of the device. The integer values are the result of the digitizer's charge measurement and are known as *ADC values*. In

addition to measuring the charge held in each potential well, the ADC values have an offset which is determined by the channel of the video card. This offset simplifies the data format by keeping all measurements positive, even in the case of a negative noise contribution. Within a small area of the image, the pixel values are distributed normally about the black level value, with the width resulting from electronic noise. However, over an entire quadrant, there is a gradient in the black level in the parallel direction ("parallel" is defined in section 2.3.9).

Because the measured signals are proportional to the energy deposited, a linear energy calibration is sufficient. The calibration requires a gain and an offset.

5.1.1 Offset calibration

One simple calculation of the offset is to average the pixel values in a quadrant. However, this method does not account for the gradient in the black level, and any anomalies due to leakage current or electric field irregularities will still be apparent after the calibration.

These issues may be overcome by the median pixel value method. Over a set of about 100 consecutive images, a black level is calculated independently for each pixel, by measuring the median value of that pixel out of the 100 images. Radiation interactions will increase the mean and slightly increase the median, but as long as radiation interactions are relatively sparse in the image (true for all measurements in this work) the effect on the median of 100 values will be negligible. The median value of each pixel is subtracted from the actual pixel values in each image to generate a CCD image with an offset of zero. In addition, the median value of each quadrant of each image is subtracted from that image, to compensate for any black level changes from one image to the next as described in Section 3.2.2.

The median pixel value method results in an improved energy resolution over other methods of subtracting the black level in the device. Figure 5.1 compares the distribution of pixel values between the median method and a simple average subtraction. The quadrant average method produces a distribution which includes two anomalies: the small peak at the far left is due to one column of pixels with a lower black level, and the larger tail between 200 and 2000 ADC units is due to some pixels with higher black level. The median pixel value method compensates for both of these features, and the main black level peak at 0 ADC units is narrower as well. The median pixel value method has a sharper peak than a true Gaussian distribution, due to statistical effects of subtracting median values. After gain calibration (described below), the main peak widths are 65 eV and 29 eV (FWHM) for the quadrant average method and pixel median value method, respectively.

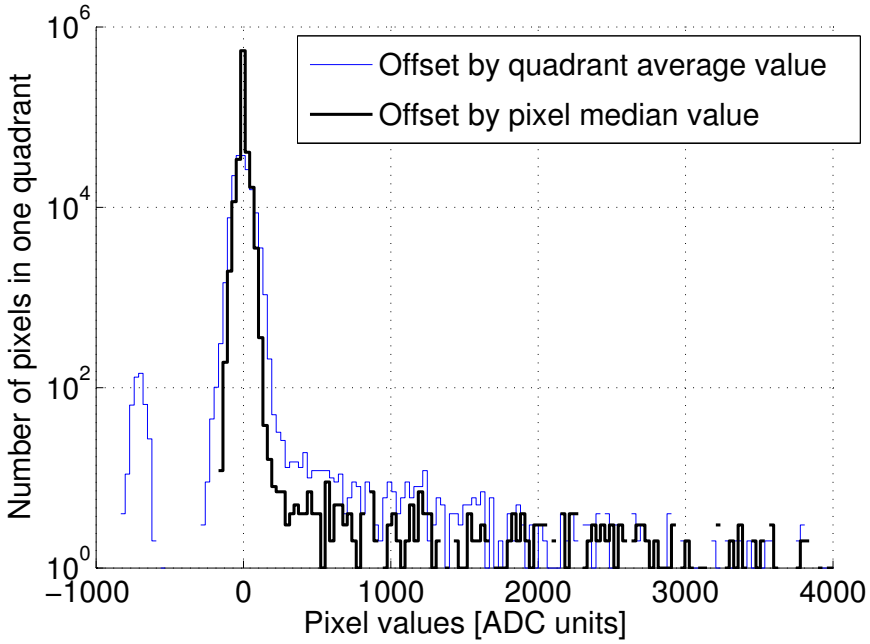

Figure 5.1: Histograms of pixel values over one quadrant of one image, as a means of comparing offset calibration methods. See text for explanation.

5.1.2 Single-pixel-based gain calibration

Low-energy x-rays from a source on the front side of the CCD will interact close to the pixel plane, minimizing drift time and diffusion width so that many interactions deposit charge in a single pixel. The gain in each quadrant may be calibrated by dividing the pixel values into bins according to the ADC value, and fitting a Gaussian function to the peak of this histogram. The x-ray peaks will be visible at higher pixel values than the electronic noise distribution, centered on the black level, and a continuum of x-ray events shared among multiple pixels (Figure 5.2).

The gain on each quadrant of the CCD seems to be stable over long periods of time. After measuring the gain in each quadrant using x-ray data, the gain values can be applied to future images to produce images with units of keV in each pixel. These will be referred to as calibrated images.

5.1.3 Multi-pixel track segmentation

Photons interacting deep within the 650-μm thickness of the CCD will spend enough time drifting toward the pixel plane that the charge carriers will spread laterally across

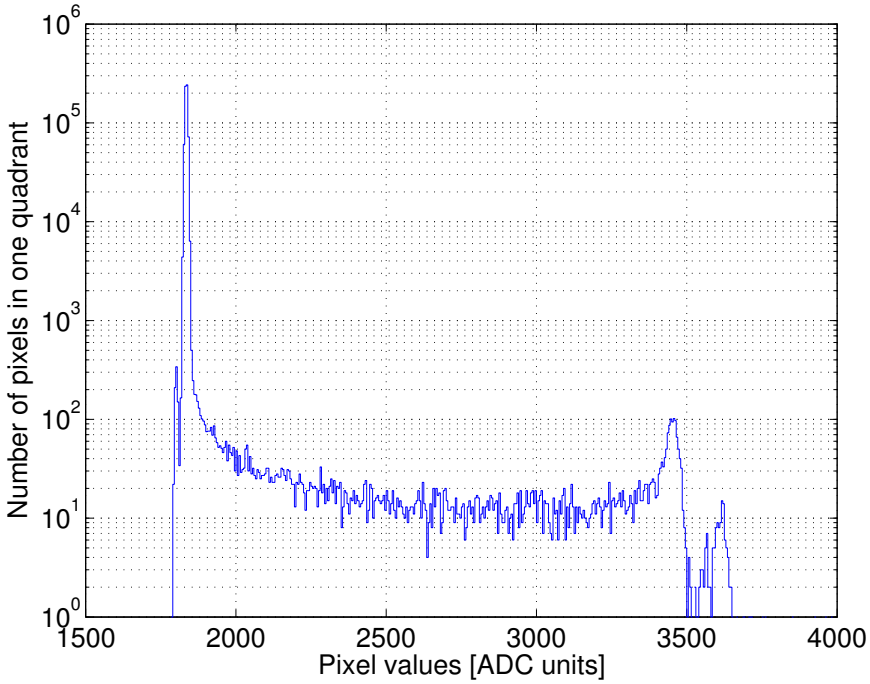

Figure 5.2: Histogram of pixel values from exposure to a ^{55}Fe x-ray source. The tall peak on the left is the black level; the two peaks on the right are the 5.9 keV and 6.5 keV peaks. The image has already been compensated for black level offset.

multiple pixels. In addition, electrons above about 50 keV are likely to traverse multiple pixel lengths before stopping, which fundamentally enables the possibility of a direction measurement. Multi-pixel events are therefore essential for both energy and direction measurements.

After the image is calibrated, tracks can be identified and segmented out of the full CCD image. The segmentation algorithm applies a threshold of 0.1 keV (3–5σ of the noise) and identifies groups of contiguous pixels above the threshold. Each group of contiguous pixels above the threshold is assumed to represent one radiation interaction. Groups of less than four pixels are ignored; this pixel threshold filters out noise and any irregular pixels.

The energy deposited in the interaction can be measured by simply summing the pixel values that are above the threshold. However, a more precise method includes pixels with values below the threshold but are neighboring the over-threshold pixels. Pixels both orthogonal and diagonal to the pixels above threshold are considered neighbor pixels. Although neighbor pixels are near the noise level, the cumulative charge diffused into these pixels from one track is significant. Figure 5.3 provides a

visual example of the energy in the neighboring pixels, with a CCD track from an ^{241}Am source of gamma rays with 59.54 keV of energy. The combined energy of the pixels above threshold (outlined in solid blue) is 59.22 keV, while the neighbor pixels (outlined in dashed blue) contain 0.33 keV to give a final energy measurement of 59.55 keV. This discrepancy is typical for 60 keV tracks, but varies significantly based on the width of diffusion. The energy spectra in Figure 5.4 also demonstrate the importance of the neighboring pixels. In the spectrum excluding neighbor pixels, the ^{241}Am full-energy peak is shifted, and its resolution degraded, due to the loss of the charge in the neighbor pixels.

The neighboring pixels are also important for measuring the initial electron trajectory, as pixel values near the noise floor contribute to the edges of the diffused track, and therefore affect the ridge-following method described in Section 5.2.7.

5.1.4 Multi-pixel-based gain calibration

In the absence of a low-energy x-ray source inside the cryostat for single-pixel gain calibration, the gain may be calibrated to the photopeak of a gamma source such as ^{241}Am. The photoelectric cross section in silicon limits the convenience of this method to low-energy photopeaks, below perhaps 200 keV. In this method, the tracks must be segmented while the pixel values are still in ADC units. The segmentation is performed as described above, except that the threshold is set at 5σ instead of 0.1 keV. (The energy value of 5σ varies with the image noise, but is about 0.09 keV on average.) The energies of segmented tracks are represented by a sum of pixel values. After finding the photopeak and calculating the gain of each quadrant, future images may be calibrated for both offset and gain before undergoing segmentation.

5.1.5 Multi-pixel energy resolution

The summed cluster energies can be divided into bins in an energy histogram to show an energy spectrum of multi-pixel tracks. This has resulted in an energy resolution of 532 eV FWHM for 59.541 keV tracks.

The energy resolution at higher energies is more difficult to measure experimentally, as the cross section for photoelectric absorption decreases rapidly. However, as an example of what might be expected, the energy resolution has been measured for photopeaks of ^{133}Ba and, over the course of the coincidence experiment, ^{137}Cs. The ^{133}Ba spectrum is shown in Figure 5.5, and photopeak widths are given in Table 5.1.

The peak widths for both ^{133}Ba and ^{137}Cs are larger than expected based on the FWHM of the ^{241}Am peak. The ^{133}Ba spectrum was acquired early in the operation of the CCD with higher readout noise. The ^{137}Cs photopeak was measured over the

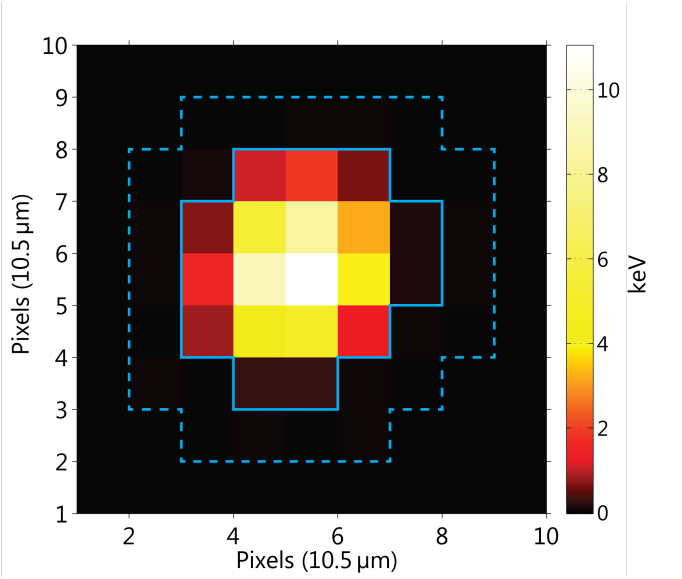

(a)

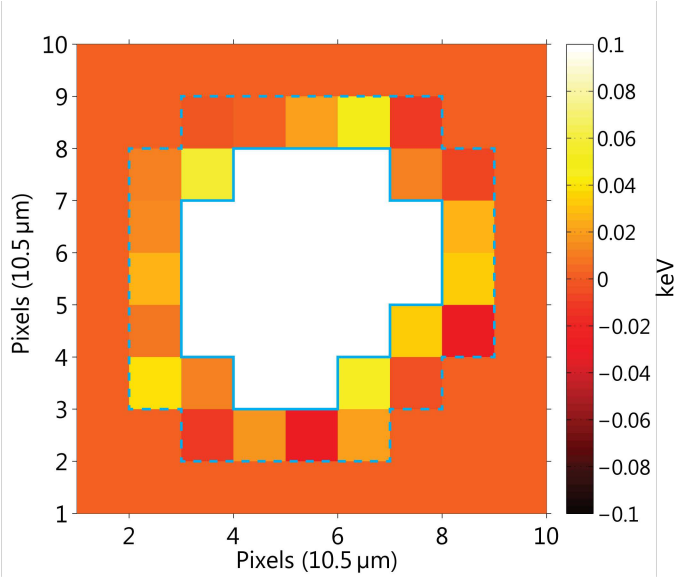

(b)

Figure 5.3: A typical CCD image from the full-energy absorption of 59.54 keV gamma rays from ^{241}Am, shown in two color scales. The pixels above threshold are outlined in a solid line.

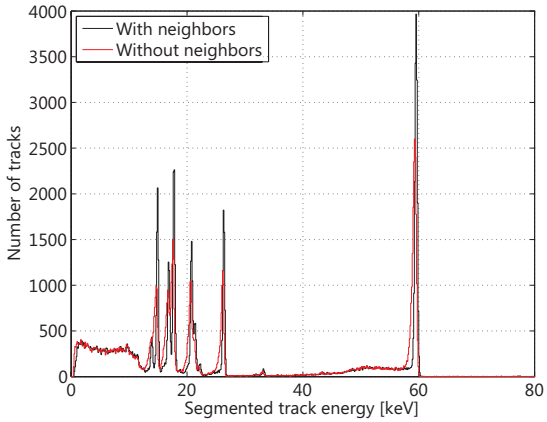

(a)

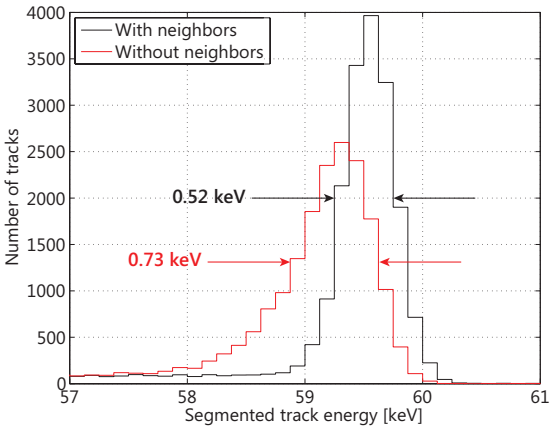

(b)

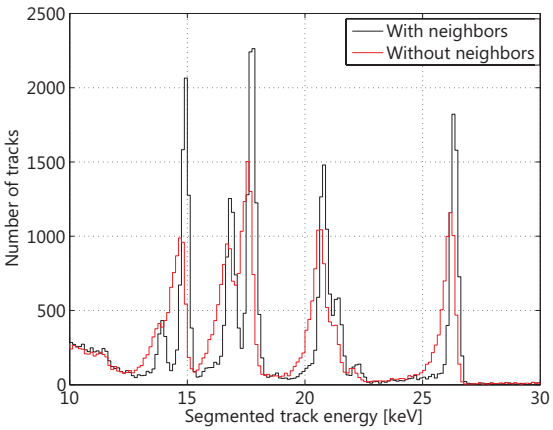

(c)

Figure 5.4: Energy spectra from an ^{241}Am source showing the effect of including neighbor pixels in the segmentation.

(a) The full spectra.

(b) View of the full-energy peak.

(c) View of the x-ray peaks.

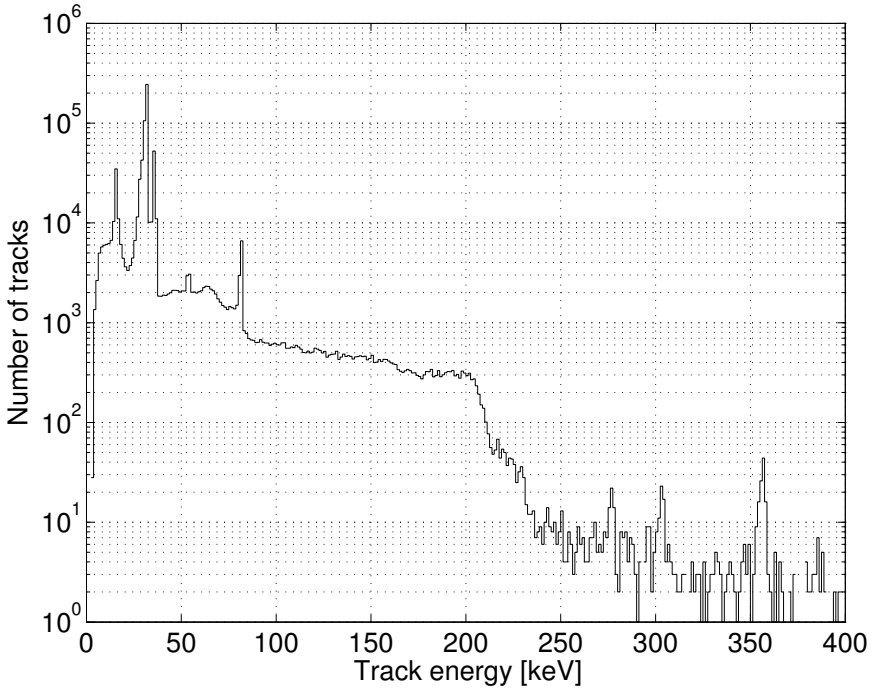

Figure 5.5: Measured energy spectrum of tracks from a ^{133}Ba source, with peaks at 53, 80, 81, 276, 303, 356, and 384 keV.

course of 104 days and may have been affected by variations in the readout electronics during that time. However, the FWHM is not expected to follow a square-root correlation with energy, because the electronic component of the noise depends on the number of pixels in the track. Therefore, higher-energy peaks will tend to be broader due to the increased contribution of readout noise from the larger track.

5.1.6 Adjustments for pixel pitch

To study the performance of a modeled detector of a different pixel pitch or noise level, several considerations are essential to a useful track segmentation.

First, the number of pixels in each track will scale with approximately the inverse of pixel area. The pixel threshold for segmentation must reflect this, as events in a large-pixel device may often only cover a single pixel. The scaling of number of pixels is evident in the position axes of the different pixel pitch images in Figure 5.6.

Also, each pixel represents an independent source of electronic noise, so for the same noise per pixel, an image at a smaller pixel pitch will have more total noise. At the same time, the amount of charge collected in each pixel will tend to scale

Peak energy [keV]	FWHM [keV]
53.2	0.79 ± 0.07
302.9	2.7 ± 0.4
356.0	3.11 ± 0.19
383.9	3.5 ± 0.7
661.7	22 ± 2

Table 5.1: Energy resolution of the CCD for photopeaks of ^{133}Ba and ^{137}Cs. The 80 and 81 keV lines of ^{133}Ba are not resolved and therefore not used for measuring resolution.

proportionally with the pixel area, for tracks of more than one pixel in length and width. Therefore, for the same value of noise per pixel, tracks at smaller pixel pitch will be difficult to segment, because the signal-to-noise ratio in each pixel is reduced by the square of the ratio of pixel pitch. Figure 5.7 illustrates this effect through tracks at three pixel pitches with the same level of noise per pixel.

In addition, the effect of including neighboring pixels in the track for energy measurement will vary greatly. At 10.5 µm, the pixel pitch is approximately equal to the average σ of the diffusion width. Thus, including an extra pixel width around the edges of the track will tend to include a small but significant fraction of the energy. However, at smaller pixel size the diffused charge may be spread over several pixel lengths away from the pixels above threshold, suggesting that multiple "layers" of neighboring pixels should be included. At larger pixel size, the neighboring pixels may not contain a significant amount of charge compared to the additional electronic noise they represent.

To address these issues, the following scaling of segmentation parameters were used in the pixel pitch and noise studies. Firstly, the pixel threshold is set to the number of pixels representing the same area as four $(10.5\,\mu\text{m})^2$ pixels. Secondly, the segmentation threshold is reduced to 3σ to accommodate the challenges at small pixel pitch. At larger pixel pitches, there is little difference between the result of a 3σ threshold and a 5σ threshold. For simplicity, the 3σ threshold is used for modeled tracks at all pixel pitches.

A scaling of the number of neighboring pixel "layers" outside of the pixels above threshold would be ideal. However this has not been implemented in this work.

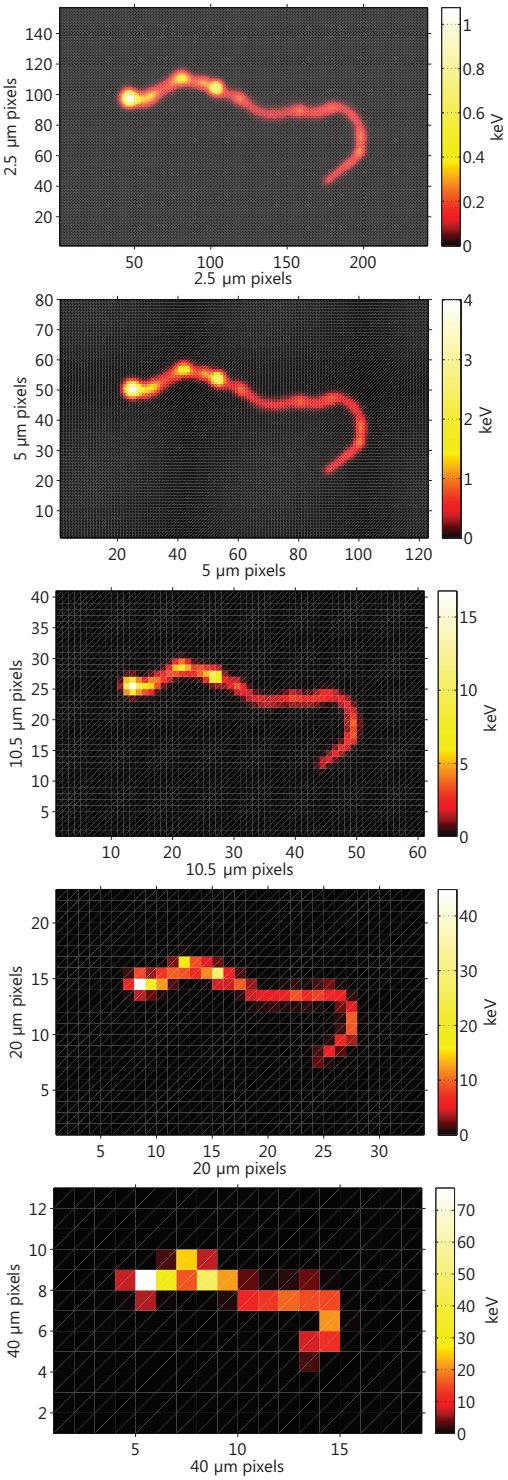

Figure 5.6: Modeled CCD responses to the same 368 keV electron. Five different pixel pitches are modeled: 2.5 µm, 5 µm, 10.5 µm, 20 µm and 40 µm.

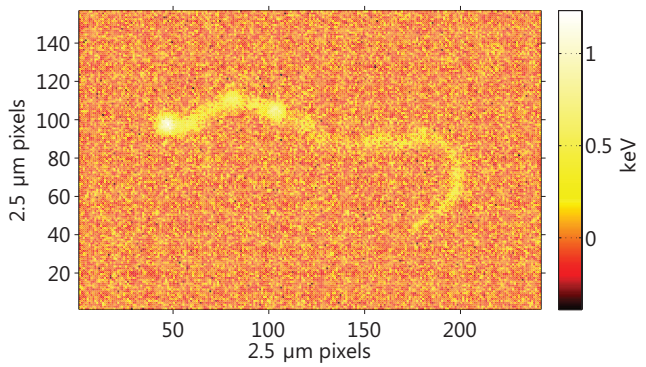

(a)

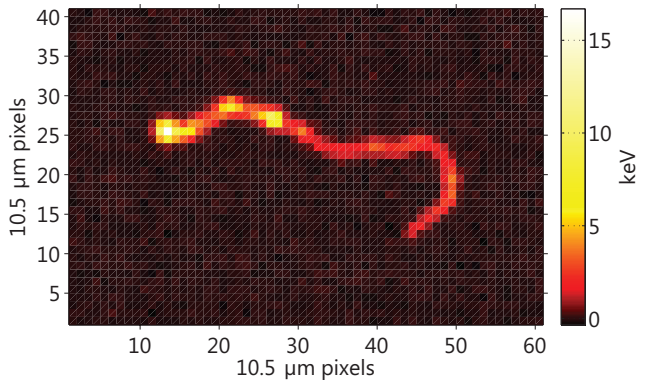

(b)

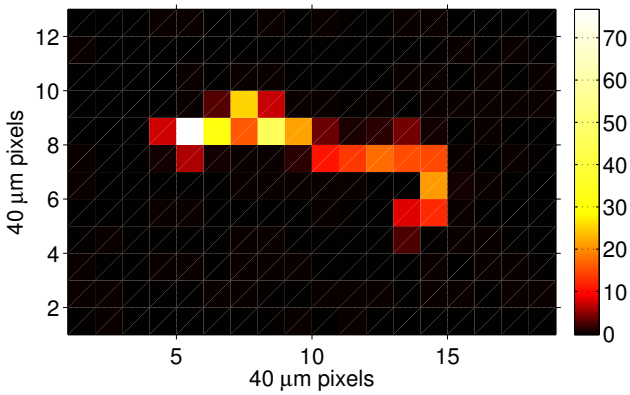

(c)

Figure 5.7: The effect of 100 eV/pixel electronic read noise on the same modeled track as in Figure 5.6, for pixel pitch of (a) 2.5 µm, (b) 10.5 µm, and (c) 40 µm. Color scales are in keV.

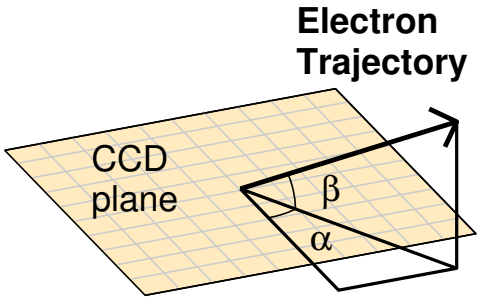

Figure 5.8: The two angles which define the 3D electron direction.

5.2 Trajectory reconstruction algorithm

The advantage of electron track Compton imaging lies in the ability to measure an initial electron trajectory with a detection system, and the precision with which the initial direction can be measured defines the background reduction in the gamma-ray image. Thus the method of measuring the trajectory is crucial. With this CCD, the trajectory is measured by an algorithm that was developed and implemented in MATLAB in this work, and discussed in detail in the following.

As a brief overview, the algorithm must first determine along where on the track image the trajectory is to be measured, and then analyze that segment for the three-dimensional electron direction. The electron direction is defined by α and β as described in section 2.3.8, and shown again here in Figure 5.8.

The trajectory reconstruction algorithm presented here is not an ideal or optimized method; a diffused electron track image is quite complex to analyze. However, the algorithm was tested on benchmarked simulated data (Chapter 4), and developed through several iterations of observing the modes of failure or poor performance. The algorithm can be described by seven steps.

The algorithm is illustrated by example electron tracks with diagrams of how the algorithm performs on these examples. Unless otherwise specified, the examples are measured tracks from the BeARING laboratory. These tracks have been hand-picked as examples on which the algorithm performs effectively, to illustrate the reasoning behind the algorithm. In contrast, section 5.2.11 describes various ways by which the algorithm can perform poorly.

5.2.1 Identify the initial segment

The first four steps of the algorithm are focused on determining which segment of the track most likely corresponds to the beginning of the trajectory. This segment is all that the direction measurement needs for measuring the initial direction. The remainder of the track is only needed for measuring the interaction energy.

5.2.2 Step 1: Apply pixel threshold

In order for a computer algorithm to most easily process the shape of the electron track, the shape is first represented by a binary image. A low threshold of 0.5 keV is applied to the original track image, and pixels with values above the threshold are given a binary image value 1 and the rest 0. The threshold value should be low enough to preserve all of the segments of the track, while high enough to remove some of the charge diffusion from the track shape and ignore excess noise. Two examples are shown in Figure 5.9, including examples of a threshold too low (0.05 keV) or too high (1.5 keV).

5.2.3 Step 2: Apply thinning method

The computer analysis is also simplified by reducing the binary image to a skeleton of a single-pixel-wide line of "1" values (Figure 5.10a). This transformation is accomplished by an algorithm built in to the MATLAB Image Processing Toolbox, which is an implementation of an iterative parallel thinning algorithm with two sub-iterations [52, algorithm A1].[1]

5.2.4 Step 3: Identify ends

The term *ends* will be used to refer to the position extremities of the projected track image, which could include the *initial end* where the electron began its trajectory or the *final end* where it finished its trajectory. To avoid confusion, the word "end" will not be used in the specific sense of the finishing point of the trajectory.

On a skeletal image such as that resulting from the previous step, the ends of the track are indicated by pixels with only a single neighboring "1" pixel (Figure 5.10b). In principle, every track might be expected to have two such ends, corresponding to the initial and final positions of the electron's path. However, in practice there can be fewer or more. If part of the track forms a loop, one or zero ends might be identified (Figure 5.10d). On the other hand, the thinning algorithm may reduce sharp elbows

[1] The algorithm is invoked by the function `bwmorph(img, 'thin')`.

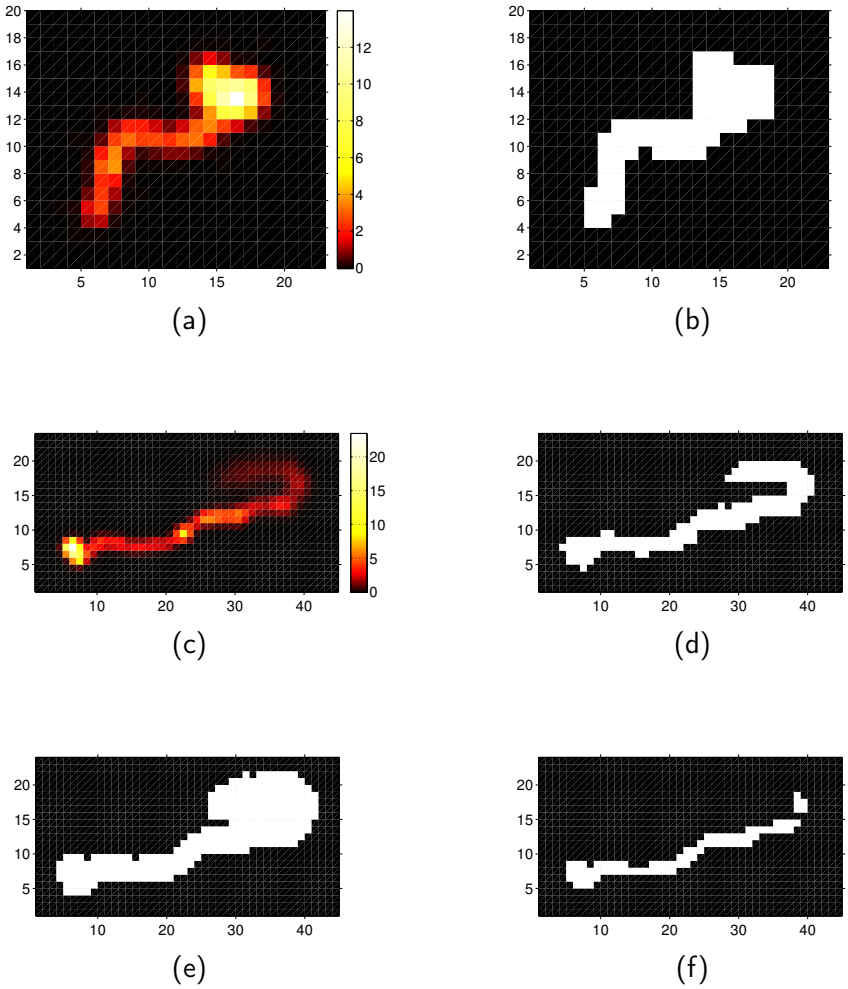

Figure 5.9: Example tracks showing threshold effects. Coordinates are in 10.5 µm pixels, and color scales are in keV (colored tracks) or binary values (black and white).
(a) Example #1 original CCD image of a track containing 215 keV.
(b) The binary image of example #1 produced by a low threshold of 0.5 keV.
(c) Example #2 original CCD image of a track containing 406 keV.
(d) The binary image of example #2 produced by a low threshold of 0.5 keV.
(e) The binary image of example #2 produced by a low threshold of 0.05 keV, which is too low.
(f) The binary image of example #2 produced by a low threshold of 1.5 keV, which is too high.

in the track image to extra spurs on the track, resulting in extra ends being identified (Figure 5.10f). Recoil electrons can also be marked as additional ends.

5.2.5 Step 4: Identify the initial segment

The initial end of the track is expected to have less energy deposited, on average, than any other part of the track. This is due to the shape of the curve of specific energy loss of an electron with respect to electron energy, for electrons of less than about 2 MeV (Figure 2.5): electrons moving more slowly deposit more energy over the same path length. In order to more accurately compare a diffuse track end with a narrow track end, the pixels around the end to a radius of two pixels are summed together (Figure 5.11). Another reason for this summing is that the pixel identified as the end may not be the center of the diffused charge at the end of the electron path, but instead a pixel near the edge of the diffused charge cloud. For example, in Figure 5.11, the elbow at the top is measured to have 19.7 keV and correctly rejected. But the pixel at the center of the region has very little energy and is not representative of the region.

The end associated with the lowest summed energy is selected as the most likely candidate for the initial segment of the electron track.

5.2.6 Measure trajectory

Once an end has been identified as the initial segment of the electron path, the trajectory along this segment is be measured in order to closely approximate the initial direction of the electron. The complexity of the electron trajectory, and resulting diffused charge distribution, requires an adaptive, flexible approach to measuring the trajectory. The algorithm implements a method of following the ridge of maximum energy along the electron path in the initial segment. The last three steps of the reconstruction algorithm define this ridge and then use the ridge to measure α and $|\beta|$.

5.2.7 Step 5: Perform ridge-following method

The projected electron track in the CCD image can be thought of as a mountain ridge, if the pixel energy is interpreted as elevation. The slopes on either side of the ridge correspond to the diffuse charge deposited in pixels on either side of the projection of the actual electron trajectory. If the electron track meets certain requirements, then the ridge of energy corresponds to the projection of the actual trajectory of the

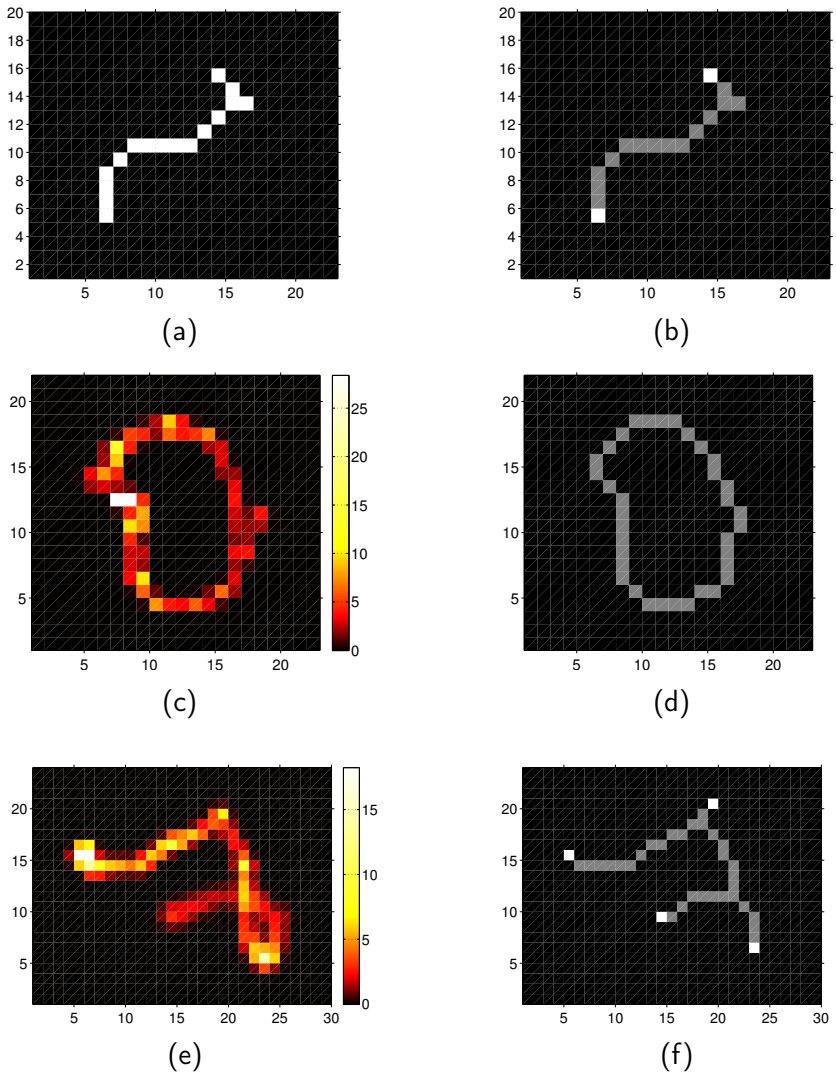

Figure 5.10: Example tracks showing the result of the thinning method. Coordinates are in 10.5 µm pixels, and color scales are in keV (colored tracks) or binary values.
(a) The result of the thinning method on the binary image of example #1.
(b) The thinned image of example #1 with the ends highlighted, as identified by the algorithm.
(c) Example #3 original CCD image of a track containing 321 keV.
(d) The thinned image of example #3. The track forms a loop, so no ends can be identified.
(e) Example #4 original CCD image of a track containing 370 keV. The electron started at the bottom center and looped over itself at the bottom right.
(f) The thinned image of example #4. The sharp elbows in the track are identified as possible starting points of the electron track.

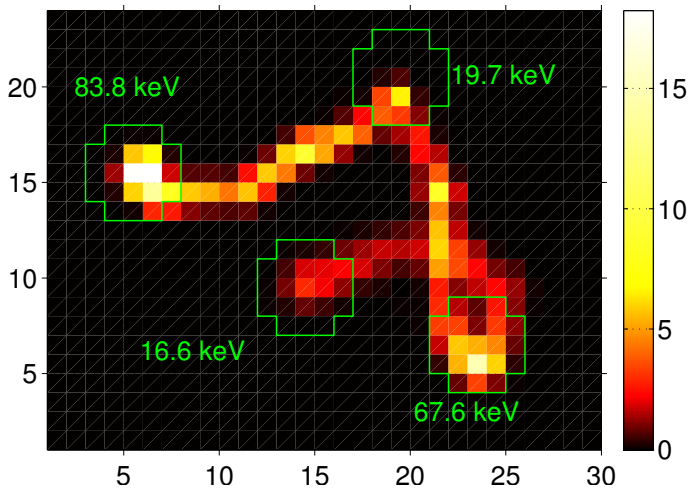

Figure 5.11: Example #4 with the region around each end outlined. The sum of pixel values in each region is shown. Coordinates are in 10.5 µm pixels, and color scale is in keV.

electron, and measuring positions along the ridge in the image will provide a good estimate of α.

For ridge-following to be effective, the energy resolution in each pixel must be fine enough to distinguish between the "peak" of the ridge and the "slopes". The projected path of the electron must be moderately straight, and not crossing over or passing near another section of track, or else the energy of pixels will include significant contributions from several parts of the track, and the ridge of energy may not follow the projected path of the electron. However, if the track is moderately straight, isolated from other segments of the track, and well-resolved in energy, the ridge should provide a good estimate of the projected trajectory of the electron, and the direction of the ridge close to the end of the track segment should approximate α.

The energy deposited in each pixel may increase or decrease along the ridge, corresponding to fluctuations in the specific energy loss of the electron. However, any point on the ridge should be identifiable by a local maximum in energy along a line perpendicular to the ridge. If the width of lateral charge spreading is relatively constant along the ridge, a line drawn perpendicular to the ridge should show a narrower cross-sectional width of energy deposition than a line drawn at any other angle. This property can be used to estimate the local direction of the ridge at a given point, by measuring cross-sections at various angles through the point and finding

the line which gives the smallest cross-sectional width.

As a conceptual overview, the ridge-following method will start with a position on the initial segment of the track about 50 µm away from the end, estimate the direction of the ridge by finding the minimum cross-sectional width, and take one "step" in the estimated direction of the ridge toward the end of the track. At the new position, the process is repeated. The series of positions, approximately along the ridge of the track, are used to estimate α, and the energy depositions are used to measure $|\beta|$ as described in the next section.

The specific method of ridge-following is described next.

In order to prevent any bias due to the location of the end pixel in the thinned image, the ridge-following method starts at a position 50 µm away from the end before taking discrete steps toward the beginning of the track. The first position for ridge-following is taken to be the center of the fifth pixel from the end of the thinned track image from step 2.

Each step of the ridge-following requires a position on the image and an initial estimate of the direction of the electron at this position. The direction at the first step is estimated from the thinned track, using the direction of the neighboring pixel in the direction of the chosen end of the track.

To measure the direction of the ridge at the current point, several cross-sectional widths are considered and the angle of the narrowest width is identified. Specifically, several lines are considered, each of which is bisected by the current position but crosses through the image at different angles. Each line extends up to 50 µm to either side of the current position, but not beyond a point where the interpolated energy is below 0.1 keV (in order to ignore separate nearby track segments). Figure 5.12b shows the lines at different angles through the initial point, with the optimal angle in green (determined as described below). The positions along each line are sampled at intervals of 1/4 pixel, and each point along each line is assigned an energy value interpolated from the pixel values surrounding it. The sample points along three different angles are shown in Figure 5.12c, and the interpolated energy values are plotted in Figure 5.12d. The difference between the yellow and green cross-sections is small, but the green is found to have the minimum value of the width metric defined next.

A width metric is calculated for each line, defined as

$$\sum_i |x_i - x_c| E_i \tag{5.1}$$

where i is the position index along one line, x_i is the distance along the line of point i, x_c is the distance along the line of the current ridge position, and E_i is the energy value interpolated at position i. For a straight or moderately curved electron path,

the width metric will be minimized for the line which crosses the electron path at right angles. Thus by selecting the line with the minimum value of width metric, the direction of the electron can be estimated. (The line with the minimum width metric has been consistently plotted in green.) Parameters recorded for the current point include the position, the angle α estimated at the current point, the FWHM of the track along the chosen cross-sectional line, and the estimated specific energy loss as modified by lateral charge spreading, which is a sum of the E_i values in units of keV/pixel. The position at each step is recentered on the energy centroid of the chosen line.

Finally, the position for the next point is defined by taking one "step" in the direction of the estimated electron path, toward the beginning of the track. The step length is 1/4 pixel. At this new position, the process described above is repeated with a new set of lines and interpolated energies. By estimating the electron direction at subpixel increments, the algorithm can make better use of the diffuse charge in the surrounding pixels. This ridge-following method is continued until the interpolated energy value at the current position is below a threshold of 0.1 keV, which is assumed to correspond to the end of the track. Figure 5.12e shows the ridge points after the ridge-following has finished, and Figure 5.12f shows the angled lines with the minimum width metric from each step.

5.2.8 Step 6: Measure β

The result of the ridge-following method is a series of about 20 measurement points (for 10.5 µm pixel pitch), covering the first 50 µm or so of the electron track as it is projected onto the image plane. However, the choice of which points to use for calculating the direction angles α and β is subtle for two significant reasons. First, points at the very beginning of the track may not be meaningful, due to the behavior of the ridge-following method on noise and pixelization around the edges of the diffuse deposited charge. The ridge-following method often changes direction in the diffuse region of the beginning of the track, before stopping at the low threshold. Thus, some points at the initial end of the track should be disregarded to avoid a bad measurement. The number of points to be disregarded is proportional to the diffusion width of the track.

Second, points farther from the beginning of the track may not be useful, because they represent the trajectory of the electron after it has deviated from its initial direction to some extent. The expected deviation at, for example, 40 µm along the track is greater for electrons with lower energy (see section 2.2) and electrons that are traveling at a steep angle relative to the pixel plane (i.e. large $|\beta|$). Unfortunately, β is one of the angles that needs to be estimated from the measurement points, using

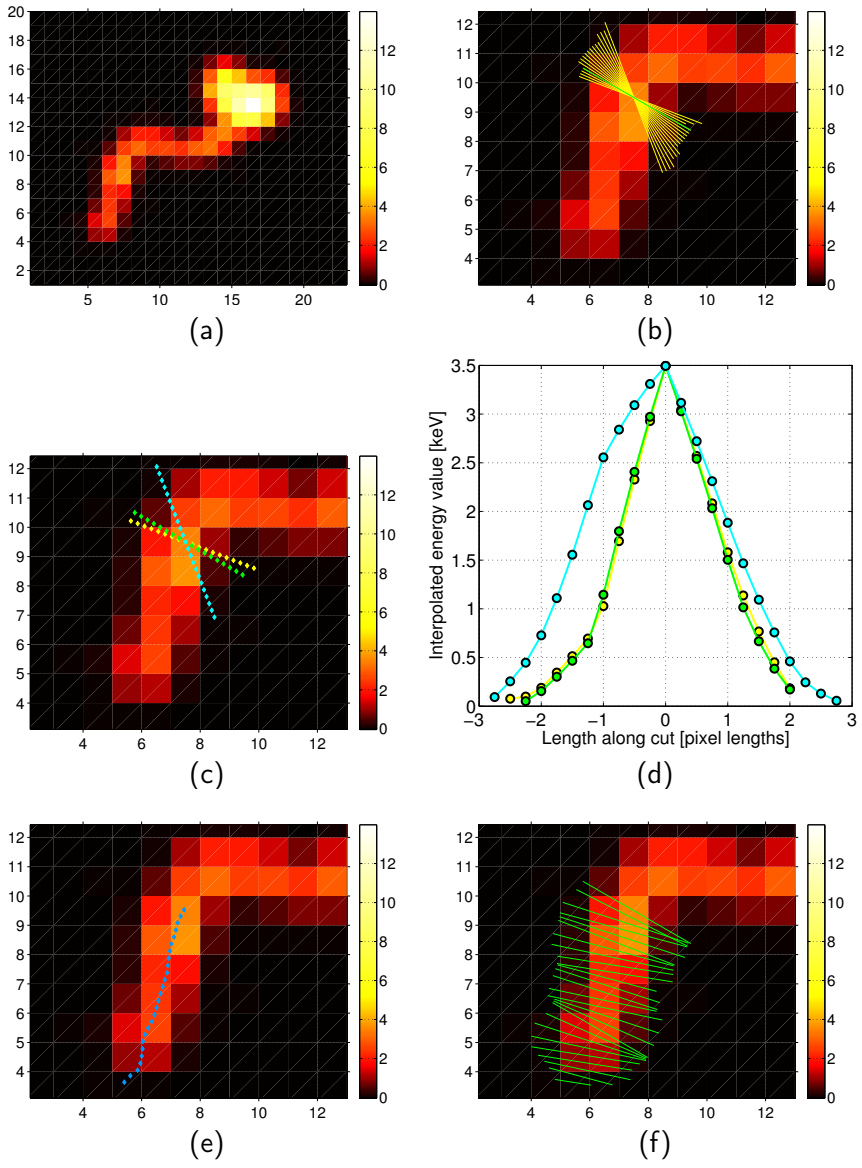

Figure 5.12: Example track showing the first step of the ridge-following method. Coordinates are in 10.5 µm pixels, and color scale is in keV.
(a) Example #1 original track image again for reference.
(b) Example #1, lines at different angles through the initial ridge position.
(c) Three of the lines from (b) illustrated with the points at which the energy is interpolated.
(d) The interpolated energies of each of the three lines in (c).
(e) The positions measured by all steps of the ridge-following method.
(f) The lines at each ridge point, at the angles with the narrowest width metric.

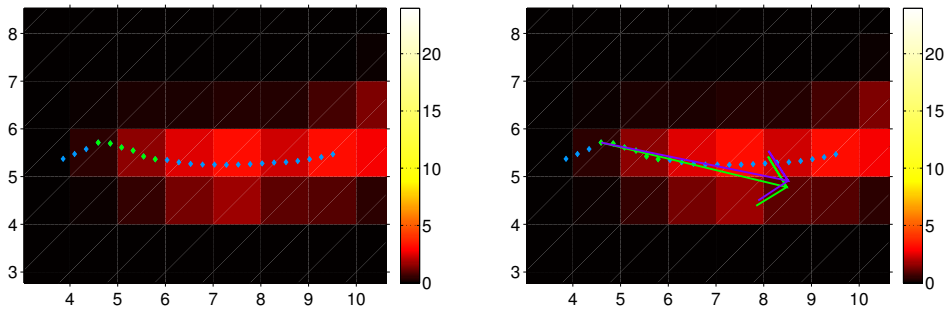

Figure 5.13: A modeled track illustrating the compromises in selecting the points to use for calculating α and $|\beta|$. The track contains 312 keV. Coordinates are in 10.5 µm pixels, and color scale is in keV.
(a) The ridge-following points alone, with the points selected for measurement highlighted in green.
(b) The points with arrows showing the true and measured initial α directions, in purple and green, respectively. The algorithm is performing better than is typical.

the following method. The example in Figure 5.13 shows the deviations both at the beginning of the track as well as farther along the track.

As described in Section 2.2, the fluctuations in the specific energy loss dE/ds of an electron in matter follow a peaked Landau distribution. The most probable value of the specific energy loss can be calculated as a function of electron energy, $dE/ds|_{\text{calc}}(E)$. This energy is deposited along the 3D path of the electron, and the resulting charge carriers deposited in the pixels have been projected through an angle β:

$$\frac{\Delta E}{\Delta R} = \left(\frac{\Delta E}{\Delta s}\right) / \cos\beta, \tag{5.2}$$

where R is a length along the plane of the pixels, and so $\Delta E/\Delta R$ is the projected specific energy loss. Then $|\beta|$ may be estimated by

$$|\beta| = \arccos\left[\frac{\frac{\Delta E}{\Delta s}|_{\text{calc}}}{\frac{\Delta E}{\Delta R}}\right] \tag{5.3}$$

which gives the correct magnitude of β if $\Delta E/\Delta s = \Delta E/\Delta s|_{\text{calc}}$ and $\Delta E/\Delta R$ is accurately measured on the track image. Figure 5.14 illustrates the concept. In this algorithm, dE/dx_{calc} is approximated from modeled electrons in Geant4.

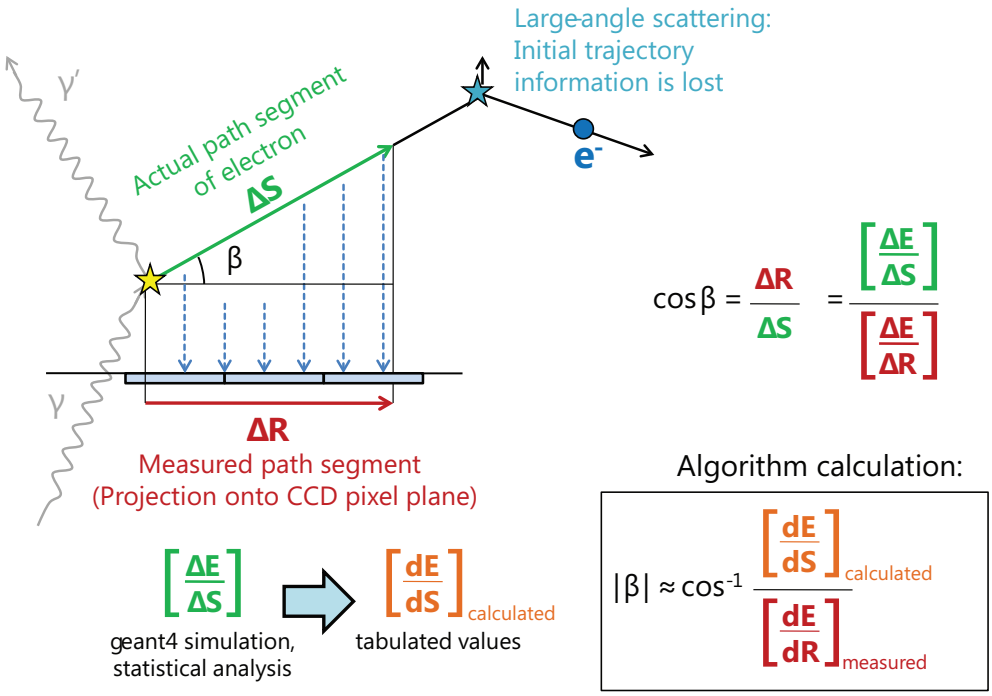

Figure 5.14: Illustration of the principle behind measuring the out-of-plane angle, β.

The calculation method is limited in that it only measures the absolute value of β, and does not indicate the sign. Also, if $dE/ds < dE/ds|_{\text{calc}}(E)$ and the trajectory is near parallel with the pixel plane, then the $\arccos$ function gives an imaginary value which is nonphysical. In this case, the algorithm will assign the closest physical solution, which is $\beta = 0$. This behavior has a marked impact on the results discussed in Chapter 6.

As mentioned above, the optimal set of measurement points is unknown and will vary with β and the energy-deposition features of the individual track. The selection of measurement points is performed only based on the track energy and estimates of β, as follows. The algorithm first chooses the set of measurement points based on an initial guess of $\beta_0 = 45°$. These points are used to calculate $|\beta|_1$ using the median of the projected specific energy loss at each point. Finally, a set of measurement points is chosen using $|\beta|_1$ and these points are used to calculate $|\beta|_2$, which is the final value estimated by the algorithm. Further iteration is not attempted because the approximate nature of the β calculation may lead to divergent behavior.

Figure 5.15c shows an example of the β measurement, with comparison to the reference value. The points indicate the differential energy measured at each step of the ridge, with the measurement points highlighted in green. The measurement

result is shown as a green line. For comparison, the $dE/ds|_{\text{calc}}$ value is shown as a black line, and $dE/ds|_{\text{calc}}/\cos\beta$ is shown in violet. In a perfect measurement, the violet and green lines would be at identical heights. In this case, the angular error in calculating $|\beta|$ is 2°, much better than average for an electron of this energy and geometry.

5.2.9 Step 7: Measure α

In contrast to β, the azimuthal angle α is quite simple to measure. The optimal set of measurement points selected using $|\beta|_1$ is also used to measure α. The α angle is measured as the median of the directions from each of the selected ridge-following points to the following point. In Figure 5.15d, the measured and true α angles are shown with arrows. For the track shown, the error in measuring α is 7°, which is better than typical for an electron of this energy and geometry.

After the reconstruction algorithm has measured α and $|\beta|$, the electron direction can be applied to the Compton imaging. Other algorithms are needed to convert the positions of photon interactions, deposited energies, and electron direction measurement into a distribution of possible incident photon directions. The details of such imaging algorithms are beyond the scope of this work.

5.2.10 Adjustments for pixel pitch

The algorithm described above is tailored specifically to electron track images at 10.5 µm pixel pitch, and is relevant to the actual device and models of this device. However, in order to understand the sensitivity achievable with different hypothetical devices, the algorithm was adapted to operate on images of different resolution. Since the electron interaction scale length and diffusion scale length remain constant while the pixel pitch changes, the algorithm should be adjusted to take this into account, while making best use of the increased or decreased information available in the image. The following describes how the reconstruction algorithm handles images of different pixel pitch.

First, energy thresholds must be adjusted to account for the different amount of charge expected in each pixel. The threshold for making the binary image in step 1, as well as the threshold for stopping the ridge-following at the end of the track, are scaled with the pixel area.

Second, the sampling intervals remain a constant fraction of the pixel pitch. These intervals include the step length for the ridge-following and the sampling interval for energy interpolation in the angled line segments. Thus, both of these intervals are always one-quarter of a pixel pitch, with the aim to use as much information as

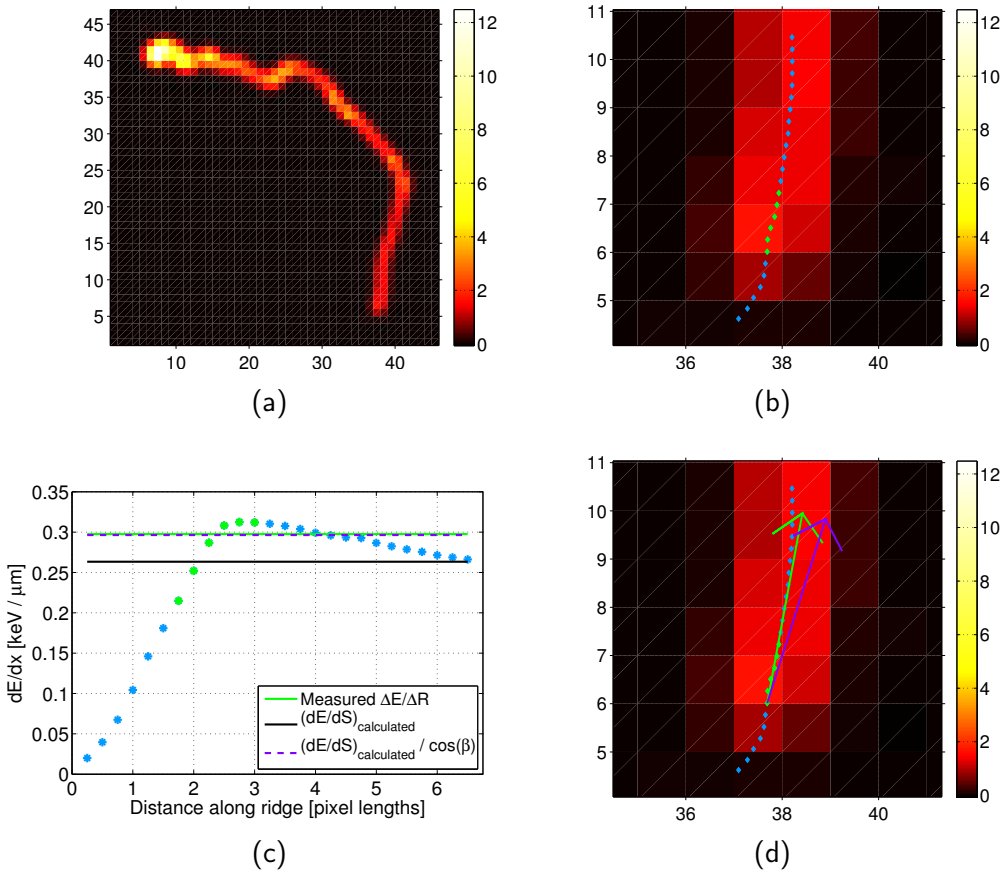

Figure 5.15: Example track showing the measurement of α and β. Coordinates are in 10.5 µm pixels, and color scale is in keV.
(a) Example #5 CCD image of a modeled electron track. The track containing 391 keV has an initial β_{true} of 27°.
(b) Example #5 track with the points used for the final calculation of α and β marked in green.
(c) The differential specific energy loss, $\Delta E/\Delta R$, measured at each step of the ridge-following method. See text for details.
(d) The measured α is marked by a green arrow, and the true α by the violet arrow.

possible from the image. For small pixel pitch, this may be excessive sampling of most tracks which are diffused over many pixel lengths. However, for the tracks very close to the pixel plane, the finely-spaced sampling can still improve the direction measurement.

The length of track to use for measuring α and β in steps 6 and 7 also scales proportionally with pixel pitch. The number of ridge points skipped at the end of the track depends on the diffusion width, but the number of ridge points after those skipped which are used for measurements is constant for different pixel pitches. Because the step length in ridge-following scales with pixel pitch, an identical number of ridge steps will cover a different physical length of track. This scaling was found to perform better than if the measurement selection length was fixed. Ideally, the set of points for a given track depends on both physical length scales (electron scattering and charge diffusion) and the information length scale (pixel pitch).

Finally, the remaining length parameters are fixed at a constant length in μm (other than rounding to an integer multiple of a sampling interval, where needed). This includes the radius of the region over which pixel values are summed to measure the energy of an edge segment in step 3 and the width of an angled line segment in step 5. Holding these parameters constant reflects the constant length scale for lateral diffusion.

The algorithm performance on different pixel pitch is not necessarily optimal, because the combined effects of electron physics, diffusion, and spatial resolution are complex. Performance metrics described in chapter 6 for pixel pitches other than 10.5 μm are meaningful as an initial comparison of hypothetical device parameters.

5.2.11 Modes of failure

The reconstruction algorithm is limited in performance on certain types of tracks, because it approaches all events in the same way. Some tracks cause an error from which the algorithm cannot recover, and it does not measure the direction at all. Other tracks merely induce a certain type of inaccuracy in the algorithm measurement. These two types of failure will be referred to as fatal and non-fatal errors, respectively. Fatal errors are recognizable by the error message produced, while non-fatal errors are recognizable mainly by the discrepancy between the measured direction and the known direction, and thus cannot easily be removed if the initial electron direction is not already known.

5.2.12 Fatal errors

There are two possible errors from which the algorithm cannot recover. First, the thinned binary image may not have any identifiable end segments in step 3. This situation usually occurs when the track is of low energy, and the binary image is symmetric enough that the thinning algorithm returns a single "1" pixel in the center. This does not count as an end since it has zero neighbors instead of one, and the ridge-following method would not have an initial direction to follow. Such a track requires a different approach to measuring, and is discussed in Section 7.3.4. The algorithm will stop with a "no ends found" error.

This situation of zero ends can also occur if the thinned binary image is a loop with no spurs, although this is much more unusual. In this case, the algorithm attempts to recover by increasing the threshold for step 1 and repeating steps 1 through 3. This will "break" a thinned loop, and ideally uncover the starting end of the track. This recovery attempt has not been optimized, but prevents the error from occurring.

The second error is also related to loop tracks. If a track has a loop with a small spur, the ridge-following method may get caught on the loop of the track and follow the loop around instead of measuring the spur. In this rare case, the ridge-following will most likely come around the loop back to the starting location, and would continue around the loop indefinitely unless this condition is recognized and the algorithm stopped. If a ridge point is closer to a previous ridge point than the step size, the algorithm has traversed a loop. This condition causes the algorithm to stop and return an "infinite loop" error. An example of a modeled track that induces this behavior in the algorithm is shown in Figure 5.16. In this case, enough charge is diffused into the gap at the top center that the ridge-following does not meet the end condition of 0.1 keV, and continues onto what is actually the final end of the track.

The "no ends found" error occurs in about 5% of 10.5 µm tracks scattered from 662 keV photons, while the "infinite loop" error occurs in 0.07% of such tracks.

5.2.13 Non-fatal errors

Non-fatal algorithm errors result in measured values of α and β, but with large angular error. This type of error is not strictly defined, but two general types of tracks which the algorithm will measure poorly are described here.

In the first case, the algorithm chooses the wrong track end to measure in step 4. If the initial track segment is close to perpendicular to the CCD, a large length of track will be projected onto the end of the track image, and an elbow or spur somewhere else in the track might be chosen instead. An energetic recoil electron, or a trajectory twisted on top of itself, can also result in significant energy deposition at the starting

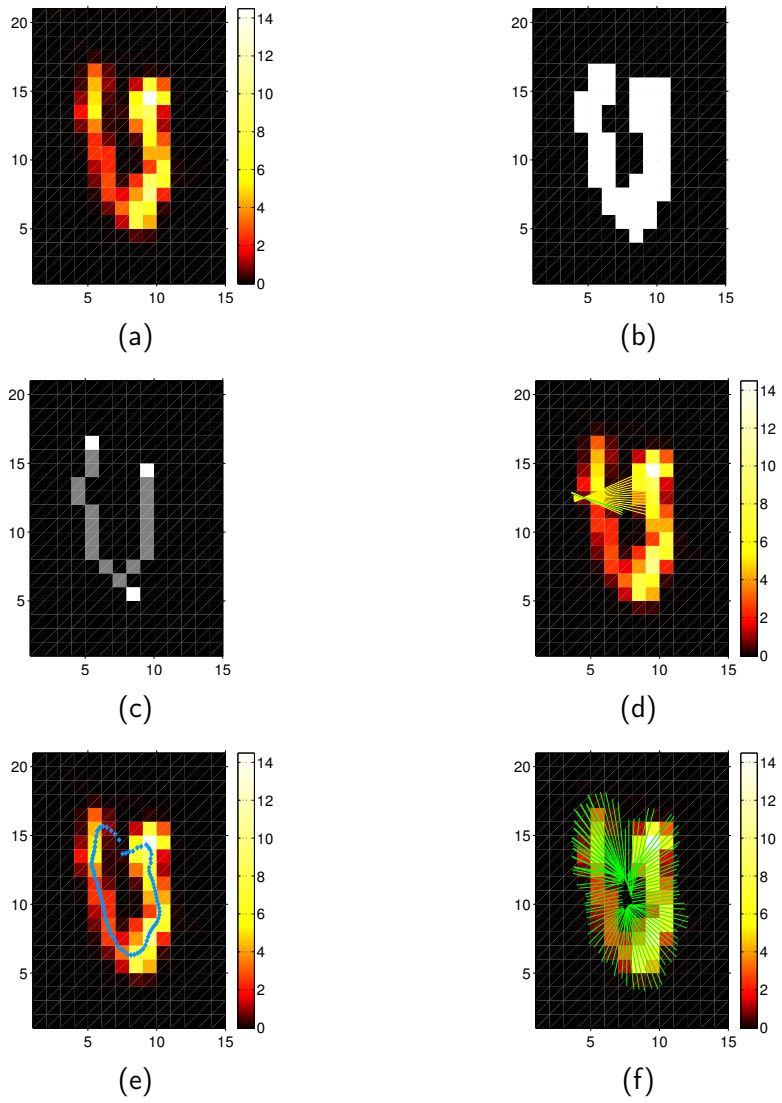

Figure 5.16: Example of a track which induces an "infinite loop" error. Coordinates are in 10.5 µm pixels, and color scale is in keV (colored tracks) or binary values (black and white).
(a) Example #6 CCD image of a modeled 375 keV electron track, upon which the algorithm returns an "infinite loop" error.
(b) The binary image.
(c) The thinned binary image.
(d) The initial angled line segments used to determine the first step of the ridge following.
(e) All the points of the ridge following. The ridge-following proceeded clockwise.
(f) All the angled line segments of the ridge following.

end of the track. Alternatively, if the starting end of the track is covered by another part of the track, it may not be identified as an end at all in step 3.

Examples of tracks for which the algorithm chooses the wrong track end are shown in Figure 5.17. The true starting position of the electron is shown with a purple X, and the true initial direction with a purple arrow. In Example #7, the electron doubles back upon its own trajectory in addition to generating two recoil electrons. The pileup of energy in the image region induces the algorithm to choose the opposite end. In Example #8, the electron finishes its trajectory in the same region it started, after traveling in a loop. Because the true initial position does not appear as a track end, the algorithm selects an elbow in the track instead.

The second case involves an electron for which the algorithm does identify the correct end of the track. If the electron elastically scatters on a nucleus near the beginning of the track, the true initial direction may be obscured by the diffusion or pixelization in the image. In particular, if the electron scatters 180°, the track will double back on itself, and an initial α angle with an offset of about 180° may be measured, even if the nuclear scattering occurred several pixel lengths away from the location of Compton scattering. Even when the initial segment is clearly distinguishable, the ridge-following may measure a nearby elbow of the track instead of the actual end.

Examples of this second type of nonfatal algorithm error are shown in Figure 5.18. In Example #9, the electron undergoes an elastic nuclear scattering of about 90° after traveling 10 µm from its initial position, and the initial segment is obscured by the diffusion. In Example #10, the electron travels farther, about 40 µm, before scattering on a nucleus. However, the 180° scatter causes the electron to double back on its trajectory, and the algorithm measures this scattered trajectory. In Example #11, the correct initial segment is clearly visible. But the algorithm's ridge-following method fails to recognize the sharp bend in the track, and measures an elbow of the track instead.

Both of these non-fatal error types are evident in the distributions of α measurement error in section 6.1.2. The frequency with which they occur depends on the electron energy and $|\beta|$ angle, and corresponds to the fraction of events not included in the forward peak fraction.

5.3 Data analysis in the coincidence experiment

The methods by which an image from the SNAP CCD may be calibrated, segmented into individual gamma-ray interactions, and then processed to measure interaction energy and initial electron direction have been described above. A benchmark of

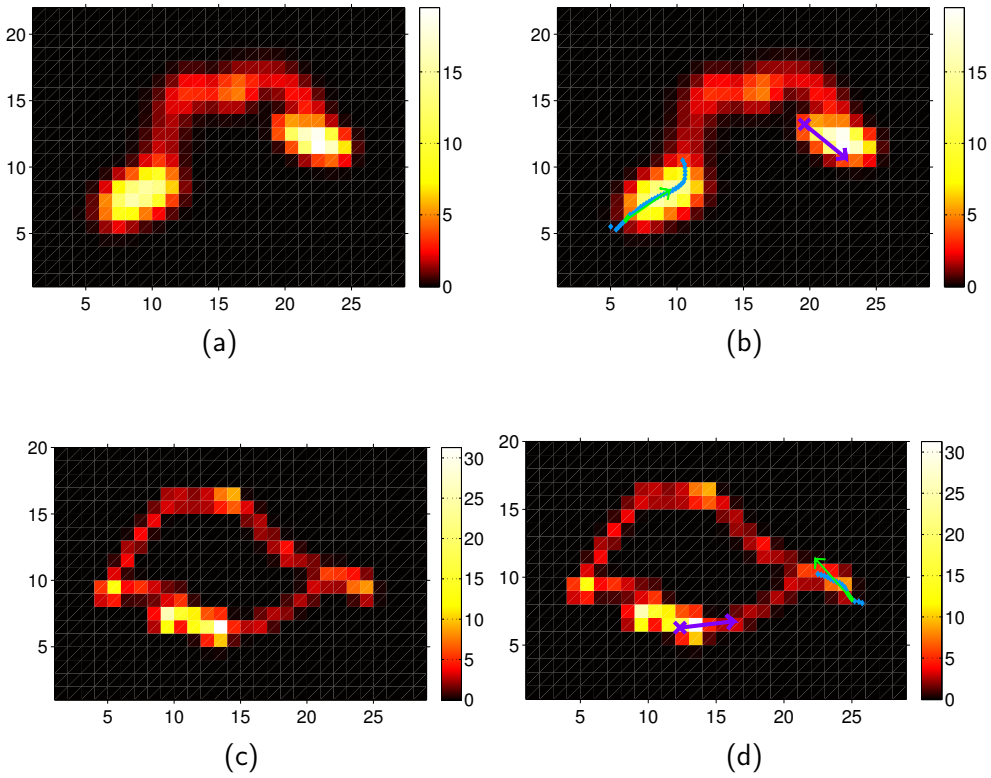

Figure 5.17: Example tracks in which the algorithm identifies the wrong end. Coordinates are in 10.5 µm pixels, and color scale is in keV.
(a) Example #7 CCD image of a modeled 447 keV track.
(b) Example #7 true (purple) and measured (green) electron directions.
(c) Example #8 CCD image of a modeled 390 keV track.
(d) Example #8 true and measured electron directions.

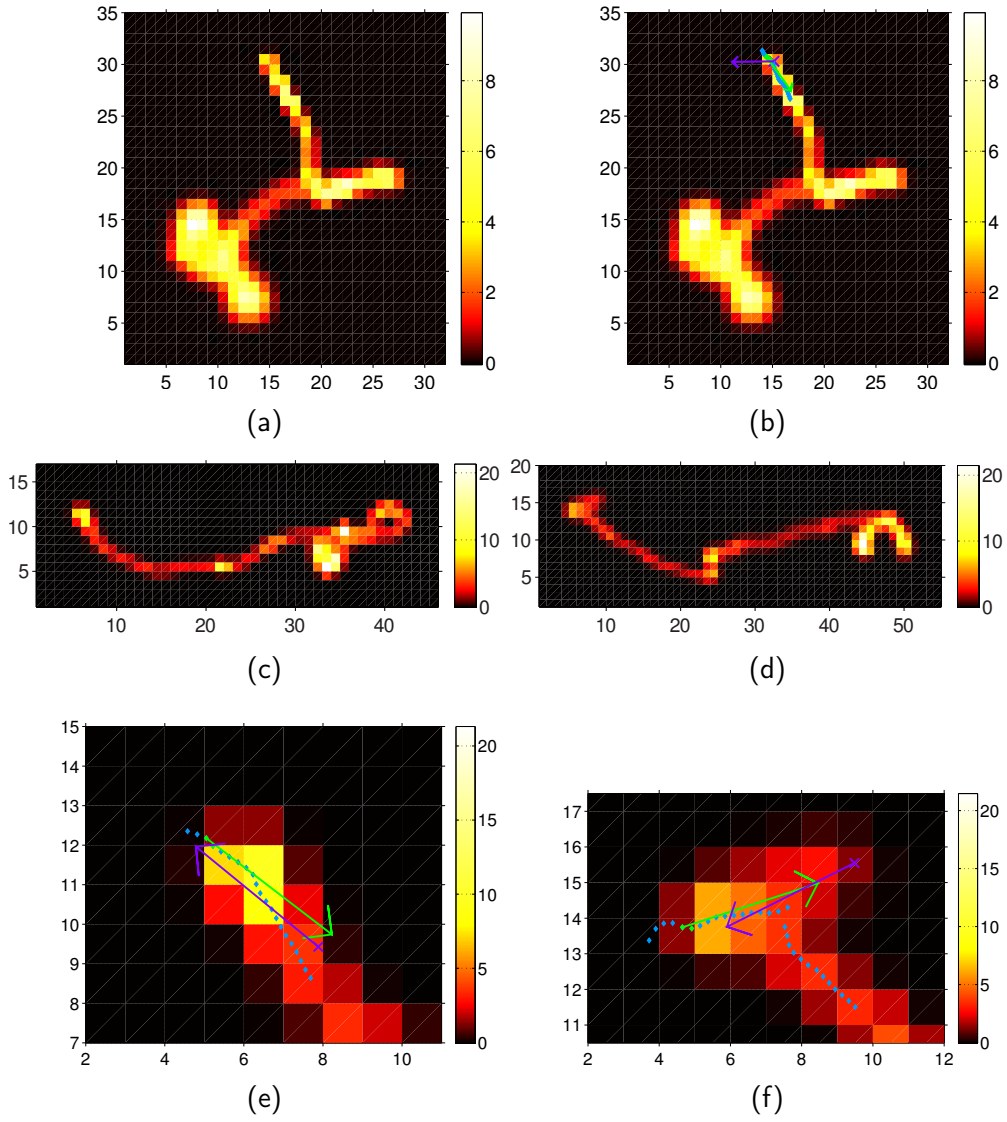

Figure 5.18: Example tracks in which the algorithm measures the correct end but performs poorly. Coordinates are in 10.5 µm pixels, and color scale is in keV.
(a) Example #9 CCD image of a modeled 492 keV track.
(b) Example #9 true (purple) and measured (green) electron directions.
(c) Example #10 CCD image of a modeled 417 keV track.
(d) Example #11 CCD image of a modeled 476 keV track.
(e) Example #10 true and measured electron directions.
(f) Example #11 true and measured electron directions.

the algorithm's angular sensitivity requires measuring electron tracks with a known initial trajectory, which was the purpose of the coincidence experiment discussed in Chapter 3.

The coincidence experiment needs some additional methods of analysis. First of all, the experiment involved a second position-sensitive detector to measure scattered gamma rays. The double-sided strip germanium detector used in this experiment has its own complexities of measuring gamma-ray interaction positions and energies. In addition, the information from the germanium detector and CCD must be analyzed to select event sequences in which the gamma ray scattered from the CCD to the germanium. These analysis methods are described in the remainder of this chapter.

5.3.1 Germanium double-sided strip detector analysis

The signals from the germanium double-sided strip detector, known as "Ge2", were recorded with 14-bit digitzers at a sampling rate of 100 MHz, as described in section 3.3. The electronic logic requires at least one strip on each side of the detector to trigger, and the open-shutter logic signal to be active, in order to record an event. A recorded event includes the signals from any triggered strips as well as neighbors to the triggered strips. Each signal includes identification of the strip it is on, the digital signal samples, energy measurement from the digitizer's internal trapezoidal filter, and a number representing how many sampling intervals have passed since the initialization of the system (the *timestamp*). During data acquisition, these raw data are saved in a single file for each shutter period, named with the shutter index number.

The raw data are then processed for energy calibration and event reconstruction. Event reconstruction, described below, is necessary to correlate signals from strips on one side of the detector with strips from the other side of the detector. Strips triggering within 100 ns of each other are grouped into time *clusters*. A cluster can include one or more gamma-ray interactions, which are assumed to be interactions of the same gamma ray. This assumption is usually valid, because the countrate in Ge2 is only $1.6\,\mathrm{s}^{-1}$ in this experiment (section 3.3.6).

If only a single strip on each side has triggered, the correlation is trivial. However, if multiple strips trigger on each side, and with the possibility of charge carriers from one interaction to be shared between two neighboring strips, the correlation is more complicated. In this case, the event reconstruction code identifies strip *couplings*, in which two strips on opposite sides measure energies that are similar (specifically, within the energy resolution). Neighboring triggered strips are assumed to be sharing the charge from at least one interaction. If the energy measured on each side does not match within 4σ of the energy resolution, or if more than two contiguous strips

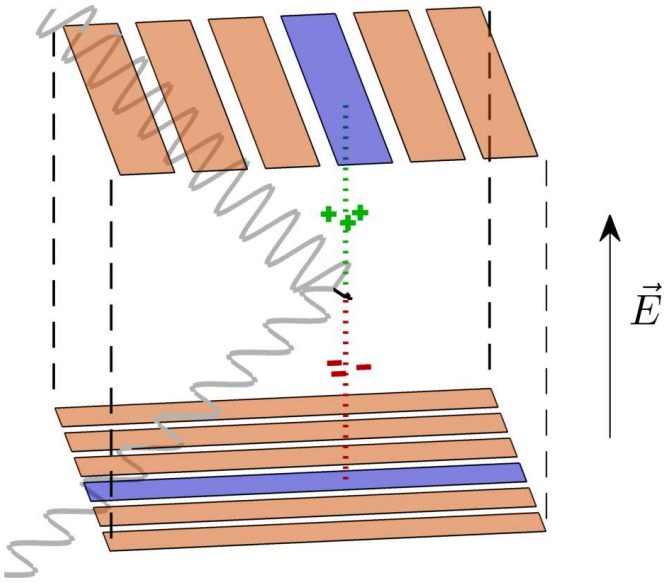

Figure 5.19: A conceptual illustration of a double-sided strip detector measuring an interaction of a gamma ray. The electrodes which collect the signal charge are highlighted in blue. The signal amplification and voltage source are not shown.

on either side have triggered, the time-clustered event is discarded. Due to the limitations of this event reconstruction algorithm, only about 34% of triggered strips are reconstructed successfully into events.

For each coupling, the interaction energy is measured as an average of that measured by each side of the detector, and the lateral positions are estimated as the center of the triggered strips on each side (or between strips, if two strips on one side shared the charge). The depth position is estimated by measuring the time at which signals from each side reach half of the maximum (t_{50}). Because the majority of the signal will be induced when the charge cloud is close to the strip electrode, t_{50} is an approximation of the time when the charge cloud arrives at that side of the detector. Then the difference between the t_{50} on either side, dt_{50}, can be mapped to the depth position of the interaction. An example is shown in Figure 5.20. The relationship is assumed to be linear for simplicity. The effective position resolution of this method is about 1.9 mm FWHM. This position resolution is limited by noise in the signal and the assumption of a linear relationship between dt_{50} and depth.

The result of event reconstruction is a list of couplings, grouped into time clusters. Each coupling has a 3D position, described by the triggered strips on either side and the dt_{50} value; an energy; and a timestamp. Figure 5.21 shows the spectrum of coupling energies over the course of the coincidence experiment. The countrate of

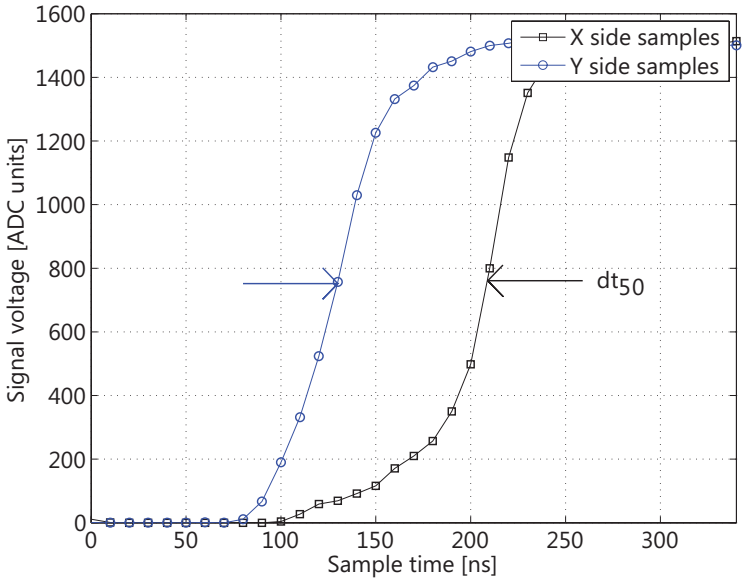

Figure 5.20: An example showing the measurement of the z position of interaction using the dt_{50} method.

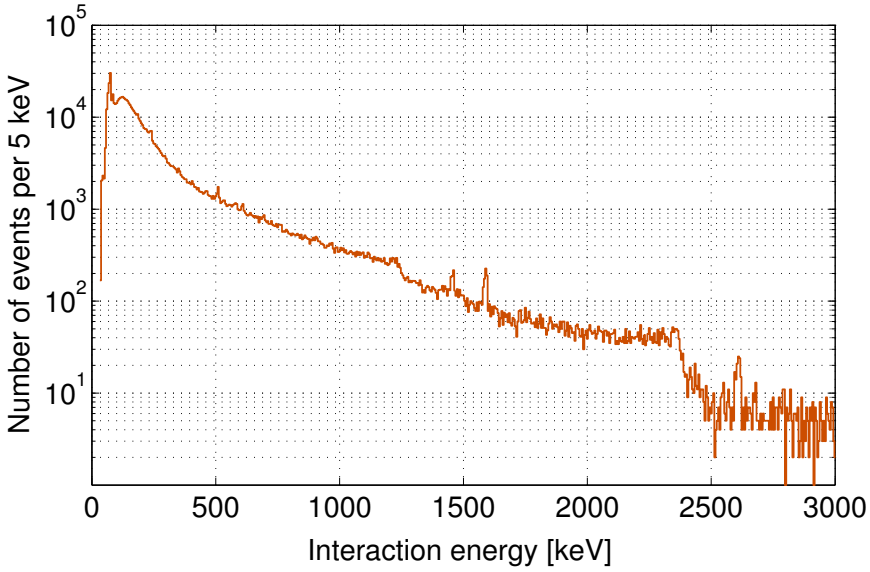

Figure 5.21: Energy spectrum of Ge2 over the course of the coincidence experiment. The visible peaks come from naturally occuring radioactive material in the laboratory background, including ^{40}K (1461 keV) and ^{208}Tl (2614 keV).

photons scattered from the CCD is negligible compared to the background radiation.

5.3.2 Coincidence candidate event sequences

As per its name, the coincidence experiment requires the correlation of data between the CCD and Ge2 so that events can be identified in which a gamma ray scatters from the CCD into Ge2. The time correlation is made trivial by saving the data streams from both detectors in filenames labeled with a unique shutter index number. However, the data from each shutter must be analyzed to pick true coincident event sequences out of the dominant background.

The CCD calibration, CCD segmentation, and Ge2 event reconstruction are each performed on the raw acquired data by a MATLAB script running continuously on a computer server. For each shutter period, the script generates files containing calibrated and segmented CCD tracks and files containing reconstructed Ge2 interactions in time clusters. In addition, summaries of each day's data are compiled for each detector, which include detector positions and interaction energies.

Another MATLAB script loads the daily summaries and analyzes them to list candidate coincident event sequences. For an event sequence to be considered a candidate, there must be a track in the CCD with energy between 140 keV and 360 keV, and a Ge2 interaction of energy between 300 keV and 520 keV in the same shutter period. This filters out potential scattering sequences which are clearly nonphysical, corresponding to a scattering angle of $\theta < 38^\circ$ or $\theta > 86^\circ$, greatly reducing the background of false coincidences. The low countrates described in section 3.3.6 ensure that pileup of multiple interactions within one shutter period is rare; however, when multiple interactions do occur in the energy windows, each possible permutation of events paired between the CCD and Ge2 is considered to be a separate coincidence candidate. For example, if there are two separate Ge2 interactions in the Ge energy window within a shutter period, as well as a CCD track in the CCD energy window in the same shutter period, two coincidence candidates are recorded. Each will include one of the Ge2 interactions, and the same CCD interaction. This method was preferred over any attempt to deduce the interaction sequence between CCD and Ge2, in order to avoid bias in the false coincident event sequences which form the overwhelming majority of coincidence candidates.

In addition, only single interactions in Ge2 are used, rather than time-clustered sequences of interactions. This is due to the potential for mistracking sequences of gamma-ray interactions.

The coincidence candidate event sequences are saved in a list for each acquisition day, with the following information:

- energy of the CCD track, E_{CCD}
- energy of the Ge2 interaction, E_{Ge2}
- total coincident energy, $E_{\text{tot}} = E_{\text{CCD}} + E_{\text{Ge2}}$
- position of the CCD track, $\vec{x}_{\text{CCD}}$. This position is not measured at the initial end of the track, because the electron track algorithm has not been performed yet. It is estimated to be the center of a 2D rectangle containing the track. The position error here is small compared to other uncertainties in the experiment.
- position of the Ge2 interaction, $\vec{x}_{\text{Ge2}}$
- adjusted position of the Ge2 interaction, $\vec{x}_{\text{Ge2},2}$. After finding an error in the position calibration, the position offset of Ge2 was shifted by 7 mm, $\vec{x}_{\text{Ge2},2} = \vec{x}_{\text{Ge2}} - (7\,\text{mm})\hat{x}$ (see section 3.3.7).
- angle of Compton scattering, calculated by interaction positions,

$$\theta_{\text{geometric}} = \arccos \frac{\hat{n}_{\text{beam}} \cdot (\vec{x}_{\text{Ge2}} - \vec{x}_{\text{CCD}})}{\|\vec{x}_{\text{Ge2}} - \vec{x}_{\text{CCD}}\|} \tag{5.4}$$

  where $\hat{n}_{\text{beam}}$ is the vector describing the direction of the collimated beam of gamma rays
- angle of Compton scattering, calculated by interaction positions, using the adjusted position of the Ge2 interaction, $\theta_{\text{geometric},2}$ as above
- angle of Compton scattering, calculated by the Compton imaging formula, equation 2.25, using measured interaction energies, θ_{Compton}
- angular resolution measure (ARM), $\Delta\theta = \theta_{\text{geometric}} - \theta_{\text{Compton}}$
- angular resolution measure (ARM) with adjusted Ge2 interaction position, $\Delta\theta_2 = \theta_{\text{geometric},2} - \theta_{\text{Compton}}$
- vector of electron direction, $\hat{n}_{e^-}$, calculated from $\theta_{\text{geometric},2}$ (equations 2.3 and 2.4)
- the calibrated and segmented electron track image
- the Ge2 reconstruction information
- the shutter index number
- indices specifying the particular CCD track and Ge2 event within the shutter period, in case there are multiple events in the shutter period

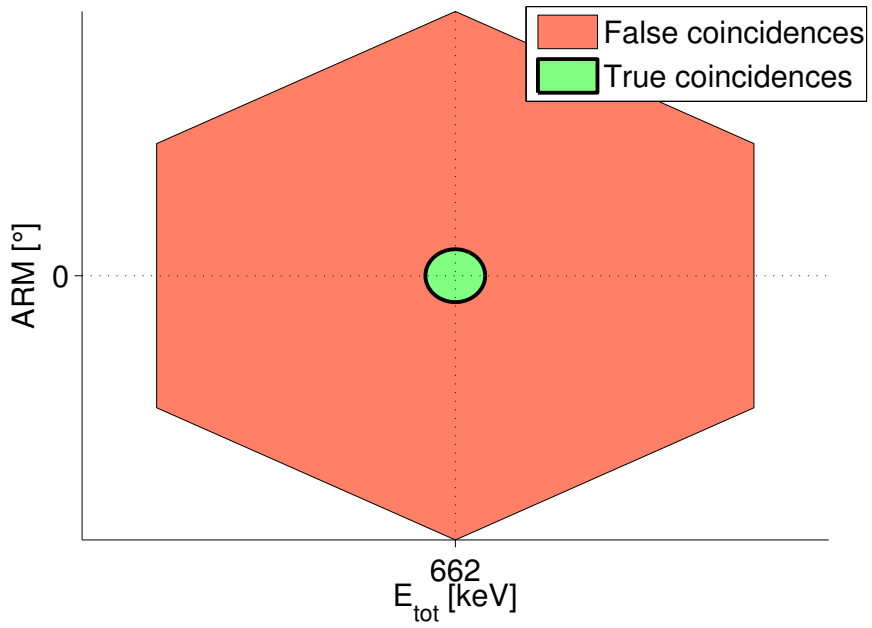

Figure 5.22: Conceptual illustration of the plot used to identify the true coincident event sequences. ARM is the angular resolution measure, which can be described as the difference between the scattering angle calculated from interaction positions and the scattering angle calculated from interaction energies [134]. The hexagonal shape of the false coincidence distribution comes from energy windows applied to E_{CCD}, E_{Ge2}, and E_{tot}.

5.3.3 Events in the true coincidence region

These coincidence candidate event sequences mainly consist of false coincidences, caused by matching a track in the CCD with a background interaction in Ge2. True coincident event sequences caused by a single gamma ray scattering from the CCD into Ge2 must be selected using total deposited energy, E_{tot}, and the angular resolution measure (ARM).

The true coincidences are expected to be found in a region centered at $\Delta\theta = 0°$ and $E_{\text{tot}} = 661.7\,\text{keV}$, as illustrated in Figure 5.22. By identifying this region, the large majority of the background events can be rejected, greatly improving the SBR. Events from this region can be measured with the electron trajectory reconstruction algorithm, and the initial electron direction measured by the algorithm compared to the direction calculated by interaction positions. The electron direction represented by the (α, β) of the algorithm can be compared to $\hat{n}_{e^-}$ to determine the algorithm error, in degrees α and β, for each coincident event.

5.4 Summary

The data analysis methods are central to this work because the measurement of the initial electron direction is challenging. In addition, the black level offset of CCD images must be calibrated using the median pixel value method in order to minimize the effect of readout noise on the measurement of track energy. The tracks of electrons above about 50 keV must be segmented from the CCD image as a multipixel event, with the energy measured as the sum of pixels above a 0.1 keV threshold as well as their neighbors.

The algorithm for reconstructing the initial direction of the electron provides the information fundamentally necessary for electron track Compton imaging. The tortuous path and fluctuations in energy deposition described in section 2.2, as well as the inherently two-dimensional CCD image, make this a challenging task. The reconstruction algorithm was developed using image processing methods to choose the initial segment of the track, and then a ridge-following method to measure positions and energy deposition along the initial segment. In particular, the energy deposition can be used to estimate the magnitude of the out-of-plane angle, $|\beta|$, to provide some three-dimensional information even from the two-dimensional track, addressing one of the shortcomings of the CCD.

The coincidence experiment from section 3.3 allows the experimental evaluation of the angular sensitivity of the reconstruction algorithm, through measuring electron tracks with known initial directions. This experiment requires a second detector, the germanium double-sided strip detector. The germanium detector requires event reconstruction in order to convert the signals from strips into an interaction position, time, and energy of deposition. In order to match the data from the CCD and germanium and extract the signal of true coincident event sequences, careful processing is needed especially due to the large background of false coincident event sequences.

In the next chapter, the angular sensitivity of the reconstruction algorithm will be presented, which defines the potential background reduction in an electron track Compton image. The angular sensitivity is evaluated from both the models from Chapter 4 and the coincidence experiment.

Chapter 6

Results

The experimental methods for measuring electron tracks in the CCD, simulation methods for modeling the CCD response to electron tracks, and the reconstruction algorithm for measuring the initial electron direction have been already been described. By measuring initial electron directions, electron track Compton imaging can be performed; by measuring electron tracks for which the initial direction can be calculated separately, the angular sensitivity of the reconstruction algorithm can be evaluated. The angular sensitivity defines the width of the cone segment in electron track Compton imaging.

This angular sensitivity is the main focus of this chapter. First, the metrics used to describe angular sensitivity will be introduced, including FWHM and peak fraction for α, and RMS for β. Next, the evaluation of angular sensitivity on modeled tracks will be presented. The modeled tracks are numerous, which allows the angular sensitivity's dependence on several variables to be assessed. These variables include track energy and $|\beta|$ for the model of the CCD used in experiments, and pixel pitch and readout noise for possible variations on the SNAP CCD. The modeled angular sensitivity for the experimental device show FWHM in α as low as 20°, with very good performance overall compared to the 360° of a conventional Compton imaging cone. The sensitivity to $|\beta|$ is about 30° RMS from the method of measuring the projected specific energy loss.

The angular sensitivity of models of CCDs with different pixel pitch are important for considering the development or utilization of different CCDs. The angular sensitivity of modeled CCDs with greater readout noise are relevant for considering the operation of CCDs at higher temperatures than the current 140 K.

All of the modeled CCD responses are for Compton-scattered electrons from a 662 keV source. Only electrons which are contained within the volume of the CCD

are used.

The coincidence experiment from Chapter 3 measured electron tracks with well-known initial directions. In this chapter the results will be presented, including the 87 events in the FWHM of the true coincidence total energy and angular resolution metric. The angular sensitivity measured on these tracks will be compared to the angular sensitivity of equivalent modeled tracks, showing very good agreement.

6.1 Metrics for angular sensitivity

The impact of electron tracking on Compton imaging depends on the precision of measuring the initial direction of the electron. The precision is difficult to quantify because of the variety of features in the electron tracks being measured (see, for example, section 5.2.13). The features in a typical distribution of angular error will be described, along with the metrics used to quantify them. The angular sensitivity of the reconstruction algorithm is expressed using these metrics.

Except in sections 6.2.2 and 6.2.3, all modeled results use a CCD model with the same basic properties as the device used in experiment, i.e. with 10.5 µm pixel pitch and with electronic readout noise of 20 eV (σ) per pixel.

6.1.1 Angular error

The first steps are to calculate the initial directions for a large number of modeled electron tracks with the reconstruction algorithm, and compute the difference between the algorithm's initial direction and the known initial direction from the model. The difference between the angle obtained from the algorithm and the true angle is defined to be Δ, for both α and β:

$$\Delta_\alpha = \alpha_{\mathsf{alg}} - \alpha_{\mathsf{true}} \tag{6.1}$$

$$\Delta_\beta = |\beta|_{\mathsf{alg}} - |\beta_{\mathsf{true}}|. \tag{6.2}$$

Here, α and β are the two angles defining the electron direction (Figure 5.8), the subscript "alg" refers to the value estimated by the reconstruction algorithm, and the subscript "true" refers to the true value known from the model. The values of β are written as absolute values, because the algorithm is limited to only measuring the magnitude of β and not its sign (section 5.2.8). The true β has a sign, but for comparison to the algorithm value the sign is ignored. A perfect measurement would result in $\Delta_\alpha = 0°$ and $\Delta_\beta = 0°$.

The angular error values can be compiled into histograms for tracks with similar characteristics in order to understand the overall algorithm performance on tracks

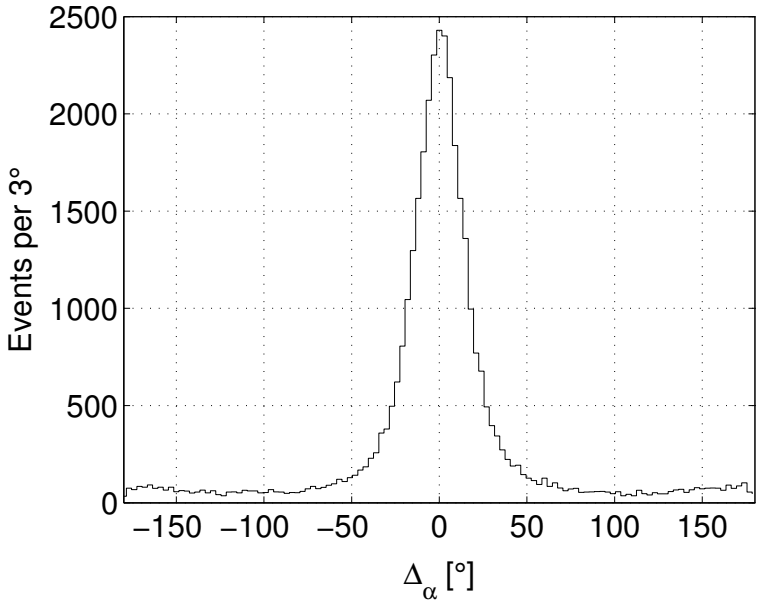

Figure 6.1: Distribution of Δ_α for electrons that do not escape the CCD volume and have energy between 250 keV and 300 keV.

with those characteristics. The characteristics examined include the electron energy and the track angle calculated from dE/dR in the reconstruction algorithm, $|\beta|_{\text{alg}}$. In addition, sections 6.2.2 and 6.2.3 will consider the response of modeled devices with different pixel pitch and noise.

Below typical distributions of Δ_α and Δ_β are shown for events selected using the characteristics above, and the features in each distribution are explained.

6.1.2 Distribution of Δ_α

The α angle is generally estimated more accurately by the algorithm than β, because it is more directly associated with the ridge measurements described in section 5.2.7. Both α_{alg} and α_{true} can have values between 0° and 360°. Empirically, it has been found that the measurement is not significantly affected by the actual value of α_{true}. Therefore, the difference in quantities, Δ_α, is sufficient to describe the algorithm performance. Δ_α can always be expressed as a value in the range of $-180°$ to 180°. Figure 6.1 shows a distribution of Δ_α for electrons of energy between 250 keV and 300 keV.

The primary feature is a large *forward peak* centered on $\Delta_\alpha = 0°$, which is similar in shape to a Gaussian distribution but with slightly larger tails. This peak consists of

events in which the algorithm measures the correct track end, and encounters none of the issues described in section 5.2.13.

The other significant feature is a component of Δ_α which is approximately evenly distributed. This component consists of events in which the electron scattered elastically on a nucleus, near the beginning of the track. There is a slight enhancement near $\Delta_\alpha = \pm 180°$, due to electrons which scatter at about 180°, covering the initial segment of the track (section 5.2.13). The constant component is called the *random component*, while the enhancement at $\pm 180°$ is the *backscatter peak*. The backscatter peak is insignificant ($< 2\%$) when the forward peak contains more than 50% of events, and it will be ignored for simplicity.

6.1.3 Metrics for Δ_α distributions

The distribution of Δ_α can be described by a single metric such as RMS (root mean square) error. However, the distribution is described more completely by two values: the full width at half maximum (FWHM) of the forward peak, and the fraction of events in the forward peak, f. Distributions of tracks for which the algorithm is not very sensitive are characterized not only by a larger FWHM, but also by a small f.

For the examples in Figure 6.2, the metrics are (a) FWHM $= 66.6 \pm 0.5°$, $f = 50.7 \pm 0.7\%$, and (b) FWHM $= 25.25 \pm 0.17°$, $f = 79.1 \pm 1.0\%$.

6.1.4 Distributions of β

The measurement of β is more complex. As a reminder, $|\beta|$ is calculated from equation 5.3:

$$|\beta| = \arccos \left[\frac{\frac{\Delta E}{\Delta s}|_{\mathsf{calc}}}{\frac{\Delta E}{\Delta R}} \right].$$

Figure 6.3 shows the distributions of $|\beta|_{\mathsf{true}}$ and $|\beta_{\mathsf{alg}}|$ from all modeled tracks. Because the electron tracks are distributed nearly isotropically in the modeled CCD, the distribution of $|\beta_{\mathsf{true}}|$ scales with $\cos \beta_{\mathsf{true}}$.

The distribution of $|\beta|_{\mathsf{alg}}$ includes a spike at exactly $|\beta|_{\mathsf{alg}} = 0°$, and a broad distribution peaking at $|\beta|_{\mathsf{alg}} = 45°$. The peak at 0° consists of events in which the algorithm measures $\frac{\Delta E}{\Delta R} \leq \frac{\Delta E}{\Delta s}|_{\mathsf{calc}}$, for which there is no physical solution for $|\beta|$ (see section 5.2.8). The peak at 45° may be related to the algorithm's initial guess of $|\beta| = 45°$.

Two approaches may be taken to examine how $|\beta|_{\mathsf{alg}}$ correlates with $|\beta_{\mathsf{true}}|$. The first approach is to choose a range of values of $|\beta_{\mathsf{true}}|$, and see what distributions of $|\beta|_{\mathsf{alg}}$ result; the second approach is to restrict $|\beta|_{\mathsf{alg}}$ to a range of values, revealing

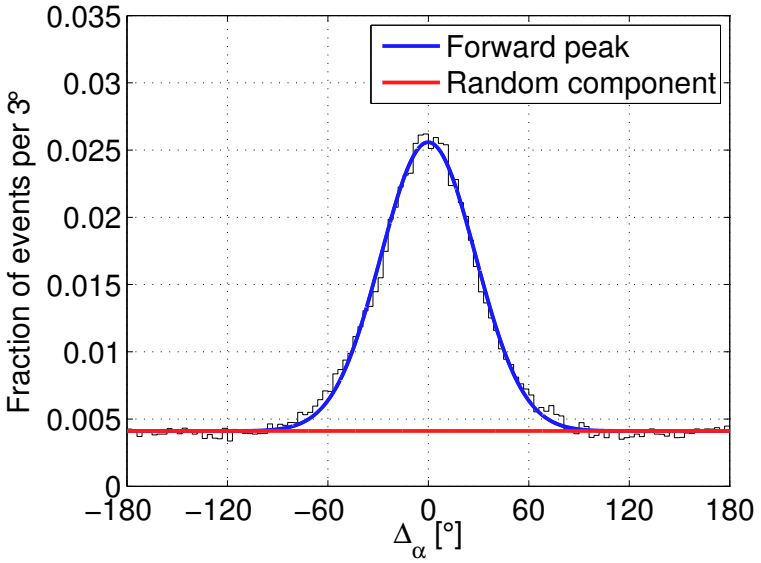

(a)

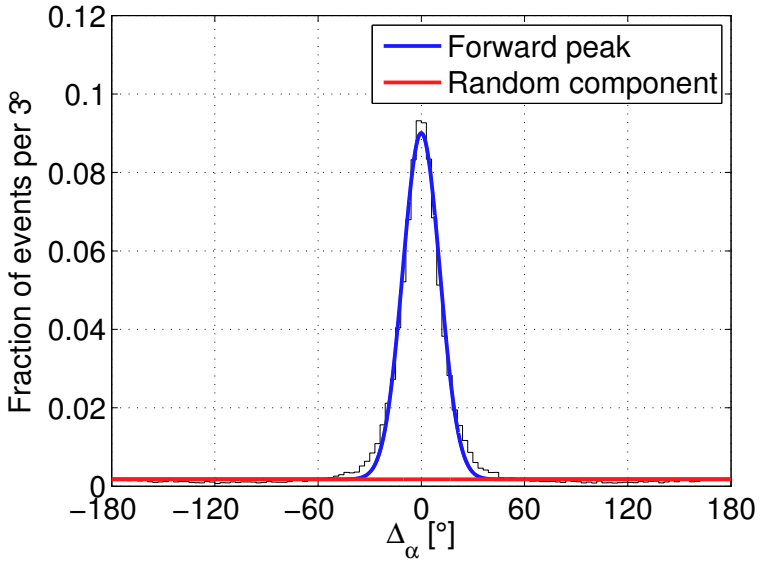

(b)

Figure 6.2: Distributions of Δ_α fitted with a Gaussian forward peak and random component, for electrons with (a) 100 keV $< E_{\text{tot}} <$ 125 keV, and (b) 400 keV $< E_{\text{tot}} <$ 425 keV.

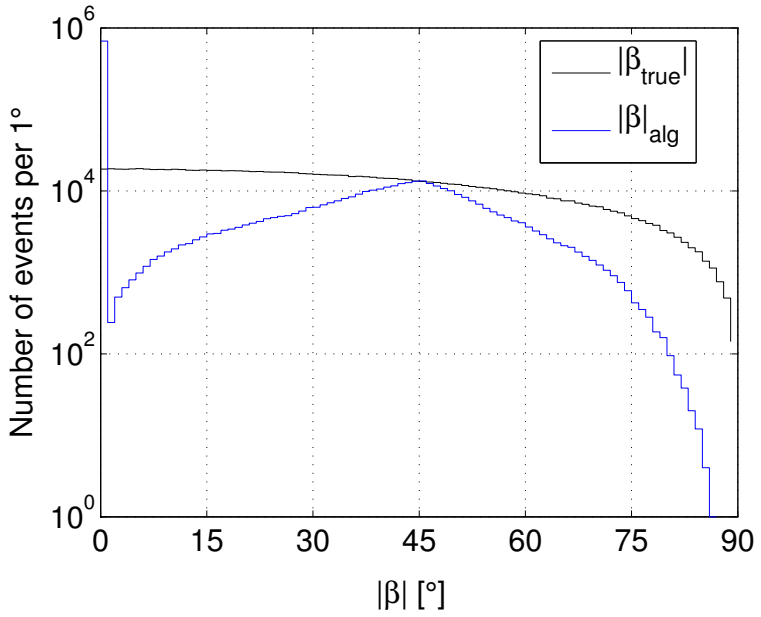

Figure 6.3: The distribution of $|\beta_{\text{true}}|$ and $|\beta|_{\text{alg}}$ for all the modeled tracks.

which $|\beta_{\text{true}}|$ values led to that measurement. For each approach, values of Δ_β can also be calculated for the selected events.

The first approach is complicated by the tendency of the algorithm to calculate $|\beta|_{\text{alg}} = 0°$. This produces distributions of Δ_β with two components, one corresponding to measurements of $|\beta|_{\text{alg}} = 0°$ and one for measurements of $|\beta|_{\text{alg}} > 0°$. The former component will by definition be located at $\Delta_\beta = -|\beta_{\text{true}}|$, and the analysis of the $|\beta|$ sensitivity will be complicated by this component.

The second approach is used in this chapter and illustrated in Figure 6.4. The first plot shows the distribution of $|\beta_{\text{true}}|$ for electrons between 300 keV and 400 keV, and $|\beta|_{\text{alg}}$ between 30° and 45°. For perfect measurements of $|\beta|_{\text{alg}}$, all values of $|\beta_{\text{true}}|$ would be in the region highlighted in yellow. The distribution in the second plot is essentially a copy of the first distribution, but reversed (due to the sign in equation 6.2) and shifted. The events with $|\beta|_{\text{alg}} = 0°$ are not included, being out of the chosen range, and can instead be studied in a separate histogram.

6.1.5 Metrics for Δ_β distributions

Distributions of Δ_β do not have well-defined components like Δ_α, and cannot be approximated as Gaussian distributions. Therefore, it is sufficient to measure the precision with the root mean square of the Δ_β values (RMS). The positions corre-

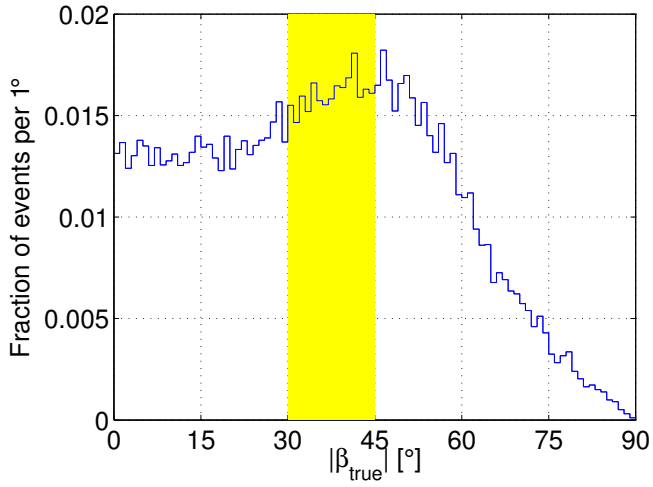

(a)

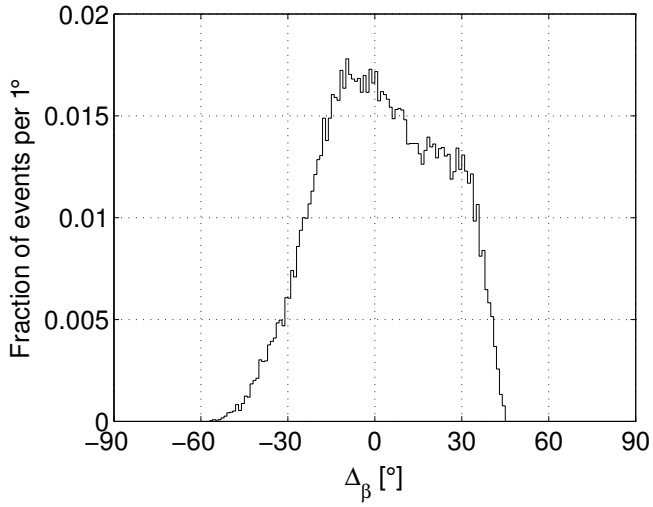

(b)

Figure 6.4: Distributions of (a) $|\beta_{\text{true}}|$, and (b) Δ_β, both for 300 keV $< E_{\text{tot}} <$ 400 keV and $30° < |\beta|_{\text{alg}} < 45°$. See text for explanation.

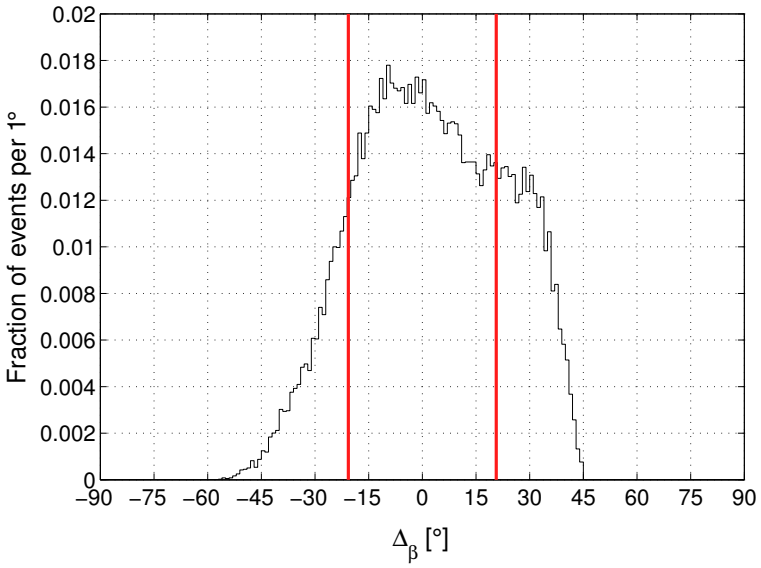

Figure 6.5: Distribution of Δ_β for electrons with $300 < E_{\text{tot}} < 400\,\text{keV}$ and $30° < |\beta|_{\text{alg}} < 45°$. The RMS is shown with a vertical red line at the positive and negative value.

sponding to the RMS value on the positive and negative sides of a distribution are shown in Figure 6.5.

The metrics of FWHM and f for α and RMS for β represent the angular sensitivity of the reconstruction algorithm to the initial electron direction, the essential measurement for electron track Compton imaging. The performance of the reconstruction algorithm will be evaluated in terms of these metrics, first for modeled tracks and then for measured tracks.

6.2 Modeled algorithm performance

Due to the low statistics in the experiment, the algorithm's performance is best understood by first considering its response to modeled data. First, the performance on a device model with the same parameters as the CCD of Chapter 3 is presented. Then, the effects of changing the pixel pitch and noise of the modeled device are shown.

The results in this section use a common set of 1.1×10^6 modeled electron tracks. Of these, 8.6×10^5 tracks were contained in the volume of the CCD. A small fraction of tracks generate a fatal error in the algorithm (section 5.2.12). Only contained tracks without fatal errors are included in the analysis in this section.

6.2.1 Models of the experimental system

The FWHM and f for α, as a function of energy and $|\beta|$, are shown in Figure 6.6. Two basic trends are apparent. First, as the electron energy increases, the FWHM decreases and f increases. This means that the reconstruction algorithm is much more effective at higher energies, at which the extrapolated range is longer.

The second trend is the increasing FWHM and decreasing f as the projection angle $|\beta|$ increases. The CCD image is a projection of the electron trajectory, and so at a high angle of projection the initial track segment is compressed into a smaller projected length.

Figure 6.7 shows the RMS value of Δ_β as a function of energy and $|\beta|$. The trends are less clear than they are in the case of α. In particular, the RMS value's dependence on track energy is small, despite the change in extrapolated range. This behavior is not yet fully understood. A possible explanation involves the statistics of energy deposition near the beginning of the track. At higher energies, less energy is deposited on average, reducing charge carrier statistics, and variations in specific energy loss are larger relative to the expected value. This is one factor that can increase the RMS value at higher energies, despite the longer extrapolated range.

The RMS value is at a minimum for events with $20^\circ < |\beta| < 45^\circ$, over most of the energy range. The algorithm performs worse on larger $|\beta|$ events because the projected track segment is reduced, as is the case with α. However, at small $|\beta|$ angles, the larger RMS is due simply to the shape of the cosine function. Near $|\beta| = 0$, the cosine varies little with angle; this means that the projected energy deposition varies little with $|\beta|$. As a result, a small uncertainty in the energy deposition corresponds to a large uncertainty in $|\beta|$.

6.2.2 Pixel pitch study

The pixel pitch is an important parameter of the CCD. Pixel pitch, along with the lateral diffusion width, defines the position resolution of the device. However, all other CCD parameters being equal, the better position resolution comes at the cost of longer readout, larger image data, and more readout noise, all due to the increased number of pixels in the same area. It is informative to understand the angular sensitivity at different pixel pitches, in order to motivate the development or utilization of smaller or larger pixel pitch devices.

Modeled responses for devices with pixel pitch of 2.5 µm, 5 µm, 10.5 µm, 20 µm and 40 µm are evaluated here. See Figure 5.6 for an example track at different pixel pitches. The algorithm for trajectory measurement at different pixel pitches is essentially the same as the algorithm for 10.5 µm, with sampling intervals adjusted

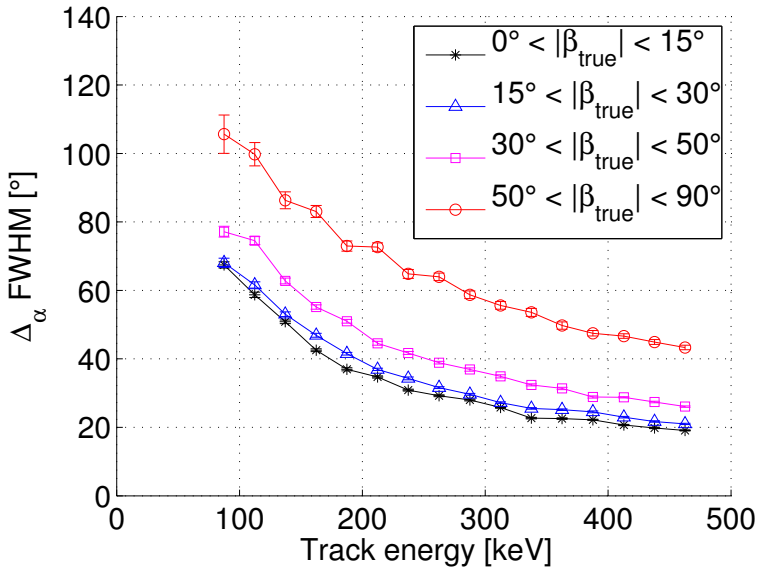

(a)

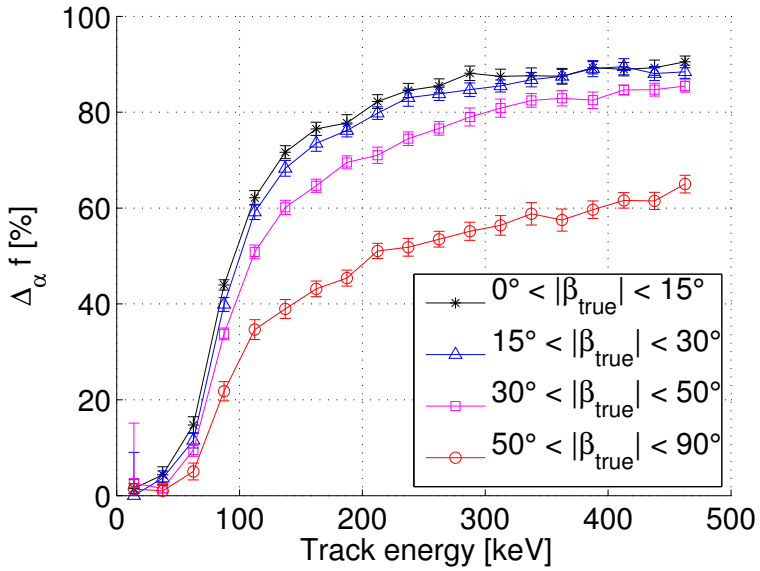

(b)

Figure 6.6: (a) The FWHM of the forward peak of the Δ_α distribution, as a function of electron energy and geometry. Data with error bars larger than 20° or with $f < 20\%$ have been removed, as these are not very meaningful. (b) The peak fraction, f, of the Δ_α distribution, as a function of electron energy and geometry. In both plots, error bars are smaller than data points except where shown.

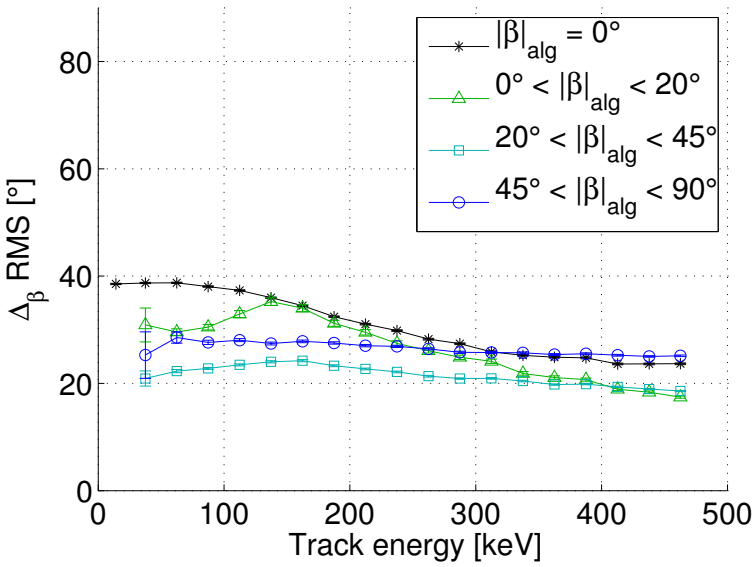

Figure 6.7: The RMS value of the Δ_β distribution, as a function of electron energy and measured geometry. The error bars are smaller than the data points.

(see section 5.2.10).

The small discrepancy between the modeled lateral charge diffusion and the more accurate approximations of repulsion and diffusion, discussed in section 4.2.3, will have more impact on the modeled CCDs with smaller pixel pitch. The effect of repulsion is to slightly reduce the spreading at track energies above 150 keV, and slightly increase it at lower track energies, compared to the diffusion-only model. The discrepancy is still small compared to the total width of charge spreading, but this inaccuracy should be kept in mind for the 2.5 µm and 5 µm results.

Readout noise has a larger impact in smaller pixel pitch devices, due to the smaller signal in each pixel and larger number of pixels. Therefore, in order to observe the impact of pixel pitch apart from noise, idealized device responses with no readout noise have been evaluated, in addition to device responses with a fixed value of 15 eV noise (1σ). The 15 eV noise corresponds approximately to the minimum readout noise measured in the experiments (see section 3.1.4).

Figure 6.8 shows the FWHM of the Δ_α forward peak as a function of energy for several pixel pitches and both with and without readout noise, and Figure 6.9 shows the peak fraction, f, similarly. In all cases, only tracks with $|\beta_{\text{true}}| < 45°$ have been selected, since the algorithm is generally less sensitive to tracks with larger $|\beta|$ angles. The modeled responses of smaller pixel pitches mostly have narrower peaks

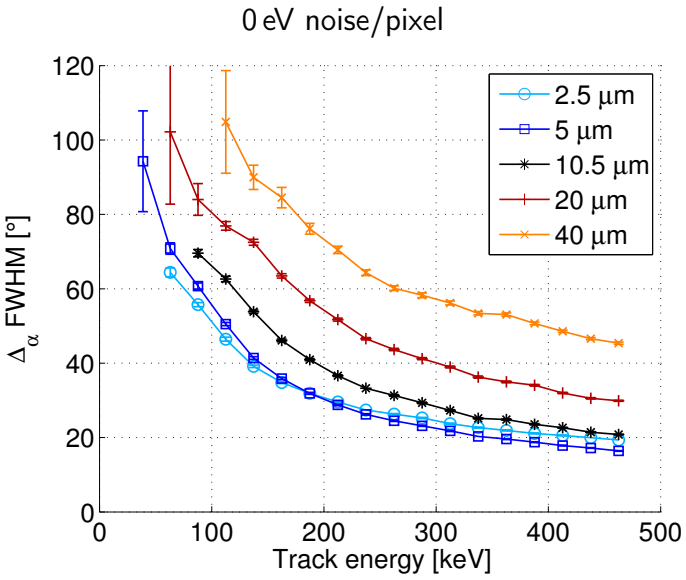

(a)

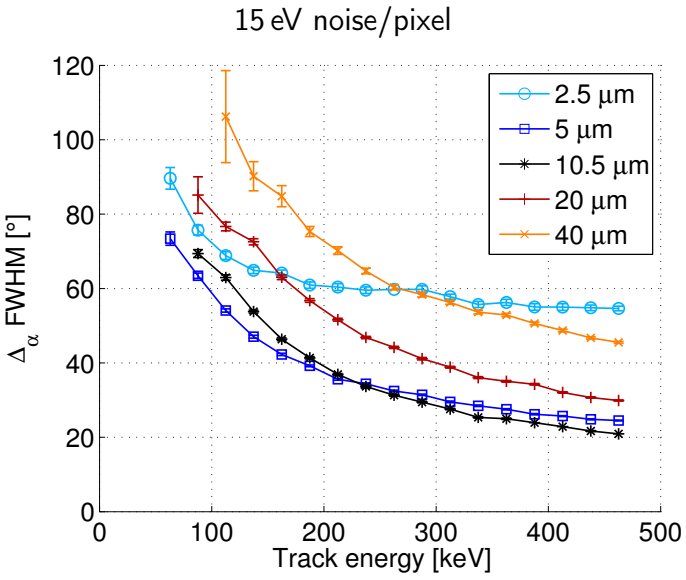

(b)

Figure 6.8: The FWHM of the Δ_α distribution as a function of energy and pixel pitch, for devices with (a) no readout noise, and (b) 15 eV readout noise (1σ, approximately the noise measured experimentally). Data with error bars larger than 20° or with $f < 20\%$ have been removed, as these are not very meaningful. Error bars are smaller than the data points except where shown.

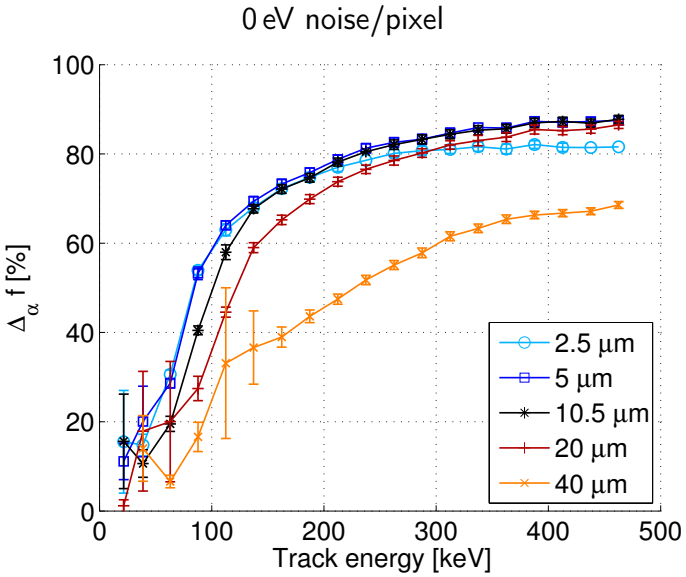

(a)

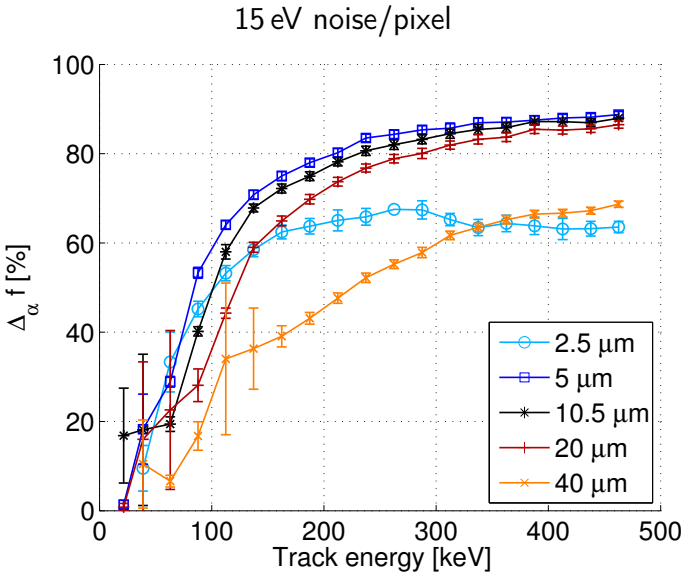

(b)

Figure 6.9: The peak fraction, f, of the Δ_α distribution as a function of energy and pixel pitch, for (a) no readout noise, and (b) 15 eV readout noise (1σ, approximately the noise measured experimentally). Data with error bars larger than 50% have been removed, as these are not meaningful. Error bars are smaller than the data points except where shown.

and larger peak fractions than larger pixel pitches at the same energy, due to the better position resolution. However, the signal-to-noise ratio is more important than position resolution for pixels smaller than about 10.5 µm with readout noise included. This is particularly evident at higher energies, for which the electron range is longer and the specific energy loss in the initial segment is smaller. The smallest pixel pitch (2.5 µm) surpasses the next larger only for tracks below 200 keV with no readout noise. Without readout noise the smaller pixel pitch should, in principle, perform no worse than larger pixel pitches, even if lateral diffusion of charge carriers limits the effective position resolution. The reduced sensitivity at 2.5 µm even without readout noise suggests that the algorithm is not performing optimally at this pixel pitch.

Figure 6.10 shows the RMS value of the Δ_β distribution in a similar manner as Figures 6.8 and 6.9. As discussed in section 6.2.1, the algorithm's calculation of $|\beta|$ is much less sensitive than the calculation of α, and the modeled response of devices with different pixel pitch reflects this. Devices with pixel pitch less than 10.5 µm are less sensitive to $|\beta|$, even with no readout noise. As with α, this points to suboptimal algorithm performance at small pixel pitch. The minimum between 50 and 75 keV is an artifact of the selection of $|\beta_{\mathsf{true}}| < 45°$, and represents a track energy where the measured energy deposition usually results in $|\beta|_{\mathsf{alg}} < 45°$ or $|\beta|_{\mathsf{alg}} = 0°$.

Overall, these results indicate that 10.5 µm pixel pitch is near optimal for this CCD and with this algorithm. This is not surprising, because the algorithm was optimized using 10.5 µm pixels. Nonetheless, a 5 µm CCD would perform better than 10.5 µm if the readout noise was low, and especially for tracks below about 200 keV.

6.2.3 Noise study

In the previous section, it was noted that 15 eV of readout noise has a significant impact for pixel pitches smaller than 10.5 µm. However, for any pixel pitch, the angular sensitivity will be degraded if the noise is large enough. Higher noise is particularly relevant for operation at higher temperatures than the current 138 K. In the experiment, readout noise magnitudes of 15 eV to 20 eV have been measured at this temperature. However, various specific noise sources make the dependence on temperature difficult to predict, although the noise can be expected to increase in approximately an exponential fashion as temperature is increased.

Only 10.5 µm pixel pitch devices have been modeled with different noise values. Noisy tracks at smaller pixel pitches are difficult to segment, because these tracks have a small signal-to-noise ratio and the segmentation algorithm is designed for tracks of only a few pixels wide. The angular sensitivity would then reflect the limitations of the segmentation algorithm rather than the limitations of the trajectory measurement.

The sensitivity of the α measurement to readout noise is shown in Figure 6.11.

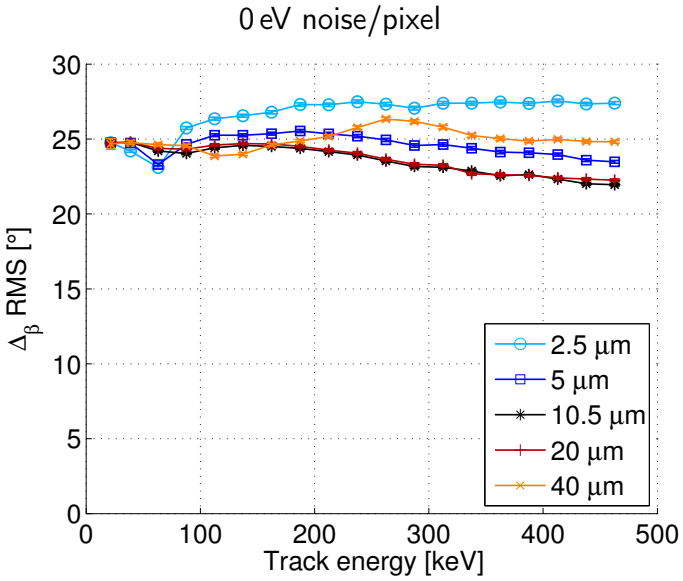

(a)

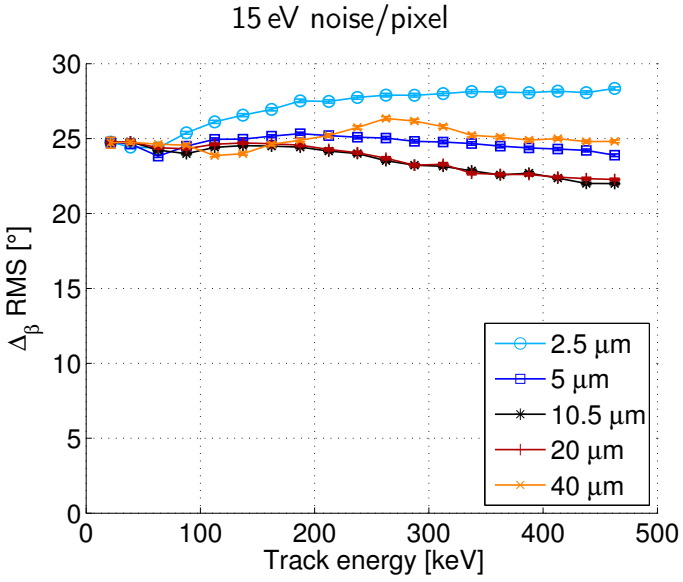

(b)

Figure 6.10: The RMS value of the Δ_β distribution as a function of energy and pixel pitch, for (a) no readout noise, and (b) 15 eV readout noise (1σ, approximately the noise measured experimentally). Error bars are smaller than the data points except where shown.

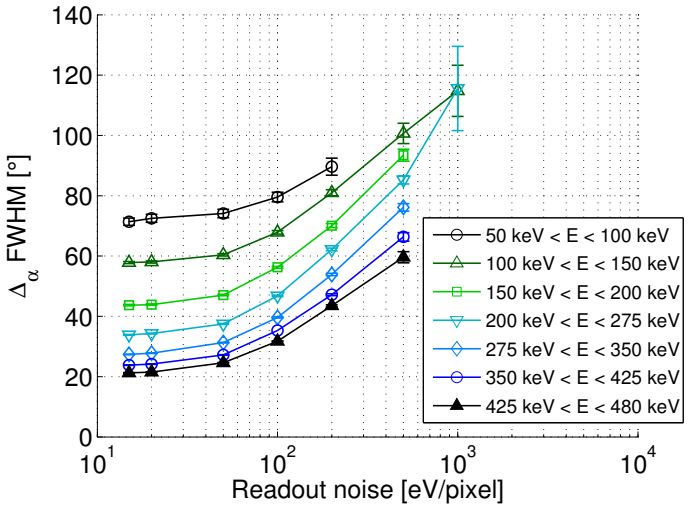

(a)

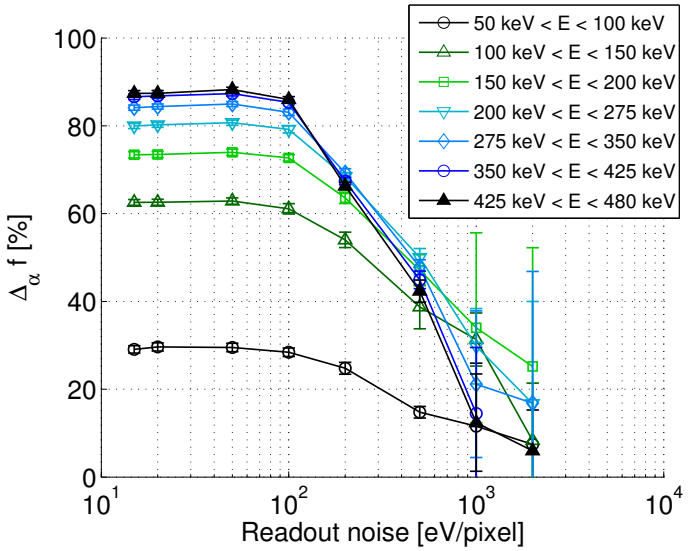

(b)

Figure 6.11: (a) The FWHM of the Δ_α distribution as a function of readout noise and electron energy. Data with error bars larger than 20° or with $f < 20\%$ have been removed, as these are not very meaningful. (b) The peak fraction, f, of the Δ_α distribution as a function of readout noise and electron energy. Data with error bars larger than 30° have been removed, as these are not very meaningful. In both figures, the error bars are smaller than the data points except where shown.

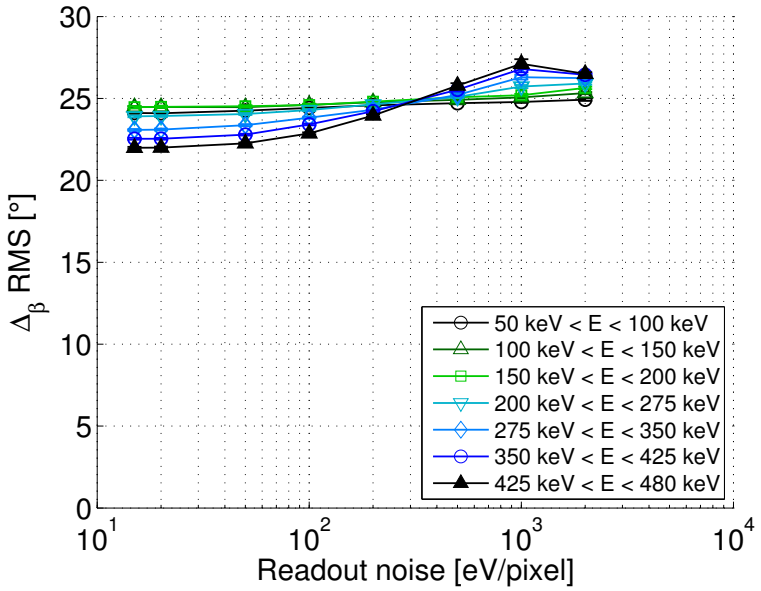

Figure 6.12: The RMS value of the Δ_β distribution as a function of readout noise and electron energy. Data representing fewer than 500 tracks have been removed, as these are not very meaningful. The error bars are smaller than the data points.

Only tracks with $|\beta_{\text{true}}| < 45°$ have been included. From 15 eV to 100 eV of noise, the α peak width begins to increase while the peak fraction remains almost constant, while above 100 eV both the peak width and peak fraction degrade until there is very little angular sensitivity at 1 keV of noise. The sensitivity for higher-energy tracks degrades more, proportionally, at a given value of noise than that of lower-energy tracks. This may be attributed to the smaller specific energy loss at higher electron energies, and therefore a lower signal-to-noise in the initial track segment.

Figure 6.12 shows the RMS value of the Δ_β distribution as a function of readout noise and energy. The limited β sensitivity is apparent, as the RMS value increases only slightly as noise is increased.

In conclusion, the electron trajectory measurement is relatively robust against increased readout noise. The peak width increases by a factor of 1.3 to 2 for noise an order of magnitude higher than found the present experimental measurements.

6.3 Results of the coincidence experiment

The coincidence experiment described in section 3.3 demonstrated electron track Compton imaging and provided a benchmark for the modeled results. In this section,

the measurements obtained by each detector individually are described, as well as the candidate coincident event sequences. Then, in section 6.4, the algorithm response to the modeled events will be compared to that of the experiment.

The experiment was operational for 104 days, from October 2010 to January 2011. During that period, there were 1.73×10^6 open shutter intervals of 0.272 s each, corresponding to 5.4 days of open shutter time, or one shutter every 5.2 seconds.

6.3.1 CCD response

As discussed in section 3.3.6, interactions in the CCD are dominated by beam interactions. The energy spectrum of all segmented events is shown in Figure 6.13. The spectrum is dominated by the Compton continuum, and a small full-energy peak is visible.

Compared to the main Compton continuum of interactions, the full-energy peak contains a factor of 4 fewer events than calculated by the photoelectric absorption cross section. This is not surprising, since electrons with 662 keV of kinetic energy have an extrapolated range in silicon of 941 µm [115, 116], and most of them will escape from the sensitive volume of the CCD before depositing their entire kinetic energy. Multiple scattering of a single incident photon will contribute to the peak only if the tracks are overlapping, an unlikely occurrence.

The other events above and below the photopeak are a combination of laboratory background radiation interactions, overlapping tracks from Compton scattering of one or more beam photons, and incompletely contained electrons from photoabsorption of beam photons.

Figure 6.14 shows the sum of energy deposition in each pixel of the CCD, from all segmented tracks in the coincidence experiment. Only part of one quadrant is shown; the other quadrant that the beam passed through was not operational. Since electron tracks are short compared to the beam width, this map of energy deposition approximates the flux of gamma rays in the CCD, which is almost entirely due to the collimated beam. The flux is roughly an ellipse which is elongated in the x direction, due to the shallow angle between the beam and the face of the CCD (see Figure 3.11a). Although the center of the ellipse is in the operational quadrant, significant areas of the beam are not incident on the sensitive volume of this quadrant.

The track energy distribution, dominated by the Compton continuum from the 662 keV gamma ray, and the elliptical spatial distribution of tracks indicate that the CCD is operating properly overall, and demonstrate that the interactions in the CCD are dominated by interactions of the beam of collimated photons.

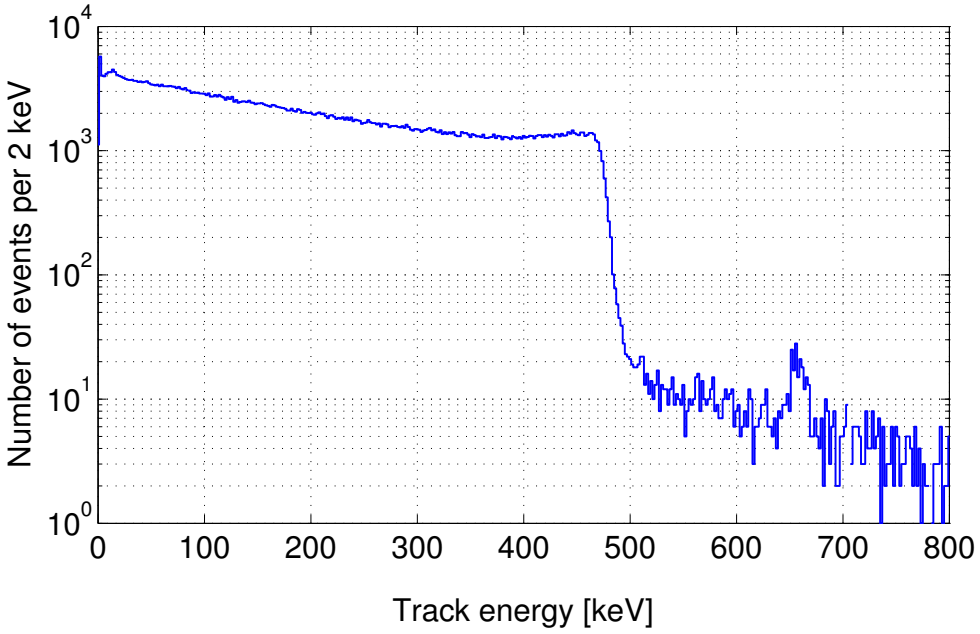

Figure 6.13: The energy spectrum of the CCD over the course of the coincidence experiment, consisting of 503 455 tracks.

6.3.2 HPGe response

The HPGe double-sided strip detector, Ge2, detected mostly background radiation due to the very low geometric efficiency for scattering. The energy spectrum of Ge2 from all of the open shutter time is shown in Figure 6.15.

Features visible in this spectrum include x-rays from the lead shielding (70 keV to 80 keV); annihilation radiation from natural positron emitters (511 keV); the Compton edge and full-energy peak of ^{40}K (1240 keV and 1461 keV, respectively); the Compton edge and full-energy peak of ^{208}Tl (2382 keV and 2615 keV, respectively); and the double-escape peak from pair production of the ^{208}Tl gamma ray (1593 keV).

In Figure 6.16, the distribution of positions of all interactions in Ge2 in the x–y plane is shown. The "rounded square" shape of the active area of germanium is visible, with several vertical gaps due to inoperable strips (see section 3.3.3). The bright spots represent interactions that trigger only one strip on each side, which are the majority of interactions. In between these are interactions from which charge is shared between two strips, on one or both sides of the detector. (As a reminder, the strip pitch is 2 mm.) Statistically significant variations in counts correspond to some combination of background radiation flux variations and defects affecting the electric field, charge transport, or signal readout.

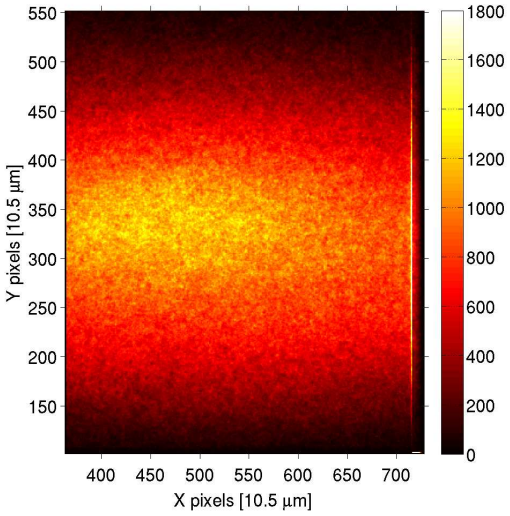

Figure 6.14: Summed image of all of the electron tracks measured in the CCD over the course of the experiment. The area shown is about 5.8 mm × 3.8 mm. The color axis is in keV of total deposited energy per pixel. The bright line near the right edge is an artifact of the device.

The energy spectrum and roughly uniform distribution of positions indicate that the interactions in Ge2 are dominated by background radiation, as expected. The signal of true coincident event sequences in the germanium strip detector is too small to measure directly in the energy spectrum or position map.

6.3.3 Coincidence candidate event sequences

As described in section 5.3.2, events in Ge2 during the same shutter period as tracks in the CCD were candidates for a coincidence sequence if the deposited energies were in the appropriate range. Over the length of the experiment, a total of 10 220 event sequences were candidates for coincidence. The distribution of these sequences in angular resolution measure (ARM) and total energy is shown in Figure 6.17. The concept of this distribution plot was introduced with Figure 5.22. As a reminder, the ARM is defined as

$$\text{ARM} = \Delta\theta = \theta_{\text{geometric}} - \theta_{\text{Compton}}. \tag{6.3}$$

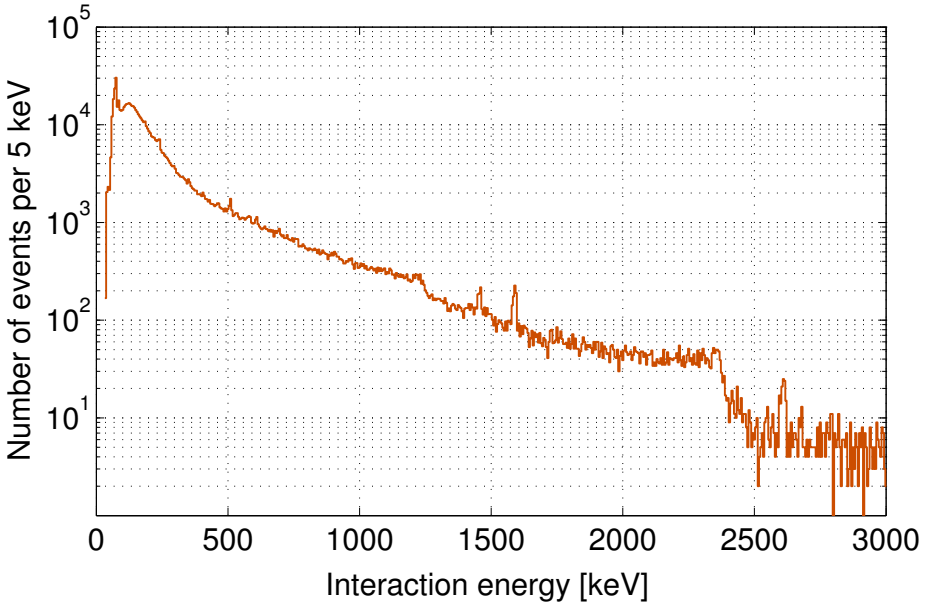

Figure 6.15: The energy spectrum of interactions in the HPGe double-sided strip detector, over the course of the coincidence experiment, showing the background radiation from the laboratory.

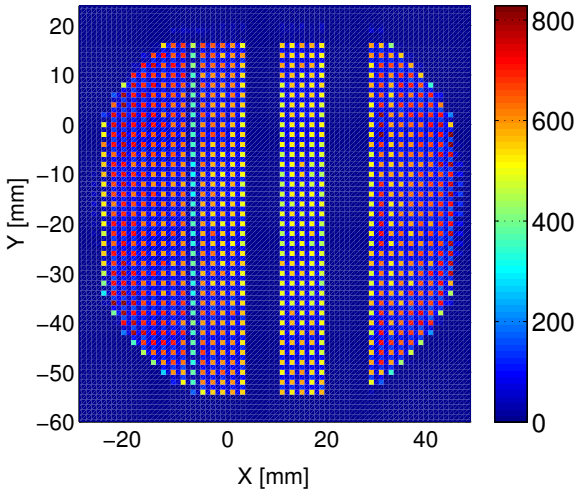

Figure 6.16: Distribution of positions of all interactions in Ge2. The color axis shows the number of counts in each position bin. Each bin is 1 mm^2, and vertical gaps correspond to inoperable electrodes.

The true coincident event sequences appear as a cluster and are expected to be centered at $E_{\text{tot}} = 661.7\,\text{keV}$ and ARM $= 0°$ (see section 5.3.3). A fit with a two-dimensional Gaussian function results in a centroid of $E_{\text{tot}} = 659.1 \pm 0.3\,\text{keV}$ and ARM $= -0.52 \pm 0.09°$.

The offset in E_{tot} may be a result of an imperfect energy calibration, or a nonlinear response of the CCD segmentation algorithm. The latter is plausible because higher-energy electron tracks have a significantly lower average specific energy loss than the tracks of 356 keV and below used to calibrate the CCD, and so the signal-to-noise ratio in the pixels is lower and a larger fraction of the charge carriers may be lost under the segmentation threshold. The ARM offset of $-0.52 \pm 0.09\,\text{keV}$ is due to an imperfect position calibration.

The FWHM of the cluster is $7.6 \pm 0.8\,\text{keV}$ in energy and $2.3 \pm 0.3°$ in ARM. The cluster contains 87 events within an ellipse with major and minor axes equal to the FWHMs (indicated in Figure 6.17b). These 87 sequences are further analyzed with the reconstruction algorithm. They include an estimated 13 sequences that are false coincidences with a correct ARM and E_{tot} only by chance, resulting in an estimated SBR of 5.7.

Because the active volume of Ge2 covers a small solid angle for scattering from the CCD, the scattering energy and initial direction of the electron are limited by kinematics. Figure 6.18 shows the distribution of the scatter energy in the CCD for the 87 event sequences in the true coincidence FWHM. The scattering energy closely corresponds to the calculated β of an electron, which is shown on the top of the figure. The uneven distribution arises from a combination of poor statistics and the inactive electrodes in Ge2. The left side of Figure 6.18 corresponds to the interactions of photons scattering toward the right side of Ge2 in Figure 6.16.

The 87 event sequences in the true coincidence FWHM each provide one CCD electron track with initial trajectory known to within 3° FWHM. These tracks can be used to perform electron track Compton imaging, as well as to evaluate the angular sensitivity of the reconstruction algorithm.

6.3.4 Algorithm performance on tracks from event sequences in the true coincidence FWHM

Since the number of useful events is small, no energy or $|\beta|$ binning is performed.

In Figure 6.19, the distributions of α_{alg} and $|\beta|_{\text{alg}}$ are compared to the distributions calculated by geometry. The expected 13 false coincident event sequences may explain some of the points measured with $\alpha > 180°$.

The comparison shows some agreement between the event sequence calculation and the algorithm reconstruction of α. However, the coincidence measurement allows

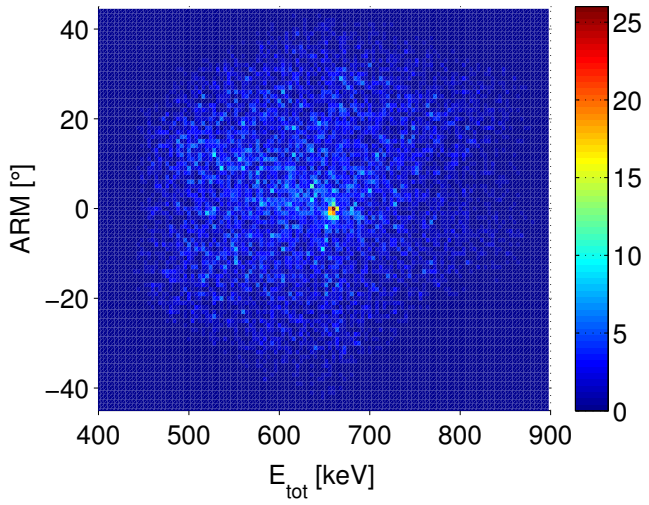

(a)

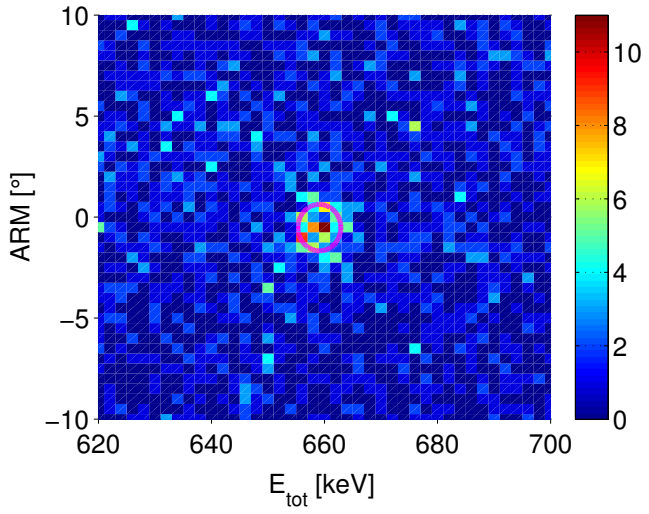

(b)

Figure 6.17: The distribution of coincidence candidate event sequences, in angular resolution measure (ARM) and total energy deposited (E_{tot}). (a) Full view. Each bin is 1° by 4 keV. (b) Expanded view of the true coincidence area. Each bin is 0.5° by 2 keV. The FWHM ellipse is indicated in magenta. In both cases, the color axis represents the number of event sequences in each bin.

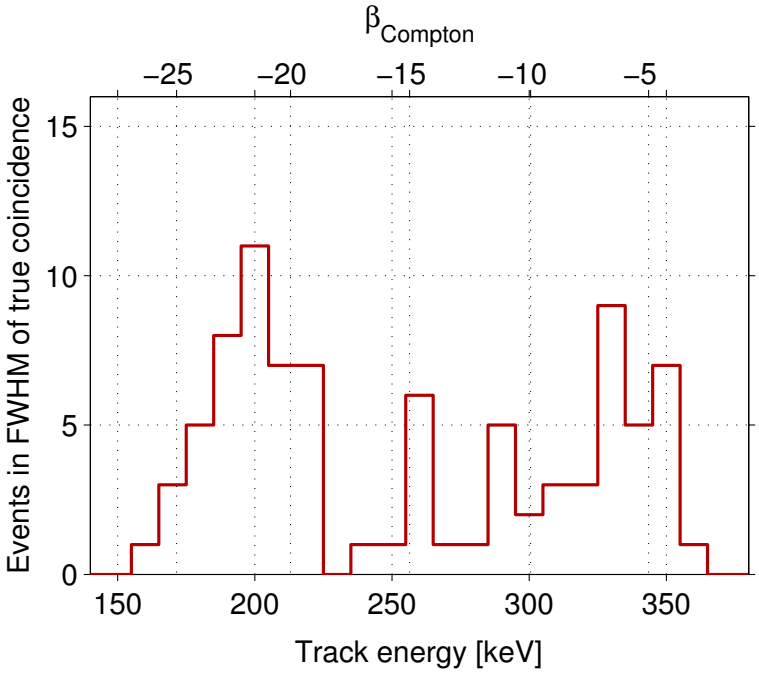

Figure 6.18: Distribution of energy deposited in the CCD for events in the FWHM of the true coincidence feature. The β angle is correlated with scattering energy. Bins are 10 keV wide.

the tracks to be considered individually, using the Δ_α and Δ_β metrics. The distributions of Δ_α and Δ_β are shown in Figure 6.20. The FWHM of the Δ_α distribution is 23.0 $\pm$ 1.6°, with a forward peak fraction of 71 $\pm$ 9%. The RMS of the Δ_β distribution is 21.4 $\pm$ 1.6°.

This is the first measurement of electron tracks with a known initial direction using this device and reconstruction algorithm. Next, this measurement will be compared to the reconstruction of modeled tracks.

6.4 Comparison between modeled and measured angular error distributions

As discussed in section 4.3, a set of modeled tracks is selected with characteristics closely approximating those of the measured tracks. There are 69 modeled tracks for each of the 87 measured tracks, for a total of 6003 modeled tracks used for comparison. Each modeled track within a subset of 69 is selected so that it has

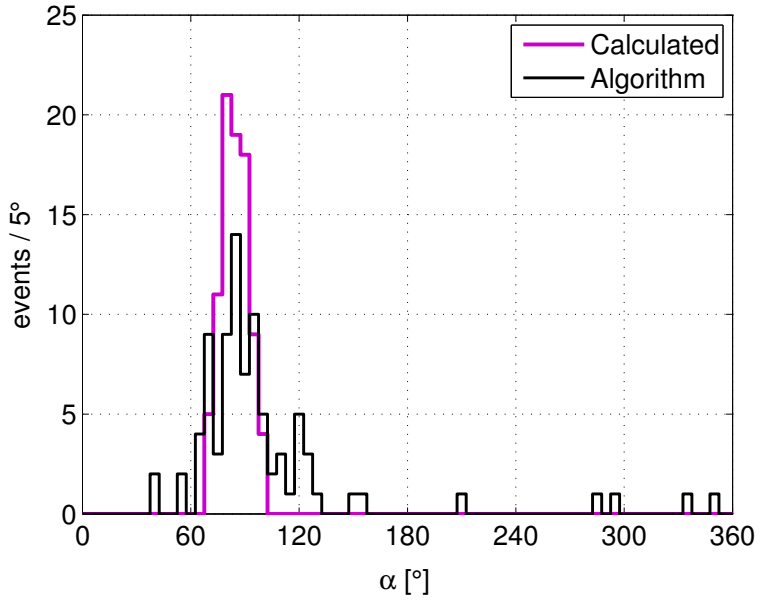

(a)

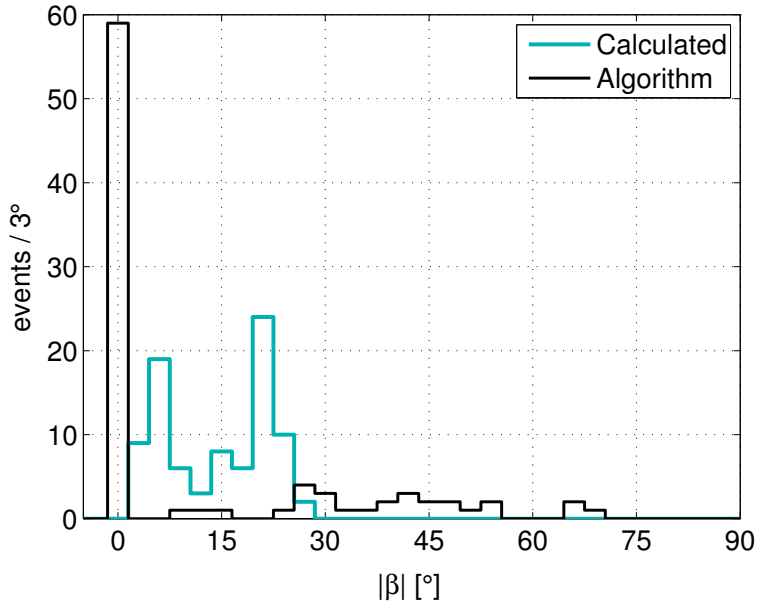

(b)

Figure 6.19: The distributions of (a) α and (b) $|\beta|$ for the 87 measured events in the true coincidence FWHM, including the values calculated by the photon kinematics and the values measured by the algorithm.

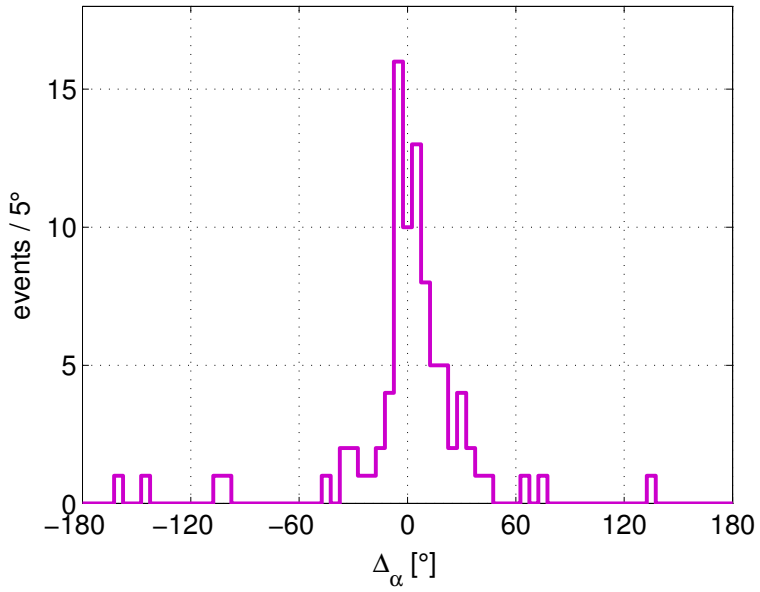

(a)

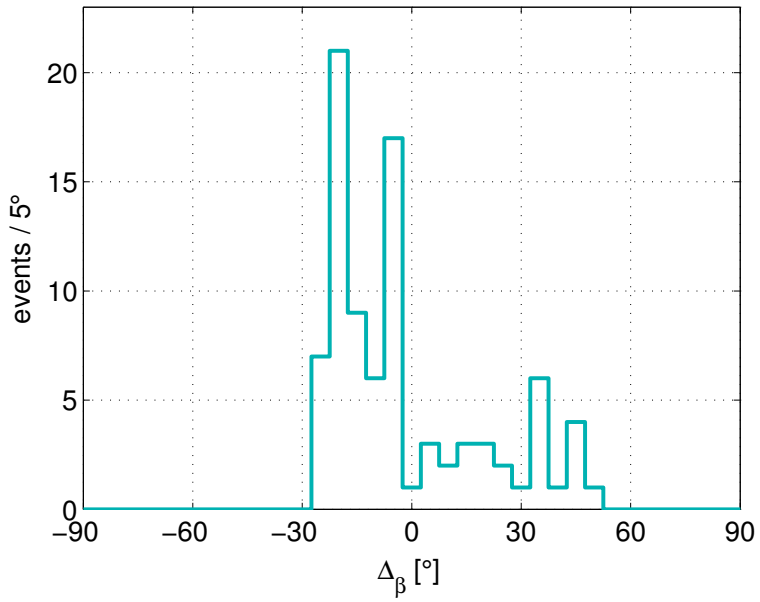

(b)

Figure 6.20: Distributions of angular error in (a) α and (b) $|\beta|$, for the 87 measured tracks from event sequences in the true coincidence FWHM.

energy within 2.5 keV and $|\beta|$ within 2° of the corresponding measured track. The reconstruction algorithm is performed on the modeled tracks, and the distributions of $\Delta_{\alpha,\beta}$ are compared to those in Figure 6.20.

Figure 6.21 shows modeled and measured distributions of Δ_α and Δ_β, with the number of modeled tracks reduced by a factor of 69 to normalize to the measured tracks. It is evident by visual inspection of Figure 6.21 that the modeled distributions agree very well with the measured distributions.

The modeled Δ_α distribution has a FWHM of 25.3 ± 0.3° and a peak fraction f of 78.9 ± 2.2%, and the modeled Δ_β distribution has an RMS value of 26.28 ± 0.24°. However, the RMS value for β cannot be compared directly to the values presented in section 6.2.1, because the values in section 6.2.1 are computed for a specific selection of $|\beta|_{\text{alg}}$, while the value given here is for all $|\beta|_{\text{alg}}$ over the range of $|\beta|_{\text{geometric}}$. This results in a different shape of distribution (compare Figure 6.21b with Figure 6.4b).

In addition to the similar appearance of the distributions, a quantitative comparison can be made to evaluate the agreement. The likelihood, $\mathcal{L}$, can be computed for the Δ_α distribution and for the Δ_β distribution, using the modeled result as the expected value in each bin, and using Poisson statistics in each bin. The likelihood for the α distribution is

$$\mathcal{L}_\alpha = \prod_i \frac{\left({E_{\alpha,i}}^{O_{\alpha,i}}\right) e^{-E_{\alpha,i}}}{O_{\alpha,i}!}. \tag{6.4}$$

Here, i denotes the index of each bin in the distribution, E_i the expected value of that bin from the modeled data, and O_i the measured counts in that bin. The β distribution can be computed similarly.

The likelihood value, or the natural logarithm of the likelihood which is more convenient, can be compared with the distribution of possible likelihoods. The distribution of possible likelihoods is computed with a Monte Carlo sampling of Poisson probability distributions in each bin, with the assumption that the modeled distribution of Δ_α represents the true probability distribution of Δ_α. The distribution of log-likelihood for 2×10^5 Monte Carlo sampled Δ_α and Δ_β distributions is shown in Figure 6.22, with the log-likelihood of the actual measurements displayed as vertical dashed lines.

If the modeled Δ_α distribution is correct, the measured likelihood is essentially sampled from the distribution of possible likelihoods, and one would expect it to fall roughly near the middle of the distribution. This test can be represented by the probability of measuring a lower likelihood than what has been measured, given that the model is correct. This probability is known as the p-value. The p-values for the

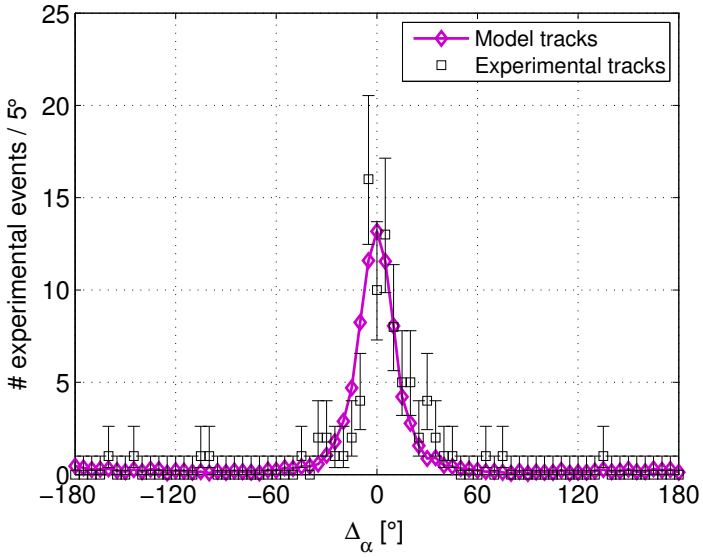

(a)

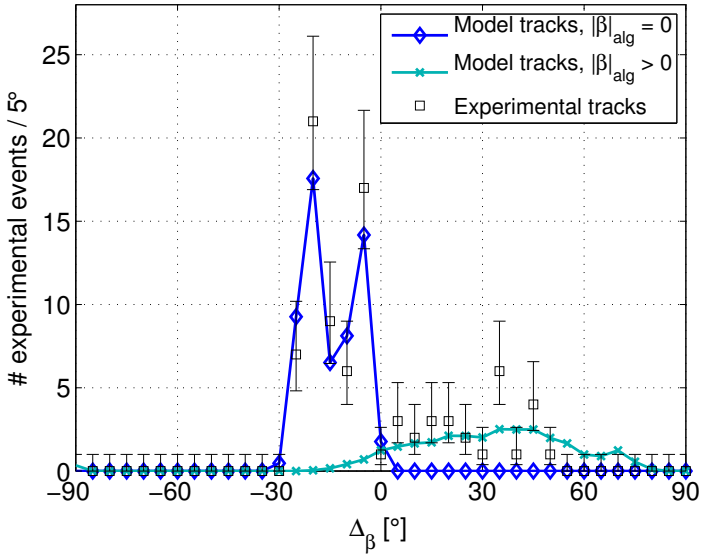

(b)

Figure 6.21: Distributions of (a) Δ_α and (b) Δ_β, for both the experimental tracks (events in the FWHM of the true coincidence feature) and modeled tracks. The modeled result has been normalized in the vertical coordinate, and uncertainties are smaller than the data points. The modeled distribution in (b) has been separated into components based on the measurement of $|\beta|_{\text{alg}}$. As discussed previously, the peaks in Δ_β correspond to the active regions of Ge2.

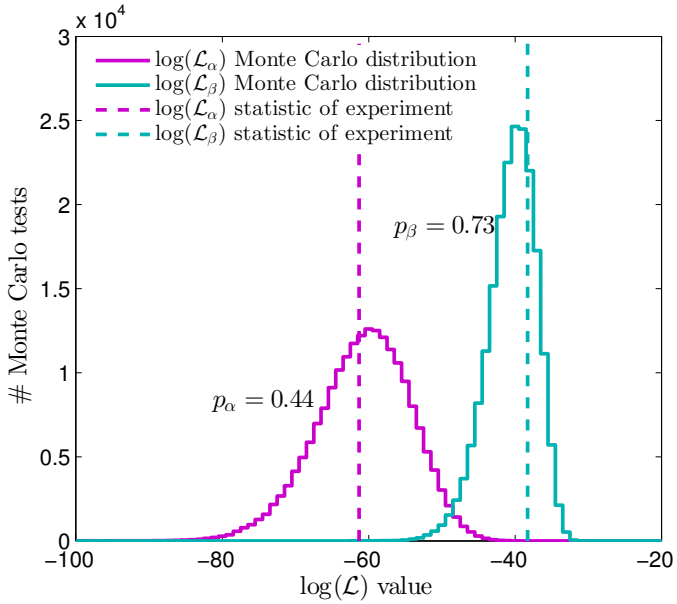

Figure 6.22: The $\log(\mathcal{L})$ for distributions of Δ_α and Δ_β (Figure 6.21), from 2×10^5 Monte Carlo distributions based on the model result, and from the experiment.

measured Δ_α and Δ_β distributions are

$$p_\alpha = 0.4429 \pm 0.0011 \tag{6.5}$$

$$p_\beta = 0.7311 \pm 0.0010. \tag{6.6}$$

Since $p > 0.05$, the measured $\Delta_{\alpha,\beta}$ distributions are consistent with the models [14].

The comparison of measured and modeled angular sensitivity is limited by the statistics in the experiment, and differences may exist. However, the moderate p-values imply that the differences between models and experiment cannot be very great for the range of energy and β sampled.

6.5 Summary

The angular sensitivity for tracks in a modeled CCD, as described by FWHM, peak fraction, and RMS, was seen to vary based on track energy, $|\beta|$, pixel pitch, and noise. For a modeled device based on the CCD used in experiments, a FWHM in α of 40° or better and a peak fraction of 70% or better are achieved for most tracks above 200 keV. The measurement of $|\beta|$ is less precise, and the RMS values near 30° represent low sensitivity.

The coincidence experiment produced 87 events in the FWHM of the gamma-ray scattering angle and total energy. These events include electron tracks with the initial trajectory known to within 3° FWHM, assuming the interactions measured in both detectors are due to the single scattering of one gamma ray. These coincidence tracks cover an energy range from 160 keV to 360 keV and a β range from $-30°$ to 0°. The angular sensitivity of these tracks shows very good agreement with an equivalent distribution of modeled tracks, both by visual inspection as well as by likelihood p-values of 0.44 and 0.73. Therefore, the algorithm outcome of modeled tracks matches that of measured tracks over this range.

Chapter 7

Conclusions

The work presented in the previous chapters represents a significant advancement in electron track Compton imaging, with the potential to enable new compact gamma-ray imaging systems that are more sensitive in the detection and localization of weak sources for applications in astronomy, security, accident mitigation, and other fields. In this closing chapter, the highlights of the work will be reviewed, the potential impact discussed, and the next steps considered.

7.1 Summary and highlights

Electron track Compton imaging has the potential for greater sensitivity to weak sources than other methods of imaging. Specifically, for each reconstructed photon sequence, the origin of the photon is restricted to a cone segment. However, this sensitivity requires fine position resolution capable of discerning the initial direction of the Compton-scattered electron, with the sensitivity gain dependent on the angular sensitivity to the initial electron direction. The initial electron direction is challenging to measure in solid-state detectors because of the limited range and tortuous path of the electron. Therefore, very fine position resolution of 100 µm or less is required.

The silicon charge-coupled device (CCD) designed for the SNAP infrared astronomy camera has 10.5 µm position resolution in two dimensions, 650 µm of sensitive thickness, and excellent energy resolution, making it suitable for measuring initial electron trajectories accurately. The limited effective area and time resolution of the CCD can be overcome, as discussed below in section 7.3.1. The SNAP CCD was set up and operated for the first time in the Berkeley Applied Research on the Imaging of Neutrons and Gamma rays (BeARING) laboratory, measuring images of electron tracks from the interactions of gamma-rays.

In parallel with the experiment, electron tracks were modeled using Geant4 physics for photon and electron interactions, and a MATLAB code for the charge carrier drift and diffusion. The Geant4 model was benchmarked using electron extrapolated range, and the MATLAB transport code was benchmarked using the width of muon tracks in the CCD. The models generate the same type of pixelized track images as the experiment, except that the models are already calibrated for energy. For both models and measurements, the tracks are segmented individually from the image and then a direction reconstruction algorithm is performed upon the track image in order to deduce the initial direction in three dimensions (angles α in the pixel plane, and β out of the pixel plane). The algorithm operates by first identifying the location of the initial segment of the track, and then measuring points along a ridge of maximum energy. The positions of the points provide α, and the measured energy loss provides the magnitude of β by comparison with the expected specific energy loss. This reconstruction algorithm achieved a FWHM in α of 40° or better for most tracks above 200 keV, and 20° at energies above 400 keV and parallel to the pixel plane. The measurement of β shows some limited sensitivity at all energies above 100 keV. The angular sensitivities of 20° to 40°, and even 70° at 100 keV, are a tremendous improvement over the 360° cone of conventional Compton imaging.

Models of CCDs with different pixel pitches indicate that smaller pixel pitch devices may improve the angular sensitivity for low-energy electron tracks, but suffer more from the same value of pixel noise due to the larger number of pixels. Larger pixel-pitch devices are less sensitive due to their poorer position resolution. Devices with 10.5 µm pixel pitch but various values of noise were modeled, and the results indicated that the angular sensitivity is only slightly degraded from 15 eV up to 100 eV per pixel, suggesting that the CCD could remain effective when warmer than the current operating temperature of 138 K.

The main experiment involved measuring interactions of photons from a collimated gamma-ray source in the CCD, in coincidence with a germanium double-sided strip detector. This experiment allows the measurement of electron tracks with the actual electron direction known from the photon kinematics to 3° FWHM. The long readout time in the CCD was a challenge, requiring short shutter times, heavy shielding, and careful event selection in order to measure true coincident event sequences. A total of 87 electron tracks were measured with well-known initial trajectories, which could be measured with the algorithm in order to evaluate the algorithm's angular sensitivity. The measured coincident event sequences were found to have a FWHM in α of 23°, in excellent agreement with the angular sensitivity calculated using modeled tracks similar to the measured tracks. The agreement was demonstrated quantitatively by the likelihood p-values of 0.44 and 0.73 for the α and β error distributions, respectively. These p-values are near to the expected average of 0.5, indicating that

the model is consistent with the experiment.

7.2 Potential impact

For the first time, electrons of energy as low as 160 keV have been successfully tracked in a solid detection material for gamma-ray imaging, with potential sensitivity below 100 keV according to models. This provides the fundamental capability for electron track Compton imaging into the energy range of many gamma-ray sources around 500 keV, with potential applications in many fields described in Chapter 1.

The CCD may not be the optimal detector for electron track Compton imaging in a solid-state device, due to the complex readout, difficulty of achieving good time resolution, and small effective area per device. However, if other electron-tracking devices are made of silicon, the modeled performance for different pixel pitch CCDs in this work may give an indication of the angular sensitivity that could be expected, depending on the position resolution of the other device. Some analysis of the impact of electron tracking on the resulting gamma-ray image has already been performed [31].

Additionally, the models used have shown good agreement with the experiment. This agreement lends a certain amount of confidence to additional results using the same model, presented here and in the future.

7.3 Future work

The goal of this work was the conceptual demonstration of electron track measurements in silicon CCDs. There is much more to be done to further evaluate electron tracking in CCDs and to consider its potential for a practical gamma-ray imaging system.

7.3.1 Device development

As discussed in section 2.3.9, the CCD falls short of the requirements of time resolution and effective area. The small effective area may be mitigated by a detector system that includes a number of CCDs. Additionally, larger and thicker devices can likely be fabricated to improve the efficiency.

The more fundamental problem with these CCDs is the slow readout of pixels necessary to maintain good energy resolution, which limits the pulse-pair time resolution to at least the readout time. The CCD used in this work takes 2.8 s to readout,

and larger CCDs require even longer. The poor time resolution inhibits a Compton imaging system from correctly matching gamma-ray interactions from the same photon sequence and rejecting interactions from a different photon sequence. In the coincidence experiment in this work, this limitation was only overcome by extensive shielding, careful event selection using the knowledge of the incident photon beam direction, and short shutter times.

One solution would be to measure the time of interaction using an electrode on the back side of the CCD, without changing the speed of the pixel readout. New CCDs with strip electrodes on the back side have been fabricated and are currently being tested [102]. This would allow the time of interaction to be measured on the strip electrode using the electron signal, and then matched to a track in the CCD image using the position of the strip and the pulse height of the strip signal.

Without good time resolution, another novel method of gamma-ray imaging may be performed instead using the electron tracks alone, without the need for coincidence. This method utilizes an analytical formula to convert the distribution of measured electron tracks, in energy and direction space, to the distribution of incident gamma rays, in energy and direction [54].

7.3.2 Experiments

The coincidence experiment measured 87 electron tracks, each with an initial direction known to 3° FWHM, providing an experimental evaluation of the angular sensitivity of the direction reconstruction algorithm, and confirming the angular sensitivity predicted by models. However, the small number of true coincident event sequences limit the ability to discern differences between experiment and model. For a more sensitive benchmark of the model's accuracy in the same energy range as this experiment, more electron tracks with well-known initial trajectories must be measured. Data could be gathered more quickly using a stronger gamma-ray source, or a larger geometric efficiency for detecting the scattered photon.

In addition, other energy ranges and geometries in the detector could be explored to further validate the models.

One factor that remains to be explored is the impact of electron tracks escaping the sensitive volume of the CCD. In an instrument with multiple layers of CCDs, such escape events might be reconstructed by combining the information from the neighboring CCDs.

7.3.3 Models

As discussed in section 4.2, the model used for charge transport included the average effects of repulsion as a component of diffusion. This is not quite accurate, since repulsion varies with charge density, and contributes to a slightly different shape of the charge distribution.

A better model would include these unique effects of repulsion. The greater accuracy would likely come at the expense of computation time, because a charge-density-dependent model would require much greater complexity than the current model.

7.3.4 Algorithm development

The reduction of background in electron track Compton imaging over conventional Compton imaging depends on the sensitivity to the initial direction of the electron. The reconstruction algorithm described in section 5.2 has achieved FWHM between 20° and 40° in α for most electrons above 200 keV, but this algorithm is by no means optimal. Several methods and parameters within the algorithm could be optimized, or an entirely different algorithm could prove to be more sensitive to the initial electron direction.

The measurement of the β angle (the track's angle of elevation above or below the pixel plane) is not very sensitive (section 6.2.1). Future work could determine the physical limit based on the fluctuations in specific energy loss (section 2.2.8), and find the optimal length of track segment over which to measure the specific energy loss. Also, the length of track segment over which to measure the electron trajectory for determining α could be optimized more precisely.

7.3.5 Imaging

This work has focused on measuring the initial electron direction, which is fundamental to electron track Compton imaging. The generation of a gamma-ray image through cone segment backprojection or other techniques will reveal the exact impact of features in the algorithm's angular sensitivity.

The non-coincident imaging method mentioned above is still in development and has not yet been evaluated or tested extensively.

7.3.6 System design and engineering

The coincidence experiment in this work has proven the basic concept of electron track Compton imaging with a CCD, but was limited by the poor time resolution and

low efficiency. A useful instrument would not only require much better time resolution in the CCD, but a number of CCDs arranged in close proximity to an absorber detector in order to maximize the efficiency for useful photon sequences, with a minimum of passive material in between detection elements. For the instrument to be compact and portable, the electronics for controlling and reading out the CCD would have to be greatly reduced.

The engineering of such a CCD-based electron track Compton imaging instrument, if feasible, is still some years in the future. However, it is clear that such an instrument has the potential for very precise measurement of gamma rays even with energy below 1 MeV.

Bibliography

[1] S. Agostinelli, J. Allison, K. Amako, J. Apostolakis, H. Araujo, et al. "Geant4 — a simulation toolkit". In: *Nucl. Instruments Methods Phys. Res. Sect. A* 506.3 (2003), pp. 250–303.

[2] J. Allison, K. Amako, J. Apostolakis, H. Araujo, P. Arce Dubois, et al. "Geant4 developments and applications". In: *IEEE Trans. Nucl. Sci.* 53.1 (2006), pp. 270–278.

[3] K. Amako, S. Guatelli, V. N. Ivanchenko, M. Maire, B. Mascialino, et al. "Comparison of Geant4 Electromagnetic Physics Models Against the NIST Reference Data". In: *IEEE Trans. Nucl. Sci.* 52.4 (2005), pp. 910–918.

[4] H. O. Anger. "Scintillation Camera with Multichannel Collimators". In: *J. Nucl. Med.* 5 (1964), pp. 515–531.

[5] E. Aprile, A. Curioni, V. Egorov, K.-L. Giboni, U. G. Oberlack, et al. "Spectroscopy and imaging performance of the liquid xenon gamma-ray imaging telescope (LXeGRIT)". In: *Proc. SPIE* 4140 (2000), pp. 333–343.

[6] P. von Ballmoos, H. Halloin, J. Paul, N. Abrosimov, K. Andersen, et al. "The MAX mission: focusing on high sensitivity gamma-ray spectroscopy". In: *5th INTEGRAL Sci. Work.* Munich, 2004, pp. 747–750.

[7] M. Bandstra, J. D. Bowen, A. Zoglauer, S. E. Boggs, W. Coburn, C. B. Wunderer, M. Amman, and P. N. Luke. "Position Calibrations and Preliminary Angular Resolution of the Prototype Nuclear Compton Telescope". In: *2006 IEEE Nucl. Sci. Symp. Conf. Rec.* Vol. 2. IEEE, 2006, pp. 770–777.

[8] M. Bandstra, K. Vetter, D. H. Chivers, T. Aucott, C. Bates, et al. "Measurements of Fukushima fallout by the Berkeley Radiological Air and Water Monitoring project". In: *2011 IEEE Nucl. Sci. Symp. Conf. Rec.* Department of Nuclear Engineering, University of California, Berkeley, 94720 USA. IEEE, 2011, pp. 18–24.

[9] G. Batignani, L. Bosisio, E. Focardi, F. Forti, M. A. Giorgi, G. Tonelli, and G. Triggiani. "Development of double side readout silicon strip detectors". In: *Nucl. Instruments Methods Phys. Res. Sect. A* 273.2 (1988), pp. 677–681.

[10] C. J. Bebek. "The SNAP space mission". In: *Nucl. Instruments Methods Phys. Res. Sect. A* 579.2 (2007), pp. 848–852.

[11] C. J. Bebek, D. E. Groom, S. E. Holland, A. Karcher, W. F. Kolbe, et al. "Development of fully depleted back-illuminated charge-coupled devices". In: *Proc. SPIE* 5499 (2004), pp. 140–150.

[12] P. Bell and J. Cassidy. "Measurement of the Gamma-Ray Energy of K^{40}". In: *Phys. Rev.* 79.1 (1950), pp. 173–174.

[13] M. J. Berger, J. H. Hubbell, S. M. Seltzer, J. Chang, J. S. Coursey, R. Sukumar, D. S. Zucker, and K. Olsen. *NIST XCOM: Photon Cross Sections Database*. `http://www.nist.gov/pml/data/xcom/index.cfm`. Accessed: 2013-11-18. National Institute of Standards and Technology.

[14] J. Beringer, J.-F. Arguin, R. M. Barnett, K. Copic, O. Dahl, et al. "Review of Particle Physics". In: *Phys. Rev. D* 86.1 (2012), p. 010001.

[15] H. A. Bethe. "Bremsformel für Elektronen relativistischer Geschwindigkeit". In: *Zeitschrift für Phys.* 76.5-6 (1932), pp. 293–299.

[16] D. Bhattacharya, T. J. O'Neill, A. Akyüz, J. Samimi, and A. D. Zych. "Prototype TIGRE Compton γ-ray balloon-borne telescope". In: *New Astron. Rev.* 48.1-4 (2004), pp. 287–292.

[17] P. F. Bloser, S. D. Hunter, J. M. Ryan, M. McConnell, R. S. Miller, T. N. Jackson, B. Bai, and S. Jung. "Applications of gas imaging micro-well detectors to an advanced Compton telescope". In: *New Astron. Rev.* 48.1-4 (2004), pp. 299–303.

[18] P. F. Bloser, F. Schopper, R. Andritschke, G. Kanbach, A. Zoglauer, and P. Lechner. "Development of silicon strip detectors for a medium energy gamma-ray telescope". In: *Nucl. Instruments Methods Phys. Res. Sect. A* 512.1-2 (2003), pp. 220–228.

[19] M. M. Blouke, J. R. Janesick, J. E. Hall, M. W. Cowens, and P. J. May. "800 $\times$ 800 charge-coupled device image sensor". In: *Opt. Eng.* 22.5 (1983), pp. 607–614.

[20] S. E. Boggs, W. Coburn, D. M. Smith, J. D. Bowen, P. Jean, J. M. Kregenow, R. P. Lin, and P. von Ballmoos. "Overview of the Nuclear Compton Telescope". In: *New Astron. Rev.* 48.1–4 (2004), pp. 251–255.

[21] S. E. Boggs and P. Jean. "Simulated Performance of a Germanium Compton Telescope". In: *Proc. 4th INTEGRAL Work.* Alicante, Spain, Oct. 2000. arXiv: 0010331 [astro-ph].

[22] S. E. Boggs, J. D. Kurfess, and J. Ryan. *Advanced Compton Telescope*. Tech. rep. NASA, 2005.

[23] N. Bohr. "On the theory of the decrease of velocity of moving electrified particles on passing through matter". In: *London, Edinburgh, Dublin Philos. Mag. J. Sci.* 25.145 (1913), pp. 10–31.

[24] W. S. Boyle and G. E. Smith. "Charge coupled semiconductor devices". In: *Bell Syst. Tech. J.* 49.4 (1970), pp. 587–593.

[25] W. H. Bragg. *Studies in Radioactivity*. London: Macmillan and Co., Ltd., 1912.

[26] F. Brown. *Fundamentals of Monte Carlo Particle Transport*. Lecture notes, available at https://laws.lanl.gov/vhosts/mcnp.lanl.gov/pdf_files/la-ur-05-4983.pdf. Accessed: 2013-12-1. Document LA-UR-05-4983. 2005.

[27] E. Caroli, J. B. Stephen, G. Cocco, L. Natalucci, and A. Spizzichino. "Coded aperture imaging in X- and gamma-ray astronomy". In: *Space Sci. Rev.* 45.3-4 (1987).

[28] A. Castoldi, P. Rehak, and P. Holl. "Signal charge sharing in multilinear drift detectors: design and experimental characterization". In: *IEEE Trans. Nucl. Sci.* 44.2 (1997), pp. 134–141.

[29] V. A. Chechin, L. P. Kotenko, G. I. Merson, and V. C. Yermilova. "The relativistic rise of the track density in bubble chambers". In: *Nucl. Instr. Meth.* 98.3 (1972), pp. 577–587.

[30] D. H. Chivers. private communication. 2010.

[31] D. H. Chivers, A. Coffer, B. Plimley, and K. Vetter. "Impact of measuring electron tracks in high-resolution scientific charge-coupled devices within Compton imaging systems". In: *Nucl. Instruments Methods Phys. Res. Sect. A* 654.1 (2011), pp. 244–249.

[32] A. Coffer. private communication. 2008.

[33] A. Coffer. private communication. 2012.

[34] A. Compton. "A Quantum Theory of the Scattering of X-rays by Light Elements". In: *Phys. Rev.* 21.5 (1923), pp. 483–502.

[35] T. Çonka-Nurdan, K. Nurdan, F. Constantinescu, B. Freisleben, N. A. Pavel, and A. H. Walenta. "Impact of the detector parameters on a Compton camera". In: *IEEE Trans. Nucl. Sci.* 49.3 (2002), pp. 817–821.

[36] C. Damerell. "Applications of silicon detectors in high energy physics and astrophysics". In: *Nucl. Instr. Meth. Phys. Res.* 226 (1984), pp. 26–33.

[37] L. T. Dauer, P. Zanzonico, R. M. Tuttle, D. M. Quinn, and H. W. Strauss. "The Japanese tsunami and resulting nuclear emergency at the Fukushima Daiichi power facility: technical, radiologic, and response perspectives." In: *J. Nucl. Med.* 52.9 (2011), pp. 1423–1432.

[38] M. A. Deleplanque, I.-Y. Lee, K. Vetter, G. J. Schmid, F. S. Stephens, et al. "GRETA: utilizing new concepts in γ-ray detection". In: *Nucl. Instruments Methods Phys. Res. Sect. A* 430.2-3 (1999), pp. 292–310.

[39] *Quadrennial Homeland Security Review*. `http://www.dhs.gov/xlibrary/assets/qhsr_report.pdf`. Accessed: 2014-4-8. U.S. Department of Homeland Security, 2010.

[40] N. Dogan, D. K. Wehe, and G. F. Knoll. "Multiple Compton scattering gamma ray imaging camera". In: *Nucl. Instruments Methods Phys. Res. Sect. A* 299 (1990), pp. 501–506.

[41] J. G. Dreyer. "Development of Superconducting High-Resolution Gamma-Ray Spectrometers for Nuclear Safeguards". PhD thesis. University of California, Berkeley, 2012.

[42] *Commonly Encountered Radionuclides*. `http://www.epa.gov/rpdweb00/radionuclides/index.html`. Accessed: 2013-11-20. U.S. Environmental Protection Agency.

[43] R. D. Evans. *The Atomic Nucleus*. Krieger Publishing Company, 1982.

[44] U. Fano. "Ionization yield of radiations. II. The fluctuations of the number of ions". In: *Phys. Rev.* 72.1 (1947), pp. 26–29.

[45] E. E. Fenimore and T. M. Cannon. "Coded aperture imaging with uniformly redundant arrays". In: *Appl. Opt.* 17.3 (1978), pp. 337–347.

[46] R. B. Firestone and L. P. Ekström. *WWW Table of Radioactive Isotopes*. `http://ie.lbl.gov/toi/`. Accessed: 2013-11-20.

[47] M. Frandes, A. Zoglauer, V. Maxim, and R. Prost. "A Tracking Compton-Scattering Imaging System for Hadron Therapy Monitoring". In: *IEEE Trans. Nucl. Sci.* 57.1 (2010), pp. 144–150.

[48] G. M. Frye. "Spark Chamber for Gamma-Ray Astronomy". In: *Rev. Sci. Instrum.* 37.10 (1966), p. 1340.

[49] A. Goldwurm. "Imaging techniques applied to the coded mask SIGMA telescope". In: *Exp. Astron.* 6.4 (1995), pp. 9–18.

[50] A. Goldwurm, P. Goldoni, A. Gros, J. Stephen, L. Foschini, et al. "Gamma-Ray Imaging with the Coded Mask IBIS Telescope". In: *4th INTEGRAL Work.* Bologna, Feb. 2001, pp. 1–4. arXiv: 0102386 [astro-ph].

[51] F. S. Goulding. "Semiconductor detectors - an introduction". In: *IEEE Trans. Nucl. Sci.* NS-25.2 (1978), pp. 916–920.

[52] Z. Guo and R. W. Hall. "Parallel Thinning with Two-Subiteration Algorithms". In: *Commun. ACM* 32.3 (1989), pp. 359–373.

[53] N. N. D. Gupta and S. K. Ghosh. "A Report on the Wilson Cloud Chamber and Its Applications in Physics". In: *Rev. Mod. Phys.* 18.2 (1946), pp. 225–290.

[54] A. Haefner and D. Gunter. private communication. 2013.

[55] T. Hasegawa, H. Hashiba, K. Akagi, T. Fujino, A. Kobayashi, and M. Matsuda. "A method of tomographic imaging using a multiple pinhole-coded aperture." In: *Radioisotopes* 27.6 (1978), pp. 311–7.

[56] E. Hatch, F. Boehm, P. Marmier, and J. DuMond. "Rotational and Intrinsic Levels in Tm^{169} and Lu^{175}". In: *Phys. Rev.* 104.3 (1956), pp. 745–752.

[57] T. Häupke, M. Kirsch, and R. Ölschläger. *Struck Innovative Systeme Homepage*. http://www.struck.de. Accessed: 2013-07-17.

[58] H. F. Helmken and G. G. Fazio. "Vidicon Spark Chamber Detector for Gamma-Ray Astronomy". In: *IEEE Trans. Nucl. Sci.* 13.1 (1966), pp. 486–492.

[59] S. E. Holland. "An Overview of CCD Development at Lawrence Berkeley National Laboratory". In: *Exp. Astron.* 14.2 (2002), pp. 83–89.

[60] S. E. Holland, C. J. Bebek, K. S. Dawson, J. H. Emes, M. H. Fabricius, et al. "High-voltage-compatable, fully depleted CCDs". In: *Proc. SPIE* 6276 (2006), pages.

[61] S. E. Holland, K. S. Dawson, N. P. Palaio, J. Saha, N. A. Roe, and G. Wang. "Fabrication of back-illuminated, fully depleted charge-coupled devices". In: *Nucl. Instruments Methods Phys. Res. Sect. A* 579.2 (2007), pp. 653–657.

[62] S. E. Holland, D. E. Groom, N. P. Palaio, R. J. Stover, and M. Wei. "Fully depleted, back-illuminated charge-coupled devices fabricated on high-resistivity silicon". In: *IEEE Trans. Electron Devices* 50.1 (2003), pp. 225–238.

[63] P. Horowitz and W. Hill. *The Art of Electronics*. Second. Cambridge University Press, 1989.

[64] E. B. Hughes, R. Hofstadter, A. Johansson, J. Rolfe, D. L. Bertsch, et al. "Characteristics of the telescope for high energy γ-ray astronomy selected for definition studies on the gamma ray observatory". In: *IEEE Trans. Nucl. Sci.* 27.1 (1980), pp. 363–369.

[65] G. J. Hurford, E. J. Schmahl, R. A. Schwartz, A. J. Conway, M. J. Aschwanden, et al. "The RHESSI Imaging Concept". In: *Sol. Phys.* 210.1-2 (2002), pp. 61–86.

[66] *INSAG-7, The Chernobyl Accident: Updating of INSAG-1*. Tech. rep. 75. Vienna, Austria: International Atomic Energy Agency, International Nuclear Safety Advisory Group, 1992.

[67] J. R. Janesick. *Scientific Charge-Coupled Devices*. First. SPIE Publications, 2001.

[68] S. Kabuki, K. Hattori, R. Kohara, E. Kunieda, A. Kubo, et al. "Development of Electron Tracking Compton Camera using micro pixel gas chamber for medical imaging". In: *Nucl. Instruments Methods Phys. Res. Sect. A* 580.2 (2007), pp. 1031–1035.

[69] O. Kadri, V. N. Ivanchenko, F. Gharbi, and A. Trabelsi. "GEANT4 simulation of electron energy deposition in extended media". In: *Nucl. Instruments Methods Phys. Res. Sect. B* 258.2 (2007), pp. 381–387.

[70] G. Kanbach, R. Andritschke, P. F. Bloser, F. Schopper, V. Schönfelder, and A. Zoglauer. "Concept study for the next generation medium-energy gamma-ray astronomy mission: MEGA". In: *Proc. SPIE* 4851 (2003), pp. 1209–1220.

[71] G. Kanbach, D. L. Bertsch, A. Favale, C. E. Fichtel, R. C. Hartman, et al. "The project EGRET (Energetic Gamma-Ray Experiment Telescope) on NASA's Gamma-Ray Observatory GRO". In: *Space Sci. Rev.* 49.1-2 (1988), pp. 69–84.

[72] R. M. Kippen. "The GEANT low energy Compton scattering (GLECS) package for use in simulating advanced Compton telescopes". In: 48.1–4 (2004), pp. 221–225.

[73] O. Klein and Y. Nishina. "Über die Streuung von Strahlung durch freie Elektronen nach der neuen relativistischen Quantendynamik von Dirac". In: *Zeitschrift für Phys.* 52.11-12 (1929), pp. 853–868.

[74] G. F. Knoll. *Radiation Detection and Measurement*. 4th. John Wiley & Sons, 2010.

[75] W. Kolbe. private communication. 2008.

[76] K. S. Krane. *Introductory Nuclear Physics*. John Wiley & Sons, 1988.

[77] H. Kubo, K. Hattori, S. Kabuki, S. Kurosawa, K. Miuchi, et al. "Balloon-borne sub-MeV gamma-ray imager using electron tracking gaseous TPC and scintillation camera". In: *IEEE Nucl. Sci. Symp.* (2006), pp. 406–410.

[78] J. D. Kurfess, W. N. Johnson, R. A. Kroeger, E. I. Novikova, B. F. Phlips, M. S. Strickman, and E. A. Wulf. "An advanced Compton telescope based on thick, position-sensitive solid-state detectors". In: *New Astron. Rev.* 48.1-4 (2004), pp. 293–298.

[79] *Lake Shore Cryotronics, Inc.* `http://lakeshore.com/`. Accessed: 2013-12-2.

[80] L. D. Landau. "On the energy loss of fast particles by ionization". In: *J. Phys.* 8 (1944), p. 201.

[81] B. Leach. *Astronomical Research Cameras, Inc.* `http://www.astro-cam.com`.

[82] I.-Y. Lee. "The GAMMASPHERE". In: *Nucl. Phys. A* 520 (1990), pp. 641c–655c.

[83] N. Lund. "A study of focusing telescopes for soft gamma rays". In: *Exp. Astron.* 2 (1992), pp. 259–273.

[84] G. Lutz. *Semiconductor Radiation Detectors*. Springer, 2007.

[85] W. A. McKinley and H. Feshbach. "The Coulomb Scattering of Relativistic Electrons by Nuclei". In: *Phys. Rev.* 74.12 (1948), pp. 1759–1763.

[86] J. E. McKisson, P. S. Haskins, G. W. Phillips, S. E. King, R. A. August, R. B. Piercey, and R. C. Mania. "Demonstration of three-dimensional imaging with a germanium Compton camera". In: *IEEE Trans. Nucl. Sci.* 41.4 (2003), pp. 1221–1224.

[87] L. Mihailescu, K. Vetter, M. T. Burks, E. L. Hull, and W. W. Craig. "SPEIR: A Ge Compton camera". In: *Nucl. Instruments Methods Phys. Res. Sect. A* 570.1 (2007), pp. 89–100.

[88] C. Møller. "Zur Theorie des Durchgangs schneller Elektronen durch Materie". In: *Ann. Phys.* 406.5 (1932), pp. 531–585.

[89] R. Mowatt-Larssen. *Al Qaeda Weapons of Mass Destruction Threat: Hype or Reality?* Cambridge, MA, 2010.

[90] G. Muehllehner and J. S. Karp. "Positron emission tomography." In: *Phys. Med. Biol.* 51.13 (July 2006), R117–37.

[91] *ESTAR: stopping-power and range tables for electrons*. http://physics.nist.gov/PhysRefData/Star/Text/ESTAR.html. Accessed: 2013-11-20. National Institute of Standards and Technology.

[92] *Results of NSS 2014 | Nuclear Security Summit 2014*. https://www.nss2014.com/en/nss-2014/results. Accessed: 2014-4-8. 2014.

[93] U. G. Oberlack, K. Bennett, H. Bloemen, R. Diehl, C. Dupraz, et al. "The COMPTEL 1.809 MeV all-sky image". In: *Astron. Astrophys. Suppl. Ser.* 120 (1996), pp. 311–314.

[94] H. Olsen. "Opening Angles of Electron-Positron Pairs". In: *Phys. Rev.* 131.1 (1963), pp. 406–415.

[95] H. M. Oluseyi, A. Karcher, W. F. Kolbe, B. T. Turko, G. Aldering, et al. "Characterization and deployment of large-format fully depleted back-illuminated p-channel CCDs for precision astronomy". In: *Proc. SPIE* 5570 (2004), pp. 515–524.

[96] T. J. O'Neill, F. Ait-Ouamer, I. Schwartz, O. T. Tümer, R. S. White, and A. D. Zych. "A New Compton Gamma Ray Telescope with Recoil Electron Tracking". In: *Int. Cosm. Ray Conf.* 1991, pp. 471–474.

[97] T. J. O'Neill, D. Bhattacharya, S. C. Blair, G. L. Case, O. T. Tümer, R. S. White, and A. D. Zych. "The TIGRE desktop prototype results for 511 and 900 keV gamma rays". In: *IEEE Trans. Nucl. Sci.* 42.4 (1995), pp. 933–939.

[98] C. E. Ordonez, A. Bolozdynya, and W. Chang. "Doppler broadening of energy spectra in Compton cameras". In: *IEEE Nucl. Sci. Symp.* 1. 1997, pp. 1361–1365.

[99] R. Orito, H. Kubo, K. Miuchi, T. Nagayoshi, A. Takada, T. Tanimori, and M. Ueno. "A novel design of the MeV gamma-ray imaging detector with Micro-TPC". In: *Nucl. Instruments Methods Phys. Res. Sect. A* 513.1-2 (2003), pp. 408–412.

[100] G. Ottaviani, L. Reggiani, C. Canali, F. Nava, and A. Alberigi Quaranta. "Hole drift velocity in silicon". In: *Phys. Rev. B* 12.8 (1975), pp. 3318–3329.

[101] R. Pavlovsky. private communication. 2012.

[102] R. Pavlovsky and P. Barton. private communication. 2014.

[103] D. B. Pelowitz, J. W. Durkee, J. S. Elson, M. L. Fensin, J. S. Hendricks, et al. *MCNPX 2.7.0 Extensions*. https://laws.lanl.gov/vhosts/mcnp.lanl.gov/pdf_files/la-ur-11-02295_mcnpx270.pdf. Accessed: 2013-12-1. Document LA-UR-11-02295. 2011.

[104] L. Pienkowski, J. Jastrzebski, J. Tys, T. Batsch, P. Jaracz, et al. "Isotopic Composition of the Radioactive Fallout in Eastern Poland after the Chernobyl Accident". In: Journal of.117 (1987), pp. 379–409.

[105] B. Plimley, D. H. Chivers, A. Coffer, and K. Vetter. "Experimental Benchmark of Electron Trajectory Reconstruction Algorithm for Advanced Compton Imaging". In: *IEEE Trans. Nucl. Sci.* 60.3 (2013), pp. 2308–2313.

[106] S. G. Prussin. *Nuclear Physics for Applications*. Wiley-VCH, 2007.

[107] B. M. Schäfer. "Coded mask imaging of extended sources with Gaussian random fields". In: *Mon. Not. R. Astron. Soc.* 000 (2003), pp. 1–10. arXiv: 0407286v1 [arXiv:astro-ph].

[108] G. J. Schmid, M. A. Deleplanque, I.-Y. Lee, F. S. Stephens, K. Vetter, et al. "A γ-ray tracking algorithm for the GRETA spectrometer". In: *Nucl. Instruments Methods Phys. Res. Sect. A* 430.1 (1999), pp. 69–83.

[109] V. Schönfelder, A. Hirner, and K. Schneider. "A telescope for soft gamma ray astronomy". In: *Nucl. Instr. Meth.* 107.2 (1973), pp. 385–394.

[110] M. Singh. "An electronically collimated gamma camera for single photon emission computed tomography. Part I: Theoretical considerations and design criteria". In: *Med. Phys.* 10.4 (1983), p. 421.

[111] G. K. Skinner. "Imaging with coded-aperture masks". In: *Nucl. Instr. Meth. Phys. Res.* 221.1 (1984), pp. 33–40.

[112] A. R. Smith, R. J. McDonald, D. C. Hurley, S. E. Holland, D. E. Groom, et al. "Radiation events in astronomical CCD images". In: *Proc. SPIE* 4669 (2002), pp. 172–183.

[113] H. Spieler. *Semiconductor Detector Systems*. Oxford University Press, 2005.

[114] S. M. Sze and K. K. Ng. *Physics of Semiconductor Devices*. 3rd. Hoboken, New Jersey: John Wiley & Sons, 2007.

[115] T. Tabata, P. Andreo, and K. Shinoda. "An analytic formula for the extrapolated range of electrons in condensed materials". In: *Nucl. Instruments Methods Phys. Res. Sect. B* 119.4 (1996), pp. 463–470.

[116] T. Tabata, V. Moskvin, P. Andreo, V. Lazurik, and Y. Rogov. "Extrapolated ranges of electrons determined from transmission and projected-range straggling curves". In: *Radiat. Phys. Chem.* 64.3 (2002), pp. 161–167.

[117] K. Tagami, S. Uchida, Y. Uchihori, N. Ishii, H. Kitamura, and Y. Shirakawa. "Specific activity and activity ratios of radionuclides in soil collected about 20 km from the Fukushima Daiichi Nuclear Power Plant: Radionuclide release to the south and southwest." In: *Sci. Total Environ.* 409.22 (2011), pp. 4885–8.

[118] A. Takada, H. Kubo, H. Nishimura, K. Ueno, K. Hattori, et al. "Observation of Diffuse Cosmic and Atmospheric Gamma Rays At Balloon Altitudes With an Electron-Tracking Compton Camera". In: *Astrophys. J.* 733.1 (2011), p. 13.

[119] A. Takada, T. Tanimori, H. Kubo, K. Miuchi, S. Kabuki, et al. "Simulation Study for the Higher Sensitivity of an Electron-Tracking Compton Camera at over 1 MeV". In: *IEEE Nucl. Sci. Symp.* 2011, pp. 1215–1221.

[120] M. Takahashi, S. Kabuki, K. Hattori, N. Higashi, S. Iwaki, et al. "Development of an electron-tracking Compton Camera using CF_4 gas at high pressure for improved detection efficiency". In: *Nucl. Instruments Methods Phys. Res. Sect. A* 628.1 (2011), pp. 150–153.

[121] R. Talman. "On the statistics of particle identification using ionization". In: *Nucl. Instr. Meth.* 159.1 (1979), pp. 189–211.

[122] T. Tanimori, H. Kubo, K. Miuchi, T. Nagayoshi, R. Orito, A. Takada, A. Takeda, and M. Ueno. "MeV [gamma]-ray imaging detector with micro-TPC". In: *New Astron. Rev.* 48.1–4 (2004), pp. 263–268.

[123] R. W. Todd, J. M. Nightingale, and D. B. Everett. "A proposed γ camera". In: *Nature* 251 (1974), pp. 132–134.

[124] O. T. Tümer, D. Bhattacharya, S. C. Blair, G. L. Case, D. D. Dixon, et al. "The Tracking and Imaging Gamma-Ray Experiment (TIGRE) for 300 keV–100 MeV gamma-ray astronomy". In: *Proc. SPIE* 2305 (1994), pp. 51–62.

[125] K. Ueno, T. Mizumoto, K. Hattori, N. Higashi, S. Iwaki, et al. "Development of the balloon-borne sub-MeV gamma-ray Compton camera using an electron-tracking gaseous TPC and a scintillation camera". In: *J. Instrum.* 7.01 (2012), pp. C01088–C01088.

[126] K. Vetter, M. T. Burks, C. Cork, M. Cunningham, D. H. Chivers, et al. "High-sensitivity Compton imaging with position-sensitive Si and Ge detectors". In: *Nucl. Instruments Methods Phys. Res. Sect. A* 579.1 (2007), pp. 363–366.

[127] K. Vetter, M. T. Burks, and L. Mihailescu. "Gamma-ray imaging with position-sensitive HPGe detectors". In: *Nucl. Instruments Methods Phys. Res. Sect. A* 525.1-2 (2004), pp. 322–327.

[128] P. M. Wanet, A. Sand, and J. Abramovici. "Physical and clinical evaluation of high-resolution thyroid pinhole tomography". In: *J. Nucl. Med.* 37.12 (1996), pp. 2017–2020.

[129] D. C. Wells, E. W. Greisen, and R. H. Harten. "FITS – a Flexible Image Transport System". In: *Astron. Astrophys. Suppl. Ser.* 44 (1981), p. 363.

[130] D. H. Wilkinson. "Ionization energy loss by charged particles, Part I. The Landau distribution". In: *Nucl. Instruments Methods Phys. Res. Sect. A* 383.2 (1996), pp. 513–515.

[131] B. Zhang and G. L. Zeng. "High-resolution versus high-sensitivity SPECT imaging with geometric blurring compensation for various parallel-hole collimation geometries". In: *IEEE Trans. Inf. Technol. Biomed.* 14.4 (2010), pp. 1121–1127.

[132] K. P. Ziock, J. Kammeraad, A. Dougan, D. Archer, D. Beckedahl, et al. *Full volume imaging gamma-ray detectors for enhanced sensitivity*. Tech. rep. Lawrence Livermore National Laboratory, 2001.

[133] A. Zoglauer. "First Light for the Next Generation of Compton and Pair Telescopes". PhD thesis. Technische Universität München, 2005.

[134] A. Zoglauer and G. Kanbach. "Doppler broadening as a lower limit to the angular resolution of next-generation Compton telescopes". In: *Proc. SPIE* 4851 (2003), pp. 1302–1309.